

**Multiscale Structure-Performance Relationships  
in Supported Palladium Catalysis  
for Multiphase Hydrogenations**



# **Multiscale Structure-Performance Relationships in Supported Palladium Catalysis for Multiphase Hydrogenations**

Proefschrift

ter verkrijging van de graad van doctor  
aan de Technische Universiteit Delft,  
op gezag van de Rector Magnificus prof. ir. K.C.A.M. Luyben,  
voorzitter van het College voor Promoties,  
in het openbaar te verdedigen  
op maandag 10 december 2012 om 12:30 uur

door

Jasper Jacobus Wilhelmus BAKKER

scheikundig ingenieur  
geboren te Dordrecht

Dit proefschrift is goedgekeurd door de promotoren:

Prof. dr. ir. M.T. Kreutzer

Prof. dr. F. Kapteijn

Prof. dr. J.A. Moulijn

Samenstelling promotiecommissie:

|                                 |   |
|---------------------------------|---|
| Rector Magnificus               | voorzitter                                |
| Prof. dr. ir. M.T. Kreutzer     | Technische Universiteit Delft, promotor   |
| Prof. dr. F. Kapteijn           | Technische Universiteit Delft, promotor   |
| Prof. dr. J.A. Moulijn          | Technische Universiteit Delft, promotor   |
| Prof. dr. ir. A.I. Stankiewicz  | Technische Universiteit Delft             |
| Prof. dr. J.W. Niemantsverdriet | Technische Universiteit Eindhoven         |
| Dr. ir. T.A. Nijhuis            | Technische Universiteit Eindhoven         |
| Ir. R.W.E.G. Reintjens          | DSM Innovative Synthesis B.V.             |
| Prof. dr. ir. C.R. Kleijn       | Technische Universiteit Delft, reservelid |

This research was partially financially supported by the DOW Chemical Company (Chapter 2 and 3) and DSM N.V. (Chapter 4).

Proefschrift, Technische Universiteit Delft

Met samenvatting in het Nederlands / With summary in Dutch

ISBN 978-90-6464-612-6

© 2012 by J.J.W. Bakker

All rights reserved. No part of the material protected by this copyright notice may be reproduced or utilised in any form or by any means, electronic or mechanical, including photocopying, recording or any information storage and retrieval system, without written permission of the author.

*Ter nagedachtenis aan mijn vader*



# Contents

## Chapter 1

|                    |   |
|--------------------|---|
| Introduction ..... | 1 |
|--------------------|---|

## Chapter 2

|   |    |
|---|----|
| Hydrodynamic properties of a novel ‘open wall’ monolith reactor ..... | 23 |
|---|----|

## Chapter 3

|   |    |
|---|----|
| Enhancement of catalyst performance using pressure pulses on macroporous structured palladium catalysts ..... | 45 |
|---|----|

## Chapter 4

|  |    |
|--|----|
| Heterogeneously palladium catalyzed continuous-flow hydrogenation using Taylor flow in capillary columns ..... | 75 |
| Appendix A - Supporting Information to Chapter 4 .....   | 85 |

## Chapter 5

|   |     |
|---|-----|
| Catalyst performance changes induced by palladium phase transformation in the hydrogenation of benzonitrile ..... | 117 |
| Appendix B - Supporting Information to Chapter 5 .....  | 157 |

## Chapter 6

|                 |     |
|-----------------|-----|
| Evaluation..... | 163 |
|-----------------|-----|

## Chapter 7

|                                      |     |
|--------------------------------------|-----|
| Summary .....                        | 173 |
| Samenvatting .....                   | 181 |
| Publications and presentations ..... | 185 |
| Dankwoord / Acknowledgements .....   | 189 |
| Curriculum Vitae.....                | 191 |



# 1

## Introduction

---

This Chapter provides a brief introduction into the different topics of catalysis engineering dealt with in this thesis focusing on the structure-performance relationship on all length scales of supported palladium catalysis applied for multiphase hydrogenation reactions.

---

## Catalytic hydrogenation by supported palladium catalysts

### *Hydrogenation*

Hydrogenation is a reaction of great industrial importance that involves the addition of hydrogen to an organic compound usually to reduce the number of unsaturated carbon-carbon bonds [1a, b]. Hydrogenation is a highly exothermic reaction and is generally carried out in the presence of a heterogeneous catalyst to increase reaction rates under moderate temperatures. In principle, gaseous dihydrogen ( $H_2$ ) gas is the hydrogenating agent. However, other hydrogen sources can be provided by hydrogen donor solvents or via transfer from one reactant molecule to another. On lab scale often liquid phase reduction is applied.

Hydrogenation yields a myriad of useful chemicals, and its use has increased profoundly from fine chemistry and pharmaceuticals, via food industry to bulk petrochemical refining industry. Examples are catalytic hydrogenations (10-20% of all reaction steps) in the synthesis of vitamins, fat hardening, and hydrogenation of alkenes and aromatics to paraffins and naphthenes, respectively. Besides the saturation of double and triple C-C bonds, hydrogenation can be used to break bonds (hydrogenolysis) and eliminate or add/change functionalities to a molecule. Examples of hydrogenolysis reactions important in petrochemical and biomass conversion processes are hydrodesulfurization (HDS), hydrodenitrogenation (HDN), and hydrodeoxygenation (HDO). Examples of changing the functionality of organic molecules are, *e.g.*, the hydrogenation of an azide or nitrile group resulting in primary amines (by hydrogenation), secondary amines (by condensation) and simple hydrocarbons (by hydrogenolysis of the C-N bond). Isomerization, reductive addition and hydrolysis are examples of other reactions that can take place under hydrogenation conditions.

A generally accepted mechanism of heterogeneously catalyzed hydrogenations was proposed by Horiuti and Polanyi in 1934 [1c]. Horiuti and Polanyi postulated that ethylene hydrogenation is not simply an addition of  $H_2$  to the double bond of ethylene. However, the hydrogenation of ethylene proceeds via a sequence of elementary steps of single dissociatively adsorbed H-atoms that are subsequently added to the adsorbed unsaturated ethylenic reactant via a *reversible* H-addition followed by an *irreversible* H-addition (Fig. 1.1). This mechanistic picture did not change significantly during the last 80 years and it is thus still considered an adequate description for the hydrogenation of unsaturated organic

compounds over transition metals [1d]. However, note that other hydrogenation mechanisms are proposed in literature, *e.g.*, hydrogenation via a hydrocarbonaceous overlayer [1e].

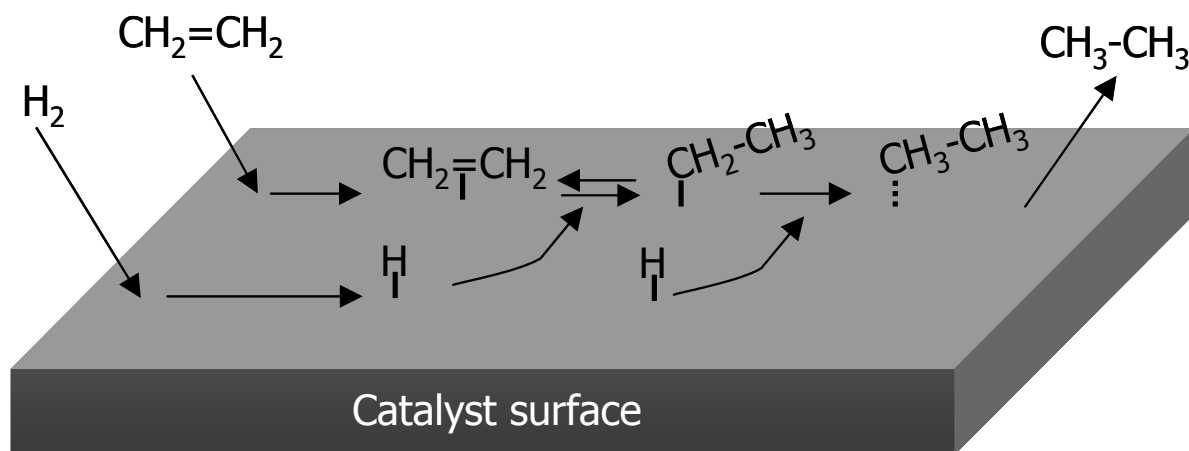


**Fig. 1.1.** Schematic representation of the Horiuti-Polanyi mechanism of the hydrogenation of ethylene on the surface of a solid catalyst.

### Palladium

Noble metals are the most commonly used heterogeneous catalysts, but also copper, nickel and various mixed metal oxides are being used, both on lab and industrial scale. This thesis focuses on Palladium (Pd), which is one of the noble metals and part of the transition metals, more specifically Group VIII of the periodic table of the elements. Pd is known for its high activity in almost all hydrogenation reactions [2]. An industrial example of the use of supported Pd catalysts is during the production of polymer-grade ethylene ( $C_2H_4$ ) where the effective removal of traces acetylene ( $C_2H_2$ ) via selective hydrogenation is imperative without hydrogenating ethylene [3].

Pd, discovered by William Hyde Wollaston in 1803, has an atomic weight of 106.4 g/mol, a density of 12.02 g/cm<sup>3</sup>, an electron configuration of [Kr] 4d<sup>10</sup>, a face centered cubic (FCC) crystal structure and it behaves as a soft acid (low electronic orbital energy level for accepting electrons). Although Pd is considered as an expensive metal, currently compared to other noble metals (*i.e.*, platinum, gold or rhodium) its base price is 2 to 3-times lower [4]. Pd can adsorb over 900 times its volume of hydrogen forming a solid solution with hydrogen, *i.e.*, Pd  $\beta$ -hydride (Pd  $\beta$ -hydride is metallic Pd that contains a substantial quantity of hydrogen within its crystal lattice), which is expelled when heated. Another important property of Pd is that H<sub>2</sub> molecules dissociate spontaneously at the surface, *i.e.*, H<sub>2</sub> molecules with low kinetic energy dissociatively adsorb at Pd surfaces with a large initial sticking coefficient. The dissociation

of H<sub>2</sub> on Pd is thus non-activated as compared to, *e.g.*, Pt/H<sub>2</sub> and Cu/H<sub>2</sub> that exhibits weakly activated and activated dissociative adsorption, respectively [5]. Pd can also be easily reduced (temperature of reduction  $\sim 20^{\circ}\text{C}$ ) compared to the other noble metals (*e.g.*, temperature of reduction of platinum  $\sim 350^{\circ}\text{C}$ ) which makes it easier to handle prior to hydrogenation and decreases processing costs.

### *Heterogeneous catalysis by supported Pd catalysts*

Heterogeneous Pd catalysts are generally dispersed as nanometer-sized crystallites (Fig. 1.2) on metal oxides or carbon supports with a high surface to bulk ratio. The support stabilizes the Pd crystallites against sintering or leaching. The most conventional supports for Pd-based hydrogenation catalysts are silica (SiO<sub>2</sub>) and  $\gamma$ -alumina ( $\gamma$ -Al<sub>2</sub>O<sub>3</sub>). These porous supports provide large surface areas in the order of 200 to 400 m<sup>2</sup>/g and they can also have intrinsic catalytic activity, related to their Brønsted or Lewis acidity/basicity. In addition, (strong) metal-support effects, hydrogen spillover effects and formation of coke, among others, make selecting the right support crucial for optimal catalyst performance.

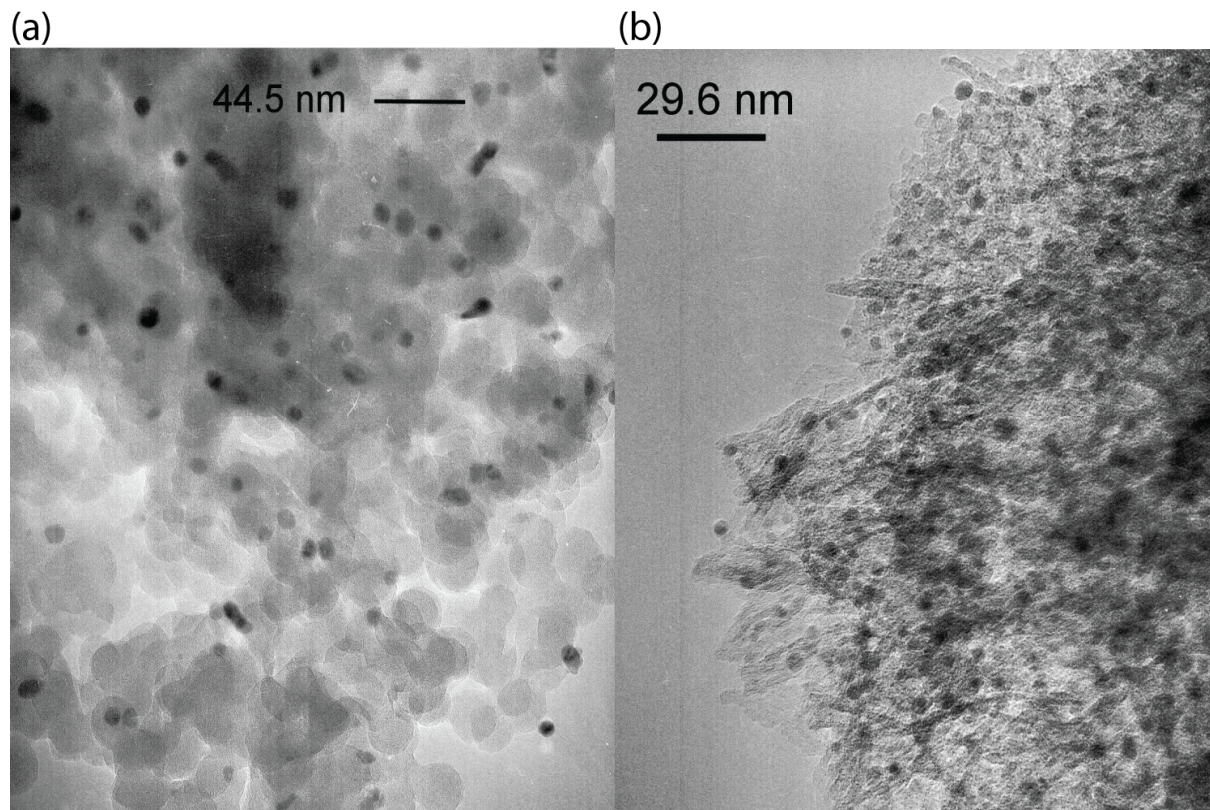


**Fig. 1.2.** TEM micrographs of nanosized Pd crystallites dispersed on colloidal silica deposited on a monolith wall (a).  $\gamma$ -Al<sub>2</sub>O<sub>3</sub>-supported Pd crystallites deposited on the wall of a capillary (b). The small black dots are Pd crystallites (as determined by EDX analysis) with an average crystallite size of 10 and 5 nm, respectively.

### *Synthesis of supported Pd catalysts*

The synthesis of these supported Pd catalysts comprises many separate preparation steps (*i.e.*, support pre-treatment, metal adsorption, washing, drying, calcination, reduction). Separately or in combination these steps can influence the final crystallite size (*i.e.*, metal dispersion) of the active species, the chemical environment around the active species and the concentration profile within the support (distribution). Thus the performance of the final catalyst can vary a lot depending on the catalyst preparation. For the deposition of Pd onto metal oxide supports, impregnation with aqueous or organic solutions by using Pd precursors as anionic  $\text{H}_2\text{PdCl}_4$ , neutral  $\text{Pd}(\text{OAc})_2$  or cationic  $\text{Pd}(\text{NH}_3)_4(\text{NO}_3)_2$  are often used [6]. In this thesis, all Pd catalysts were synthesized by wet impregnation using a neutral trimeric  $[\text{Pd}(\text{OAc})_2]_3$  precursor dissolved in toluene [7].  $\text{Pd}(\text{OAc})_2$  was selected since it is a weak field ligand ( $\pi$ -donor ligand), with a lower Pd-ligand bond strength, making it easier to substitute the ligands (OAc) with surface groups of the support. Moreover, Pd is a 12 electron complex which makes it ‘eager’ to add more ligands also enhancing interaction with support groups. The adsorption of the Pd precursor on the heterogeneous support will mainly occur via the weak to medium interaction (compared to strong precursor-support interactions valid for ionic precursors) with hydroxyl groups and coordinatively unsaturated sites (*e.g.*,  $\text{Al}^{3+}$ ) [8].

### *Intrinsic properties of a catalyst*

Intrinsic properties that affect catalyst performance include steric factors, electronic factors, and ensemble effects. A non-exhaustive list of intrinsic properties are the size (and distribution thereof) of metal crystallites, crystallographic planes and ‘defective’ sites on the surface of the crystallites and synergetic effects between different metals (*e.g.*, bimetallic catalyst), promoters (*e.g.*, adding electropositive alkali metals), and supports (*e.g.*, strong metal-support interactions (SMSI)). Note that the reaction environment changes the catalyst, and some of its properties, *e.g.*, the tendency of a metal to form hydrides or carbides, only reveal themselves when the catalyst is under operating conditions.

The ‘defect’ sites on the surface of a catalyst (step, kink, holes etc.) are coordinatively unsaturated and facile energy dissipation results in the most active sites for catalysis. The terrace or plane sites are saturated and are less or non active for catalysis. However, these plane sites are favorable for product desorption. Rate and product distribution that depend on the metal crystallite size are called *structure sensitive* reactions. Structure sensitivity is related to how reactants chemisorb on different parts of the surface of a metal crystallite, *e.g.*, step,

kink, and plane sites. In general, hydrogenolysis and coking are *structure sensitive* reactions and hydrogenation and dehydrogenation are *structure insensitive* reactions. However, there is no real consensus in the scientific literature for possible structure insensitivity and every hydrogenation reaction should be studied separately.

### *The role of a catalyst*

The role of a catalyst is to provide an energetically favorable pathway for the desired reaction, thereby increasing reaction rates by means of lowering the activation energy and increasing selectivity. The most important aspect of catalysis by *d*-metals is the involvement of the localized (compared to non-localized *s* and *p* bands) and partially filled *d*-bands with energies close to the Fermi level (measure of the energy of the least tightly held electrons within a solid). The *d*-band needs to be only partially filled with electrons so that it can accept electrons from adsorbing reactants since a full *d*-band cannot accept electrons. Catalytically active metals possess between 6 and 10 *d*-electrons and their localized *d*-band causes electrostatic repulsion and splitting between molecular bonding and antibonding orbitals of the reactant. This *d*-band interacts with molecular bonding and antibonding orbitals of the chemisorbed reactant, primarily the frontier orbitals, *i.e.*, highest occupied molecular orbital (HOMO) and lowest unoccupied molecular orbital (LUMO) to accept and donate electrons, respectively. The HOMO and LUMO nearly always dominate the bonding because strong interactions between orbitals require that the energy difference is small (and overlap between the orbitals is large).

Due to the interaction between the *d*-band and the frontier orbitals, new metal-reactant orbitals are formed (thus making new external bonds) and internal reactant bonds are weakened or even broken. Moreover, new bonds can be formed between different intermediate surface species as can be seen in Fig. 1.1. Finally, the Pauli repulsion between the *d*-band and the electron orbitals of the product causes this newly formed product to desorb. The interaction between *d*-metals and reactants follow Sabatier's principle: one should avoid too strong adsorption (in that case desorption is rate limiting), which occurs for metals that have a low *d*-band filling and one should avoid too weak adsorption, which occurs for metals with more fully filled *d*-bands. Therefore, an optimum in catalyst performance exists (volcano shape). This correlation where the catalyst activity scales with the adsorption heat of the reactant is called the Brønsted-Polanyi relation [9].

### *Bonding to metal surfaces*

Often the Blyholder model is used to explain diatomic bonding to metal surfaces. In the Blyholder model, with CO as adsorbing model species, a dative bond between the  $5\sigma$  and metal  $d$ -states is formed leading to charge donation which is compensated by backdonation into the molecular  $2\pi^*$  orbital [10]. However, this model is not fully sufficient; hence modifications were made in the Nilsson-Pettersson model where the  $\sigma$ -donation leads to repulsive interaction whereas the  $\pi$ -interaction causes the attraction between the metal surface and the adsorbing molecule. This  $\sigma$ -repulsion is then minimized by rehybridization of the electronic structure. Moreover, the  $\sigma$ -repulsion is minimized and the  $\pi$ -attraction maximized when the center of the  $d$ -band shifts to the Fermi level. This is how bonding is related to trends in energies of adsorption as described in the  $d$ -band model of Nørskov and Hammer [11]. In case of adsorption of unsaturated hydrocarbons a similar model is used as the Blyholder model: the Dewar-Chatt-Duncanson model where there is  $\pi$ -donation and  $\pi^*$ -backdonation to and from the metal, respectively. However, in contrast to the Blyholder model for diatomic molecules, this model is adequate in describing the bonding of unsaturated hydrocarbons to metals [12].

As mentioned briefly in the previous paragraph, the origin of catalytic trends and reactivity of a heterogeneous  $d$ -metal catalyst can be explained by the  $d$ -band model that was developed by Nørskov and Hammer. This model correlates catalytic reactivity with the energy difference between the center of the  $d$ -band and the Fermi level (Fig. 1.3). Reactivity increases when the  $d$ -band center shifts closer to the Fermi level. Several important parameters of Pd and other noble metals are listed in Table 1.1 [11, 12, 15]. Pd differs from the other noble metals since it has the thinnest  $d$ -band [13] which means that the  $d$ -orbitals are spatially less extended thereby increasing the stabilization of repulsion-dominated adsorption mode of a reactant (metal-HOMO interactions) and explaining the high selectivity for hydrogenating the ethylenic bond. For example, the repulsive interaction with a C=C group (HOMO) becomes stronger with increasing  $d$ -band width. Hence, the chemisorption of C=C is more probable for Pd. In contrast, the attractive interaction with a C=O group (LUMO) increases with increasing  $d$ -band width. The backdonation properties of Pd, when comparing the  $d$ -band centers (and Fermi levels) of the noble metals listed in Table 1.1, are higher than that of platinum and lower than that of ruthenium and rhodium. Note that chemoselectivity can also be (partially or fully) governed by, *e.g.*, steric control related to surface crowdedness, reactant geometry, and size confinement issues in small pores.

*Kinetic models*

Kinetic parameters can be estimated from reaction concentration data using several models with (some) physical meaning. The most used models are the ones developed by Langmuir-Hinshelwood and Hougen-Watson [14]. The Langmuir-Hinshelwood model proposes that both reacting molecules adsorb on the catalyst surface and undergo a bimolecular reaction. This model propose that the rate of reaction is governed by a surface reaction (rate determining step), thus all of the adsorption/desorption steps are in quasi-equilibrium and a Langmuir isotherm can be used to relate surface to bulk concentrations. In addition, Hougen-Watson type models propose that also adsorption or desorption steps can be the rate limiting step. Another often applied model is the Eley-Rideal type that proposes that a reaction is taking place between an adsorbed surface species and an impinging (non-adsorbed) molecule [14].

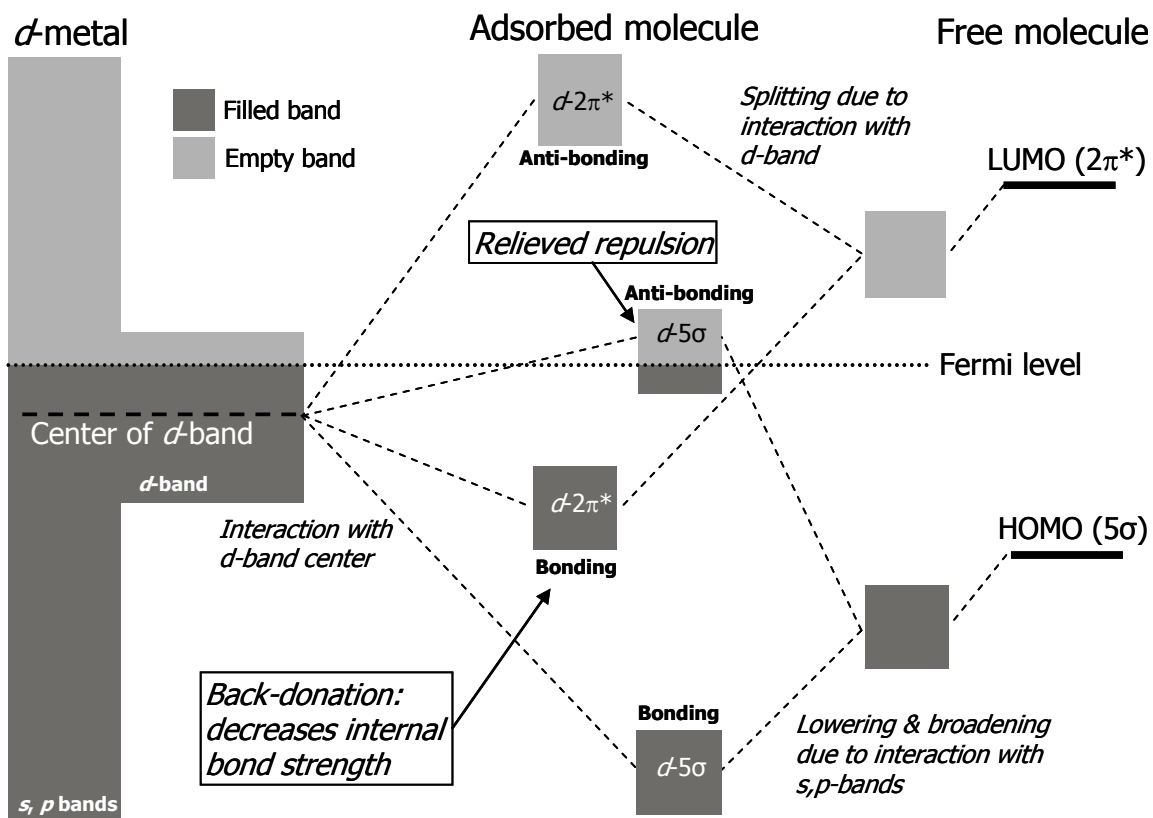


**Fig. 1.3.** The essence of catalysis is depicted in this energy diagram that represents the reactivity according to the  $d$ -band model with CO as model species [9, 12]. The chemisorption bond becomes stronger and the internal bond becomes weaker as the bonding orbital part of the original antibonding molecular orbital ( $2\pi^*$ ) is filled with electrons by metal backdonation from the  $d$ -band. The emptying of the antibonding orbital part of the original bonding molecular orbital ( $5\sigma$ ) results in a stronger chemisorption bond (relieved Pauli repulsion). The extent of orbital filling is dependent on the energy levels of the  $d$ -band center and Fermi level, the orbital coupling matrix, and the relative energy levels of molecular orbitals involved [9].

**Table 1.1**  
 Important parameters of Pd and several other noble metals  
 related to their adsorption strength and reactivity [11, 12, 15]

| Noble metal<br>(crystal structure) | Center of <i>d</i> -band<br>(eV) <sup>1</sup> | Filling<br>degree of<br><i>d</i> -band | Width of <i>d</i> -band<br>(eV) <sup>2</sup> | Fermi level ~<br>Work function<br>(eV) <sup>3</sup> |
|------------------------------------|---|--|--|---|
| Palladium (fcc)                    | -1.83   | 0.9                                    | 2.78   | -5.22   |
| Platinum (fcc)                     | -2.25   | 0.9                                    | 3.9  | -5.64   |
| Ruthenium (hcp)                    | -1.41   | 0.7                                    | 3.87   | -4.71   |
| Rhodium (fcc)                      | -1.73   | 0.8                                    | 3.32   | -4.98   |

<sup>1</sup> Difference between the *d*-band center and the Fermi level of the metal for (111) and (0001) surfaces.

<sup>2</sup> Width of *d*-band compared to Cu (= 1 eV).

<sup>3</sup> Work function measured of polycrystalline materials by photoelectric effect and is equal to the Fermi level in the free electron gas model, however, for real surfaces there will be a small difference due to dipole effects across the surface.

### *Extrinsic catalytic effects*

Many reactions in industrial processes involve gas, liquid, and solid phases in which the solid is a heterogeneous catalyst and the other phases are the reactants. This renders a complex interplay of mass and heat transfer phenomena between the phases involved, backmixing, inter and intraparticle diffusions, maldistribution etcetera.

Activity and selectivity can be an intrinsic characteristic of the catalytic material but can also be influenced by extrinsic effects (“the journey of the reactants to the catalytically active sites”), *i.e.*, external transfer and internal mass transport and when several reactants are used (*e.g.*, H<sub>2</sub> and an organic molecule) by the relative combination of the extrinsic effects. In a homogeneous catalytic reaction where all substances (reactant(s), product(s) and catalyst) are in the same phase, the effect of mass transport between phases is mostly negligible. However, in a heterogeneous catalytic reaction, the catalyst is in a different phase from the reactant(s). Consequently, if intrinsic reaction rates are faster than the mass transport, rate of reaction and selectivity rely on mass transfer or diffusion between these phases. This results in a myriad of resistance steps all of which can control the performance of a catalyst (Fig. 1.4).

The extrinsic process can be modeled by eight steps

- 1) Diffusion of gaseous reactant(s) ( $H_2$ ) from gas phase to liquid phase via film layer.
- 2) Diffusion of the reactant(s) from the bulk phase (boundary layer) to the external surface of the catalyst pellet (film diffusion).
- 3) Diffusion from the mouth of the pore, through the pores, to the internal catalytic surface (intraparticle diffusion).
- 4) Adsorption and migration on the surface of the catalyst.
- 5) Reaction at the specific active site.
- 6) Desorption of the product(s) from the surface.
- 7) Diffusion from the interior to the pore mouth at the external surface.
- 8) Diffusion from the external pellet surface to the bulk fluid.

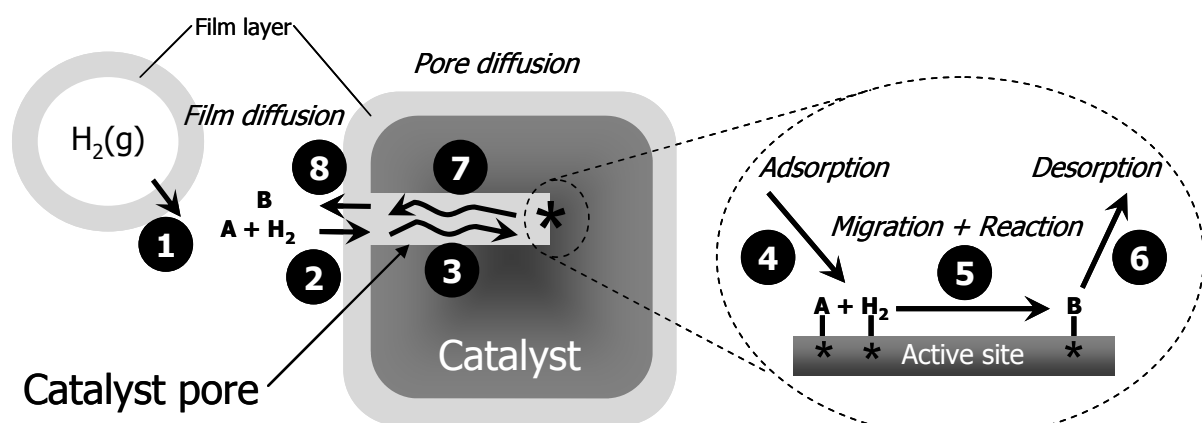


**Fig. 1.4.** Individual steps of a heterogeneous gas-liquid-solid reaction  $A + H_2 \rightarrow B$  on a porous catalyst [16].

External mass transfer is affected by reaction conditions such as the ratio of concentrations of reactant and catalyst, solvent, co-solvent, additives, reactor configuration, energy input, and prevailing hydrodynamic flow pattern. Internal mass transport is dictated by the reactants diffusion coefficients, catalyst particle size or thickness of the coating layer, average pore size, porosity, and tortuosity. For consecutive reactions  $A \rightarrow B \rightarrow C$ , in continuous reactors, where the intermediate (B) is the desired product, narrow residence time distributions are vital, *i.e.*, plug flow behavior (no axial dispersion).

Another important aspect in heterogeneously catalyzed reactions is the probability of deactivation, *i.e.*, loss of catalyst activity. There are many different mechanism of deactivation as explained by Moulijn *et al.* [17]. Preventing (irreversible) deactivation is of principal importance since supported Pd catalysts in general and monolithic catalysts (see next paragraph) in particular are expensive and laborious to synthesize. Therefore, reuse without much loss in activity (after a regeneration treatment) is a prerequisite. The loss of activity should thus not be permanent, as it is for metal leaching or irreversible poisoning. However, some loss of high initial activity by, *e.g.*, metal sintering or carbonaceous deposit formation is unavoidable.

In this thesis these aspects are dealt with in **Chapter 2, 3, and 4** (extrinsic effects) and **Chapter 4 and 5** (intrinsic catalytic effects) on various length scales.

### **Structured catalysts in heterogeneous reactions – Monoliths**

A monolith (Fig. 1.5) consists out of thousands of small (channel diameter  $\sim 1$  mm) parallel straight square channels, separated by thin walls. “Classical” ceramic monoliths for automotive applications consist of macroporous cordierite, and are used as structured supports for different catalytically active materials. Monolithic catalysts are thus used nowadays for various gas phase applications (*e.g.*, in the automotive industry) and as an alternative for solid catalyzed gas-liquid reactions [18]. An example where Pd-based monoliths are commercially deployed is in the hydrogenation step of the anthraquinone process [19]. The advantages of using monolithic catalysts include low-pressure drop, ease of scale-up, high mass transfer rates, low axial mixing and elimination of a separation step.

The use of structured catalysts or reactor internals such as monoliths allow for the decoupling of the various contributions and their individual optimization [20, 21]. In monolithic reactors, external mass transfer can be decoupled from internal mass transfer by independently varying the wall thickness and the channel diameter. Compared to packed bed reactors, monoliths have the advantage that pressure drop and internal diffusion lengths are decoupled. Monolithic reactors fit well into the relatively new world of process intensification. Process intensification leads to a substantial decrease in equipment size, production-capacity ratio, energy consumption, and/or waste production.

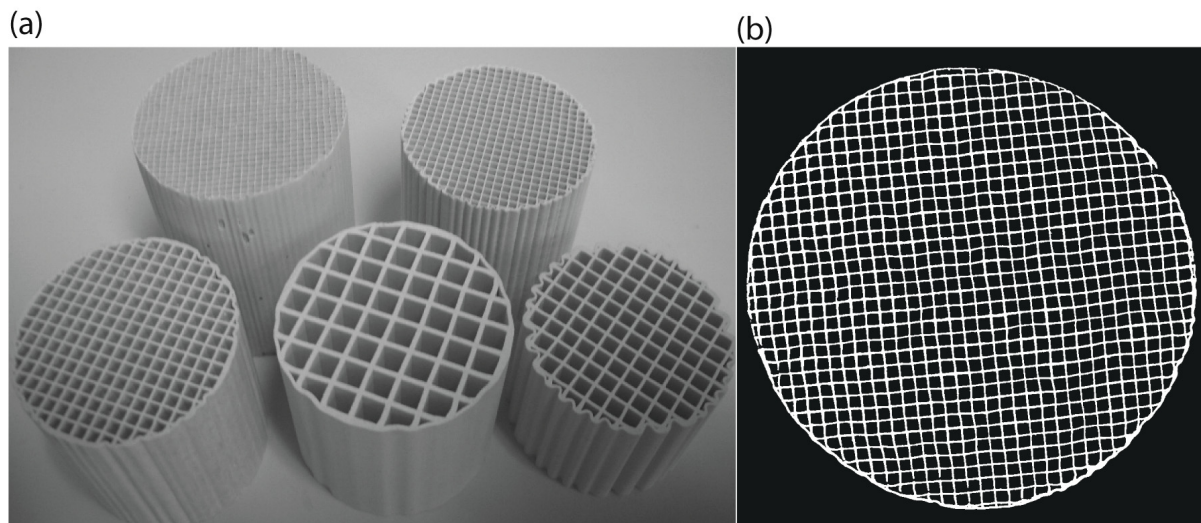


**Fig. 1.5.** Several examples of cordierite monoliths with different channel diameters (a) and a cross-section of a cordierite monolith with square channels of  $\sim 1$  mm diameter (b).

#### *Preparation of cordierite monoliths to increase surface area*

The specific surface area of these macroporous cordierite monoliths itself is too low ( $< 0.5$   $\text{m}^2/\text{g}$ ) to support and stabilize an active phase (e.g., Pd), and thus a supporting material (washcoat) with a high specific surface area (e.g.,  $\text{SiO}_2$ ,  $\gamma\text{-Al}_2\text{O}_3$ ) must be deposited on the monolith walls. A major drawback is that the macropores in the walls of cordierite monoliths will be filled with these high surface area support particles, thereby increasing the internal diffusion lengths or even making it inaccessible for reactants as shown by Crezee *et al.* for ruthenium on carbon coated cordierite monoliths [22]. Therefore, eggshell washcoated monoliths have also been prepared by using a coating material with a larger particle size than the macropores of the cordierite. Preparation of these supported cordierite monolithic catalysts is discussed in depth in a review paper by Nijhuis *et al.* [23]. A disadvantage for the eggshell washcoated monoliths is the lower catalyst inventory when compared to packed bed reactors which decreases the activity per unit reactor volume.

Cordierite monoliths can also be first coated with a low surface area layer which transforms the square channels in round channels, enhancing liquid mass transfer under Taylor flow conditions. Another advantage is that then a thin coating with a high surface area can be applied, thereby decreasing the internal diffusion length. This procedure results in the so-called high-performance monoliths [24]. The application of these monoliths with thin coatings confirmed that catalyst performance is enhanced. However, this enhanced performance is at the cost of an even lower catalyst loading per unit of reactor volume compared to packed-bed or eggshell washcoated monolithic reactors.

### Mullite monoliths with highly porous walls

An alternative approach is to synthesize monoliths with highly permeable walls that allow convective transport through them. This new type of monolith is synthesized by the Dow Chemical Company consisting of high-porosity acicular mullite (ACM) which was originally developed for diesel soot filters. Several images of an ACM monolith wall at different magnifications are presented in Fig. 1.6. ACM monoliths distinguish themselves from cordierite monoliths by the permeability of the micro-structured walls enabling convective transport through them. In contrast to cordierite, the walls of the ACM monoliths are made up of an *open network* of interlocking elongated ceramic grains with lengths and diameters in the micrometer range. The ceramic grain size and the pore diameter size are tunable.

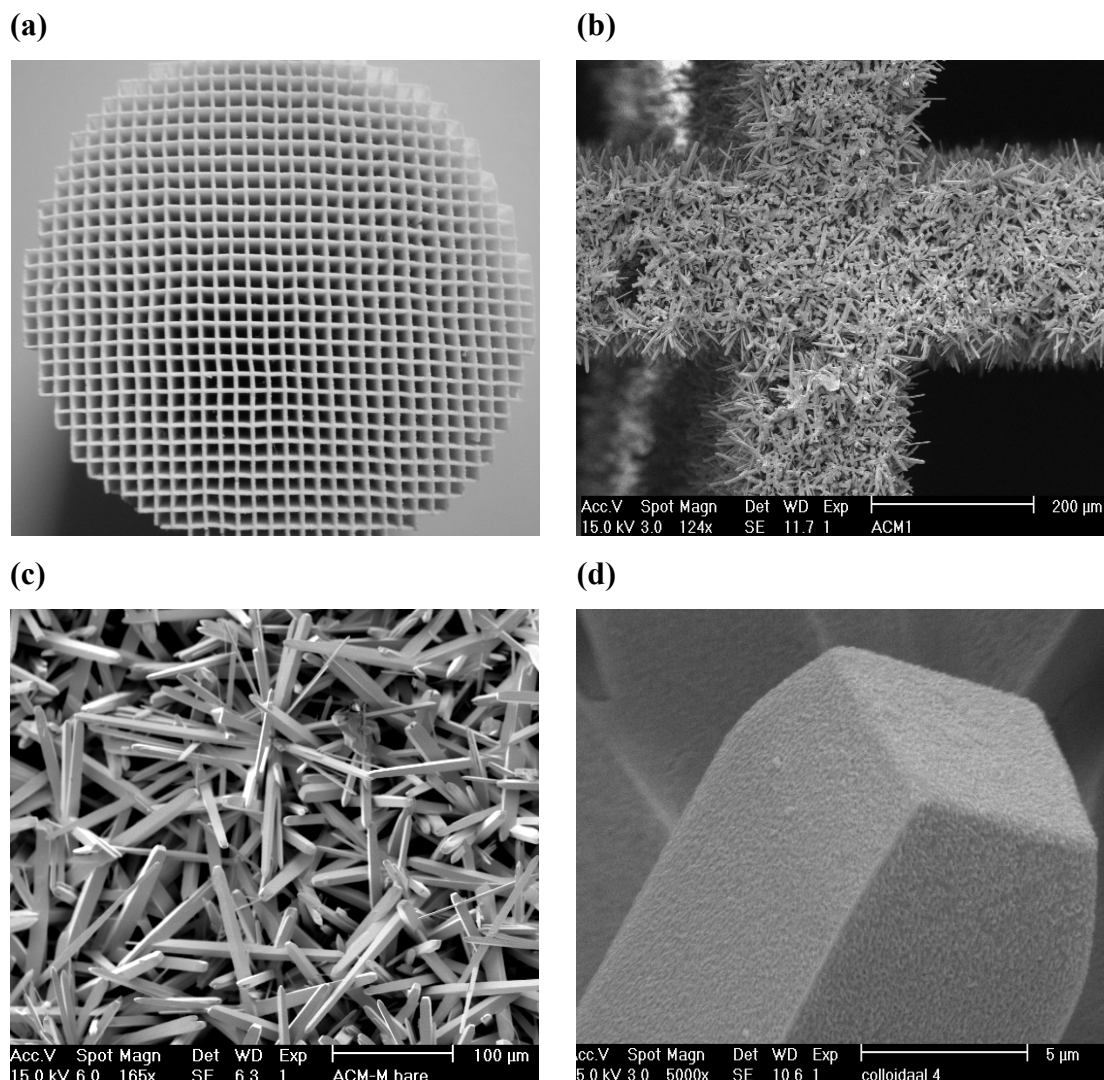


**Fig. 1.6.** Photograph (a) and SEM images (b, c, and d) of acicular mullite (ACM) monoliths at different magnifications: macroscopic, mesoscopic, and microscopic. (a) Cross-section of an ACM monolith displaying the square channels with a diameter of  $\sim 1$  mm, (b) Wall-intersection of an ACM monolith (c) Shows the open porous structure of an ACM monolith wall, (d) A mullite grain coated with a thin layer of colloidal silica.

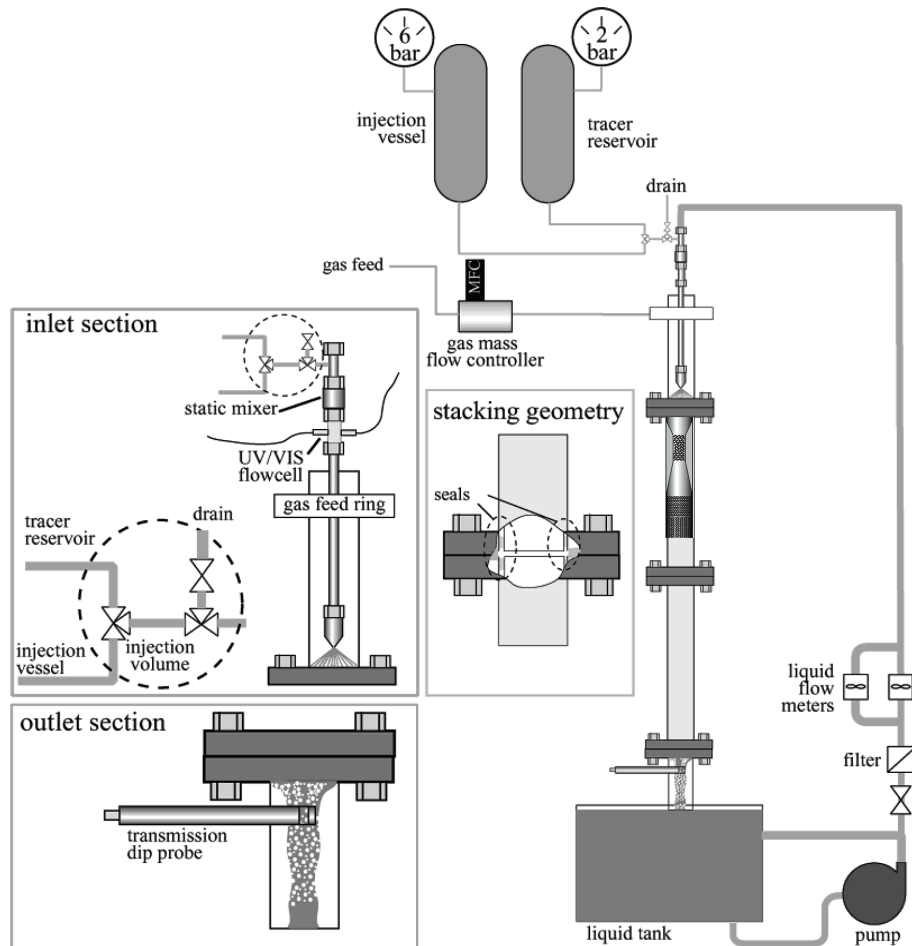
The properties of the ACM monoliths will be investigated in **Chapter 2** and **3**. **Chapter 2** focuses on the hydrodynamic properties of these new monoliths. **Chapter 3** investigates the extrinsic catalytic properties of the ACM monoliths under internal mass transfer limited conditions. Synthesis of supported catalysts on macroscopic bodies such as monoliths is not straightforward and special attention needs to be given to the correct distribution of the support (concentration profiles) and active phase on macroscopic (monolith scale, radial and axial distribution), mesoscopic (within the walls of the monolith), and microscopic (within the coated support layer) levels. Therefore, a detailed description of the deposition of a high surface area support and nanosized Pd crystallites including the characterization thereof is also presented in **Chapter 3**.

#### *Monolith reactors*

Two monolith reactor setups were used in this PhD research and are depicted in Fig. 1.7. For hydrodynamic studies a reactor was used in continuous co-current downflow configuration using stacked monoliths with intermixing areas. Cordierite and ACM with and without a silica coating were applied in these cold-flow studies to determine their hydrodynamic behavior. The gas and liquid are supplied at the inlet by a static mixer system (Fig. 1.7a). Hydrodynamic studies can be excellently carried out in this set-up, as has been shown with classical cordierite monoliths to study the effect of channel size and linking residence time distribution and feed maldistribution [25, 26]. For successful use of monolithic structures in multiphase reactions a uniform gas-liquid distribution is critical, because redistribution inside these structures is not possible. If the gas-liquid distribution over the top of the monolith entrance or if channel geometry is not perfect, the gas and liquid holdup and superficial velocities will vary from channel to channel, thereby adding a convective maldistribution term to the two-zone description of axial mixing.

Hydrogenation studies were performed in a batch reactor (with a continuous feed of H<sub>2</sub>) supplied with a stirrer with colloidal silica supported Pd-based monoliths as stirrer blades: the monolithic stirrer reactor (MSR, Fig. 1.7b). Previously, the MSR was used for several reactions, *e.g.*, enzyme catalyzed reactions [27], etherification of alcohols [28] and the hydroformylation of alkenes [29].

(a)



(b)

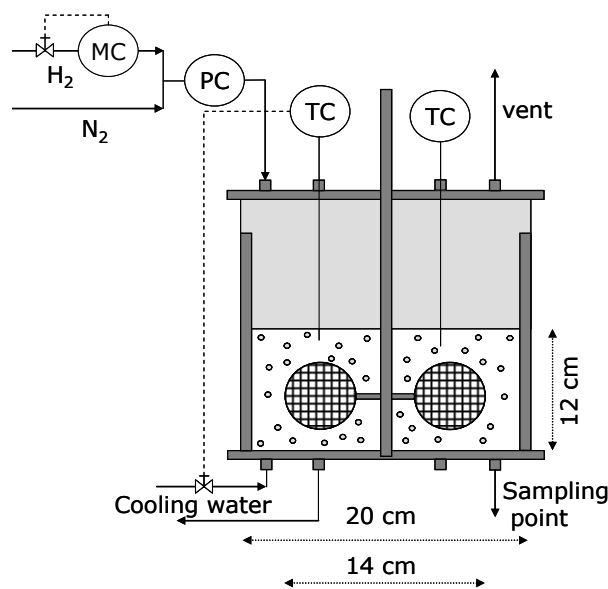


**Fig. 1.7.** Reactor setups for monoliths used in this PhD research. (a) Cold flow reactor setup operated in a downflow configuration using stacked monoliths with intermixing areas in between monoliths and a static mixer inlet system. (b) Monolithic stirrer reactor (MSR) with two monolith pieces as stirrer blades.

### Multiphase flow through small channels

The most important flow regime for co-current gas-liquid reactions in small diameter channels is Taylor flow (also called segmented flow). Taylor flow is a two-phase co-current flow pattern where the gas and liquid move consecutively through the channels as separate slugs (Fig. 1.8a). This well-structured two-phase flow pattern is observed in capillaries and monoliths. The recirculation (Fig. 1.8b) inside liquid slugs enhances radial mass transfer and a thin “static” liquid film, typically ranging in thickness from 5 to 50  $\mu\text{m}$  between the wall and the bubble train, forms a small but noticeable barrier for the mass transfer rate in gas-liquid operated monolith channels. Hence, this flow pattern exhibits excellent mass-transfer characteristics.

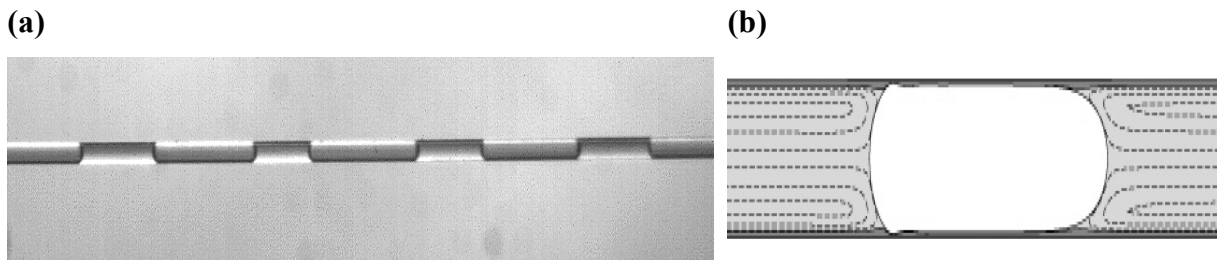


**Fig. 1.8.** (a) Gas-liquid Taylor flow in a capillary channel (inner diameter = 530  $\mu\text{m}$ ): alternating gas bubbles and liquid slugs. (b) Schematic representation of Taylor flow showing the recirculation pattern in the liquid slugs and the thin static layer between the moving alternating liquid slugs and gas bubbles, and the wall containing the catalyst.

Moreover, backmixing is suppressed by the presence of gas bubbles when compared to single-phase laminar flow. Axial mixing does only occur inside the channels of a cordierite monolith by the diffusion into and out of the thin liquid film. A simple model developed by Kreutzer and co-workers [30] can be used to estimate the mass transfer of the gas component ( $\text{H}_2$ ) and the liquid reactant to the catalyst on the wall for reactions operated in the Taylor flow regime. This model consists out of three mass transfer terms

- Dissolved gas and liquid compounds transfer from the liquid slug to the catalyst on the wall via the film layer.
- Transfer from the gas slug directly to the catalyst wall via the film layer.
- Gas transfer from the cap of the gas slugs to the liquid slugs.

In this model, the film layer near the wall is the largest resistance to mass transfer. Other, important parameters are the length of the liquid slugs and the gas and liquid superficial velocities.

## Flow Chemistry

Flow chemistry, also referred to as plug flow, microchemistry or continuous flow chemistry is the process of performing chemical reactions in a tube or pipe [31-35]. Reactive components are brought together in a mixing junction and subsequently flow together through a temperature-controlled pipe or tube. In flow chemistry, a chemical reaction is performed in a continuously flowing stream rather than in batch production. Flow chemistry is a well-established technique for use at a large scale when manufacturing large quantities of a given material. However, the production of fine chemicals is still heavily dependent on batch processes, particularly in the pharmaceutical sector. Hence, it is relatively new to use it in fine chemistry and the laboratory environment on smaller scales; and only since the last decade have scientists in academia as well as in industry begun to focus on developing flow devices [36, 37].

The microscale flow device used in this thesis is a reactor made from a gas chromatograph fused silica capillary which could also be seen as an idealized single channel of a monolith reactor or as a reactor on itself for production of fine chemicals. A very important and interesting characteristic of this type of capillaries is the visibility of the hydrodynamic flow pattern during reaction. When operated in the Taylor flow regime, it provides excellent plug flow behavior of alternating gas and liquid slugs and thus an accurate measure for residence times. This will be further explored in **Chapter 4**. Further advantages compared to microchip reactors are the simplicity, low cost and there is no need for clean room facilities.

In comparison with round-bottomed flasks or autoclaves the advantages of flow chemistry and the use of flow devices can be summarized as

- Allows multiple reactions to be performed in a serial fashion. One reaction can follow another, separated by solvent, each cleaning out the previous reaction.
- Possibility to combine classical multi-step batchwise synthesis into a single continuous operation without the necessity for isolation of (dangerous and/or reactive) intermediates between steps [38]. It allows only a small amount of

hazardous intermediate to be formed at any instant. Azide chemistry is one such area where flow devices such as our capillary might will a significant impact, **Chapter 4** shows that the hydrogenation of azides to their corresponding amines can be safely performed in our continuous flow device.

- Enables quick variation of reaction conditions on small scales (*e.g.*,  $\mu\text{l}$  or  $\text{ml}$ ). Parameters such as reaction time, temperature, reagent ratio, concentration and reagents themselves can all be rapidly varied.
- Can be used as rapid screening tool, *e.g.*, to improve traditional batch chemistry or for optimization purposes. In contrast, reactions performed in round-bottomed flasks are difficult and time-consuming to optimize.
- The surface area to volume ratio of the reaction mixture is many orders of magnitude greater than a round bottom flask or autoclave which enables almost instantaneous heating or cooling and therefore ultimate temperature control. Therefore, better temperature control can be maintained for exothermic or endothermic reactions improving consistency and yield.
- Higher flow rates and a numbering-up can be used to easily produce kilogram quantities.

Summarizing, the major advantages of flow chemistry are faster and safer reactions, cleaner products, controlled operation at unprecedeted conditions, quick reaction optimization, easy scale-up and the integration of typically separate processes (such as synthesis, work-up and analysis). **Chapter 4** focuses on the fabrication and use of a simple gas chromatograph fused silica capillary as flow device for hydrogenation reactions catalyzed by wall-coated supported Pd. A schematic overview of this flow device is presented in Fig. 1.9.

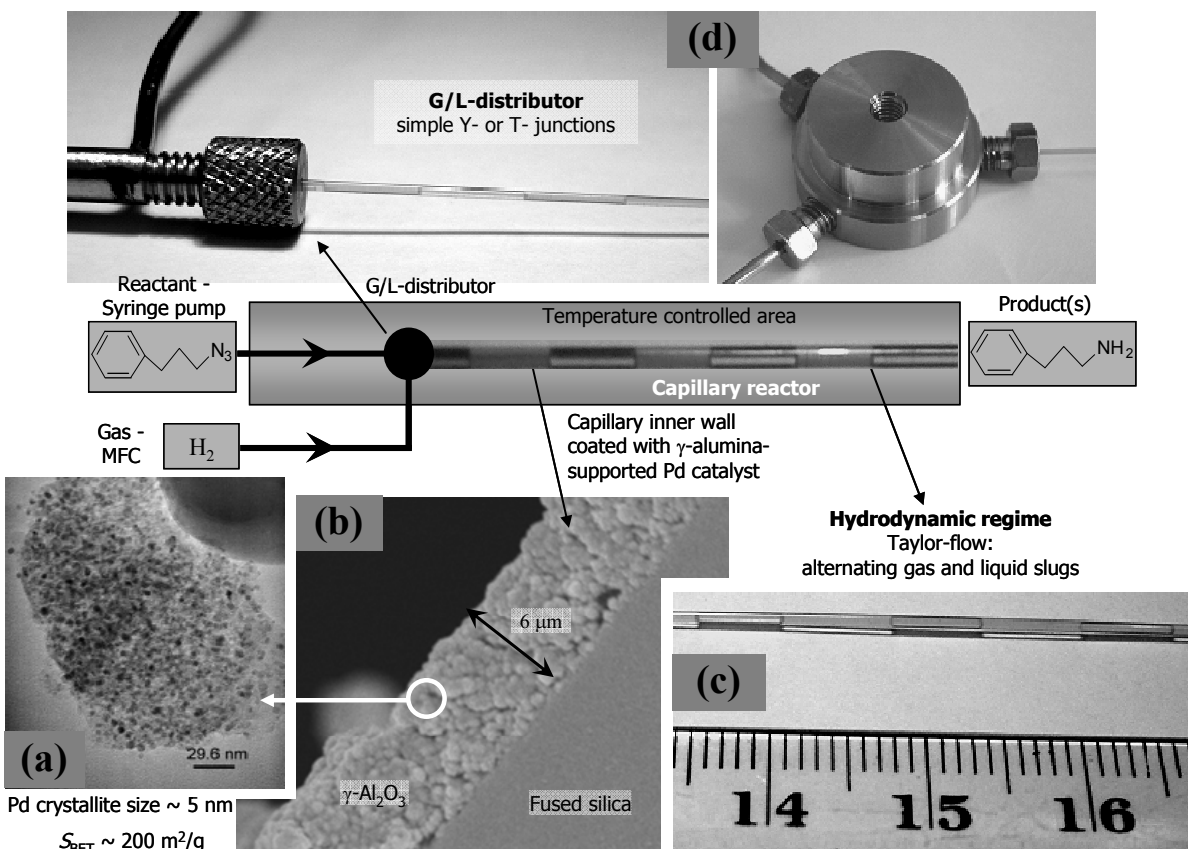


**Fig. 1.9.** Schematic presentation of the capillary flow device with some highlighted features shown in the photographs. (a) TEM and (b) SEM micrograph of the heterogeneous catalytic system immobilized on the fused silica capillary wall. (c) Structured hydrodynamic two-phase flow regime: Taylor flow. (d) Simple T- and Y-junctions used as gas-liquid distributors.

### Outline and scope of this thesis

**Chapter 2** focuses on the differences in hydrodynamic behavior of Taylor flow operated acicular mullite (ACM) monoliths and classical cordierite monoliths by means of cold flow tracer residence time distribution experiments. These ACM monoliths contain highly porous walls and distinguish themselves by their high permeability of the walls from the commonly used cordierite monoliths.

**Chapter 3** continues to explore the usability of ACM monoliths coated with a Pd/SiO<sub>2</sub> catalyst in the chemoselective hydrogenation of a functionalized pentyne in a multiphase flow operated monolithic stirrer reactor. Catalyst performance was enhanced compared to cordierite monoliths coated with Pd/SiO<sub>2</sub> for this model hydrogenation reaction when

operated under internal diffusion controlled conditions. In addition, this Chapter focuses on the preparation and characterization of these Pd/SiO<sub>2</sub> coated ACM monoliths.

**Chapter 4** deals with a new flow device that is developed for evaluating wall-coated  $\gamma$ -Al<sub>2</sub>O<sub>3</sub>-supported Pd-catalyzed hydrogenations operated in the well-structured Taylor flow regime. Here, I explore how visible features under hydrogenation conditions can be used in labscale multiphase heterogeneous catalysis. The uncomplicated construction and simple visual monitoring can be a powerful tool in the hands of synthetic chemists. I exemplify this by conducting several (chemoselective) hydrogenation reactions (C=C-R, C≡C-R and R-N<sub>3</sub>) catalyzed by Pd/ $\gamma$ -Al<sub>2</sub>O<sub>3</sub> in a capillary flow device. Experimental details, results and discussion of the performed hydrogenations in the capillary flow device can be found in **Appendix A**.

The topic of **Chapter 5** is structure sensitivity of  $\gamma$ -Al<sub>2</sub>O<sub>3</sub>-supported Pd catalysts, in particular the effect of intrinsic structural changes due to Pd  $\beta$ -hydride formation at higher hydrogen pressure. The intrinsic property of Pd to absorb hydrogen into its lattice has strong influence on activity and yield as shown in the hydrogenation of an aromatic nitrile while varying hydrogen pressures. The obtained experimental results are explained by a combination of the *d*-band theory of reactivity and frontier orbital theory. In addition, a mechanistic concept for the Pd-catalyzed hydrogenation of benzonitrile is revealed, explaining the differences in observed selectivity.

**Chapters 2 to 5** are published in peer reviewed magazines and can be read independently. Finally, **Chapter 6** and **Chapter 7** evaluate and summarize the obtained results of this PhD research, respectively.

## Bibliography

- [1] a) J.A. Moulijn, P.W.N.M. van Leeuwen, R.A. van Santen, *Catalysis: an integrated approach to homogeneous, heterogeneous and industrial catalysis*, Elsevier, Amsterdam, 1993; b) J. Hagen, *Industrial catalysis – A practical approach*, Wiley-VCH, Weinheim, 2006; c) J. Horiuti, M. Polanyi, *Trans. Faraday Soc.* 30 (1934) 1164; d) M.A.G. Hevia, B. Bridier, J. Pérez-Ramírez, *App. Catal. A* (2012) In press. e) W.M.H. Sachtler, Y.Y Huang, *Appl. Catal. A* 191 (2000) 35.
- [2] H.F. Rase, *Handbook of commercial catalysts: heterogeneous catalysts*, CRC Press, New York, 2000.
- [3] D.B. Tiedtke, T.T.P. Cheung, J. Leger, S.A. Zisman, J.J. Bergmeister, G.A. Delzer, *13<sup>th</sup> Ethylene Producers Conference* 10 (2001) 1.
- [4] <http://www.platinum.matthey.com>
- [5] A.C. Luntz, *Surf. Sci.* 603 (2009) 1557.
- [6] M.L. Toebe, J.A. van Dillen, K.P. de Jong, *J. Mol. Catal. A* 173 (2001) 74.
- [7] J.A. Schwarz, C. Contescu, A. Contescu, *Chem. Rev.* 95 (1995) 477.
- [8] J.A.R. van Veen, G. Jonkers, W.H. Hesselink, *J. Chem. Soc., Faraday Trans. 1* 85 (1989) 389.
- [9] I. Chorkendorff, J.W. Niemantsverdriet, *Concepts of modern catalysis and kinetics*, Wiley-VCH, Weinheim, 2007, 215.
- [10] G. Blyholder, *J. Phys. Chem.* 68 (1964) 2772.
- [11] B. Hammer, J.K. Nørskov, *Adv. Catal.* 45 (2000) 71.
- [12] A. Nilsson, L.G.M. Pettersson, J.K. Nørskov, *Chemical bonding at surfaces and interfaces*, Elsevier B.V., Amsterdam, 2008, 255.
- [13] A. Ruben, B. Hammer, P. Stoltze, H.L. Skriver, J.K. Nørskov, *J. Mol. Catal. A*. 115 (1997) 421.
- [14] M.A. Vannice, *Kinetics of catalytic reactions*, Springer Verlag, New York, 2005.
- [15] D.R. Lide, *CRC Handbook of chemistry and physics*, 89<sup>th</sup> ed., CRC Press, Taylor & Francis Group, Boca Raton, 2008.
- [16] R. Dittmeyer, G. Emig, *Simultaneous Heat and Mass Transfer and Chemical Reaction*. In G. Ertl; *et al.* (Eds.): *Handbook of heterogeneous catalysis*. Vol. 8, 2<sup>nd</sup> edition, Wiley-VCH Verlag, Weinheim, 2008, 1727.

- [17] J.A. Moulijn, A.E. van Diepen, F. Kapteijn, *Appl. Catal. A* 212 (2001) 3.
- [18] J.A. Moulijn, M.T. Kreutzer, T.A. Nijhuis, F. Kapteijn, *Adv. Cat.* 54 (2011) 249.
- [19] C.T. Berglin, W.A. Herrman, European Patent 102934 A2, 1984.
- [20] F. Kapteijn, J.J. Heiszwolf, T.A. Nijhuis, J.A. Moulijn, *CATTECH* 3 (1999) 24.
- [21] M.T. Kreutzer, F. Kapteijn, J.A. Moulijn, *Cat. Today* 1 (2006) 111.
- [22] E. Crezee, B.W. Hoffer, R.J. Berger, M. Makkee, F. Kapteijn, J.A. Moulijn, *Appl. Catal. A* 251 (2003) 1.
- [23] T.A. Nijhuis, A. E. W. Beers, T. Vergunst, I. Hoek, F. Kapteijn, J.A. Moulijn, *Catal. Rev. Sci. Eng.* 43 (2001) 345.
- [24] A.F. Pérez-Cadenas, M.M.P. Zieverink, F. Kapteijn, J.A. Moulijn, *Catal. Today* 105 (2005) 623.
- [25] M.T. Kreutzer, J.J.W. Bakker, F. Kapteijn, P.J.T. Verheijen, J.A. Moulijn, *Ind. Eng. Chem. Res.* 44 (2005) 4898.
- [26] A.A. Yawalkar, R. Soot, M.T. Kreutzer, F. Kapteijn, J.A. Moulijn, *Ind. Eng. Chem. Res.* 44 (2005) 2046.
- [27] K.M. de Lathouder, J.J.W. Bakker, M.T. Kreutzer, F. Kapteijn, J.A. Moulijn, S.A. Wallin, *Chem. Eng. Res. Dev.* 84 (2006) 390.
- [28] I. Hoek, T.A. Nijhuis, A.I. Stankiewicz, J.A. Moulijn, *Appl. Catal. A* 266 (2004) 109.
- [29] A.J. Sandee, R.S. Ubale, M. Makkee, J.N.H. Reek, P.C.J. Kamer, J.A. Moulijn, P.W.N.M. van Leeuwen, *Adv. Synt. Catal.* 343 (2001) 201.
- [30] M.T. Kreutzer, P. Du, J.J. Heiszwolf, F. Kapteijn, J.A. Moulijn, *Chem. Eng. Sci.* 69 (2001) 6015.
- [31] a) A. Kirschning, *Beilstein J. Org. Chem.* 5 (2009) 15; b) A. Kirschning, *Beilstein J. Org. Chem.* 7 (2011) 1046.
- [32] M. Irfan, T.N. Glasnov, C.O. Kappe, *ChemSusChem* 4 (2011) 300.
- [33] T. Wirth, *ChemSusChem* 5 (2012) 215.
- [34] J.P. McMullen, K.F. Jensen, *Annu. Rev. Anal. Chem.* 3 (2010) 19.
- [35] S.V. Ley, I. R. Baxendale, *Chimia* 62 (2008) 162.
- [36] G. de Maria, *Chem. Today* 28 (2010) 26.
- [37] L. Malet-Sanz, F. Susanne, *J. Med. Chem.* 55 (2012) 4062.
- [38] D. Webb, T.F. Jamison, *Chem. Sci.* 1 (2010) 675.

# 2

## **Hydrodynamic properties of a novel ‘open wall’ monolith reactor**

---

The hydrodynamic behavior of high-porosity ceramic acicular mullite (ACM) monoliths operated in gas–liquid Taylor flow was investigated by cold-flow tracer residence time distribution (RTD) experiments and compared with the hydrodynamic behavior of classical cordierite monoliths in terms of static liquid fraction, maldistribution, and mass exchange between the dynamic liquid zone and the static liquid zone. The piston-dispersion-exchange (PDE) model was successfully fitted to the experimental data. The multiphase fluid mechanics were indeed different for ACM and cordierite monoliths: in contrast to the classical cordierite system, the mass exchange between static liquid and dynamic liquid was much higher and the liquid phase could access the open volume of the permeable ACM monolith wall. On the other hand, the larger velocity maldistribution, larger static liquid fraction, and the liquid interaction between adjacent ACM microchannels resulted in less plug flow behavior.

---

This Chapter is published in *Catal. Today* 105 (2005) 385.

## Introduction

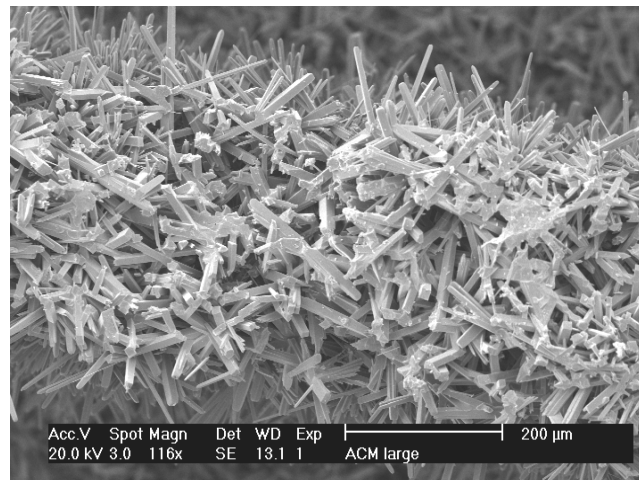
Monolithic catalysts are used nowadays for various gas phase applications (*e.g.*, in the automotive industry) and as an alternative for solid catalyzed gas-liquid reactions [1-5]. The advantages of using monolithic catalysts include low-pressure drop [6, 7, 8], ease of scale-up [2, 9], high mass transfer rates [10-12], low axial mixing [13], and elimination of a separation step [2].

“Classical” ceramic monoliths for automotive applications are made of cordierite, and are used as structured supports for different catalytically active materials. A monolith consists of many millimeter sized parallel straight microchannels, separated by thin walls. On these walls, a washcoat (*e.g.*, silica,  $\gamma$ -alumina or carbon) can be deposited with a high specific surface area. On this washcoat the catalytic phase, usually a precious metal, is dispersed [14, 15].

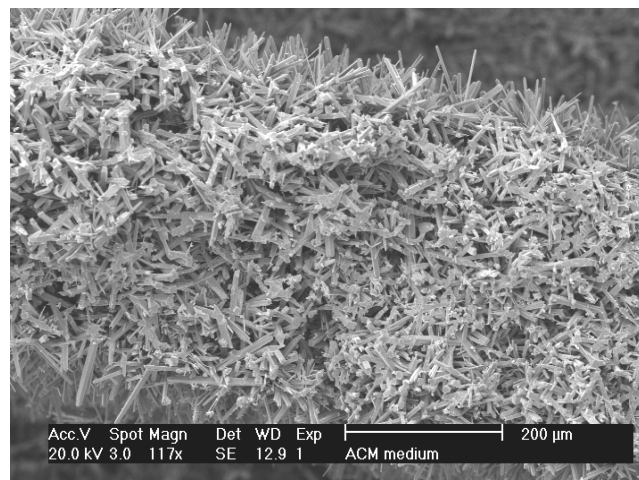
A new type of monolith was synthesized by the Dow Chemical Company and consists of high-porosity acicular mullite (ACM) [16, 17]. This ACM monolith distinguishes itself from a cordierite monolith by the permeability of the micro-structured walls. In contrast to the cordierite walls, the walls of the ACM monoliths are made up of an open network of interlocking elongated ceramic grains with lengths and diameters in the micrometer range. The ceramic grain size and the pore diameter size are tunable [16]. Fig. 2.1 shows three SEM micrographs of the ACM monolith walls with different ceramic grain sizes and pore diameters. In this Chapter, ACM monoliths with medium (Fig. 2.1b) and large pores (Fig. 2.1a) are investigated. ACM monoliths with large and small pores (Fig 2.1.c) are applied in reactive experiments in Chapter 3. There are two possibilities to exploit the unique features of ACM monoliths

- For fast reactions that suffer from diffusional limitations, the deposition of a thin conformal catalyst layer ( $< 10 \mu\text{m}$ ) on the ACM grains maintains the open structure of the walls and minimizes the diffusional limitations.
- For reactions where mass transfer is not a limiting factor, the high porosity of the ACM monolith walls allows the catalyst loading per unit volume to be maximized [18].

(a) - ACM-L



(b) - ACM-M



(c) - ACM-S

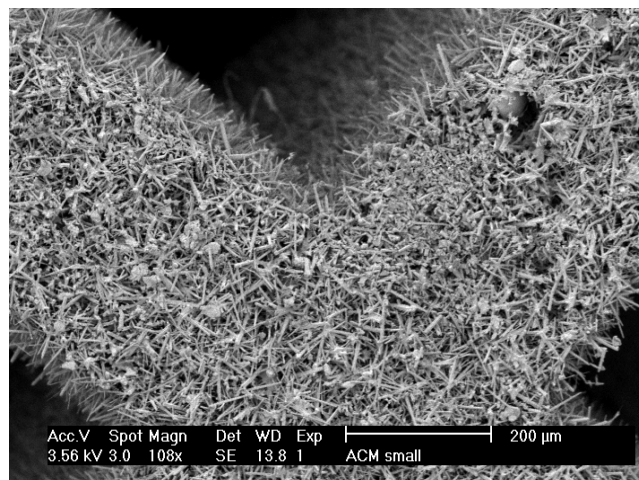


**Fig. 2.1.** SEM micrographs of the grain structure of ACM monolith walls. (a) ACM monolith wall with large pores (average pore size  $\sim 45$   $\mu\text{m}$ ). (b) ACM monolith wall with medium pores (average pore size  $\sim 18$   $\mu\text{m}$ ). (c) ACM monolith wall with small pores (average pore size  $\sim 5$   $\mu\text{m}$ ).

The most important flow regime for co-current gas-liquid reactions in small diameter channels is Taylor flow (also called bubble-train flow or segmented flow) [19, 20]. Taylor flow is a two-phase co-current flow pattern where the gas and liquid move consecutively through the channels as separate slugs. This two-phase flow pattern is observed in capillaries and monoliths [21-25]. The recirculation inside liquid slugs enhances radial mass transfer and a thin “static” liquid film, typically ranging in thickness from 5 to 50  $\mu\text{m}$  between the wall and the bubble train, forms a small but noticeable barrier for the mass transfer rate in gas-liquid operated monolith channels. Hence, this flow pattern exhibits excellent mass-transfer characteristics [10, 26, 27]. Moreover, backmixing is suppressed by the presence of bubbles when compared to single-phase laminar flow. Axial mixing is only possible inside the channels of a cordierite monolith by the diffusion into and out of the thin liquid film. However, for successful use of monolithic structures in multiphase reactions a uniform gas-liquid distribution is critical, because redistribution inside these structures is not possible. If the gas-liquid distribution over the top of the monolith entrance or if channel geometry is not perfect, the gas and liquid holdup and superficial velocities will vary from channel to channel, thereby adding a convective maldistribution term to the two-zone description of axial mixing [28].

The objective of this study was to determine the hydrodynamic behavior of the bare and coated ACM monoliths operated in co-current two-phase downflow, and to compare the hydrodynamic behavior of the ACM monoliths with “classical” cordierite monoliths.

## Experimental

### Materials

ACM monoliths of 15.5 cm in length and 4 cm in diameter with a cell density of 400 cpsl (mean channel diameter is  $\sim 1$  mm) were prepared by a proprietary Dow process to produce monoliths with medium (labeled as ACM-M) and large (labeled as ACM-L) elongated grains made of mullite. The wall thickness is 0.24 mm and the wall porosity, determined by mercury porosimetry, is 62% and 71% with an average pore size of 18 and 45  $\mu\text{m}$  for ACM-M and ACM-L, respectively. ACM-L monoliths were also coated (labeled as ACM-LC) with a colloidal silica layer, representative of a catalyst support, to see if the coating would influence the hydrodynamic behavior. The silica coating was prepared by dipping pre-treated ACM-L

monoliths for 2 min, with a constant immersion speed and withdrawal speed of 5 mm/s, into a diluted Ludox® SM-30 (Adrich®) solution (10 wt%) containing colloidal silica particles of 7 nm in diameter (wall porosity decreased to 54% and 63% for ACM-M and ACM-L, respectively). After rotational drying and calcination a silica coating distributed on the mullite grains leaving the ‘open’ wall structure of the ACM-L samples intact. The reader is referred to Chapter 3 for a detailed description of the coating procedure and the obtained results.

Cordierite monoliths of equal outer dimensions and cell density (mean channel diameter is  $\sim$  1.1 mm) were used for comparison. The wall thickness of the cordierite samples is 0.18 mm with a wall porosity of 36% (average pore size is 8  $\mu\text{m}$ ). Water and air were used as fluids for all experiments.

### *Method*

Cold flow (room temperature) water-air RTD experiments in monoliths under Taylor flow were performed in a downflow configuration by introducing a pulse of a colored dye (Ecoline blue ink, Royal Talens) in the feed of the reactor and recording the exit concentration at various superficial gas velocities and superficial liquid velocities. The superficial gas velocity  $u_G$  was varied between 0.01 and 0.22 m/s and the superficial liquid velocity  $u_L$  between 0.06 and 0.20 m/s.

A schematic drawing of the experimental setup can be found in Chapter 1 (Fig. 1.7a). The monolith section with a total length of 94 cm consisted out of six monolith blocks that were stacked on top of each other with a small gap of 2 mm between consecutive monoliths. No attempt was made to align the monolithic channels in the junction between consecutive monoliths. This monolith configuration thus contains five gas-liquid redistribution zones.

Both the inlet and outlet pulse were measured by spectroscopy in the visual range. A detailed description of these measurement techniques can be found in Kreutzer *et al.* [28]. The reproducibility of the outlet curves was found to be very good. An overall mass balance revealed that the difference between the inlet and outlet is within 10%.

## Theory

### *RTD-data transformations*

The experimentally determined absorbance versus time curves are converted into concentration versus time by using the Lambert-Beer law

$$A = \alpha(\lambda)BC = -\log\left(\frac{I - I_{dark}}{I_{ref} - I_{dark}}\right) \quad (2.1)$$

where  $A$  is the absorbance,  $\alpha(\lambda)$  is the wavelength-dependent absorption coefficient,  $B$  is the path length,  $C$  is the tracer concentration,  $I$  is the intensity at concentration  $C$ ,  $I_{ref}$  is the intensity of water and  $I_{dark}$  is the intensity with the light source switched off.

The concentration versus time curve can be transformed into an  $E(t)$ -curve by dividing the concentration versus time curve by the area under that curve. By calculating the first moment of an  $E(t)$ -curve the mean residence time  $\tau_M$  is obtained. The  $E(t)$ -curve, normalized by time results in the  $E(\theta)$ -curve and is defined by

$$E(\theta) = \frac{\int_0^\infty tC(t) dt}{\int_0^\infty C(t) dt} \cdot \frac{C(t)}{\int_0^\infty C(t) dt} \quad (2.2)$$

where the first factor represents the first moment: the mean residence time  $\tau_M$  and  $\theta$  is the dimensionless time  $t/\tau_M$ .

### *Liquid holdup*

From the liquid flow rate and the experimentally determined  $\tau_M$ , the ‘experimental’ dynamic liquid holdup  $\phi$  can be calculated by

$$\phi = \frac{\phi_L \tau_M}{V} \quad (2.3)$$

where  $\phi_L$  is the liquid flow rate and  $V$  the open volume of the monolith.

The total liquid holdup is composed out of the dynamic liquid slugs and the static liquid. The static liquid is composed of a thin liquid film and liquid inside the monolith wall.

For comparison, the ‘capillary’ dynamic liquid holdup  $\varepsilon_L$  using the bubble velocity  $u_B$  can be calculated by

$$\varepsilon_L = 1 - \frac{u_G}{u_B} \approx \frac{u_L}{u_{TP}} \quad (2.4)$$

where  $u_G$  and  $u_L$  are the superficial gas and liquid velocity, respectively, and  $u_B$  ( $u_B$  is somewhat larger than the total superficial velocity  $u_{TP}$  which is the sum of  $u_G$  and  $u_L$ ) in square capillary channels can be estimated, for  $u_B \leq 0.73$  m/s, by

$$\frac{u_B}{u_{TP}} = a \left( \ln(Ca) \right)^2 + b \ln(Ca) + c \quad (2.5)$$

where  $Ca$  = capillary number ( $\eta u_B / \gamma$ ), and  $a$ ,  $b$ , and  $c$  are fit parameters with the values 0.0653, 0.8579, and 3.8908, respectively.

### *Fitting the $E(\theta)$ -curves*

The  $E(\theta)$ -curves are fitted with the piston-dispersion-exchange (PDE) model (Fig. 2.2) that is commonly used for fixed bed reactors [29, 30, 31]. The PDE model consists of a dynamic liquid zone with axial dispersion and a stagnant liquid zone with mass exchange between the two zones. The PDE model thus contains three parameters that characterize the hydrodynamics: (1) the stagnant liquid fraction,  $SLF$ , that the pulse of tracer exchanges with, located either in the film or within the channel wall, (2) a dimensionless mass transfer parameter  $N$  ( $N = k \cdot a \cdot L / ((1-SLF) \cdot u_{TP})$ , where  $ka$  is the mass transfer parameter between the dynamic and static liquid,  $L$  is the column length, and  $u_{TP}$  is the total superficial velocity) that describes how fast tracer in the dynamic liquid zone exchanges with the stagnant liquid, and (3) a dimensionless dispersion parameter  $P$  that quantifies the extent of maldistribution either being caused by a (normal) distribution of velocities over the channels or by axial dispersion. Note that the axial dispersion is low to non-existing in Taylor flow since the gas bubbles

prohibit this and therefore can be modeled as plug flow. The dispersion parameter  $P$  is a fit parameter that is used to lump all maldistribution effects.

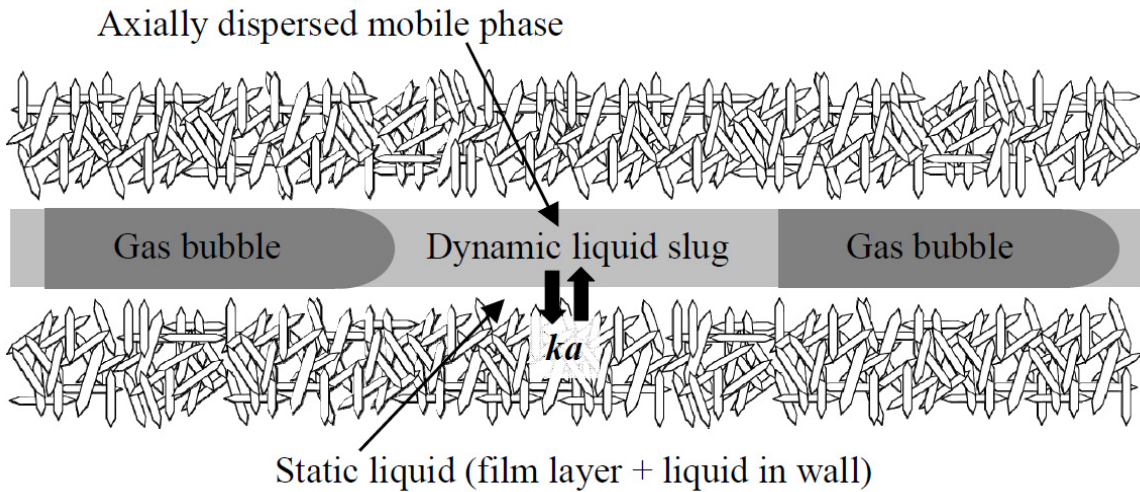


**Fig. 2.2.** Schematic representation of the PDE model for Taylor flow in ACM monoliths.

Basically, there is also a fourth fit parameter: the mean residence time ( $\tau_M$ ). This parameter, used to transpose the measured curve to a dimensionless curve, has an impact on the estimated PDE parameter values. The mass transfer and dispersion parameters are sensitive towards deviations from  $\tau_M$  [31]. The basic differential equations are derived from a mass balance of the tracer component. In dimensionless form, the transport equations for the dynamic and the stagnant zone are

$$\frac{\partial C_{\text{dyn}}}{\partial \theta} = \frac{1}{\phi P} \frac{\partial^2 C_{\text{dyn}}}{\partial x^2} - \frac{1}{\phi} \frac{\partial C_{\text{dyn}}}{\partial \theta} - \frac{N}{\phi} (C_{\text{dyn}} - C_{\text{st}}) \quad (2.6)$$

$$\frac{\partial C_{\text{st}}}{\partial \theta} = \frac{N}{SLF} (C_{\text{dyn}} - C_{\text{st}}) \quad (2.7)$$

where  $C_{\text{dyn}}$  is the concentration in the dynamic liquid phase,  $C_{\text{st}}$  is the concentration in the static liquid phase,  $\phi$  is the dynamic liquid fraction,  $SLF$  is the static liquid fraction ( $1-\phi$ ),  $N$  is the dimensionless mass transfer parameter for the exchange between the dynamic and static liquid zone.

For the equations the following dimensionless parameters are used

$$\theta = \frac{tu_{\text{TP}}\phi}{L}$$

$$P = \frac{u_{\text{TP}}L}{D}$$

$$x = \frac{z}{L}$$

$$N = \frac{kaL}{u_{\text{TP}}\phi}$$

(2.8-2.11)

where  $L$  is the monolith column length,  $\theta$  is the dimensionless time,  $t$  is time,  $z$  is the axial coordinate,  $ka$  is the mass transfer group,  $P$  is the dimensionless dispersion parameter and  $D$  is the dispersion coefficient. The initial and boundary conditions that lead to the solution for the RTD of the PDE differential equations are

$$C_{\text{dyn}} = 0, \quad C_{\text{st}} = 0 \quad \text{at } t = 0$$

$$C_{\text{dyn}} = \delta(0) \quad \text{at } x = 0 \quad (2.12-2.14)$$

$$\frac{\partial C_{\text{dyn}}}{\partial x} = 0 \quad \text{at } x = 1$$

#### *Calculating the liquid penetration depth into a porous wall due to passing gas bubbles*

The liquid velocity inside the walls  $u_w$  as a result of pressure pulses induced by the capillary Laplace pressure  $\Delta P_L$  of passing gas bubbles can be calculated with Darcy’s law. The validity of Darcy’s law for the representation of non-inertial, incompressible flows in porous media is widely accepted [32].

According to Darcy's law,  $u_W$  is related to the permeability  $\kappa$  by

$$u_W = \frac{\Delta P_L \kappa}{L_W \eta} \quad (2.15)$$

where  $\eta$  is the dynamic viscosity,  $\kappa$  is the permeability of the ACM wall, and  $L_W$  is the wall thickness. The capillary Laplace pressure due to the flowing bubbles is

$$\Delta P_L = \frac{\gamma}{d_C - 2\delta} \quad (2.16)$$

where  $d_C$  is the channel diameter of the monolith channel,  $\delta$  is the liquid film thickness, and  $\gamma$  is the surface tension. The film thickness can be estimated with

$$\frac{\delta}{d_C} = \frac{0.66 Ca^{2/3}}{3.34 Ca^{2/3} + 1} \quad (2.17)$$

With the length of the bubbles and the bubble velocity the contact time can be calculated. The length of an average bubble  $L_B$  can be estimated with

$$L_B = \Psi_{UC} \varepsilon_G d_C \quad (2.18)$$

where  $\Psi_{UC}$  is the dimensionless unit cell length depending on  $u_L$ ,  $u_G$ , and the gas-liquid distributor [25,26] and  $\varepsilon_G$  is the gas hold-up ( $=1-\varepsilon_L$ ). The penetration depth  $L_P$  can be calculated with

$$L_P = \frac{L_B}{u_B} u_W \quad (2.20)$$

## Results

A comparison of representative dimensionless RTD curves ( $E(\theta)$ -curves) of ACM-L, ACM-LC, ACM-M, and cordierite at equal superficial velocities is presented in Fig. 2.3. The dimensionless breakthrough times of the  $E(\theta)$ -curves were 0.3 and 0.4 for ACM and cordierite monoliths, respectively. The dimensionless time of the peak maximum was different for the ACM monoliths compared to the cordierite monolith, indicating a different static liquid fraction (*SLF*) [28] with ACM-M having the largest *SLF*. The cordierite monoliths had a peak maximum of 2 or higher, while that for the ACM monoliths ranged from 1.2 to 1.5 with the ACM-L samples having the lower values. The width of the  $E(\theta)$ -curves of the cordierite samples was smaller than that of the ACM-M and ACM-L samples. The tailing part was for all  $E(\theta)$ -curves more or less equal.

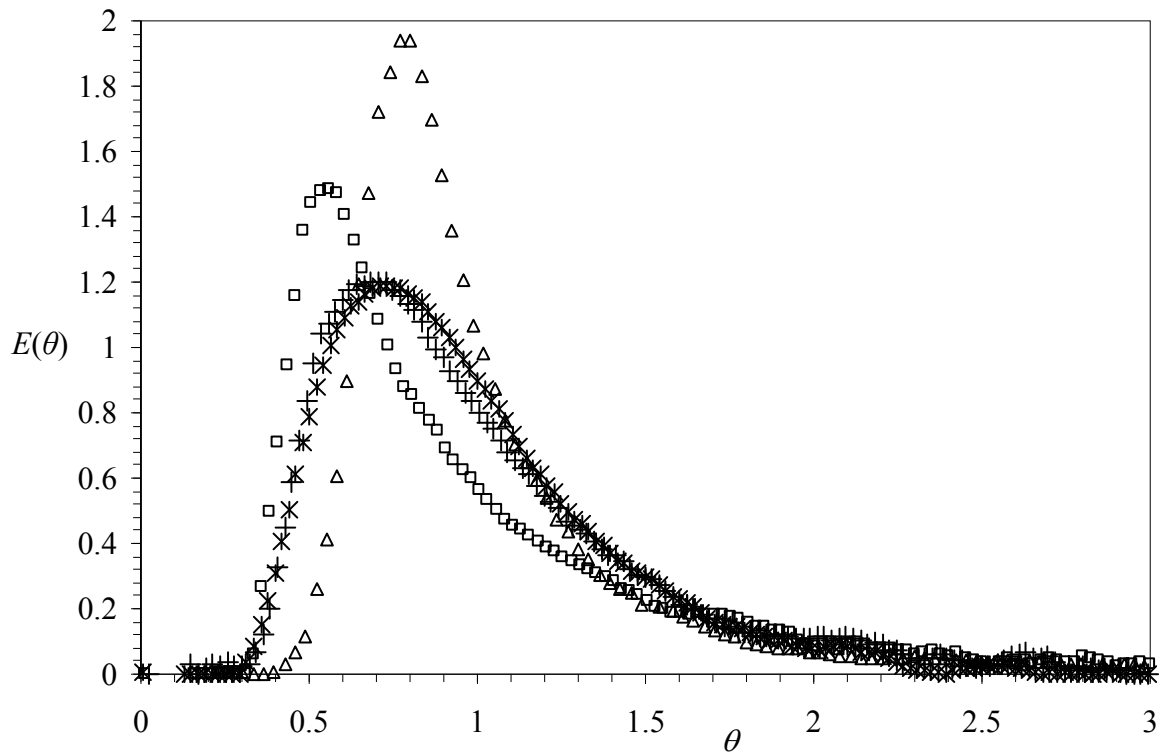


**Fig. 2.3.** Representative  $E(\theta)$ -curves obtained using ACM-M ( $\square$ ), ACM-L (+), ACM-LC (\*), and cordierite monoliths ( $\Delta$ ) for gas-liquid Taylor flow all measured at  $u_L = 0.12$  m/s and  $u_G = 0.14$  m/s.

The experimentally determined  $E(\theta)$ -curves were correlated by the PDE model. Some examples of fitted  $E(\theta)$ -curves and the areas of interest are shown in Fig. 2.4. Most  $E(\theta)$ -curves could be fitted to the PDE model. Moreover, the fitted PDE curves were checked by

careful visual inspection of the fit and the residuals, and poor fits were excluded from the following analysis.

The dispersion parameter  $P$  as a function of the total liquid holdup  $\varepsilon_L$  is depicted in Fig. 2.5,  $ka$  as a function of  $u_G$  with  $u_L$  constant at 0.14 m/s is presented in Fig. 2.6 and Fig. 2.7 shows the  $SLF$  as a function of  $u_{TP}$ . The drawn lines in Figs. 2.4, 2.5, and 2.6 merely represent guides to the eye for the PDE parameters. It is concluded that the differences between ACM-L and ACM-LC are minimal. Fig. 2.5 shows a strongly increasing  $P$  value with increasing  $\varepsilon_L$  for cordierite monoliths whereas the  $P$  value for the ACM samples is much less or even independent on changes of  $\varepsilon_L$ . The mean  $P$  of the ACM-M and ACM-L monoliths was around 26 and 18, respectively. There is a strong dependence of  $u_G$  on  $ka$  for ACM-L (Fig. 2.6). The mean value of  $ka$  for the ACM-L monolith (0.21) is significantly higher than the mean  $ka$  values for the cordierite monolith (0.11) and the ACM-M monolith (0.09). Fig. 2.7 shows that the  $SLF$  is independent on the chosen  $u_{TP}$ . The mean  $SLF$  of ACM-L (and ACM-LC) was 0.22, 0.27 for ACM-M and 0.14 for cordierite.

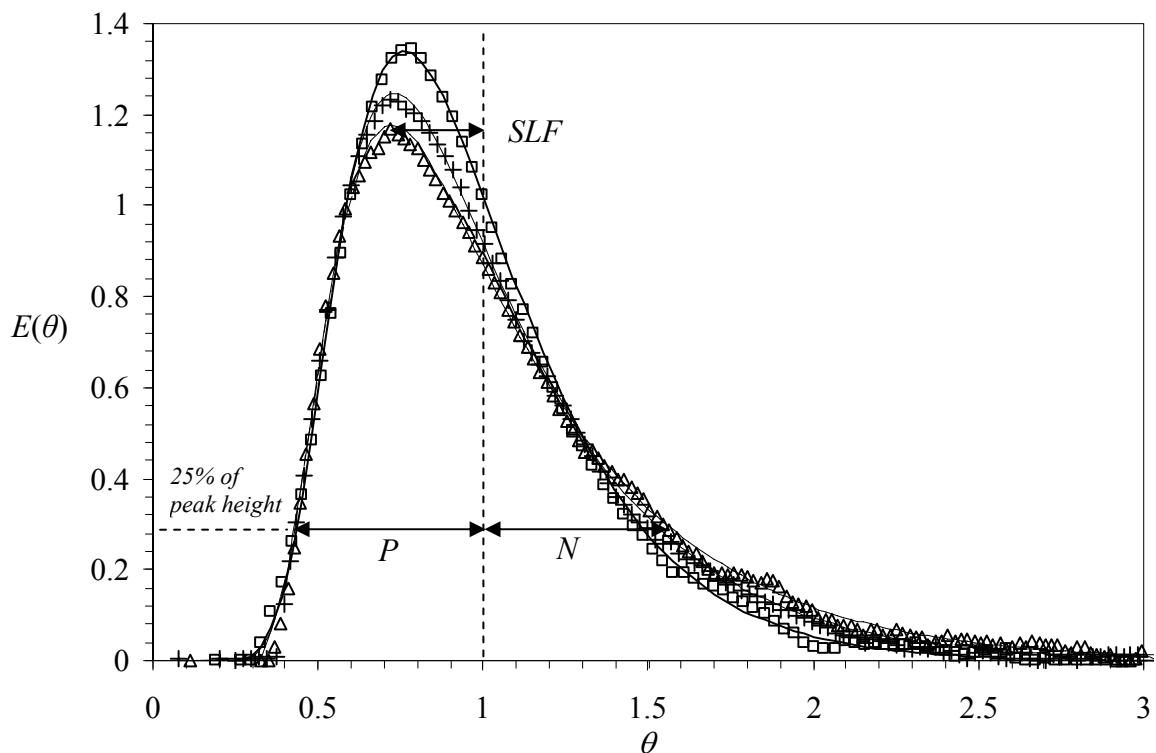


**Fig. 2.4.** Examples of  $E(\theta)$ -curves obtained using ACM-L samples for gas-liquid Taylor flow at various  $u_L$  values and  $u_G$  values:  $u_L = 0.18$  m/s and  $u_G = 0.12$  m/s ( $\square$ ),  $u_L = 0.13$  m/s and  $u_G = 0.13$  m/s (+) and  $u_L = 0.11$  m/s and  $u_G = 0.21$  m/s ( $\Delta$ ). The markers represent measured data and the lines represent the fitted data using the PDE model. The areas of interest are indicated in the graph. The best-fit PDE parameters are:  $N = 1.1$ ,  $SLF = 0.19$ , and  $P = 23$  ( $\square$ );  $N = 0.8$ ,  $SLF = 0.20$ , and  $P = 18$  (+);  $N = 0.8$ ,  $SLF = 0.20$ , and  $P = 14$  ( $\Delta$ ).

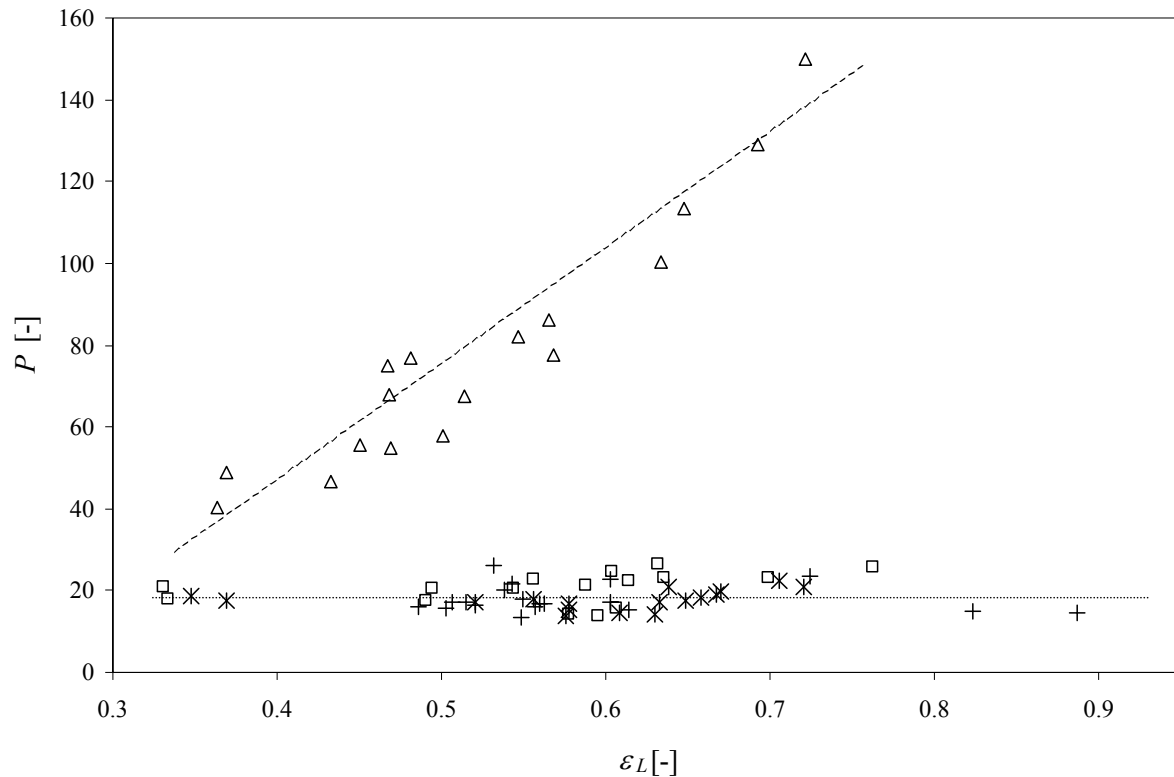


**Fig. 2.5.** The dispersion parameter  $P$  versus  $\varepsilon_L$  for ACM-M (□), ACM-L (+), ACM-LC (\*) and cordierite ( $\Delta$ ). The drawn lines are an indication of the trends.

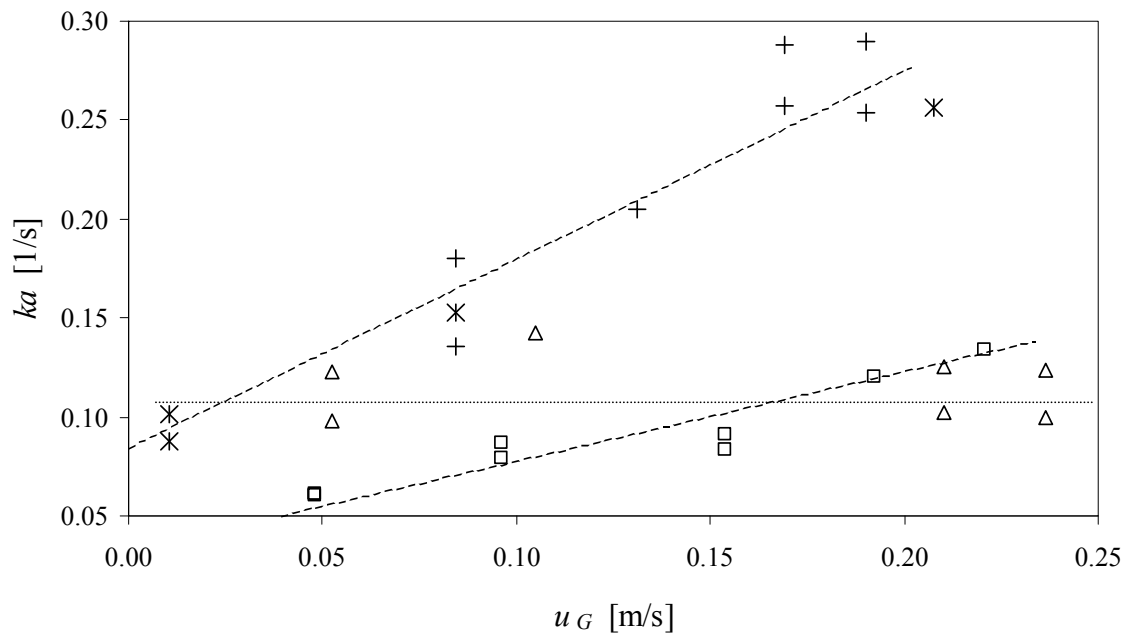


**Fig. 2.6.** The mass transfer group  $ka$  versus  $u_G$  at constant  $u_L$  of 0.14 m/s for ACM-M (□), ACM-L (+), ACM-LC (\*) and cordierite ( $\Delta$ ). The drawn lines are an indication of the trends.

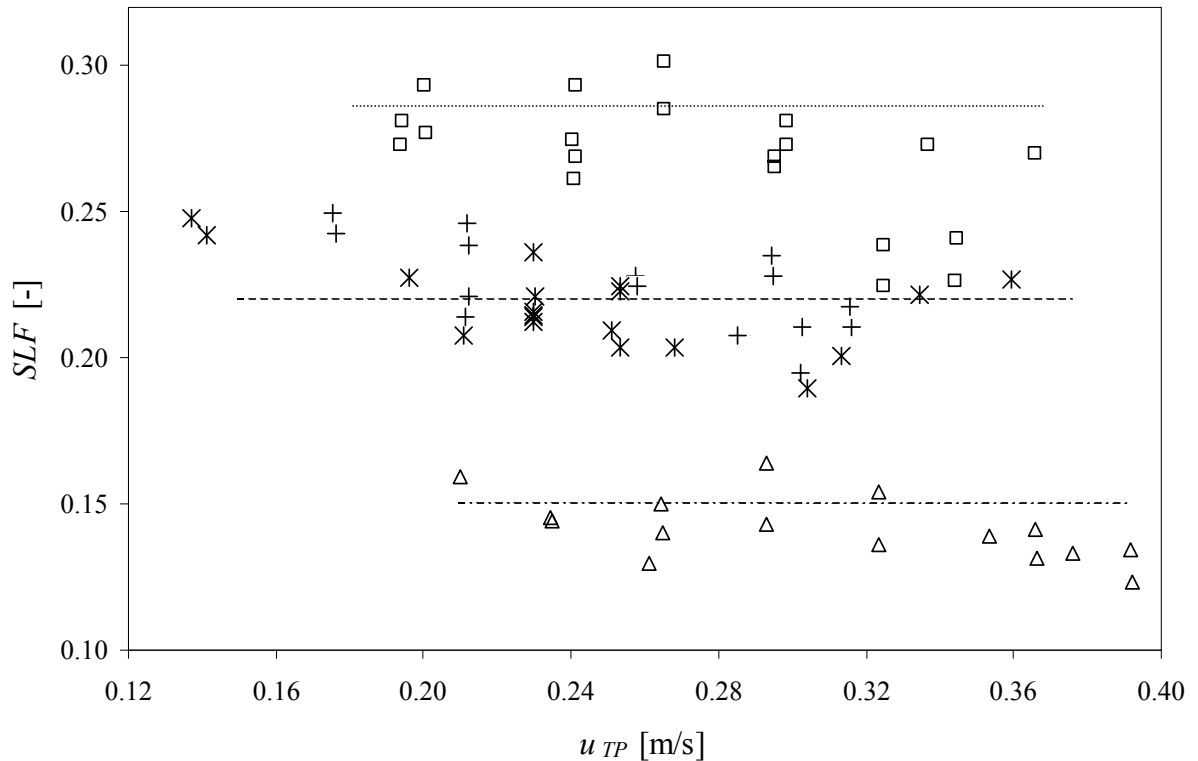


**Fig. 2.7.** The static liquid fraction  $SLF$  as a function of  $u_{TP}$  for ACM-M (□), ACM-L (+), ACM-LC (\*), and cordierite ( $\Delta$ ). The drawn lines are an indication of the trends.

## Discussion

### Dispersion parameter

The dimensionless dispersion parameter  $P$  as a function of  $\varepsilon_L$  is depicted in Fig. 2.5. Larger  $P$  values represent more plug flow behavior, thus less peak broadening. Analysis of frontal photographs of ACM and cordierite samples revealed that the standard deviation of the distribution in channel size was about 20% higher for the ACM samples. Naturally, a channel size distribution leads to a velocity distribution, with higher velocities in the larger channels. If the velocities in the channels are not uniform but Gaussian distributed, then the contribution of the non-uniform velocity to the RTD cannot be distinguished from axial dynamic dispersion inside the channels, as both mechanisms give the same bell-shaped RTD. The difference in channel size distribution alone cannot account for the big difference in  $P$  values and the different trends with variation of  $\varepsilon_L$  (by variation of  $u_L$  or  $u_G$ ) between ACM and cordierite monoliths.

For cordierite monoliths with only one void space between long blocks, it was found that  $P$  was primarily determined by the hydrodynamics outside the monolith block, such as the type and position of the distributor and the number of re-distribution zones between blocks [28]. In cordierite, fluid elements cannot ‘switch’ from a channel with a faster bubble-train flow to a channel with a slow bubble-train flow. As a result, changing the hydrodynamics of the feed zone and the stacking zones by changing  $\varepsilon_L$  had a noticeable effect on  $P$ . This strong dependence of  $P$  on  $\varepsilon_L$  for the cordierite monoliths was not observed for monolith blocks with less void spaces in between [28], so the observed dependence on  $\varepsilon_L$  is most likely related to the hydrodynamics in the six voids between the short monolith blocks used in this study. Apparently, a low  $\varepsilon_L$  tends to cause some de-mixing of gas and liquid in these spaces, while for a sufficiently high  $\varepsilon_L$  a good redispersion occurs. Hence, the dispersion behavior of the cordierite monoliths used in this study was predominantly influenced by external hydrodynamics.

For the ACM monoliths, fluid elements can – within limits – switch from channels with a fast bubble-train to a channel with a slow bubble-train. This radial dispersion will manifest itself in the RTD as an ‘observed’ axial dispersion. In any case, the fact that lower  $P$  numbers are obtained for ACM monoliths must be related to hydrodynamics inside the channels, caused by the higher velocity maldistribution and the higher  $SLF$ , because the distributor and geometry were the same for both ACM and cordierite monoliths. The dissimilar trend of the dispersion behavior for ACM monoliths with variation of the total liquid holdup when compared with cordierite monoliths showed that the dispersion behavior of ACM monoliths was mostly dominated by internal hydrodynamics.

#### *Mass transfer parameter*

The  $ka$  values as a function of  $u_G$  at constant  $u_L$  are given in Fig. 2.6. A higher  $ka$  value represents better mass transfer between the dynamic and static liquid zone. The very open structure of the wall in the ACM-L samples (mean pore size is 2.5 times bigger than the ACM-M mean pore size and 5.6 times bigger than the cordierite mean pore size) should allow for much faster diffusion inside the wall. Additionally, there is also an effect of the ACM channel wall roughness: the large grains might induce some secondary flow in the film that enhances the mass transfer. Further, the permeable ACM monoliths allow the gas bubbles to push liquid into the wall, adding radial convection to the otherwise only diffusive exchange with the static zone. This is in contrast to gas bubbles in cordierite channels with rather

impermeable walls, which can only push the liquid forward, allowing only a small fraction of lubricating film between the bubble and the wall. A schematic representation of this radial convection in an ACM-L monolith is given in Fig. 2.8. Equating the Laplace bubble pressure with the laminar pressure losses due to flow through the permeable wall (Darcy's law [32]) showed that for all experimental conditions, surface tension could force liquid completely through the ACM-L channel walls. So this suggests that the capillary Laplace pressure of gas bubbles moving through the ACM monolith channels are able to push liquid not only into but completely through the channel walls, adding convection to the otherwise diffusive mass transfer process inside the channels and creating radial liquid transport between adjacent channels. As a result, the reactor volume occupied by the wall participates fully in the ACM-L structures. For the ACM-M monolith, with a 4 times lower permeability, this was not, or at least to a much lesser extent, the case.

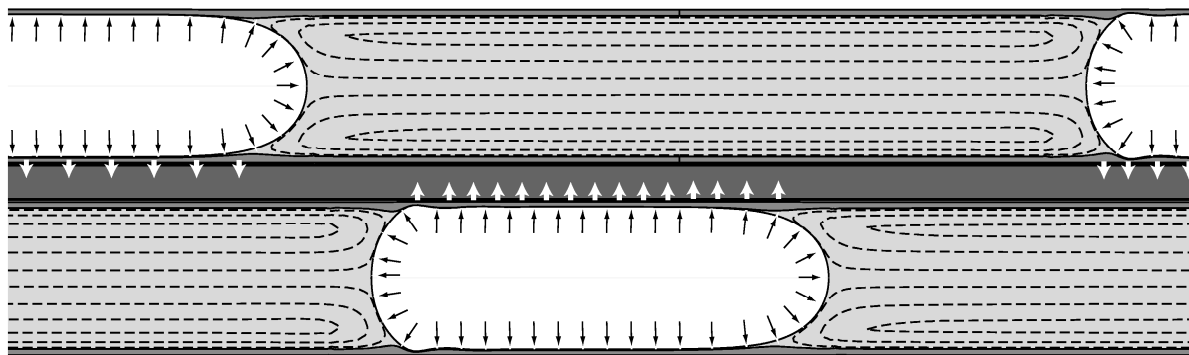


**Fig. 2.8.** Schematic representation of gas-liquid Taylor flow in ACM monoliths: a passing liquid bubble pushes the liquid inside the porous ACM wall. The black arrows represent the surface tension forces and the white arrows represent the radial convective transfer of liquid into the ACM walls.

From Fig. 2.6 one can see that an increase of  $u_G$  at constant  $u_L$  induced a strong increase of the  $ka$  of ACM-L (and to a lesser extent also an increase of the  $ka$  of ACM-M) but did not have an effect on the  $ka$  of cordierite. An increase in  $u_G$  results in longer gas slugs with a longer contact time, which results in a longer pulsating effect. Therefore, a stronger pulsating effect leads to a radial convection contribution that penetrates deeper into the wall and adds more to the overall mass transfer. The increase of  $u_G$  also induced higher  $ka$  values for ACM-M, although for ACM-M the radial convection effect is, as expected, smaller.

### *Static liquid fraction*

The *SLF* (*SLF* = liquid film + liquid in wall fraction) is more or less independent on  $u_{TP}$  in the measured range (Fig. 2.7). The *SLF* of the ACM-L monoliths was about 50% larger than the *SLF* of the cordierite monoliths, while that of the ACM-M monoliths was even about 90% larger. Coating the ACM-L with a thin layer of colloidal silica did hardly change its RTD behavior. Only a small delay in the peak maximum of the  $E(\theta)$ -curve is observed ascribed to the small decrease of porosity of ACM-LC due to the silica coating. The higher *SLF* values of ACM when compared to cordierite are ascribed to the much larger porosity and permeability of the ACM monolith walls. It should be stressed here that the curves were dimensionalized based on the moments of the curve alone, so the amount of column volume occupied by the walls was not explicitly taken into account in any of the curve fits. The *SLF* of the cordierite agrees, within experimental error, with the *SLF* that may be estimated from film thickness correlations for square capillary channels [33]. The higher *SLF* values for ACM-M when compared to ACM-L were due to the much lower permeability of the ACM-M walls. Therefore the Laplace pressure of the gas slugs was not able to push the liquid out of the wall into an adjacent channel. Moreover, an important additional effect is that when the permeability of the walls is high enough, *i.e.*, for the ACM-L samples, there will be a decrease of the film layer thickness when compared to ACM-M and cordierite.

## Conclusions

The residence time distribution measurements under Taylor flow conditions show that the multiphase fluid mechanics are different for cordierite and ACM monoliths. The tracer does not significantly penetrate the macroporous wall of a classical cordierite monolith, but does access the open interior ACM wall. ACM monoliths have higher static liquid fractions when compared to the cordierite structures, *i.e.*, the walls of the ACM monoliths participate in the hydrodynamic process.

The pressure pulse effect of Taylor-bubbles is significant for ACM-L monoliths. For ACM-M monoliths this effect is much less significant. The accessibility of catalyst in the solid structure is greatly enhanced for ACM-L monoliths. Thus, by tailoring the wall morphology of a monolith, one can design more efficient reactors for catalyzed gas-liquid reactions.

The mass transfer parameter of the different ACM monoliths varies, with ACM-L structures having the largest mass transfer parameter. For the ACM-L monoliths, the mass transfer rate is significantly higher between the liquid bulk and the wall interior than for the classical monolith or for the ACM-M monolith. The grain structure of the ACM-L monoliths influences the hydrodynamic process and there even is interaction between adjacent monolithic channels.

The ability of liquid elements to switch from channel to channel, the higher static liquid fractions and the larger velocity maldistribution induced less plug flow behavior when compared to cordierite monoliths.

### Notation

|             |   |
|-------------|---|
| ACM-L       | Acicular mullite with large grains                                    |
| ACM-LC      | Acicular mullite with silica coated large grains                      |
| ACM-M       | Acicular mullite with medium grains                                   |
| $B$         | Path length, m  |
| $C$         | Concentration, kg/kg  |
| $Ca$        | Capillary number, defined as $(\eta u_B) / \gamma$ , -                |
| $C_{dyn}$   | Concentration in the dynamic phase, kg/kg                             |
| $C_{st}$    | Concentration in the static phase, kg/kg                              |
| cpsi        | Cell per square inch  |
| $D$         | Dispersion coefficient, m <sup>2</sup> /s                             |
| $d_C$       | Channel diameter, m   |
| $E(\theta)$ | Dimensionless residence time distribution, -                          |
| $I$         | Intensity, counts/s   |
| $I_{dark}$  | Intensity without light source, counts/s                              |
| $I_{ref}$   | Intensity of pure water, counts/s                                     |
| $ka$        | Mass transfer group (exchange between static and dynamic liquid), 1/s |
| $L$         | Length of the monolith column, m                                      |
| $L_B$       | Length of the bubble, m   |
| $L_W$       | Wall thickness, m   |
| $N$         | Dimensionless mass transfer parameter based on the PDE model, -       |
| $P$         | Dimensionless dispersion parameter based on the PDE model, -          |
| $r$         | Radius of a monolith channel, m                                       |
| $SLF$       | Static liquid fraction based on the PDE model, -                      |
| $t$         | Time, s   |
| $u_B$       | Bubble velocity, m/s  |
| $u_G$       | Superficial gas velocity, m/s   |
| $u_L$       | Superficial liquid velocity, m/s                                      |
| $u_{TP}$    | Total superficial velocity, m/s                                       |
| $u_W$       | Liquid velocity in the wall, m/s                                      |
| $V$         | Volume monolith open to flow, m <sup>3</sup>                          |
| $x$         | Dimensionless length, -   |
| $z$         | Axial length coordinate, m  |

*Greek letters*

|                   |   |
|-------------------|---|
| $\alpha(\lambda)$ | Wavelength-dependent absorption coefficient |
| $\gamma$          | Surface tension, N/m                        |
| $\delta$          | Liquid film thickness, m                    |
| $\Delta P_L$      | Laplace pressure, Pa                        |
| $\varepsilon_L$   | Total liquid holdup based on $u_b$ , -      |
| $\varepsilon_G$   | Gas holdup, -                               |
| $\phi$            | Dynamic liquid fraction (holdup), -         |
| $\eta$            | Dynamic viscosity, Pa·s                     |
| $\kappa$          | Permeability, m <sup>2</sup>                |
| $\theta$          | Dimensionless time, -                       |
| $\phi_L$          | Liquid flow rate, m <sup>3</sup> /s         |
| $\tau_M$          | Mean residence time, s                      |
| $\Psi_{UC}$       | Dimensionless total unit cell length, -     |

## Bibliography

- [1] F. Kapteijn, J.J. Heiszwolf, T.A. Nijhuis, J.A. Moulijn, *Cattech* 3 (1999) 24.
- [2] F. Kapteijn, T.A. Nijhuis, J.J. Heiszwolf, J.A. Moulijn, *Catal. Today* 66 (2001) 133.
- [3] A. Cybulski, J.A. Moulijn, *Structured catalysts and reactors*, Marcel Dekker, New York, 1998.
- [4] R.M. Machado, D.J. Parrillo, R.P. Boehme, R.R. Broekhuis, US patent 6,005,143 (1999).
- [5] S. Roy, T. Bauer, M. Al-Dahhan, P. Lehner, T. Turek, *AIChE J.* 50 (2004) 2918.
- [6] J.J. Heiszwolf, L.B. Engelvaart, M.G. van den Eijnden, M.T. Kreutzer, F. Kapteijn, J.A. Moulijn, *Chem. Eng. Sci.* 56 (2001) 805.
- [7] C.N. Satterfield, F. Öznel, *Ind. Eng. Chem. Fund.* 16 (1977) 61.
- [8] M.T. Kreutzer, J.J. Heiszwolf, F. Kapteijn, J.A. Moulijn, C.R. Kleijn, *AIChE J.* 51 (2005) 2428.
- [9] M.T. Kreutzer, J.J. Heiszwolf, F. Kapteijn, J.A. Moulijn, *Chem. Eng. Sci.* 60 (2005) 22.
- [10] M.T. Kreutzer, P. Du, J.J. Heiszwolf, F. Kapteijn, J.A. Moulijn, *Chem. Eng. Sci.* 56 (2001) 823.
- [11] C.O. Vandu, J. Ellenberger, R. Krishna, *Chem. Eng. Proc.* 44 (2004) 4999.
- [12] J.M. van Baten, R. Krishna, *Chem. Eng. Sci.* 59 (2004) 2535.
- [13] M. Winterbottom, H. Marwan, R. Natividad, *Can. J. Chem. Eng.* 81 (2003) 838.
- [14] T.A. Nijhuis, A.E.W. Beers, T. Vergunst, I. Hoek, F. Kapteijn, J.A. Moulijn, *Catal. Rev.* 43 (2001) 345.
- [15] T. Vergunst, M. Linders, F. Kapteijn, J.A. Moulijn, *Catal. Rev. Sci. Eng.* 43 (2001) 291.
- [16] J.R. Moyer, N.N. Hughes, *J. Am. Ceram. Soc.* 77 (1994) 1083.
- [17] S.A. Wallin, A.R. Prunier, J.R. Moyer, US Patent 6,306,335 (2001).
- [18] K.M. De Lathouder, J.J.W. Bakker, M.T. Kreutzer, F. Kapteijn, J.A. Moulijn, S.A. Wallin, *Chem. Eng. Sci.* 95 (2004) 5027.
- [19] G.I. Taylor, *J. Fluid Mech.* 10 (1960) 161.
- [20] F.P. Bretherton, *J. Fluid Mech.* 10 (1961) 166.

- [21] N. Reinecke, D. Mewes, *Int. J. Multiphase Flow* 25 (1999) 1373.
- [22] M.D. Mantle, A.J. Sederman, L.F. Gladden, S. Raymahasay, J.M. Winterbottom, E.H. Stitt, *AIChE J.* 48 (2002) 909.
- [23] L.F. Gladden, M.H.M. Lim, M.D. Mantle, A.J. Sederman, E.H. Stitt, *Catal. Today* 79 (2003) 203.
- [24] H. Lui, C.O. Vandu, R. Krishna, *Ind. Eng. Chem. Res.* 44 (2004) 4884.
- [25] S. Laborie, C. Cabassud, L. Durand-Bourlier, J.M. Lainé, *Chem. Eng. Sci.* 54 (1999) 5723.
- [26] J.J. Heiszwolf, M.T. Kreutzer, M.G. van den Eijnden, F. Kapteijn, J.A. Moulijn, *Catal. Today* 69 (2001) 51.
- [27] G. Berčič, A. Pintar, *Chem. Eng. Sci.* 52 (1997) 3709.
- [28] M.T. Kreutzer, J.J.W. Bakker, F. Kapteijn, J.A. Moulijn, P.J.T. Verheijen, *Ind. Eng. Chem. Res.* 44 (2005) 4898.
- [29] J. Villermaux, W.P.M. van Swaaij, *Chem. Eng. Sci.* 24 (1969) 1097.
- [30] I. Iliuta, F. Thyrion, O. Muntean, M. Giot, *Chem. Eng. Sci.* 51 (1996) 4579.
- [31] D. Stegeman, F.E. van Rooijen, A.A. Kampermans, S. Weijer, K.R. Westerterp, *Ind. Eng. Chem. Res.* 35 (1996) 378.
- [32] J.C. Giddings, *Unified separation science*, Wiley, New York, 1991.
- [33] T.C. Thulasidas, M.A. Abraham, R.L. Cerro, *Chem. Eng. Sci.* 54 (1999) 61.

# 3

## **Enhancement of catalyst performance using pressure pulses on macroporous structured palladium catalysts**

---

The enhancement of catalyst performance by inducing convection inside a macroporous catalyst carrier is investigated. The catalyst carrier used was an acicular mullite (ACM) monolith with highly permeable microstructured walls. The monolith walls were coated with colloidal silica and impregnated with Pd. After performing the proper preparation steps, the high permeability of the walls was preserved and the catalyst was uniformly distributed with a low effective diffusion length. The catalyst performance of the selective hydrogenation of 3-methyl-1-pentyn-3-ol was investigated in a monolithic stirrer reactor, under internal diffusion-limited conditions, using different silica-supported palladium monoliths. At 2.3 bar H<sub>2</sub>, 20 mol/m<sup>3</sup> alkyne, and 24°C, using equal catalyst loadings, the activity per unit monolith volume was 100% greater and the maximum yield of the alkene was 9% greater for the ACM monolith than for the eggshell-coated monolith with impermeable walls. This confirms that internal diffusional limitations were reduced. Pressure pulses of passing gas bubbles inside the monolith channels induced a convective enhancement, thereby making mass transfer limitations inside the highly permeable walls absent.

---

This Chapter is published in Ind. Eng. Chem. Res. 46 (2007) 8574.

## Introduction

Heterogeneous catalysis in liquids is severely hindered by slow diffusion inside particles, with detrimental effects on activity, selectivity, and stability of the catalyst. There are three ways to overcome diffusional problems: (1) one can make a less active catalyst, tilting the balance of diffusion and reaction in favor of the latter; (2) one can make a smaller catalyst, which is very effective because diffusional time scales with the square of length; (3) one can force the liquid to flow through the porous catalytic material. The subject of this Chapter is the design of structured catalysts that exploit this third option: convective enhancement of catalyst effectiveness.

It is illustrative to consider some characteristic numbers: assume a spherical catalyst particle with  $d_p = 0.6$  mm, with a first-order rate constant of  $k_V = 0.1$  s<sup>-1</sup> and an intraparticle diffusion coefficient  $D_{\text{eff}} = 10^{-10}$  m<sup>2</sup>/s. Then, the characteristic time for reaction  $1/k_V$  amounts to 10 s and the characteristic time for diffusion is  $(d_p/6)^2/D_{\text{eff}}$  equals 100 s. I can balance these times by either reducing the catalyst's activity tenfold or by making a 0.6 mm eggshell catalyst with a 70  $\mu$ m active layer. Both these measures increase the required catalyst volume tenfold. Alternatively, if I am able to transport matter through the catalyst with an intraparticle velocity of only  $d_p/k_V = 60$   $\mu$ m/s, the diffusional problems vanished and the per-volume activity can be maintained. For a more comprehensive theoretical analysis of convective enhancement, the reader is referred to Nir & Pismen [1].

Several reports of intraparticle convective enhancement of reactions rates have been reported in the open literature. The rich dynamics of multiphase flow is usually used to create such convection, and more often than not, a gas phase is involved. Wilhite and co-workers [2] showed that both selectivity and yield could be improved in trickle beds by operating in the pulsing regime. It is well known in electrochemistry that evolution of gas disrupts concentration boundary layers. Intraparticle production of CO<sub>2</sub> by immobilized yeast cells and the subsequent convection caused by this gas is known to enhance the effectiveness of this reaction [3]. Van den Heuvel and co-workers [4, 5] have designed convective enhancement on purpose by entrapping a gas bubble inside a catalyst particle and subsequently subjecting that particle to variation in static pressure by recycling the particle in a vertical loop reactor. As the particle traverses this loop, the variation in pressure causes the bubble to shrink and expand, squeezing liquid in and out of the particle.

In this study I used monoliths as structured support materials [6-9]. A monolith consists out of thousands of small ( $\sim 1$  mm) parallel straight channels, separated by thin walls in which

external mass transfer can be decoupled from internal mass transfer by independently varying the wall thickness and the channel diameter [10]. The channel walls of a monolith are usually coated with large surface area catalyst carriers to create an eggshell catalyst [11]. A disadvantage, in particular for the eggshell washcoated monoliths, is the lower catalyst inventory when compared to packed-bed reactors. Convective enhancement would be a welcome method to increasing the activity per unit monolith volume.

When local or temporal pressure variations are used to induce flow inside the particle, it is imperative that the permeability is high. In recent years, various groups have reported the synthesis of high-porosity support materials for catalysts that exhibit such a high permeability [12-17]. Here, I use high-porosity honeycomb monoliths, where the walls consist of fused, interlocked, micro-structured acicular mullite grains with a continually interconnected open pore system (Fig. 3.1a and 3.1b) [18-20]. By controlling nucleation and crystal growth, different mullite grain sizes and consequently different pore sizes can be produced. For a comparison, a less porous cordierite monolith wall is shown in Fig. 3.1c.

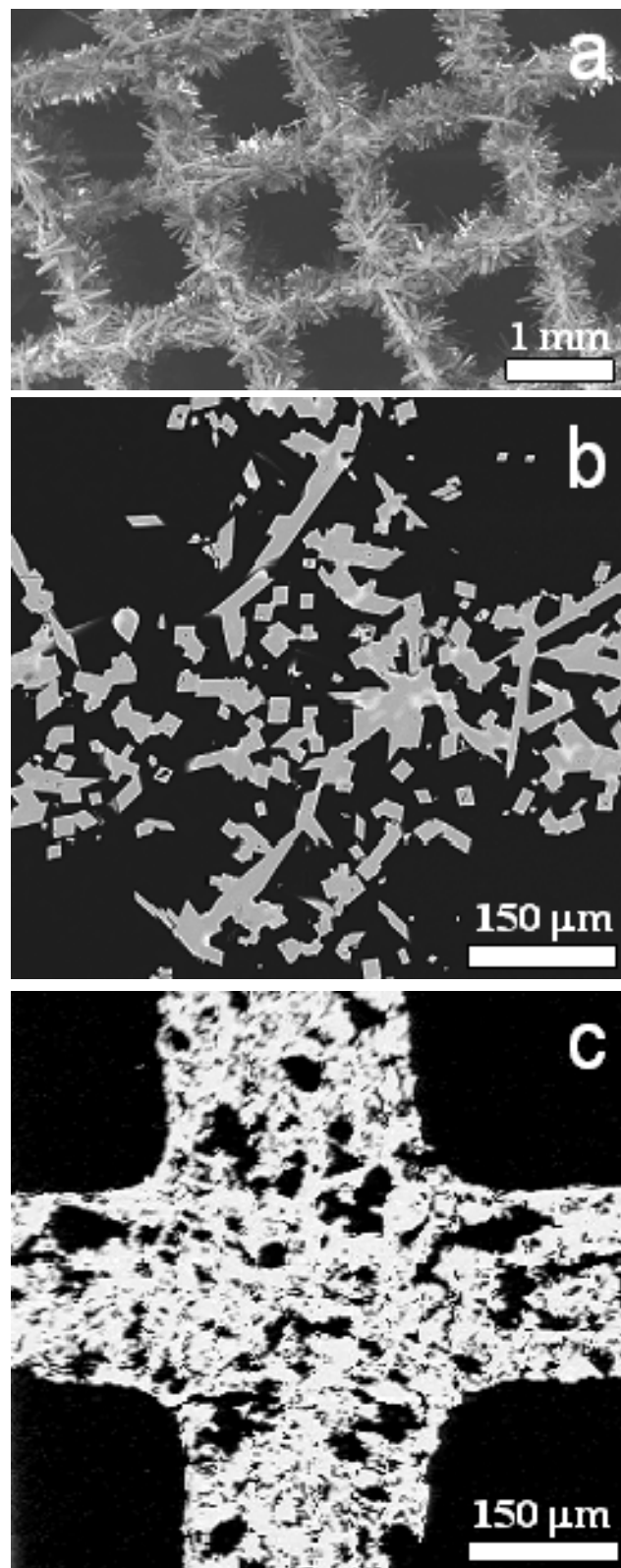


**Fig. 3.1.** (a) SEM micrograph of the micro-structured walls of the acicular mullite (ACM) monolith. (b) Backscattered electron image (BEI) of a polished cross section of a wall intersection showing the highly permeable walls made of interlocked elongated mullite grains with an interconnected pore system. (c) BEI of a polished cross section of a cordierite monolith wall intersection.

One can conceive many different hydrodynamic mechanisms that create pressure pulses. In this Chapter, I will explore the use of Laplace pressures in capillary channels as the forcing mechanism. For a gas bubble traversing a capillary channel, a pressure jump exists over the gas-liquid interface of magnitude  $\gamma/d_{\text{ch}}$ , where  $\gamma$  is the surface tension and  $d_{\text{ch}}$  is the channel diameter. The alternating passing of bubbles on both sides of the wall of a monolithic catalyst support creates an alternating pressure difference over the wall (Fig. 3.2). The Laplace pressure associated with passing bubbles ( $\gamma/d_{\text{ch}}$ ), creates pressure differences over the channel walls (Fig. 3.2a). This pressure difference generates flow with velocity  $u_{\text{wall}}$  through the walls with intrinsic permeability  $K$  (Fig. 3.2b). The ratio of diffusion time  $t = L^2/D_{\text{eff}}$  (with  $D_{\text{eff}} \sim 0.2 \cdot D$ ) and reaction time  $t = C/r_{\text{obs}}$  can be based on the coating thickness  $L_{\text{coat}}$  (Fig. 3.2c). A similar ratio of characteristic times can be defined for diffusion through the wall using the wall thickness  $L_{\text{wall}}$  and  $D_{\text{eff}} = (\varepsilon_p/\tau_p) \cdot D \sim 0.7 \cdot D$  (Fig. 3.2d). Such pressure pulsing is a known technique in membrane science to prevent filter cake build-up and to improve liquid fluxes for microfiltration [21].

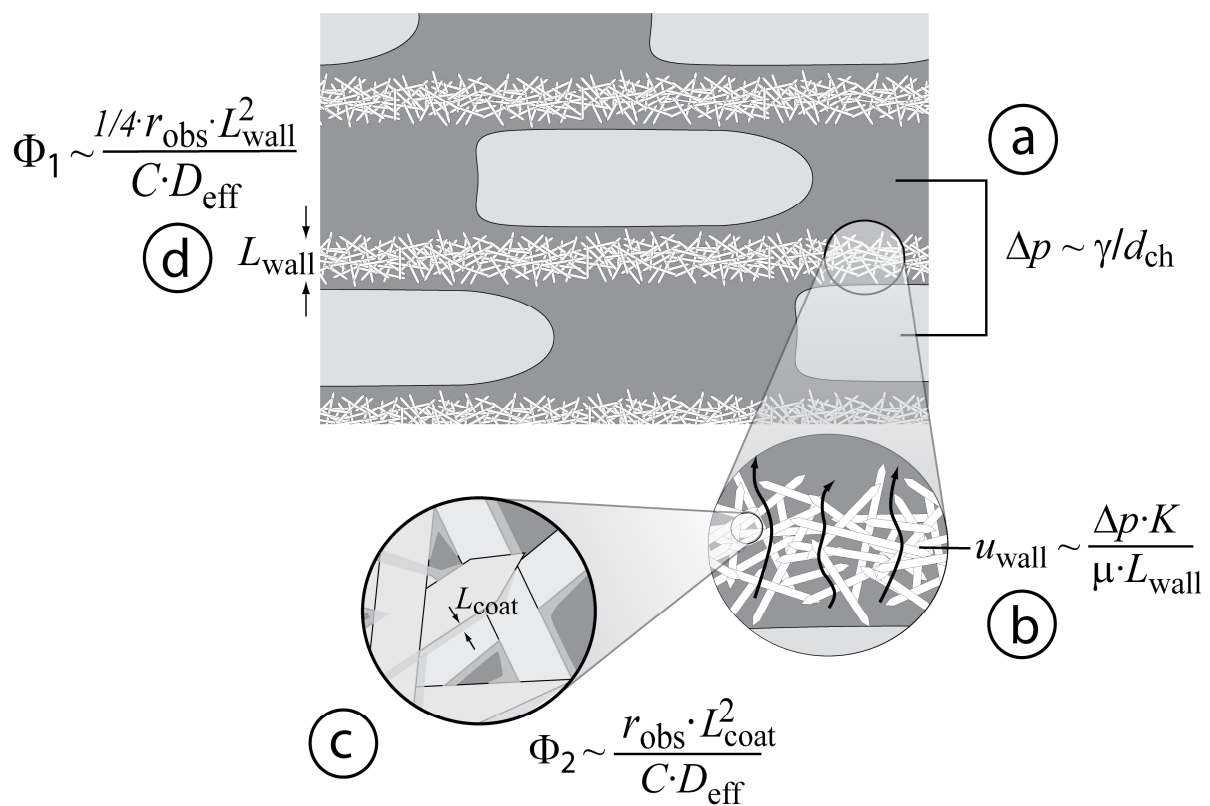


**Fig. 3.2.** Artists' impression of the mechanism of convective enhancement in ACM monolith channels. (a) The Laplace pressure associated with passing gas bubbles, creates a pressure differences over the channel walls. (b) The pressure difference generates a flow through the walls. (c) The ratio of diffusion time  $t = L_{\text{coat}}^2/D_{\text{eff}}$  and reaction time  $t = C/r_{\text{obs}}$  can be based on the coating thickness  $L_{\text{coat}}$ . (d) A similar ratio of characteristic times can be defined for diffusion through the wall based on the wall thickness  $L_{\text{wall}}$ .

In Chapter 2, I have used breakthrough curves and residence time distribution (RTD) experiments to show that these bubbles significantly enhance the exchange of matter between the liquid in these highly porous walls and the liquid that flows through the channel [22]. In this Chapter, I make a case using reactive experiments.

The primary aim of this research is to demonstrate the advantage of these ACM monoliths with highly porous walls in multiphase reactive experiments, in comparison to cordierite monoliths for reactions that suffer from internal diffusion limitations. A Pd-catalyzed selective hydrogenation of a functionalized alkyne, where the maximum yield of intermediate is a direct measure for the extent of diffusion limitation, was used as a test reaction.

The specific surface area of ACM monoliths itself is too low ( $< 0.5 \text{ m}^2/\text{g}$ ) to support and stabilize the active phase (*i.e.*, Pd), and thus a supporting material of high specific surface area, *i.e.*, silica, must be deposited onto the grains of the ACM monoliths. So, the second aim is the development of a catalyst preparation method by means of a dipcoating procedure that deposits colloidal silica inside the walls. The colloidal silica coating should

- Increase the specific surface area and provides anchoring sites.
- Have an open connected network of mesopores fully accessible to the reactants.
- Have a short effective diffusion length.
- Be uniformly distributed throughout the wall and over the complete monolith length.
- Leave the interconnected pore system intact (avoid major pore plugging) to fully benefit from the high permeability of the ACM walls.

## Experimental

### *Monoliths*

ACM monoliths of 5 cm in length and 4 cm in diameter with a cell density of 400 cpsi were prepared by a proprietary Dow process to produce monoliths with acicular mullite grains ( $\sim 1.7\text{Al}_2\text{O}_3\text{-SiO}_2$ ) [23]. Two different ACM monoliths were used with different wall porosity and mean pore size (ACM-L and ACM-S, Fig. 2.1 Chapter 2). Cordierite monoliths of equal dimensions and cell density were used for comparison. See Table 3.1 for the different properties of the monoliths used in this study.

The intrinsic permeability of the ACM walls containing a three-dimensional network of interconnected pores can be estimated by a modified Kozeny-Carmen equation [24-27], defined as

$$K = \frac{\varepsilon \cdot (d_{\text{pore,m}})^2}{32 \cdot \tau} \quad (3.1)$$

where  $K$  is the intrinsic permeability,  $\varepsilon$  is the wall porosity,  $d_{\text{pore,m}}$  is the mean pore diameter, and  $\tau$  is the tortuosity which equals 1.06 for the open ACM walls. The dependence of  $K$  on  $(d_{\text{pore,m}})^2$  in this equation was verified by experimentally determined permeability's of a few ACM monolith walls with different mean pore sizes. Porosities and pore sizes of the ACM and cordierite monoliths were determined by Hg intrusion porosimetry.

**Table 3.1**  
Properties of the different monoliths used in this study

| Property   | Acicular mullite large pores<br>(ACM-L) | Acicular mullite small pores<br>(ACM-S) | Cordierite |
|--|---|---|------------|
| Channel size - mm                                      | 1                                       | 1                                       | 1.1        |
| Wall thickness - $\mu\text{m}$                         | 240                                     | 240                                     | 180        |
| Specific surface area - $\text{m}^2/\text{g}$          | 0.22                                    | 0.54                                    | 0.21       |
| Wall porosity - %                                      | 71                                      | 62                                      | 36         |
| Average pore size - $\mu\text{m}$                      | 45                                      | 5                                       | 8          |
| Pore volume<br>up to pore size of 10 $\mu\text{m}$ - % | 10                                      | 80                                      | 60         |
| Intrinsic permeability - $10^{-12} \text{ m}^2$        | 40                                      | 1                                       | < 0.5      |

### *Catalyst preparation*

The catalyst preparation step is crucial because the original porous structure of the walls must be kept intact and equal amounts of silica must be deposited evenly inside the walls over the full length of the monolith. To achieve this I used a modified pore filling method originally introduced by Beauseigneur *et al.* [28] by dipcoating the ACM monoliths for 2 min in diluted aqueous colloidal silica suspensions (Ludox® supplied by Aldrich) at a constant immersion and withdrawal speed of 10 cm/min. As a silica source, different Ludox® solutions, *i.e.*, SM30, HS40, and AS40 with surface areas of 345, 220, and 135 m<sup>2</sup>/g, respectively, were used. These Ludox® solutions contain negatively charged nanometer size monodisperse silica particles in an aqueous solution containing positive counter ions. The colloidal silica solution was diluted by demineralized water to obtain different silica concentrations and gently homogenized using magnetic stirring for 3 min. Normally the pH of the colloidal solution was around 10 but for some experiments the pH was adjusted to 4 by adding a few drops of HNO<sub>3</sub> (J.T. Baker, 65%). Prior to dipcoating, the ACM samples were treated in HNO<sub>3</sub> for 1 h to enhance the mechanical interlocking between the mullite and the colloidal silica particles. After this pre-treatment they were rinsed with demineralized water and dried for 2 h at 120°C. After dipcoating, the samples were dried. The drying method strongly affects the silica distribution over the monolith. To select the best drying method, the following recipes were used to dry the samples

- Drying in static air at room temperature or at elevated temperature in an oven.
- Drying in static air while rotating the sample.
- Drying in a Whirlpool AVM840 microwave at 200 W for 20 min.
- Dipping in liquid N<sub>2</sub> and freeze drying at 0.37 mbar for 15 h.

All dried samples were calcined at 450°C for 4 h with a heating rate of 2°C/min.

The silica-coated monoliths were impregnated with Pd(II) acetate trimer (Alpha Aesar, 45.9 wt% Pd) dissolved in toluene (J.T. Baker) for 24 h [29]. Liquid is forced to flow and circulate through the channels by stirring above the monolith using a specially developed glass reactor (Fig. 3.3). After impregnation the monoliths were washed with *n*-hexane (Aldrich), dried at 120°C for 4 h, calcined for 4 h at 250°C with a heating rate of 1°C/min. Reduction took place *in-situ* with H<sub>2</sub> at ambient temperature for 2 h prior to reaction. For comparison, cordierite monoliths were slurry-coated with silica (Davisil™ grade 645 (Aldrich): particle size 36 - 75 µm with a specific surface area of 290 m<sup>2</sup>/g) as described by Nijhuis *et al.* [11].

The cordierite monoliths were not coated with colloidal silica because in an earlier study it was found that the colloidal silica was mainly deposited inside the cordierite walls which increased the effective diffusion distance that led to ineffective use of the catalyst, *i.e.*, lower activity and selectivity compared to the slurry-coated cordierite monoliths [30]. The coated cordierite monoliths were impregnated with Pd according to the procedure described above.

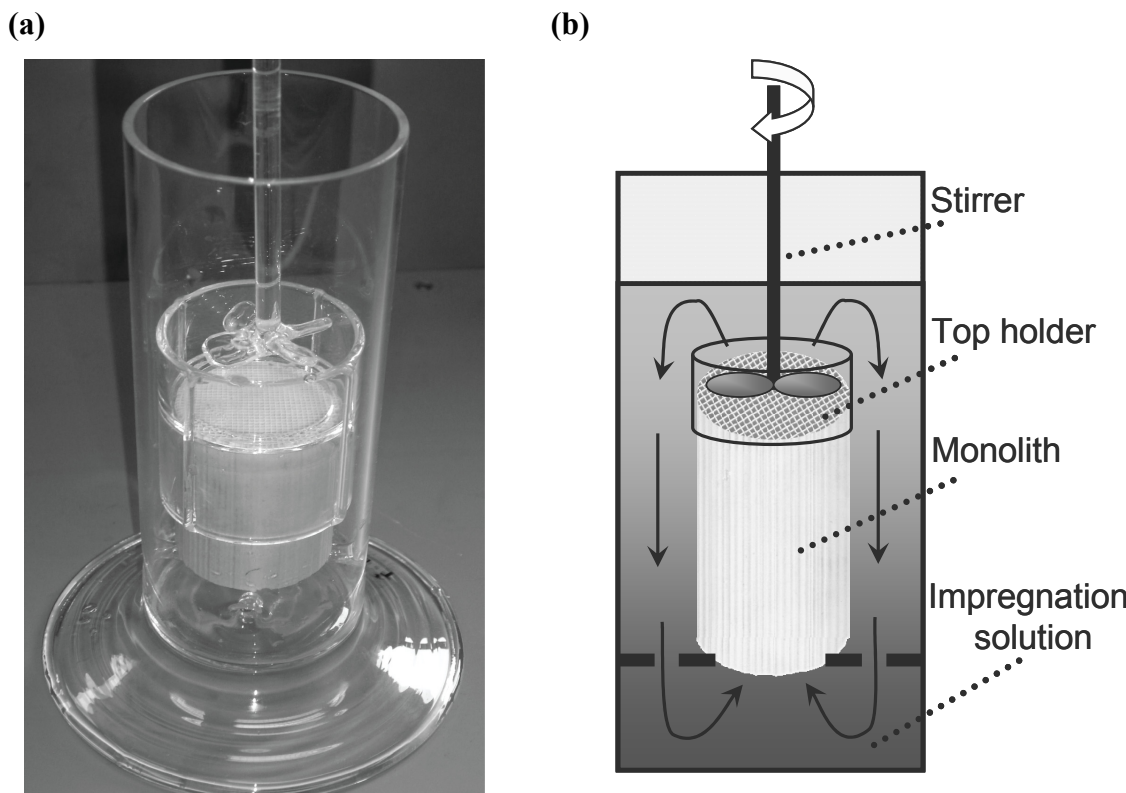


**Fig. 3.3.** Monolith forced-flow impregnation device. Photograph (a) and a schematic representation (b) of the monolith forced-flow impregnation device.

#### Catalyst characterization

After drying and calcination, ultrasonic treatment was conducted to determine the adhesion of the silica to the acicular mullite. The silica-coated monoliths were characterized by weight analysis, visual inspection, X-ray fluorescence (XRF) using a Philips PW2400, scanning electron microscopy (SEM) using a Philips XL20 equipped with a SED detector, backscatter electron imaging (BEI) and electron probe microanalysis (EPMA) using a JEOL 8800 Superprobe, N<sub>2</sub> physisorption using a Quantachrome Autosorb-6B, atomic force microscopy (AFM) using a Parc Scientific Instruments Autoprobe M5 and Hg porosimetry was performed using a CE instruments Pascal 140 and 440. The Pd impregnated silica-coated monoliths were characterized by CO chemisorption using a Quantachrome Autosorb-1C, EPMA, high

resolution transmission electron microscopy (HRTEM-EDX) using a Philips CM30T with a LaB<sub>6</sub> filament and LINK EDX and instrumental neutron activation analysis (INAA). Samples for the characterizations were taken from different positions of the monolith.

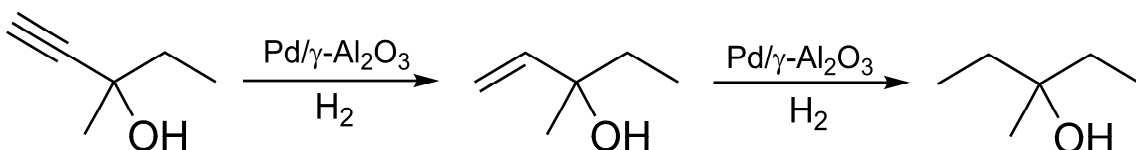
Maldistribution of silica occurs on various length scales

- Macroscale ( $\sim$  mm) - monolith length in axial and radial direction.
- Mesoscale ( $\sim$   $\mu\text{m}$ ) - width of the wall and ACM pore characteristics.
- Microscale ( $\sim$  nm) - silica coverage over the ACM grains and morphology of the silica coating.

Macroscale variations in silica loading were quantified by inspecting SEM micrographs and by measuring the specific surface area and weight increase, at different places of the monolith. Mesoscale variations were quantified by degree and extent of pore plugging, the pore size distribution, and wall porosity by performing Hg porosimetry, inspecting SEM and BEI images and element maps (EPMA). Microscale variations were quantified by studying the silica coating coverage, thickness and morphology on ACM grains from SEM, TEM, and AFM images. N<sub>2</sub> physisorption was done to determine the mean pore size, pore size distribution, and specific surface area of the silica coating.

#### *Hydrogenation experiments*

The selective hydrogenation of 3-methyl-1-pentyn-3-ol (Fluka,  $> 98\%$  pure) was chosen as a model reaction (Scheme 3.1) [31-33].



**Scheme 3.1.** Selective hydrogenation of 3-methyl-1-pentyn-3-ol ('alkyne') over a Pd catalyst to the desired 3-methyl-1-penten-3-ol ('alkene') and the overhydrogenation to 3-methyl-3-pentanol ('alkane').

This is a consecutive reaction, with the intermediate product (the 'alkene') being the desired one. The maximum yield of the alkene strongly depends on the extent of diffusion limitations, which makes this reaction well suited to investigate the impact of diffusion on catalyst performance. The semi-batch hydrogenation experiments were conducted in a monolithic stirrer reactor. This reactor type has been used for several studies [34-37] and has great potential in the fine chemical industry. The applied conditions were 1.17 and 2.3 bar H<sub>2</sub>, 600 rpm, and  $24.4 \pm 0.3^\circ\text{C}$ . The alkyne was dissolved in 2500 g of ethanol (100%, technical pure).

The initial concentration of alkyne was 20 mol/m<sup>3</sup>. Before hydrogenation, the reactor was flushed with N<sub>2</sub>. A forward pressure controller was used to maintain the reactor pressure, and the H<sub>2</sub> flow through the pressure controller was recorded. The H<sub>2</sub> usage was monitored and liquid samples were taken at regular intervals for analysis by GC using a CP-SIL 8 column. Freshly prepared monolithic catalysts were allowed to deactivate during several runs until the concentration profiles were stable and reproducible for several runs. For most samples, two pre-runs sufficed.

## Results and Discussion

### *Catalyst preparation and characterization*

The drying step was very important because the wall permeability of the ACM samples was high and the adhesion of the colloidal silica to the grains was weak. So, careful optimization of the drying step was of utmost importance to prevent clogged channel walls and non-uniform silica distribution over all length scales.

During drying the gelling process starts: the surface silanol groups condense to form siloxane bonds resulting in coalescence and particle interbonding, forming fractal aggregates (xerogel) that eventually results in the final coating. Static air-drying on a horizontal rotational dryer resulted in inhomogeneous distribution of the silica particles with most silica present at the outer parts of the monolith, *i.e.*, macroscale 'eggshell' silica distribution [38]. In static air-drying, the drying gel flows from the inside outwards, where most of the evaporation occurs at the outer surface. This convection drags the colloidal silica particles to the outer surface. An overview of the silica distribution analysis of ACM-L monoliths with different drying methods applied is presented in Table 3.2. Using an oven in static air increased the drying rate, and the accumulation of silica at the external surface of the monolith even increased. This problem can to some extent be overcome by increasing the viscosity of the dipcoating solution by lowering the pH. Indeed, increasing the viscosity resulted in a better macroscale distribution after static air-drying. However, it also increased the amount of plugged pores and decreased the specific surface area of the silica coating.

In freeze-drying, convection of the colloidal silica solution does not occur, and a uniform distribution on the macrolevel was obtained (Table 3.2). However, on the mesolevel a 500 nm thick layer on top of the ACM grains was formed that blocked the largest pores. Similar observations when applying freeze-drying, after coating membranes with colloidal silica,

were made by Murru *et al.* [39]. On the microlevel, freeze-drying resulted in very rough non-uniform silica fractal agglomerates, attached to the surface of the mullite grains.

The most uniform silica distribution at all length scales was obtained using microwave drying. Weight analysis, N<sub>2</sub> physisorption, SEM, and Hg porosimetry analysis (Table 3.2) showed that the silica was homogenously distributed on the macroscale, while preserving the open wall geometry (mesoscale). In a microwave, the water was heated evenly throughout the sample and this caused the water to evaporate evenly throughout the monolith. Microwave drying was applied for all silica-coated monoliths used in the hydrogenation experiments.

**Table 3.2**

Silica distribution analysis at different positions of ACM-L using several drying techniques

| Drying technique           | Part of monolith | N <sub>2</sub> physisorption and Hg porosimetry |        | Weight analysis |        | SEM  |                    |
|----------------------------|------------------|---|--------|-----------------|--------|--|--------------------|
|                            |                  | Top/Bottom                                      | Middle | Top/ Bottom     | Middle | Top/ Bottom  | Middle             |
| Static air drying, rotated |                  | 18  | 8      | 76              | 24     | Clogged walls, most pores blocked                                  | Some pores blocked |
| Static air drying, oven    |                  | 21  | 5      | 82              | 18     | Clogged walls, most pores blocked                                  | Some pores blocked |
| Freeze-drying              |                  | 13  | 13     | 53              | 47     | Top layer formation, thereby blocking the largest pores            |                    |
| Microwave drying           |                  | 14  | 12     | 56              | 44     | Small area with blocked pores at entrance and exit of the monolith |                    |

The monoliths were dip coated in an 8 wt% colloidal silica solution; this resulted in a silica loading of 4 wt%.

The silica content deposited on the ACM monoliths, determined by weight analysis and several XRF measurements showed a linear dependence on the silica concentration of the dip-coating solution (Fig. 3.4). Increasing the silica content resulted in increased silica coverage of the mullite grains. However, a larger number of pores were completely blocked, negatively affecting the macroporosity and permeability of the walls (SEM inserts Fig. 3.4).

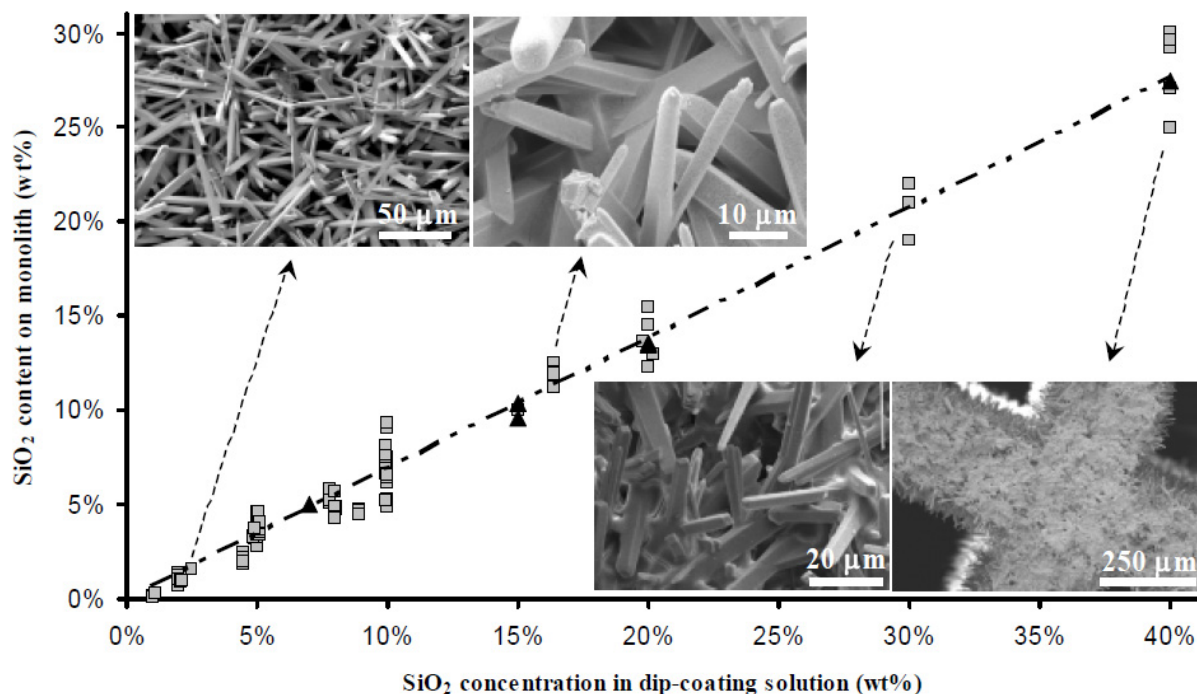


**Fig. 3.4.** Silica deposition onto the ACM monoliths; the silica content on these monolith is linearly dependent on the silica concentration in the dipcoating solution (□ = weight analysis, ▲ = XRF analysis). Inserts: SEM micrographs of the walls of ACM monoliths coated with different amounts of colloidal silica. The walls loose their macroporosity and permeability, which causes an increase of the effective diffusion length.

Upon microwave drying, the relative amount of pores between 1 and 10  $\mu\text{m}$  in ACM-L structure was reduced to 5%, as determined by comparing the Hg porosimetry diagrams measured after dipcoating with the diagrams of bare samples. An EPMA element map of silica indicated that the colloidal silica was distributed uniformly throughout the wall (Fig. 3.5a). Hg porosimetry measurements showed that the mean pore diameter of the ACM samples hardly changed but the wall porosity decreased by 5%. About 70% (estimated from the pore volume decrease of pores  $< 5 \mu\text{m}$ ) of the deposited silica content of the ACM-L samples was accumulated in the small interstitial voids where the mullite grains attach to one another (Fig. 3.6a and 3.6c). Similar observations were made by Meille *et al.* [40] when coating FeCr alloy fibers with colloidal alumina. The thickness of the silica coating in these junctions was between 2 and 5  $\mu\text{m}$ . The rest of the colloidal silica ( $\sim 30\%$ ) was deposited on the mullite grains forming a nonuniform layer ranging from 30 to 500 nm in thickness (Fig. 3.6b).

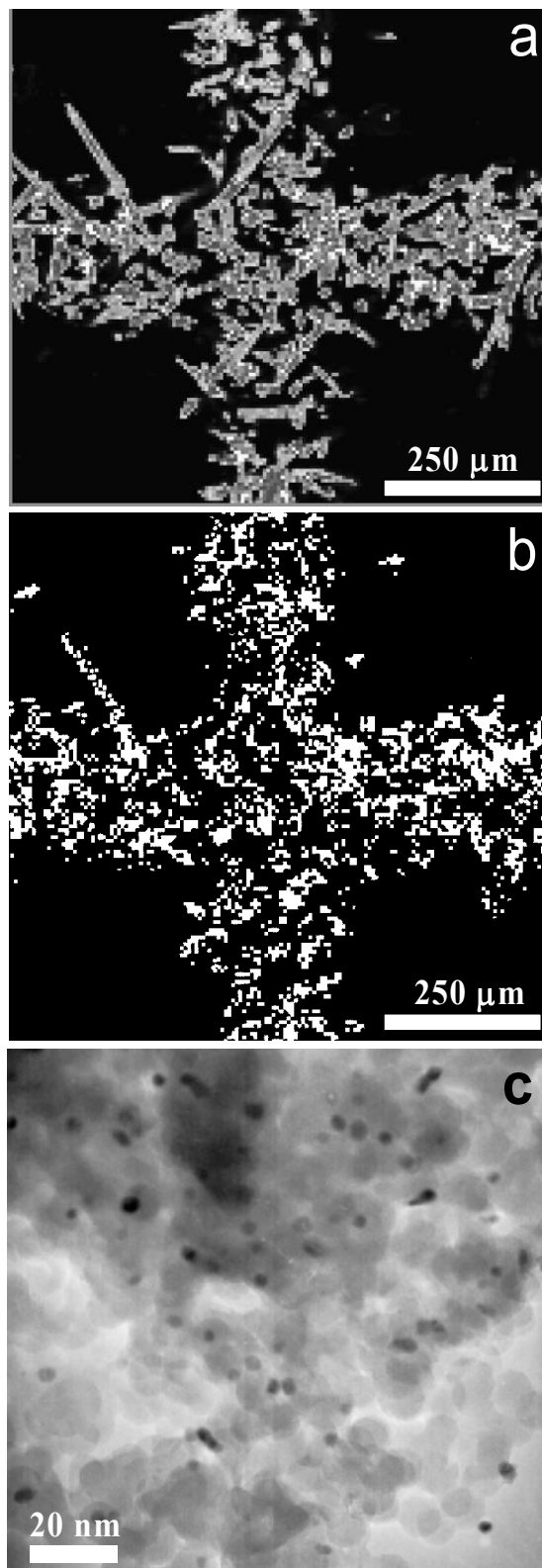


**Fig. 3.5.** (a) EPMA element map of silica of an intersection of the ACM-L wall. The grayscale represents the amount of silica present (mullite and colloidal silica). (b) EPMA Pd element map of an intersection of the ACM monolith wall. The white areas represent Pd. (c) TEM micrograph of a colloidal silica-supported 2 wt% Pd catalyst on a mullite grain: the black dots are Pd crystallites (as determined by EDX) and the gray dots are colloidal silica HS40 particles.

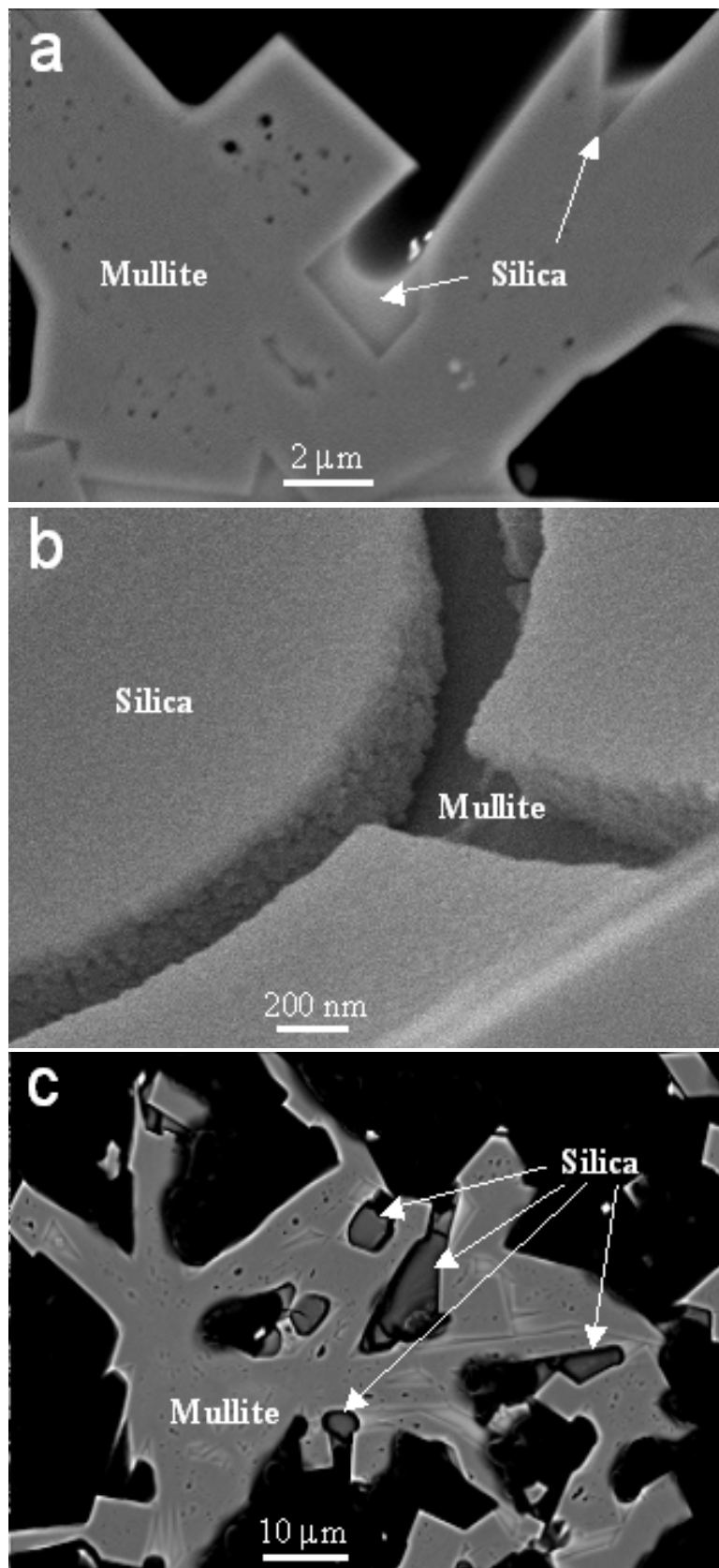


**Fig. 3.6.** (a) Backscatter electron image (BEI) of a polished cross section of silica-coated mullite grains. (b) SEM micrograph of a cracked silica layer (thickness  $\sim 500$  nm) on a mullite grain. (c) BEI of a polished cross section of silica-coated mullite grains.

The morphology of the silica surface was investigated with AFM and showed a very rough surface indicating a nonuniform layer thickness. The specific surface area determined at different positions by  $N_2$  physisorption increased from  $0.2\text{ m}^2/\text{g}$  for bare ACM-L to around  $13\text{ m}^2/\text{g}_{\text{monolith}}$  ( $S_{\text{BET}} = 325\text{ m}^2/\text{g}_{\text{silica}}$ ) for a sample coated with 4 wt% SM30 colloidal silica. The adsorption and desorption isotherm of  $N_2$  were nearly parallel, so all pores were easily accessible. The colloidal silica coating had a narrow pore size distribution with a mean pore size of 4.2 nm (interparticle pores).

In order to obtain the optimum coating morphology on a cordierite monolith, the particle size of the Davisil™ silica slurry should be around 5 to 10  $\mu\text{m}$ , to result in a thin enough coating while blocking most macropores to avoid deposition inside the wall. This was achieved after ball milling the silica slurry for about 20 h. The amount of silica present was 4 wt% mainly deposited on the outside of the channel walls (eggshell coating). SEM pictures of the coated samples revealed that the thickness of the silica layer varied between 5 and 15  $\mu\text{m}$  ( $S_{\text{BET}} = 280\text{ m}^2/\text{g}_{\text{silica}}$  with an average pore size of 12 nm), where the lower values were predominantly found on the flat wall surface and the higher values were found in the corners of the channel. After 24 h of impregnation all Pd present in the impregnation solution was deposited on the monolith (as determined by INAA). Without forced circulation through the monolith channels, I have found uneven distribution of the impregnated Pd, and I have avoided such inhomogeneities by using the specially developed glass reactor (Fig. 3.3). A uniform macroscale Pd distribution was observed, visualized by the brownish color of Pd and by CO chemisorption at different locations of the monolith (*i.e.*, top, middle and bottom part). Drying did not influence the Pd distribution because of the strong interaction of the  $\text{Pd}(\text{OAc})_2$  with the silanol groups on the silica surface via precursor grafting (ligand substitution in an organic solvent) [41]. An EPMA element map of Pd indicated that Pd was distributed uniformly throughout the wall (Fig. 3.5b) and Pd was also found on the mullite grains themselves. At locations with higher silica content, higher Pd concentrations were also found.

The Pd dispersion was 30% (mean Pd crystallite size of 4 nm) for a SM30 silica-supported 2 wt% Pd on ACM-L sample. For HS40, the mean crystallite size was determined to be 5 nm (HRTEM, see Fig. 3.5c for a representative image). A lower Pd dispersion was measured when a monolith was coated with the lower surface area colloidal silica, *e.g.*, AS40. Furthermore, the Pd was mostly dispersed homogeneously throughout the silica coating with some clusters of Pd crystallites. The dispersion was also 30% (2 wt% Pd as determined by INAA) for slurry-coated cordierite monoliths.

## Hydrogenation experiments

Two monolith pieces with 4 wt% silica per unit monolith mass and 2 wt% Pd per unit silica mass were used in all hydrogenations experiments. No Pd leaching into the reaction mixture was observed. The samples withdrawn during hydrogenation were analyzed by GC and compared with the H<sub>2</sub> consumption. Mass balances over all components were always within 5%. The average Pd crystallite size of the ACM and cordierite samples were identical and prepared from the same precursor ruling out ‘structure’ effects (see Chapter 4 Appendix A for a more detailed discussion). Hereby I assumed that the different silica supports (Davisil™ and colloidal silica for cordierite and ACM, respectively) had no notable effect on the performance. The concentration profiles for an experiment at 600 rpm, 1.17 bar H<sub>2</sub> pressure, an initial alkyne concentration ( $C_{Y,0}$ ) of 20 mol/m<sup>3</sup> and 24.4°C is presented in Fig. 3.7. At this pressure, I make the reasonable assumption that diffusion of the alkyne is not limiting, based on the zero-order behavior observed for the reacting alkyne: if diffusion limitations were present, the reaction order would shift towards unity. The zero-order behavior of the alkyne, however, cannot be used to exclude possible diffusion limitations for H<sub>2</sub>. The ratio  $C_{H_2} \cdot D_{H_2} / C_Y \cdot D_Y$  shows which component suffers most from diffusion limitations. At the start of the reaction, this ratio was 1.6 or higher, and it increased during hydrogenation because H<sub>2</sub> is added during the reaction, so the alkyne should always suffer more from diffusion limitations than H<sub>2</sub>: the zero order behavior of the organic compound also indicates that diffusion of H<sub>2</sub> was not adversely influencing the reaction. To calculate  $C_{H_2} \cdot D_{H_2} / C_Y \cdot D_Y$ , I estimated  $C_{H_2}$  and  $D_{H_2}$  in ethanol using averaged experimentally determined H<sub>2</sub> Henry’s law constants [42-44] and diffusion coefficients [45-47]:  $C_{H_2} \sim 4.2$  mol/m<sup>3</sup> and  $D_{H_2} \sim 6 \cdot 10^{-9}$  m<sup>2</sup>/s.  $D_Y$  was estimated using a modified Wilke Chang equation [48, 49] and compared with diffusion coefficients from similar molecules in ethanol [50] using the molar volume of the alkyne, estimated with the Tyn and Calus method [51], of 128 cm<sup>3</sup>/mol and a solvent association parameter of 3.3:  $D_Y \sim 0.8 \cdot 10^{-9}$  m<sup>2</sup>/s.

These concentration profiles (Fig. 3.7) were used to determine the kinetic parameters  $k_1$ ,  $k_2$ ,  $K_Y$  and  $K_E$  for the following Langmuir-Hinshelwood-Hougen-Watson type rate expressions based on quasi-equilibrium adsorption steps and rate determining surface reactions

$$r_1 = \frac{k_1 K_Y C_Y C_{H_2}}{1 + K_Y C_Y + K_E C_E} \quad (3.2)$$

$$r_2 = \frac{k_2 K_E C_E C_{H2}}{1 + K_Y C_Y + K_E C_E} \quad (3.3)$$

where  $r_1$  is the reaction rate of alkyne to alkene and  $r_2$  is the reaction rate of alkene to alkane. Both reactions were first order in  $H_2$ , so no specific assumption was made with respect to (non)-competitive adsorption. The alkyne adsorbs strongly on the Pd surface ( $K_Y = 1.3 \pm 0.1 \text{ mol}^{-1} \text{ m}^3$ ), and the first reaction was zero order for alkyne concentrations higher than  $3 \text{ mol/m}^3$ . The second reaction was mostly first order in the alkene, and the fitted adsorption constant for the alkene was much lower,  $K_E = 0.08 \pm 0.01 \text{ mol}^{-1} \text{ m}^3$ . The ratio of the reaction rate constants was  $k_1/k_2 = 0.7 \pm 0.2$ ; in fact, a comparable fit can be obtained by setting  $k_1/k_2 \equiv 1$ . This indicates that the rate of hydrogenation of an adsorbed alkyne was comparable to that of an adsorbed alkene; the observed faster reaction of the former was mostly due to stronger adsorption [31, 52].

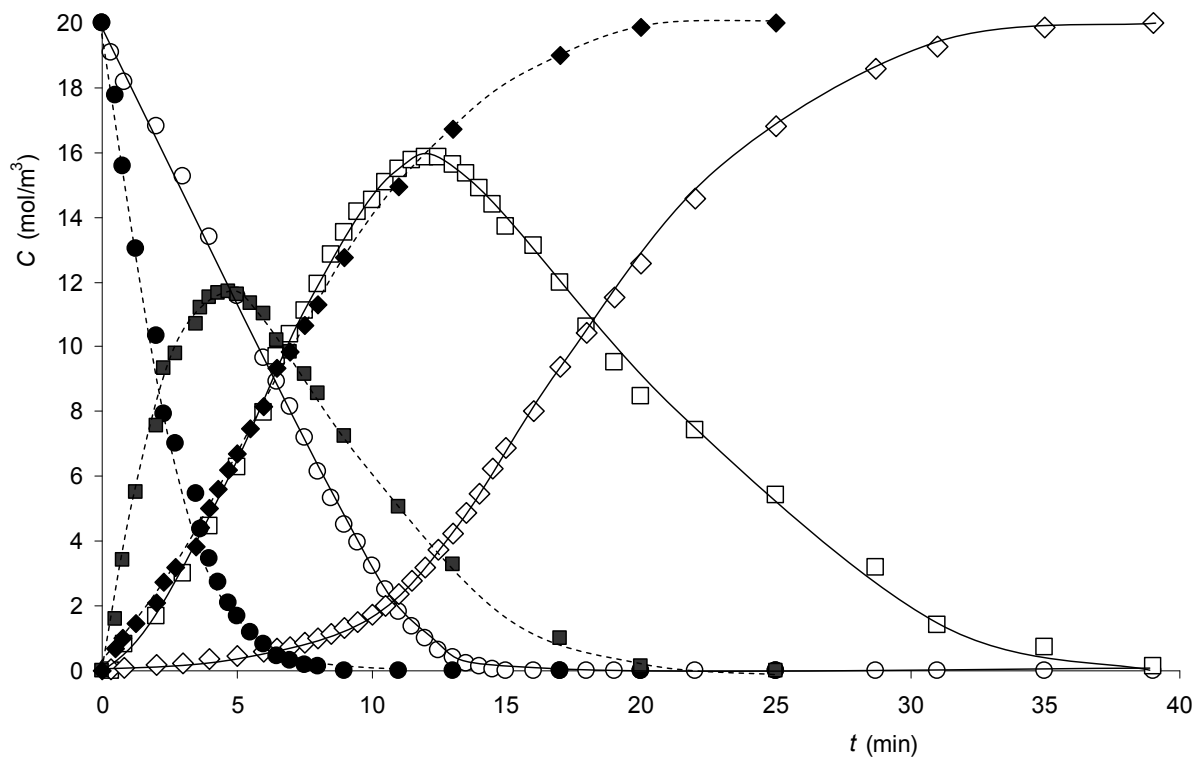


**Fig. 3.7.** Concentration ( $C$ ) vs. time profiles ( $t$ ) for alkyne hydrogenation at low and high  $H_2$  pressure in a monolithic stirrer reactor using two ACM-L monoliths (2 wt% Pd supported on 4 wt% SM30 silica). The solid lines show the fitted kinetics. Low  $H_2$  pressure: 1.17 bar,  $20 \text{ mol/m}^3$ , solvent = ethanol,  $24.4^\circ\text{C}$ : alkyne concentration ( $\circ$ ), alkene concentration ( $\square$ ), alkane concentration ( $\diamond$ ). High  $H_2$  pressure: 2.3 bar,  $20 \text{ mol/m}^3$ , solvent = ethanol,  $24.4^\circ\text{C}$ . The closed symbols and dashed lines represent the concentration of the different compounds at high  $H_2$  pressure.

Subsequent experiments were performed at 600 rpm, 2.3 bar H<sub>2</sub> (C<sub>H<sub>2</sub></sub> ~ 8.2 mol/m<sup>3</sup>) and C<sub>Y,0</sub> = 20 mol/m<sup>3</sup>. A representative concentration versus time profile for these conditions is shown in Fig. 3.7.

The Pd monolith performance was expressed in activity as determined from the initial reaction rate  $r_{V,\text{SiO}_2}$  and the maximum yield  $Y_{\text{max}}$  of the intermediate product

$$r_{V,\text{SiO}_2} = \frac{V_{\text{R}} (dC_{\text{Y}}/dt)_{t=0}}{V_{\text{SiO}_2}} \quad (3.4)$$

$$Y_{\text{max}} = \frac{C_{\text{E,max}}}{C_{\text{Y,0}}} \quad (3.5)$$

A comparison of  $r_{V,\text{SiO}_2}$  and  $Y_{\text{max}}$  (mean values taken over several runs) is shown in Fig. 3.8 for two ACM samples (ACM-L and ACM-S) and a cordierite sample. All three monoliths had a comparable amount of silica coated onto them, and the Pd loading per unit silica weight was also constant for all samples. In other words, the difference in performance was due to the difference in morphology of the wall structure.  $r_{V,\text{SiO}_2}$  and  $Y_{\text{max}}$  increase as diffusional limitations decrease, so the ranking in  $r_{V,\text{SiO}_2}$  and  $Y_{\text{max}}$  is also a ranking of extent of diffusional limitations. The activity per unit silica volume was twice as high for ACM-L (large pores), compared with the dense cordierite wall structure. Moreover, this higher activity was obtained at higher yields, which indicate that diffusional limitations were reduced. In the following, the various concentration gradients that occur in the reactor and the impact of these gradients on the catalyst performance are described.

#### *Gas-liquid mass transfer*

The gas to liquid mass transfer group  $k_{\text{GL}} \cdot a$  for H<sub>2</sub> in ethanol was determined at different stirrer speeds by measuring the pressure evolution upon a step change in pressure, as described by Dietrich and co-workers [53]. The response time of the pressure transducer was about 1 s. At stirrer speeds above 550 rpm, equilibrium between the gas and liquid phase established within a second, indicating that the mass transfer group  $k_{\text{GL}} \cdot a$  was at least 1 s<sup>-1</sup> and mass transfer from the gas to the liquid was never limiting in my experiments.

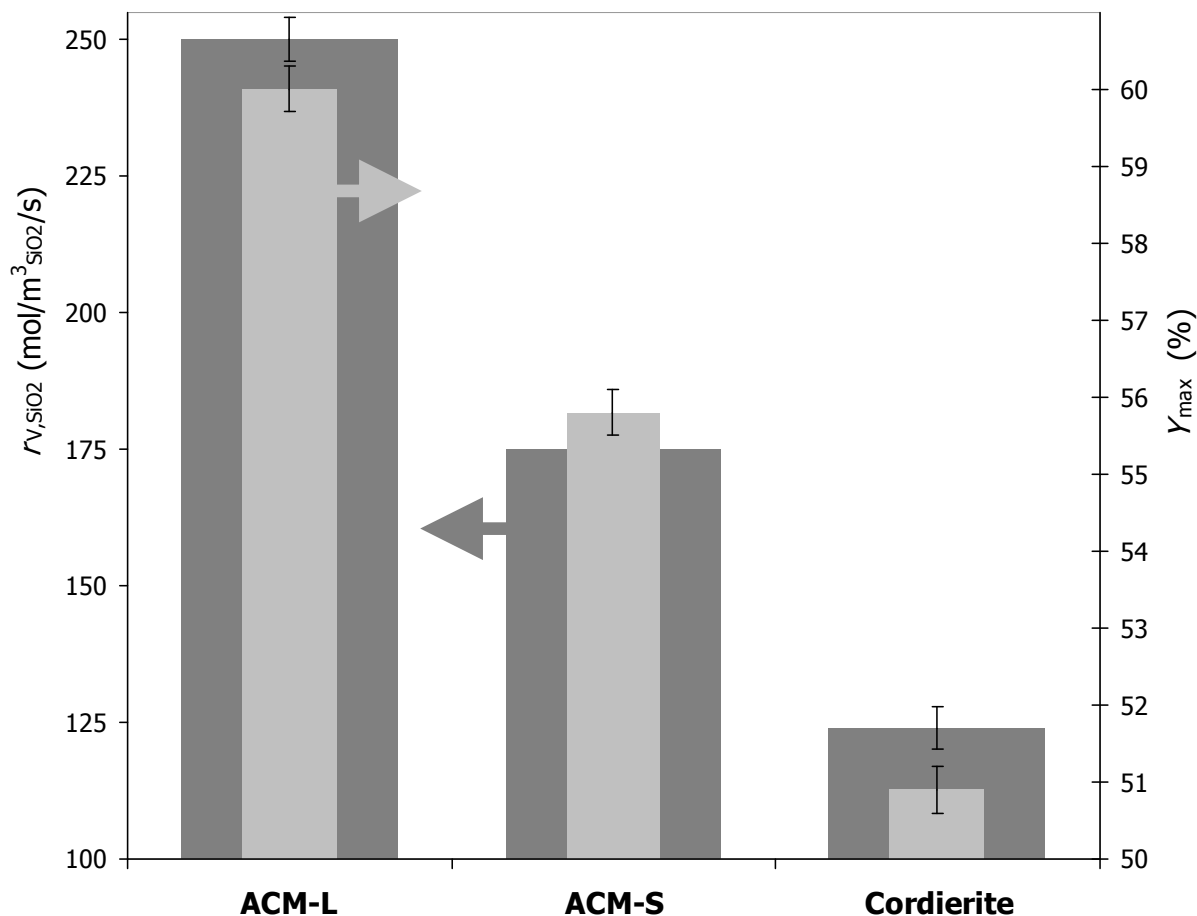


**Fig. 3.8.** Comparison of mean initial activities per unit silica volume  $r_{V,SiO_2}$  (dark grey, left y-axis) and mean maximum yields  $Y_{max}$  (light grey, right y-axis) of the desired product (the intermediate: 3-methyl-1-penten-3-ol) of the hydrogenation of 3-methyl-1-pentyn-3-ol averaged over 4 stabilized runs for ACM-L, ACM-S and cordierite. Conditions: 2.3 bar, 20 mol/m<sup>3</sup>, solvent = ethanol, 24.4°C.

#### *Channel to wall mass transfer*

Estimating the mass transfer rate from the liquid in the channels to the wall was complicated by the uncertainty of the velocity inside the channels and uncertainty as to the hydrodynamic flow pattern inside the channels. When the stirrer was suddenly stopped, I observed that gas bubbles left the monolithic channels, which was a strong indication that multiphase Taylor flow occurred inside the channels. Based on the results of Kritzinger and co-workers [54], the velocity will be between 10% and 20% of the rotational velocity of the monolith stirrer, or  $u_{bubble} = 0.25\text{-}0.50$  m/s. For such a linear velocity of the bubble train inside the channels, I calculated the mass transfer rate to the wall using the correlations in Kreutzer *et al.* ( $k_{LS} \sim 0 (10^{-3})$ ) [55]. The ratio of the observed reaction rate and the maximum mass transfer rate, the Carberry number  $Ca$ , was  $< 0.05$ , both for H<sub>2</sub> and the alkyne. So, the monolith stirrer reactor

was operated under conditions where concentration gradients inside the channel or in the bulk outside the channel could be ignored: all mass transfer limitations, if any, occurred inside the wall structure and/or inside the colloidal silica coating.

*Gradients inside the silica coating*

It is illustrative to use the maximum yield of the intermediate product  $Y_{\max}$  to calculate the extent of diffusional limitations. With the previously determined kinetic parameters, the balances over the catalytic material are

$$D_{\text{org,eff}} \frac{d^2 C_Y}{dx^2} - \frac{k_1 K_Y C_Y C_{H_2}}{1 + K_Y C_Y + K_E C_E} = 0 \quad (3.6)$$

$$D_{\text{org,eff}} \frac{d^2 C_E}{dx^2} - \frac{-k_1 K_Y C_Y C_{H_2} + k_2 K_E C_E C_{H_2}}{1 + K_Y C_Y + K_E C_E} = 0 \quad (3.7)$$

$$D_{\text{org,eff}} \frac{d^2 C_A}{dx^2} - \frac{-k_2 K_E C_E C_{H_2}}{1 + K_Y C_Y + K_E C_E} = 0 \quad (3.8)$$

$$D_{\text{H2,eff}} \frac{d^2 C_{H_2}}{dx^2} - \frac{k_1 K_Y C_Y C_{H_2} + k_2 K_E C_E C_{H_2}}{1 + K_Y C_Y + K_E C_E} = 0 \quad (3.9)$$

For these intra-particle balances, the boundary conditions are symmetry in the center at  $x = 0$  and bulk concentration  $C = C_{\text{bulk}}$  on the outside at  $x = L_{\text{coat}}/2$ . These balances may be normalized using a Thiele modulus  $\phi_1$  for the first reaction

$$\phi_1 = L_{\text{coat}} \sqrt{\frac{k_1}{D_{\text{org,eff}}}} \quad (3.10)$$

I have solved the balances (3.6)-(3.10) and the accompanying bulk concentration profiles for comparison with the experimental data, and to establish the correlation between  $Y_{\max}$  and  $\phi_1$ .

Fig. 3.9 quantifies how  $Y_{\max}$  varies with  $\phi_1$ , based on the kinetic parameters that I obtained from Fig. 3.7: as the extent of diffusion limitation increases, more alkene is converted to alkane before it leaves the catalyst. As the arrows indicate in Fig. 3.9, one can now estimate  $\phi_1$  using the measured value of  $Y_{\max}$  from Fig. 3.8.

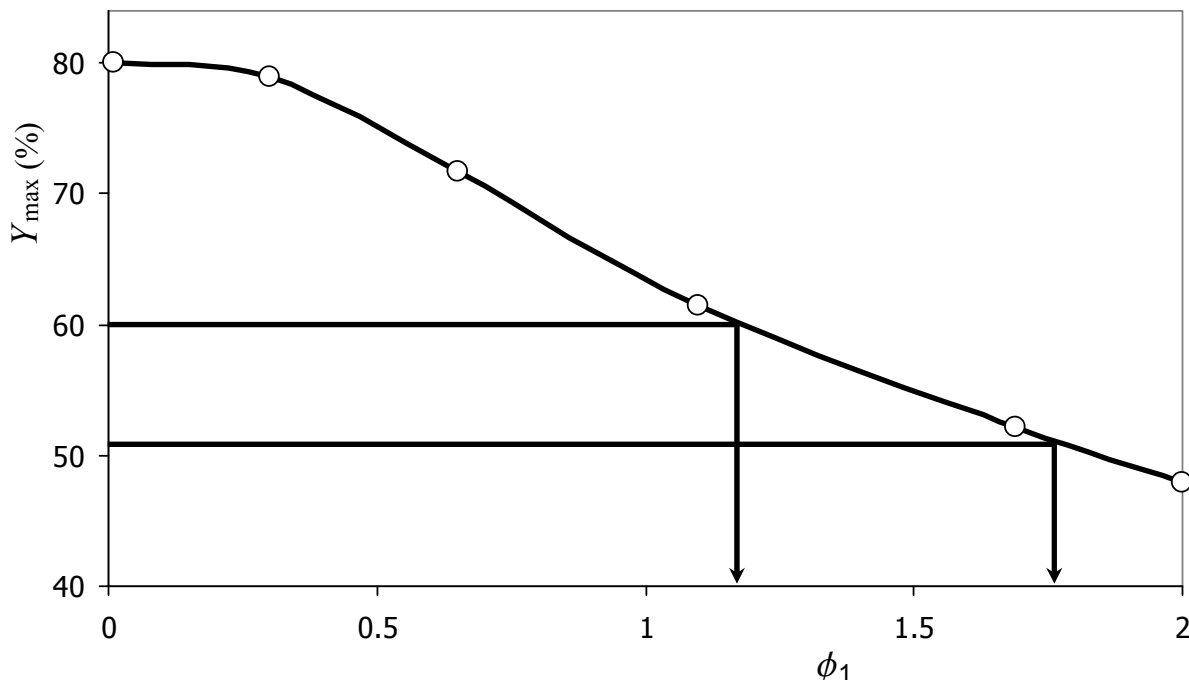


**Fig. 3.9.** The relation between maximum yield  $Y_{\max}$  and Thiele modulus  $\phi_1$ . The arrows show how the observed  $Y_{\max}$  may be used to estimate  $\phi_1$  for the first reaction.

At the higher pressure of 2.3 bar, the diffusion limitations have reduced the  $Y_{\max}$  (Fig. 3.9). ACM-L samples had an  $Y_{\max}$  of 60.0%, and the  $\phi_{1, \text{ACM-L}}$  is  $\sim 1.2$ . Likewise, the  $\phi_{1, \text{ACM-S}}$  for ACM-S samples was  $\sim 1.5$  ( $Y_{\max} = 55.8\%$ ) and the  $\phi_{1, \text{CORD}}$  for the cordierite was estimated as  $\sim 1.8$  ( $Y_{\max} = 50.9\%$ ). Comparison of the observed  $r_{V, \text{SiO}_2}$  leads to the same order of increasing diffusion limitations: the ACM-L sample exhibited the highest activity and the least diffusion limitations, whereas the cordierite sample had the lowest initial activity and suffered most from internal diffusion limitations.

The characteristic length for diffusion in the silica-coated cordierite samples was unambiguous: the average silica coating thickness on cordierite  $L_{\text{coat,c}}$  as determined from multiple SEM images was about 7  $\mu\text{m}$ . I assumed that  $D_{\text{eff}}$  and  $k_1$  were roughly the same for

all monolithic catalysts to find that the ratio of Thiele moduli was a ratio of characteristic lengths

$$\frac{\phi_{l, \text{ACM-L}}}{\phi_{l, \text{CORD}}} = \frac{L_{\text{coat, ACM-L}} \sqrt{k_l/D_{\text{eff}}}}{L_{\text{coat, CORD}} \sqrt{k_l/D_{\text{eff}}}} \approx \frac{L_{\text{coat, ACM-L}}}{L_{\text{coat, CORD}}} \quad (3.11)$$

Then, from the estimates in Fig. 3.9, the characteristic length for diffusion that describes the ACM-L structures was about 4.6  $\mu\text{m}$ . Two possible ways to define a characteristic diffusional length for the open wall structure are presented in Fig. 3.2. Clearly, the dominant characteristic length was the thickness of the silica coating. Moreover, the results suggest that the mass transfer in the pores between the mullite grains, outside the silica coating, was not limiting.

#### *Gradients outside the silica coating*

In the previous section, I showed that the experimental data can be interpreted by describing the interplay of diffusion and reaction inside the thin silica coating on the mullite grains or on the cordierite wall. The success of this approach indicates that transport in the pores between the mullite grains did not negatively impact the performance. Note that if this interstitial mass transport was dominated by diffusion, it would be slower than transport inside the silica coating, as can be deduced from the ratio of characteristic times of diffusion

$$\frac{(\frac{1}{2}L_{\text{wall}})^2/D_{\text{eff,wall}}}{L_{\text{coat}}^2/D_{\text{eff,coat}}} \approx \left(\frac{120\mu\text{m}}{4.6\mu\text{m}}\right)^2 \frac{0.2}{0.7} \gg 1 \quad (3.12)$$

The yields in Fig. 3.8 showed that the 7  $\mu\text{m}$  layer in the cordierite samples exhibited more transport limitations than the ACM samples. The subsequent analysis using Fig. 3.9 and eq. (3.11) estimated the diffusional distance at about 4.6  $\mu\text{m}$  for the ACM samples, which was of the same order of magnitude as the coating thickness determined using SEM. In this section, I present an estimate of the convection inside the pores between the mullite grains, and I show that the order of magnitude of this convection is sufficient to eliminate transport limitations. I only performed this analysis for the ACM samples: in the cordierite eggshell catalysts the silica coating was directly exposed to the fluid in the channels.

The energy dissipation of mechanical energy occurring in the Newtonian fluid flow in the porous ACM walls was dominated by viscous stresses ( $Re_p < 1$ ), so the creeping fluid velocity inside the wall  $u_{\text{wall}}$  was governed by Darcy's law [56]

$$u_{\text{wall}} = \frac{(\gamma/(d_{\text{ch}} - 2\delta))K}{\mu L_{\text{wall}}} \quad (3.13)$$

where  $K$  is the intrinsic permeability,  $\mu$  is the viscosity of the fluid, the pressure pulses were created by the surface tension of passing bubbles and is of the order  $\gamma/d_{\text{ch}}$ , where  $\gamma$  is the surface tension,  $\delta$  is the film thickness, and  $d_{\text{ch}}$  is the channel diameter.

For ACM-L catalysts, the velocity that was caused by pressure pulsing was  $\sim 10$  mm/s, and at that velocity it takes about 1/40th of a second to push liquid through the wall. The frequency of the passing bubbles  $(L_{\text{bubble}} + L_{\text{slug}})/u_{\text{bubble}}$  was of the order of 30 Hz, so every passing gas bubble results in a significant convective enhancement of the flow inside the wall. The experiments with ACM-S monoliths confirmed that the permeability of the walls was crucial for the convective enhancement: lower permeability decreased the convective enhancement thereby increasing the mass transfer limitations to the silica coating inside the wall. Leighton and co-workers [57] determined mass transfer enhancement of pulsating flow through a porous medium, and found more than an order of magnitude enhancement with respect to pure diffusion at frequencies above 1 Hz. My reactive experiments confirmed this enhancement, and showed that convective enhancement using high-porosity structured catalyst supports is an attractive alternative to eggshell coatings on structured monolithic catalyst supports.

## Conclusions

The performance of multiphase Pd catalytic reactors can be enhanced by using a high-porosity macroporous support structure. In this Chapter, a honeycomb monolith structure was used in which the wall consisted of interlocked elongated acicular mullite (ACM) grains with large interstitial voids ( $\sim 45$   $\mu\text{m}$ ) between them. Multiphase flow created local pressure pulses that induced flow inside the walls of this support structure. The hydrogenation experiments showed that this added convection inside the support structure improved the activity and selectivity alike.

Under diffusion-limited conditions, the activity per unit monolith volume was 100% greater for the open ACM monoliths than for cordierite monoliths with impermeable walls. In these comparative experiments, equal amounts of Pd and SiO<sub>2</sub> per unit catalyst were used, so the differences in performance were due to differences in structure. Not only was the activity higher for the ACM structure, the maximum yield of alkene was also 9% higher, which confirmed that internal diffusional limitations were reduced compared to the cordierite structure.

The high permeability of the ACM walls was crucial for convective enhancement, as the experiments with acicular monoliths with smaller macropores confirmed. To preserve this permeability, maintaining the open structure after the silica-coating step was essential. Microwave drying was found to be the best drying method to ensure that the silica was distributed evenly throughout the monolith walls. The silica coating obtained after microwave drying mostly filled the small voids where the mullite grains meet and created a thin conformal coating on the mullite grains. The average diffusion length was short and the open structure of the walls was unaffected by the coating process. With the proper monolith impregnation device and Pd deposition technique, a uniform Pd distribution over the complete monolith structure and silica coating was achieved.

**Notation**

|                       |  |
|-----------------------|--|
| $a$                   | Specific surface area, $\text{m}^2/\text{m}^3$   |
| $d_{\text{ch}}$       | Channel diameter, m  |
| $d_{\text{p}}$        | Particle size, m   |
| $C$                   | Concentration, $\text{mol}/\text{m}^3$   |
| $C_{\text{bulk}}$     | Bulk concentration of the organic compound, $\text{mol}/\text{m}^3$                                  |
| $C_{\text{E,max}}$    | Maximum concentration of the desired alkene product, $\text{mol}/\text{m}^3$                         |
| $C_{\text{Y,0}}$      | Initial alkyne concentration, $\text{mol}/\text{m}^3$  |
| $D$                   | Diffusion coefficient, $\text{m}^2/\text{s}$   |
| $D_{\text{H}_2}$      | Diffusion coefficient of $\text{H}_2$ in ethanol, $\text{m}^2/\text{s}$                              |
| $D_{\text{org, eff}}$ | Effective diffusion coefficient of the organic compound, $\text{m}^2/\text{s}$                       |
| $D_{\text{Y}}$        | Diffusion coefficient of the alkyne in ethanol, $\text{m}^2/\text{s}$                                |
| $D_{\text{eff}}$      | Effective intraparticle diffusion coefficient = $(\varepsilon/\tau) \cdot D$ , $\text{m}^2/\text{s}$ |
| $K$                   | Intrinsic permeability, $\text{m}^2$   |
| $k_{\text{GLA}}$      | Gas-liquid mass transfer group, 1/s  |
| $k_{\text{LS}}$       | Liquid-solid mass transfer coefficient, m/s  |
| $K_{\text{A}}$        | Alkane adsorption constant, $\text{m}^3/\text{mol}$  |
| $K_{\text{E}}$        | Alkene adsorption constant, $\text{m}^3/\text{mol}$  |
| $K_{\text{Y}}$        | Alkyne adsorption constant, $\text{m}^3/\text{mol}$  |
| $k_{\text{v}}$        | First order rate constant, 1/s   |
| $k_1$                 | Alkyne reaction rate constant, 1/s   |
| $k_2$                 | Alkene reaction rate constant, 1/s   |
| $d_{\text{pore,m}}$   | Mean pore diameter, m  |
| $L_{\text{coat}}$     | Coating thickness, m   |
| $L_{\text{coat,c}}$   | Coating thickness of silica coating on cordierite sample, m  |
| $L_{\text{coat,m}}$   | Coating thickness of silica coating on mullite sample, m   |
| $L_{\text{bubble}}$   | Bubble length, m   |
| $L_{\text{slug}}$     | Slug length, m   |
| $L_{\text{wall}}$     | Wall thickness, m  |
| $p$                   | Pressure, Pa   |

---

|                      |   |
|----------------------|---|
| $Re_p$               | Reynolds number based on pore diameter, -   |
| $r_{\text{obs}}$     | Observed reaction rate per unit volume, mol/m <sup>3</sup> /s                                   |
| $r_{V,\text{SiO}_2}$ | Observed reaction rate per unit silica volume, mol/m <sup>3</sup> <sub>SiO<sub>2</sub></sub> /s |
| $r_1$                | Reaction rate of the alkyne to the alkene, mol/m <sup>3</sup> /s                                |
| $r_2$                | Reaction rate of the alkene to the alkane, mol/m <sup>3</sup> /s                                |
| $t$                  | Time, s   |
| $L_{\text{wall}}$    | Wall thickness, m   |
| $u_{\text{wall}}$    | Interstitial velocity inside the wall, m/s  |
| $u_{\text{bubble}}$  | Bubble velocity inside the channel, m/s   |
| $V_R$                | Reactor volume, m <sup>3</sup>  |
| $V_{\text{SiO}_2}$   | Silica volume, m <sup>3</sup>   |
| $x$                  | Intraparticle coordinate, m   |
| $Y_{\text{max}}$     | Maximum yield of alkene, mol/mol%   |

*Greek letters*

|                         |  |
|-------------------------|--|
| $\varepsilon$           | Porosity of the wall (void volume / total volume), %                   |
| $\phi_l$                | Thiele modulus of the first reaction, -                                |
| $\phi_{l,\text{CORD}}$  | Thiele modulus of the cordierite monolith, -                           |
| $\phi_{l,\text{ACM-S}}$ | Thiele modulus of the small pore mullite monolith, -                   |
| $\phi_{l,\text{ACM-L}}$ | Thiele modulus of the large pore mullite monolith, -                   |
| $\delta$                | Film thickness, m  |
| $\Phi$                  | Ratio of diffusion time and reaction time, -                           |
| $\gamma$                | Surface tension, N/m   |
| $\mu$                   | Viscosity, Pa·s  |
| $\tau$                  | Tortuosity (actual distance a molecule travels / shortest distance), - |

## Bibliography

- [1] A. Nir, L.M. Pismen, *Chem. Eng. Sci.* 32 (1977) 35.
- [2] B.A. Wilhite, R. Wu, X. Huang, M.J. McCready, A. Varma, *AIChE J.* 47 (2001) 2548.
- [3] V. Bringi, B.E. Dale, *Biotechnol. Prog.*, 6 (1990) 205.
- [4] J.C. van den Heuvel, I. Portegies Zwart, L.H.J. Vredenbregt, *Chem. Eng. Sci.* 51 (1996) 2391.
- [5] J.C. van den Heuvel, I. Portegies Zwart, S.P.P. Ottengraf, *J. Porous Media* 1 (1998) 123.
- [6] F. Kapteijn, T.A. Nijhuis, J.J. Heiszwolf, J.A. Moulijn, *Catal. Today* 66 (2001) 133.
- [7] F. Kapteijn, J.J. Heiszwolf, T.A. Nijhuis, J.A. Moulijn, *CATTECH* 3 (1999) 24.
- [8] A. Cybulski, J.A. Moulijn, *Catal. Rev. Sci. Eng.* 36 (1994) 179.
- [9] R.M. Machado, R.R. Broekhuis, A.F. Nordquist, B.P. Roy, S.R. Carney, *Catal. Today* 105 (2005) 305.
- [10] M.T. Kreutzer, F. Kapteijn, J.A. Moulijn, *Catal. Today* 111 (2006) 111.
- [11] T.A. Nijhuis, A.E.W. Beers, T. Vergunst, I. Hoek, F. Kapteijn, J.A. Moulijn, *Catal. Rev.-Sci. Eng.* 43 (2001) 345.
- [12] M.V. Twigg, J.T. Richardson, *Trans IChemE, Part A* 80 (2002) 183.
- [13] P. Tribollet, L. Kiwi-Minsker, *Catal. Today* 105 (2005) 337.
- [14] J. de Greef, G. Desmet, G.V. Baron, *Catal. Today* 105 (2005) 331.
- [15] D.R. Cahela, B.J. Tatarchuk, *Catal. Today* 105 (2005) 33.
- [16] A.A. Khassin, A.G. Sipatrov, G.K. Chermashetseva, T.M. Yurieva, V.N. Parmon, *Top. Catal.* 32 (2005) 39.
- [17] J. de Jong, B. Ankone, R.G.H. Lammertink, M. Wessling, *Lab Chip* 2005, 5, 1240.
- [18] J.R. Moyer, N.N. Hughes, *J. Am. Ceram. Soc.* 77 (1994) 1083.
- [19] S.A. Wallin, A.R. Prunier Jr., J.R. Moyer, U.S. Patent 6,306,335, 2001.
- [20] K.M. de Lathouder, J.J.W. Bakker, M.T. Kreutzer, F. Kapteijn, J.A. Moulijn, S.A. Wallin, *Chem. Eng. Sci.* 95 (2004) 5027.
- [21] Z.F. Cui, S. Chang, A.G. Fane, *J. Mem. Sci.* 221 (2003) 1.
- [22] J.J.W. Bakker, M.T. Kreutzer, K.M. de Lathouder, F. Kapteijn, J.A. Moulijn, S.A. Wallin, *Catal. Today* 105 (2005) 385.
- [23] S.A. Wallin, C.P. Christenson, D.H. West, M. Cornell, H.J.M. Gruenbauer, W.O. Patent 01/45828 A1, 2001.

- [24] I. Nettleship, Key Engineering Materials 122 (1996) 305.
- [25] Y. Ohzawa, K. Nomura, K. Sugiyama, Mat. Sci. Eng. A255 (1998) 33.
- [26] J.F. Despois, A. Mortensen, Acta Materialia. 53 (2005) 1381.
- [27] B.A. Latella, L. Henkel, E.G. Mehrtens, J. Mater. Sci. 41 (2006) 423.
- [28] P.A. Beauseigneur, I.M. Lachman, M.D. Patil, S.H. Swaroop, R.R. Wusirika, U.S. Patent 5,334,570, 1994.
- [29] M.L. Toebe, J.A. van Dillen, K.P. de Jong, J. Mol. Catal. A: Chemical 173 (2001) 75.
- [30] I. Hoek, Towards the catalytic application of a monolithic stirrer reactor. PhD Thesis, Technical University of Delft, 2004.
- [31] T.A. Nijhuis, G. van Koten, F. Kapteijn, J.A. Moulijn, Catal. Today 79 (2003), 315.
- [32] M.P.R. Spee, J. Boersma, M.D. Meijer, M.Q. Slagt, G. van Koten, J.W. Geus, J. Org. Chem. 66 (2001) 1647.
- [33] T.A. Nijhuis, G. van Koten, J.A. Moulijn, Appl. Cat. A 238 (2003) 259.
- [34] R.K.E. Albers, J.J. Houterman, T. Vergunst, E. Grolman, J.A. Moulijn, AlChE J. 44 (1998) 2459.
- [35] A.J. Sandee, R.S. Ubale, M. Makkee, J.N.H. Reek, P.C.J. Kamer, J.A. Moulijn, P.W.N.M. van Leeuwen, Adv. Synth. Catal. 1 (2001) 201.
- [36] I. Hoek, T.A. Nijhuis, A.I. Stankiewicz, J.A. Moulijn, Chem. Eng. Sci. 59 (2004) 4975.
- [37] K.M. de Lathouder, J.J.W. Bakker, M.T. Kreutzer, S.A. Wallin, F. Kapteijn, J.A. Moulijn, Chem. Eng. Res. Dev. 84 (2006) 390.
- [38] T. Vergunst, F. Kapteijn, J.A. Moulijn, Appl. Catal. A 213 (2001) 179.
- [39] M. Murru, A. Prabowo, A. Gavriilidis, J. Membrane Sci. 248 (2005) 27.
- [40] V. Meille, S. Pallier, G.V. Santa Cruz Bustamante, M. Roumanie, J.P. Reymond, Appl. Catal. A 286 (2005) 232.
- [41] J.A. Schwarz, C. Contescu, A. Contescu, Chem. Rev. 95 (1995) 477.
- [42] Purwanto, R.M. Deshpande, R.V. Chaudhari, H. Delmas, J. Chem. Eng. Data 41 (1996) 1414.
- [43] M.S. Wainwright, T. Ahn, D.L. Trimm, J. Chem. Eng. Data 32 (1987) 22.
- [44] T. Katayama, T. Nitta, J. Chem. Eng. Data 21 (1976) 194.
- [45] E. Sada, S. Kito, T. Oda, T. Ito, Chem. Eng. J. 10 (1975) 155.
- [46] K. Sporka, J. Hanika, V. Ruzicka, Collect. Czech. Chem. Commun. 34 (1969) 3145.

- [47] W.A. Roth, K. Scheel, *Landolt-Börnstein physikalisch-chemische Tabellen*, Springer, Berlin, 1932.
- [48] C.R. Wilke, P. Chang, *AIChE J.* 1 (1955) 264.
- [49] M.A. Lusis, G.A. Ratcliff, *AIChE J.* 17 (1971) 1492.
- [50] B.E. Poling, J.M. Prausnitz, J.P. O'Connell, *The properties of gases and liquids*. Fifth edition. The McGraw-Hill Companies, Inc., Boston, 2001.
- [51] M.T. Tyn, W.F. Calus, *Processing* 21 (1975) 16.
- [52] P. Kacer, P. Spurna, L. Cerveny, *J. Mol. Catal. A* 202 (2003) 269.
- [53] E. Dietrich, C. Mathieu, H. Delmas, J. Jenck, *Chem. Eng. Sci.* 47 (1992) 3597.
- [54] H.P. Kritzinger, B.C. Deelder, C.R. Kleijn, J.J. Derksen, H.E.A. van den Akker, *Proceeding of FEDSM*. Montreal, Quebec, Canada, 2002.
- [55] M.T. Kreutzer, F. Kapteijn, J.A. Moulijn, J.J. Heiszwolf, *Chem. Eng. Sci.* 60 (2005) 5895.
- [56] A.E Scheidegger, *The physics of flow through porous media*. University of Toronto Press, Toronto, 1974.
- [57] A. Chandhok, N. Voorhies, M.J. McCready, D.T. Leighton Jr., *AIChE J.* 36 (1990) 1259.

# 4

## **Heterogeneously palladium catalyzed continuous-flow hydrogenation using Taylor flow in capillary columns**

---

Taylor flow in standard GC capillary columns, with a heterogeneous Pd catalyst on the walls, gave rapid information about catalytic processes in them. The residence time and conversion was monitored visually, greatly simplifying bench-scale optimization. Examples show the benefits of the elimination of pore diffusion and axial dispersion. Further, I demonstrated how to quickly identify deactivating species in multistep synthesis without intermediate workup.

---

This Chapter and parts of appendix A are published in ChemCatChem. 3 (2011) 1155.

## Introduction

This Chapter explores how visible features of Taylor flow (or segmented flow) under reaction conditions can be used in lab-scale multiphase heterogeneous catalysis. Continuous-flow microreactors are now routinely used in bench-scale synthesis [1] and optimization [2] applications, because of their small reactant inventory, negligible heat effects at small scales and fast mixing [3]. However, miniaturizing multiphase heterogeneous catalysis on chips is considerably more difficult than homogeneous liquid phase chemistry. Several applications of gas-liquid [2b, 4] and gas-liquid-solid [5] reactions have been reported. In these continuous-flow devices, the catalyst was immobilized on the wall of the channel [5a, 6] or incorporated as powder [5e, 7]. A powder packed-bed gas-liquid microreactor may appear ideal for off-the-shelf catalysts, but in practice such reactors are cumbersome: critical packing parameters vary from one instance to the next and channeling and flow hysteresis abound, as has been recently visualized [8]. For immobilized catalysts, Kobayashi *et al.* have advocated creating a thin film of liquid on the walls, sheared along by a fast-flowing gas stream [5a]. A drawback of this system is that it is hard to control or visualize how long the reactants are in contact with the catalyst, because both phases each move at their own velocity. Especially for more complex pathways, the spread in residence time reduces yields.

Here, I overcome monitoring and yield problems using wall-catalyzed Taylor flow (Fig. 4.1). Flow segmentation has found widespread use in liquid-liquid [4c, 9] and gas-liquid [4d, 10] applications, motivated by good contact between fluid phases. In this Chapter, I highlight that the flow pattern also enhances contact with a catalyst on the wall, inspired by pilot-plant studies for monolith-based reactors [11]. I focus on using standard capillary columns, readily available to the bench chemist. The uncomplicated construction and, equally important, simple visual monitoring will be a powerful tool in the hands of synthetic chemists.

## Experimental

Experimental details can be found in Appendix A.

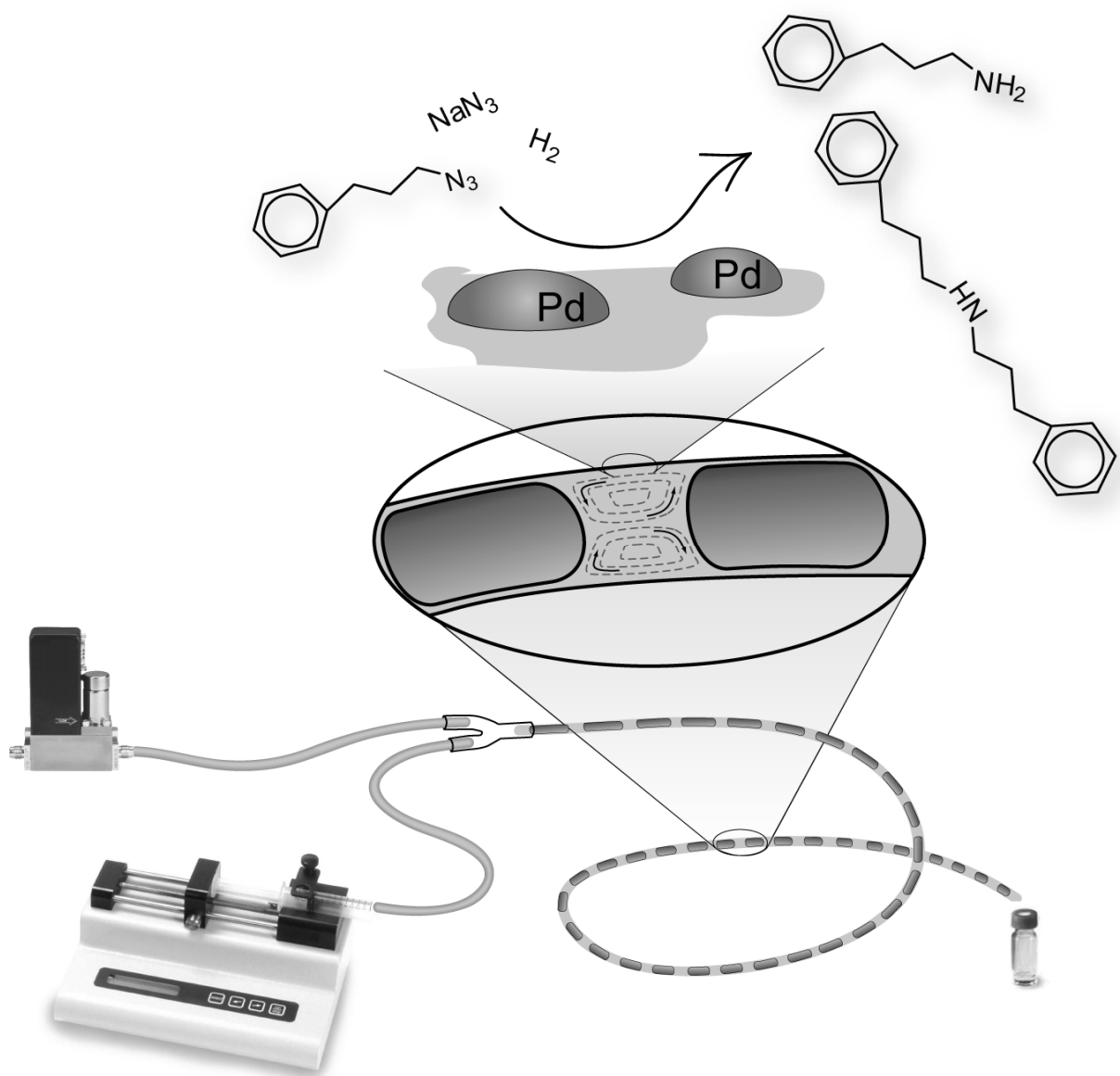


**Fig. 4.1.** Continuous capillary microreactor with a Pd catalyst immobilized on the inner wall operated in Taylor gas-liquid flow.

## Results & Discussion

I used commercially available fused-silica capillaries coated with a 6  $\mu\text{m}$  thick layer of high surface area  $\gamma\text{-Al}_2\text{O}_3$  that I pretreated and impregnated with a  $\text{Pd}(\text{OAc})_2$  solution (Fig. 4.2). This resulted in nanosized Pd crystallites evenly dispersed on the  $\gamma\text{-Al}_2\text{O}_3$  coating layer (Fig. 4.2c). I tested their activity with the well-studied hydrogenation of cyclohexene [12]. In a 17 cm capillary (residence time  $\sim 4$  s) the conversion was 43% at 20°C, without deactivation, increasing to  $> 99\%$  for a 50 cm piece.

The Taylor flow regime (Fig. 4.2d) is an especially useful flow pattern in synthesis because the chemistry can be followed visually [4b, 9c]. From the velocity of the bubbles, the reaction time is determined, and the conversion rate is seen from the decreasing length of the bubbles, as they move through the capillary (Fig. 4.3). I fully exploit this fact by visually measuring the conversion accurately, provided that conditions are chosen such that hydrogen consumption is significant. Bubble-to-bubble variation requires that several tens of bubbles are measured, but then, the visual method and GC-analysis agree within 5%. Rapidly available quantitative kinetic data thus allow fast fine-tuning to maximize yields or minimize deactivation.

Before I discuss such an optimization, I first show that Taylor flow ensures an optimal yield. Previously, we reported that mass transfer to the wall in Taylor flow is extremely fast [11]. I confirm this by measuring the activation energy of the hydrogenation of cyclohexene. In my capillary, I determined  $34 \text{ kJ mol}^{-1}$  at  $T < 57^\circ\text{C}$ , is in agreement with literature [13] and ruling out transport limitations inside or outside the porous  $\gamma\text{-Al}_2\text{O}_3$  layer, which would have lowered this value. More results and discussion about the hydrogenation of cyclohexene can be found in Appendix A.

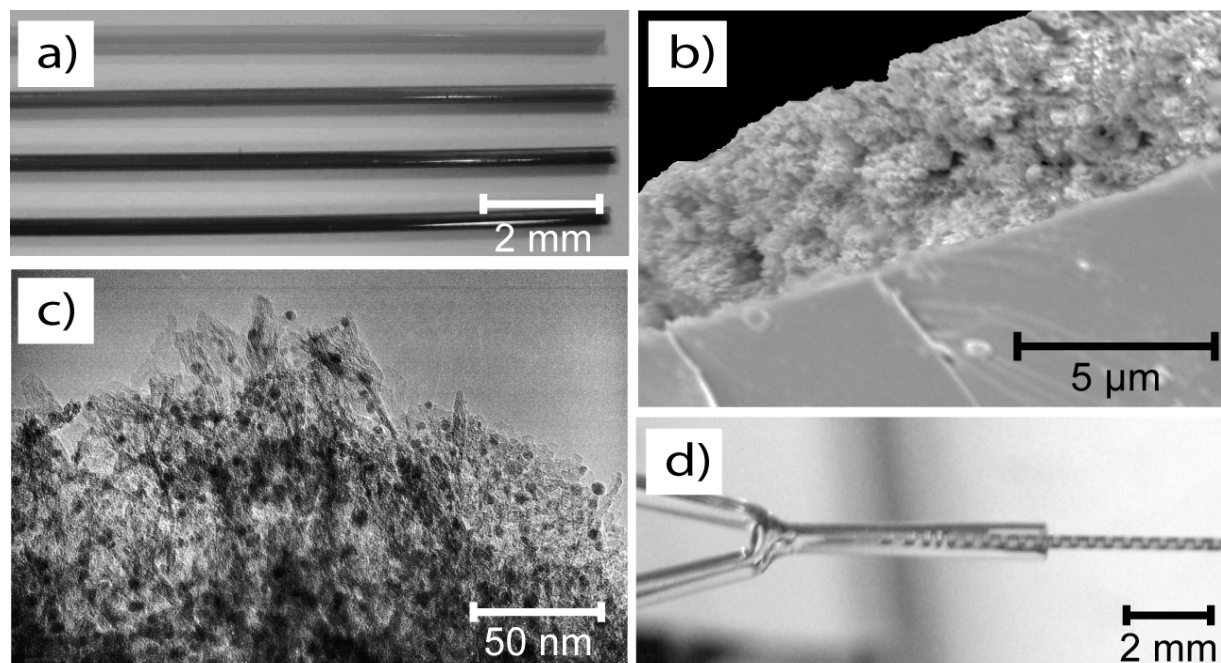


**Fig. 4.2.** (a) Darkening of a capillary after Pd impregnation (from top to bottom: 0, 1.1, 2.7 and 5.7 wt% Pd). (b) SEM micrograph of porous  $\gamma\text{-Al}_2\text{O}_3$  layer coated on the inner wall of the capillary. (c) TEM micrograph of 5 nm Pd crystallites (black dots, EDX analysis) supported on  $\gamma\text{-Al}_2\text{O}_3$  (5.7 wt% Pd). (d) Formation of Taylor flow at the capillary inlet.

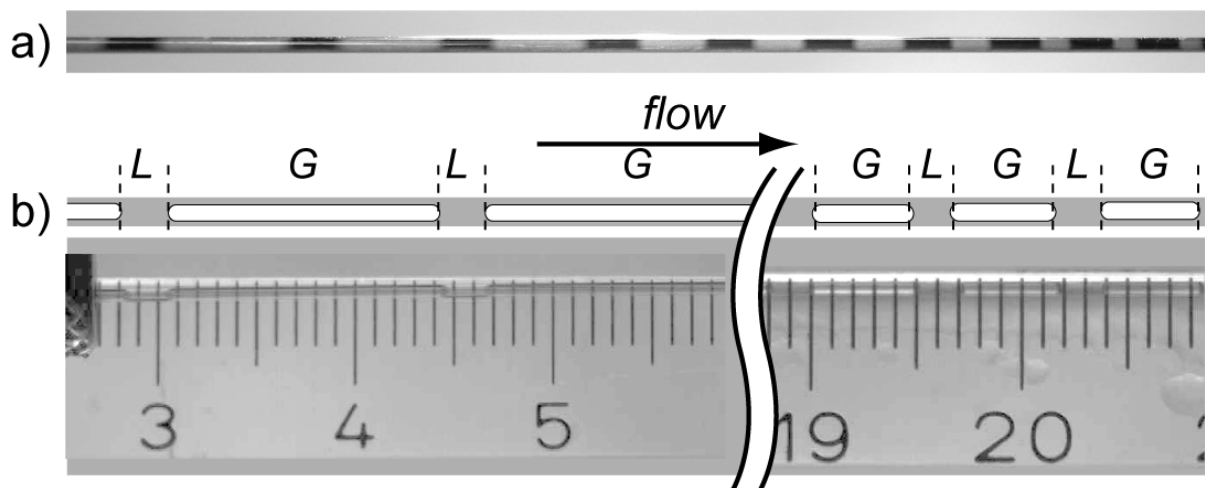
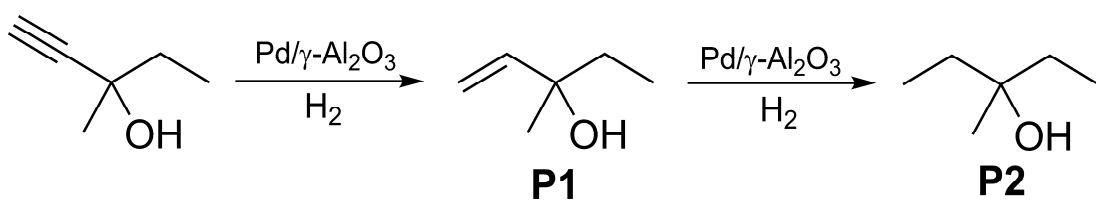


**Fig. 4.3.** (a) Visual observation of shrinking bubbles during a hydrogenation reaction in a Pd-capillary. (b) Measurement of the bubble length from photographs at the inlet and outlet of a capillary.

Apart from eliminating diffusional effects, Taylor flow hardly exhibits axial dispersion [14], which is notorious for low yields in continuous-flow reactors and polydisperse particles in continuous crystallization [15]. I illustrate the improvement with the selective Pd-catalyzed hydrogenation of 3-methyl-1-pentyn-3-ol to **P1** (Scheme 4.1) without over-hydrogenation to **P2**. Kinetic modeling showed that, for a feed of  $0.032 \text{ mol l}^{-1}$ , the maximum possible yield is 78-81%, which is obtained only at precisely the right residence time [16]. Any distribution of residence time reduces the yield. In a one-day optimization, I approach the theoretical optimum, obtaining a yield of  $(78 \pm 2)\%$  **P1** using Taylor flow (Fig. 4.4). Without  $\text{H}_2$  bubbles, the yield of **P1** would have been  $\sim 57\%$ . More results and discussion about the hydrogenation of 3-methyl-1-pentyn-3-ol can be found in Appendix A.



**Scheme 4.1.** Selective hydrogenation of 3-methyl-1-pentyn-3-ol over a Pd catalyst to the desired 3-methyl-1-penten-3-ol (**P1**) and the overhydrogenation to 3-methyl-3-pentanol (**P2**).

Now that I have established the benefits of Taylor flow in Pd-capillaries for single step hydrogenation reactions, I return to rapid optimization of a multistep synthesis. As an

example to demonstrate the benefit of Taylor flow, I synthesize primary amine **5** via hydrogenation of the intermediate azide **4** (Scheme 4.2).

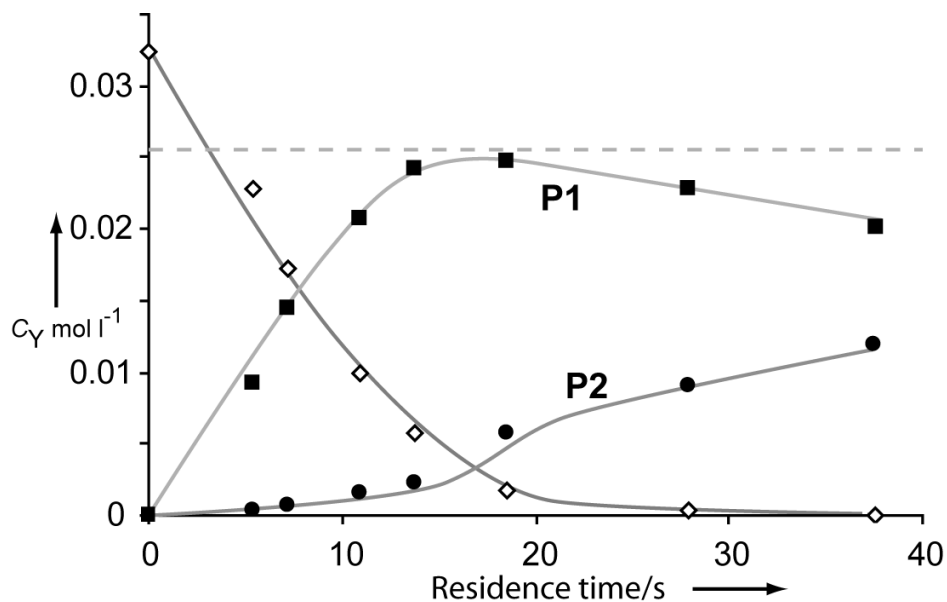
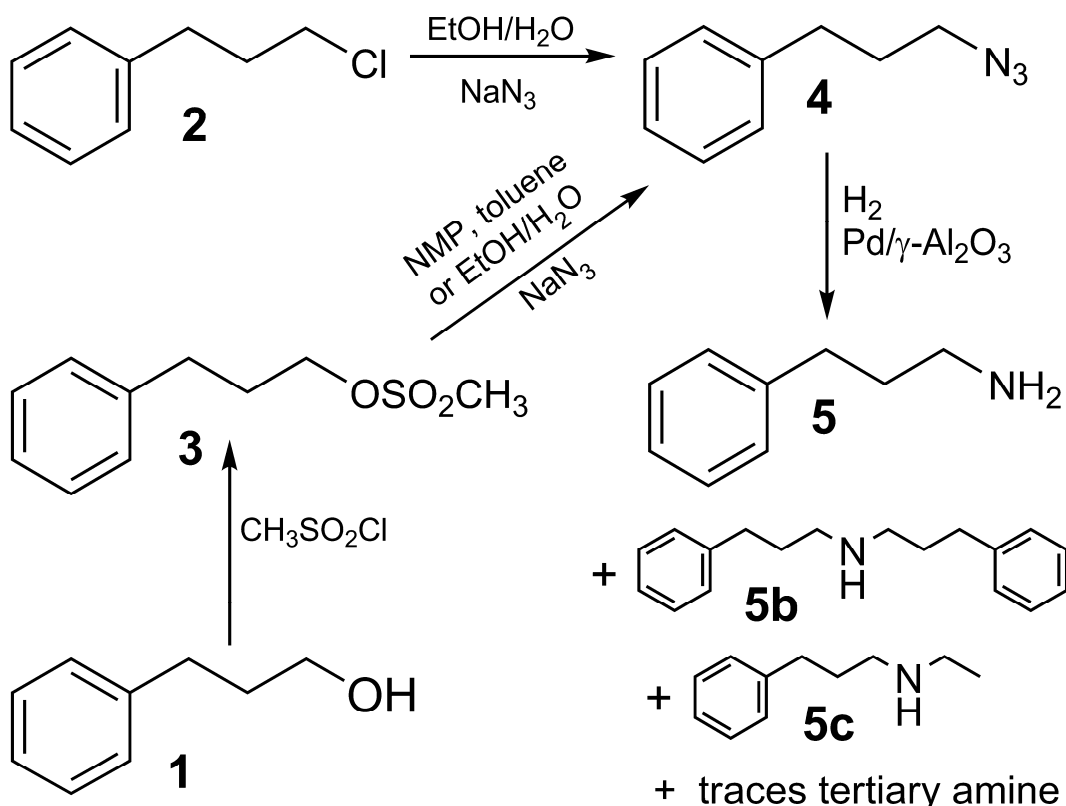


**Fig. 4.4.** Effluent concentrations as a function of residence time of the hydrogenation of 3-methyl-1-pentyn-3-ol in ethanol over a 0.02 wt% Pd catalyst operated in Taylor flow at 24°C. The dashed line shows the maximum obtainable yield.

The hydrogenation of the nitrogen-containing compounds over Pd catalysts is a good example of strongly adsorbing, or even poisoning, reactants and products. Such deactivation is better analyzed in continuous flow than in repeated batch experiments. Moreover, azide chemistry benefits greatly from miniaturized synthesis, because the toxic and explosive properties of azides complicate handling large quantities. Azide **4** was synthesized from **3** or **2** in various solvents, and subsequently hydrogenated without intermediate work-up, *i.e.*, purification was postponed until the toxic and explosive **4** was converted. The optimization problem, then, is to keep the hydrogenation to the primary amine **5** going as long as possible until deactivation of the catalyst by strongly adsorbing compounds in the synthesis mixture.

I probe how much the various compounds deactivate Pd, one by one, by measuring how much they reduce the rate of the hydrogenation of cyclohexene – in the azide hydrogenation, bubbles do not shrink due to the formation of N<sub>2</sub>, so I use a simple test reaction, which does exhibit bubble shrinkage because it does not produce a gas. This works because I am predominantly interested in the adsorption strength for the various deactivating compounds, which enters in the same way into the rate expression for the hydrogenation of both azide and cyclohexene. These *spiking* experiments are cumbersome in batch but easy in this continuous

system. Now, only conversion needed to be monitored to determine the adsorption strength  $K$  of the various components on the catalyst, and switching to an unspiked feed shows whether adsorption is reversible (Fig. 4.5). Rapidly, the population balance on the Pd surface for these complex synthesis mixtures was determined and used in the optimization of the hydrogenation process and synthesis route.



**Scheme 4.2.** Synthesis routes for 3-phenyl-propyl-amine **5** via hydrogenation of 3-phenyl-propyl-azide **4**.

Based on these rapid spiking experiments, I found that **3** adsorbs irreversibly whereas azides, including residual  $\text{NaN}_3$ , adsorb reversibly. Adsorption of **5** was minimized by  $\text{H}_2\text{O}$  in the feed, because the ammonium complex that is formed hardly adsorbs. Condensation reactions, giving **5b** and **5c**, occurred less at high dilution and low temperature, and were solvent-sensitive. Toluene as solvent competed significantly with **4** for adsorption on the Pd surface, whereas ethanol enhanced condensation. An optimum of 2 kg of amine **5** could be synthesized using 1 g Pd, using **2** as starting material, in ethanol/ $\text{H}_2\text{O}$  without catalyst regeneration (entry 7, Table A2 in Appendix A). This was achieved in the same capillaries, showing that kilolab quantities can readily be made in the same bench-scale equipment, with only longer time-on-stream. More results and discussion about the hydrogenation of **4** can be found in appendix A.

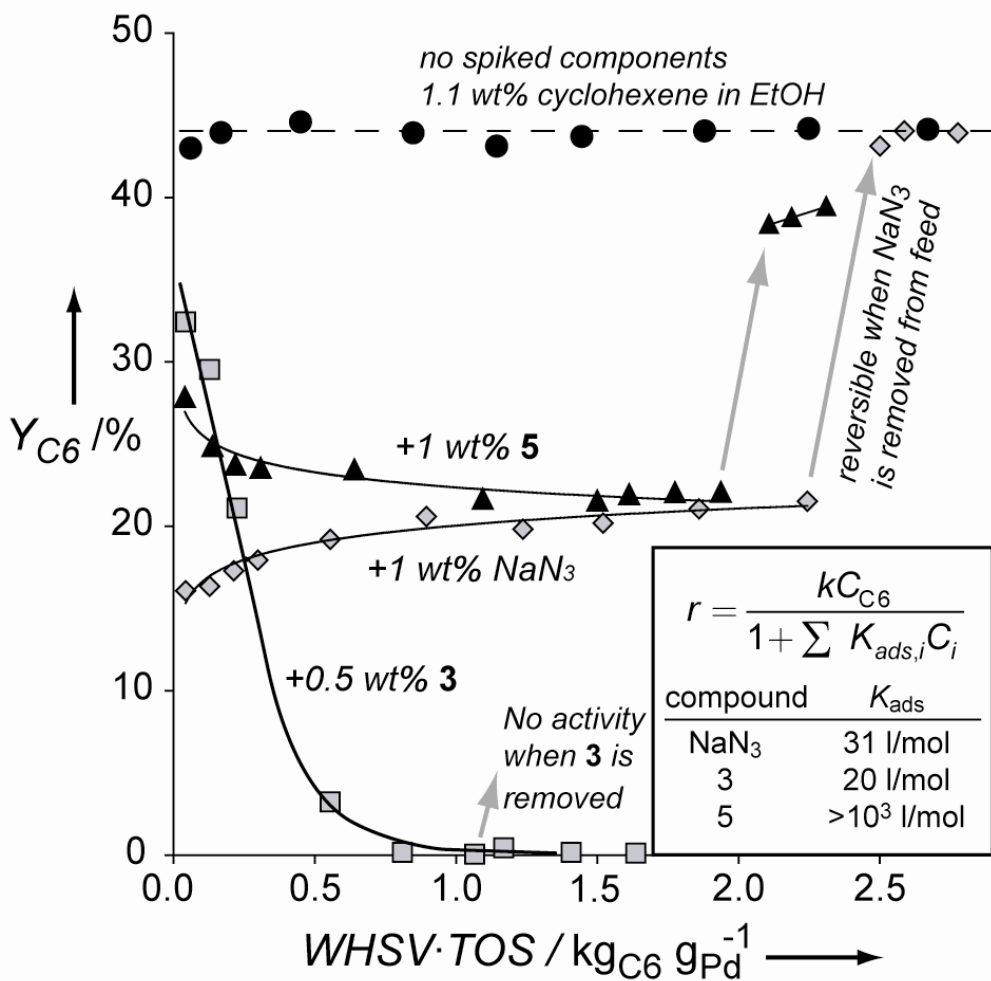


**Fig. 4.5.** Spiking of cyclohexene (C6) hydrogenation at 24°C with components from Scheme 4.2 to determine the strength and reversibility of adsorption on the Pd catalyst.

### Conclusions

Taylor flow accelerates optimization of continuous-flow hydrogenations using heterogeneous catalysis. Conversion can be monitored visually, which gives hands-on control over the activity and deactivation of the catalyst. Reagents exchange rapidly with the catalyst and without axial dispersion, yields are the same as in batch. I have shown that continuous-flow analysis allows a fast optimization of various aspects of heterogeneous catalysis and synthesis routes, such as solvent effects, competitive adsorption and irreversible poisoning.

## Bibliography

[1] a) B. Ahmed-Omer, J.C. Brandt, T. Wirth, *Org. Biomol. Chem.* 5 (2007) 733; b) H.R. Sahoo, J.G. Kralj, K.F. Jensen, *Angew. Chem. Int. Ed.* 46 (2007) 5704; c) G. Shore, S. Morin, M. G. Organ, *Angew. Chem. Int. Ed.* 45 (2006) 2761.

[2] a) D. Belder, M. Ludwig, L.W. Wang, M.T. Reetz, *Angew. Chem. Int. Ed.* (2006), 45, 2463; b) E.R. Murphy, J.R. Martinelli, N. Zaborenko, S.L. Buchwald, K.F. Jensen, *Angew. Chem. Int. Ed.*, 119 (2007) 1764; c) K. Geyer, J.D.C. Codée, P.H. Seeberger, *Chem. Eur. J.* 12 (2006) 8434; d) J.P. McMullen, M.T. Stone, S.L. Buchwald, K.E. Jensen, *Angew. Chem. Int. Ed.* 49 (2010) 7076; e) O. Trapp, S. K. Weber, S. Bauch, W. Hofstadt, *Angew. Chem. Int. Ed.* 46 (2007) 7307.

[3] a) M. Brivio, W. Verboom, D.N. Reinhoudt, *Lab Chip* 6 (2006) 329; b) P.D.I. Fletcher, S. J. Haswell, E. Pombo-Villar, B.H. Warrington, P. Watts, S.Y.F. Wong, X. Zhang, *Tetrahedron* 58 (2002), 4735; c) K. Jänisch, V. Hessel, H. Löwe, M. Baerns, *Angew. Chem. Int. Ed.* 43 (2004) 406.

[4] a) P.W. Miller, N.J. Long, A.J. de Mello, R. Vilar, H. Audrain, D. Bender, J. Passchier, A. Gee, *Angew. Chem. Int. Ed.* 46 (2007) 2875; b) A. Leclerc, M. Alame, D. Schweich, P. Pouteau, C. Delattre, C. de Bellefon, *Lab Chip* 8 (2008) 814; c) Y. Önal, M. Lucas, P. Claus, *Chem. Ing. Tech.* 77 (2005) 101; d) B.K.H. Yen, A. Günther, M.A. Schmidt, K.F. Jensen, M.G. Bawendi, *Angew. Chem. Int. Ed.* 44 (2005) 5447.

[5] a) J. Kobayashi, Y. Mori, K. Okamoto, R. Akiyama, M. Ueno, T. Kitamori, S. Kobayashi, *Science* 304 (2004) 1305; b) S. Saaby, K.R. Knudsen, M. Ladlow, S. V. Ley, *Chem. Commun.* 23 (2005) 2909; c) S. Tadepalli, R. Halder, A. Lawal, *Chem. Eng. Sci.* 62 (2007) 2663; d) E.V. Rebrov, E.A. Klinger, A. Berenguer-Murcia, E.M. Sulman, J.C. Schouten, *Org. Process Res. Dev.* 13 (2009) 991; e) N. Yoswathananont, K. Nitta, Y. Nishiuchi, M. Sato, *Chem. Commun.* 1 (2005), 40.

[6] a) C.H. Hornung, B. Hallmark, M.R. Mackley, I.R. Baxendale, S.V. Ley, *Adv Synth. Catal.* 352 (2010) 1736; b) J.F. Ng, Y.T. Nie, G.K. Chuah, S. Jaenicke, *J Catal.* 269 (2010) 302; c) N.W. Wang, T. Matsumoto, M. Ueno, H. Miyamura, S. Kobayashi, *Angew. Chem. Int. Ed.* 48 (2009) 4744; d) E.V. Rebrov, A. Berenguer-Murcia, H.E. Skelton, B.F.G. Johnson, A.E.H. Wheatley, J.C. Schouten, *Lab Chip* 9 (2009) 503.

- [7] a) B. Desai, C. O. Kappe, *J. Comb. Chem.* 7 (2005) 641; b) A.R. Bogdan, B.P. Mason, K.T. Sylvester, D.T. McQuade, *Angew. Chem. Int. Ed.* 46 (2007) 1698; c) A. Kirschning, W. Solodenko, K. Mennecke, *Chem. Eur. J.* 12 (2006) 5972.
- [8] D. van Herk, P. Castano, M. Makkee, J.A. Moulijn, M.T. Kreutzer, *Appl. Catal. A-Gen.* 365 (2009) 199.
- [9] a) J.R. Burns, C. Ramshaw, *Lab Chip* 1 (2001) 10; b) G. Dummann, U. Quittmann, L. Groschel, D.W. Agar, O. Worz, K. Morgenschweis, *Catal. Today* 79 (2003) 433; c) H. Song, D.L. Chen, R.F. Ismagilov, *Angew. Chem. Int. Ed.* 45 (2006) 7336.
- [10] A. Günther, K. F. Jensen, *Lab Chip* 6 (2006) 1487.
- [11] M.T. Kreutzer, P. Du, J.J. Heiszwolf, F. Kapteijn, J.A. Moulijn, *Chem. Eng. Sci.* 56 (2001) 6015.
- [12] M.W. Losey, M.A. Schmidt, K.F. Jensen, *Ind. Eng. Chem. Res.* 40 (2001) 2555.
- [13] M. Boudart, R.J. Madon, J.P. O'Connell, *AIChE. J.* 24 (1978) 904.
- [14] M.T. Kreutzer, A. Gunther, K.F. Jensen, *Anal. Chem.* 80 (2008) 1558.
- [15] S.A. Khan, A. Gunther, M.A. Schmidt, K.F. Jensen, *Langmuir* 20 (2004) 8604.
- [16] T.A. Nijhuis, G. van Koten, F. Kapteijn, J.A. Moulijn, *Catal. Today* 79 (2003) 315.

## **Appendix A - Supporting Information to Chapter 4**

### Capillary preparation, characterization and reactive testing

#### *Capillary*

A commercially available fused silica capillary column with an inner diameter of 530  $\mu\text{m}$  coated with a thin porous  $\gamma\text{-Al}_2\text{O}_3$  layer (supplied by Restek: Rt-Alumina<sup>TM</sup> PLOT column, aluminum oxide Porous Layer Open Tubular column) resulting in an open inner diameter of 518  $\mu\text{m}$  were used as a flow device. The thickness of the fused silica capillary wall was 50  $\mu\text{m}$ , and the outer coating of polyimide was 20  $\mu\text{m}$  thick (Fig. A1) as determined with SEM. This polyimide coating provides increased elasticity, flexibility, and tensile strength to the fused silica column and it can withstand temperatures up to 350°C in air or 400°C in N<sub>2</sub>.

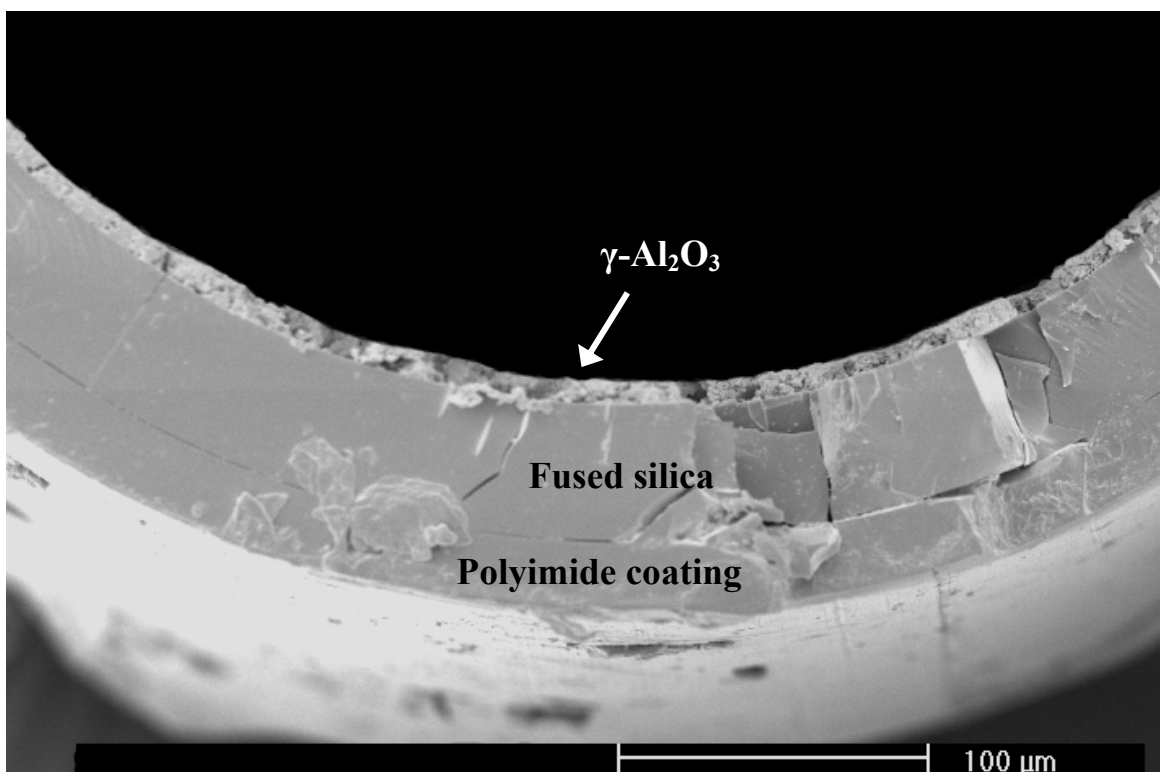


**Fig A1.** SEM micrograph of the fused silica capillary flow device coated with a  $\gamma\text{-Al}_2\text{O}_3$  layer of 6  $\mu\text{m}$ .

#### *Pretreatment & preparation*

Prior to the catalyst preparation, the capillaries were heated for 4 h at 260°C with a heating rate of 2°C min<sup>-1</sup> to reactivate the deactivated  $\gamma\text{-Al}_2\text{O}_3$  (these columns were deactivated with Na<sub>2</sub>SO<sub>4</sub> by the supplier), rinsed with water (Milli-Q) at 1 ml min<sup>-1</sup> for 30 min followed by a flow of 1 ml(STP) min<sup>-1</sup> N<sub>2</sub> for 30 min and subsequently dried under flowing air in an oven for 2 h at 120°C.

A solution of Palladium(II) acetate ( $\text{Pd}(\text{OAc})_2$ , Alfa Aesar, 45.9 wt% Pd) in toluene (J.T. Baker) was prepared and stirred for 60 min. The capillaries were filled with the  $\text{Pd}(\text{OAc})_2$  solution, capped on both sides with GC septa. Capillaries were impregnated for 24 h with solutions of different  $\text{Pd}(\text{OAc})_2$  amounts aiming for Pd catalysts between 0.003 and 7 wt% Pd (per  $\gamma\text{-Al}_2\text{O}_3$  weight). After the impregnation the capillary was emptied and washed six times with *n*-hexane followed by flowing  $\text{N}_2$  for 20 min at room temperature. After flushing, they were dried and calcined with a flow of air for 1 h at 120°C, followed by 2 h at 250°C, and then cooled to room temperature, with a heating rate up and down of 2°C min<sup>-1</sup>. Reduction/activation of the Pd crystallites took place at room temperature for 12 h prior to a hydrogenation experiment. The  $\text{H}_2$  flowrate and pressure during this period was 1 ml(STP) min<sup>-1</sup> and 1.1 bar, respectively.

### *Characterization*

The amount of Pd in a capillary was determined by atomic absorption spectroscopy (AAS) on a Perkin-Elmer 4100ZL. Inductively coupled plasma optical emission spectrometry (ICP-OES) was performed to determine the amount of leached Pd in a reaction mixture using a Perkin Elmer Optima 5300DV. Solutions of the hydrogenation products in the appropriate solvent were used as matrix in the calibration samples for the ICP-OES analyses. High-resolution transmission electron microscopy (HRTEM) was performed using a Philips CM30T electron microscope with a LaB6 filament as a source of the electrons equipped with an energy dispersive X-ray Spectrometer (EDX). Scanning electron microscopy (SEM) was performed using a Philips XL20 electron microscope to investigate the thickness and homogeneity of the  $\gamma\text{-Al}_2\text{O}_3$  layer. The  $\gamma\text{-Al}_2\text{O}_3$  layer thickness was determined at several points in the capillary and was  $6 \pm 0.5 \text{ }\mu\text{m}$  ( $\sim 0.05 \text{ g}_{\text{alumina}} \text{ g}_{\text{cap}}^{-1}$ ).  $\text{N}_2$  physisorption (Quantachrome Autosorb-6B) was used to determine the specific surface area  $S_{\text{BET}}$ , the average pore diameter and the pore volume of the  $\gamma\text{-Al}_2\text{O}_3$  coating. The  $S_{\text{BET}}$  of the  $\gamma\text{-Al}_2\text{O}_3$  layer was 195 m<sup>2</sup> g<sup>-1</sup>, the average pore diameter was 10 nm (broad distribution) and the pore volume was 0.47 cc g<sup>-1</sup> (porosity was 0.63).

AAS revealed that  $\sim 80\%$  of the aimed amount of Pd was deposited on the  $\gamma\text{-Al}_2\text{O}_3$  resulting in 5.7 wt% Pd loading (units:  $\text{g}_{\text{Pd}} \text{ g}_{\text{alumina}}^{-1}$ ) for an aimed amount of 7 wt% and all Pd was deposited with aimed amounts below 3 wt%. Pd crystallites ( $d = 5 \text{ nm}$ , determined with HRTEM-EDX and CO chemisorption) were homogenously distributed over the entire length of a capillary of 0.5 m for the 5.7 wt% capillary. Capillaries with lower wt% Pd resulted in

smaller Pd crystallites (as determined with HRTEM): for example for 1.1 and 2.7 wt% Pd the average crystallite size of Pd was 2.4 and 3.3 nm, respectively.

#### *Equipment*

The Pd-impregnated capillaries were connected to a gas mass flow controller for the H<sub>2</sub> supply (Bronkhorst HI-TEC model F-200CV-FAC-33-V with a maximum of 1 H<sub>2</sub> ml(STP) min<sup>-1</sup>) and to a syringe pump (Harvard, PHD2000 programmable) containing a 50 ml syringe (SGE Europe Ltd.) filled with a liquid reactant/solvent mixture. Simple quartz Y-mixer (Restek) and stainless steel T- and Y-mixers (Valco and Swagelok) were used as gas-liquid distributors which were attached upstream of a capillary flow device.

#### *Hydrogenation procedures*

Continuous flow experiments were performed in the Taylor flow regime. The analysis of the reaction mixture effluent by HPLC and/or GC analysis was only considered after a stable flow pattern of Taylor flow had established inside the transparent capillary via visual observation. Prior to an hydrogenation experiment, the capillaries were reduced for 12 h at room temperature in a H<sub>2</sub> flow of 1 ml(STP) min<sup>-1</sup> unless specifically stated otherwise. The capillaries were submerged in a stirred temperature controlled water bath (IKA RCT basic and IKA ETS-D4 Fuzzy). The progress of the hydrogenations were measured using off-line GC analysis (and HPLC for the hydrogenation of 3-phenyl-propyl-azide) and also by visual observation of the H<sub>2</sub> bubble shrinkage during the hydrogenation of 3-methyl-1-pentyn-3-ol and cyclohexene.

A capillary of 0.5 m was cut into several pieces of equal length and these pieces were tested separately for cyclohexene hydrogenation activity. This gave hydrogenation conversions within 3% confirming that the Pd was distributed homogenously in the axial direction, as was also shown by TEM analysis of the separate pieces. No (detectable) activity was observed for capillaries (with  $\gamma$ -Al<sub>2</sub>O<sub>3</sub>) without Pd when performing the hydrogenation of cyclohexene, 3-methyl-1-pentyn-3-ol and 3-phenyl-propyl-azide. The carbon balances were closed within  $\pm$  2.4% for cyclohexene and 3-methyl-1-pentyn-3-ol hydrogenation. This was equal to the experimental error of the GC analysis ( $\sim$  2.5%). The hydrogenation of 3-phenyl-propyl-azide was followed with HPLC. The carbon balance for this hydrogenation was closed within  $\pm$  4%.

### *Characterization of spent catalysts*

The Pd content on the capillary was measured with AAS before and after all hydrogenation reactions and no decrease of the Pd content was observed except for the hydrogenation of 3-phenyl-propyl-azide in NMP (*N*-methylpyrrolidone). Note that the other solvents used in the hydrogenation of 3-phenyl-propyl-azide (ethanol/water and toluene) did not exhibit any observable Pd leaching. After reaction, several product mixtures were analyzed by inductively coupled plasma optical emission spectroscopy (ICP-OES) and no Pd was detected in these mixtures. TEM analysis of the post-mortem catalyst at several points did not show a crystallite size decrease or an accumulation of Pd (possible readsorbed of leached Pd) at the end part of the capillary for the hydrogenation of 3-methyl-1-pentyn-3-ol, cyclohexene and 3-phenyl-propyl-azide in ethanol, ethanol/water and toluene.

### *Mechanisms of deactivation*

Continuous experiments with increasing time on stream (TOS) for the hydrogenation of cyclohexene and 3-methyl-1-pentyn-3-ol showed no deactivation under kinetically controlled conditions and capillary flow devices could be used for several weeks without deactivation. The Pd catalyst in the hydrogenation of 3-phenyl-propyl-azide displayed deactivation which was mainly caused by poisoning (reversible and irreversible adsorption) and surface rearrangements (including slight sintering) of Pd crystallites (described in more detail at the end of this Appendix) except for the hydrogenation of 3-phenyl-propyl-azide in NMP, where the reaction mixture had a yellowish color and the capillary became completely yellow again (was dark colored) pointing towards full Pd dissolution without readsorption of leached Pd downstream or at the end of the capillary. AAS analysis of the used capillaries in the hydrogenation of 3-phenyl-propyl-azide in NMP showed that most Pd leached into the reaction mixture (less than 0.2 wt% left from the 5.7 wt% Pd originally on the capillary) caused by strong complex formation with components in the highly polar reaction mixture. Moreover, N<sub>2</sub> physisorption revealed that the  $S_{\text{BET}}$  of the  $\gamma$ -Al<sub>2</sub>O<sub>3</sub> support decreased significantly from 195 to 100 m<sup>2</sup> g<sup>-1</sup> indicating  $\gamma$ -Al<sub>2</sub>O<sub>3</sub> sintering and/or dissolution because of the high pH ( $\sim$  10) of the reaction mixture. In addition, regeneration attempts by H<sub>2</sub> and N<sub>2</sub> flow at elevated temperatures did not result in any activity increase, also indicating Pd loss for the azide hydrogenation in NMP.

## The hydrogenation of 3-methyl-1-pentyn-3-ol: determination of conversion and rate by visual inspection of shrinking H<sub>2</sub> bubbles

The hydrogenation of 3-methyl-1-pentyn-3-ol was studied over a Pd/ $\gamma$ -Al<sub>2</sub>O<sub>3</sub> catalyst at different Pd loadings to determine capillary properties, visual decrease of H<sub>2</sub> bubble sizes, concentration vs. residence time plots and turnover frequencies (TOFs). Influences on catalyst performance of intrinsic and extrinsic effects are discussed.

### *GC-analysis*

Samples of 3-methyl-1-pentyn-3-ol hydrogenation (Scheme 4.1, Chapter 4) were analyzed using a Varian CP-3380 GC with a Chrompack CP-SIL 8 CB (PBX5) column of 60 m (internal diameter 0.25 mm; injector temperature = 220°C; ramp = 10°C min<sup>-1</sup>; FID temperature = 330°C). Retention times were: 7.8 min (3-methyl-1-pentyn-3-ol), 8.1 min (3-methyl-1-penten-3-ol), 9.6 min (3-methyl-3-pentanol), and 4.0 min (ethanol). 3-methyl-1-pentyn-3-ol, 3-methyl-1-penten-3-ol, 3-methyl-3-pentanol (Fluka), and dry ethanol (Aldrich) were used as received.

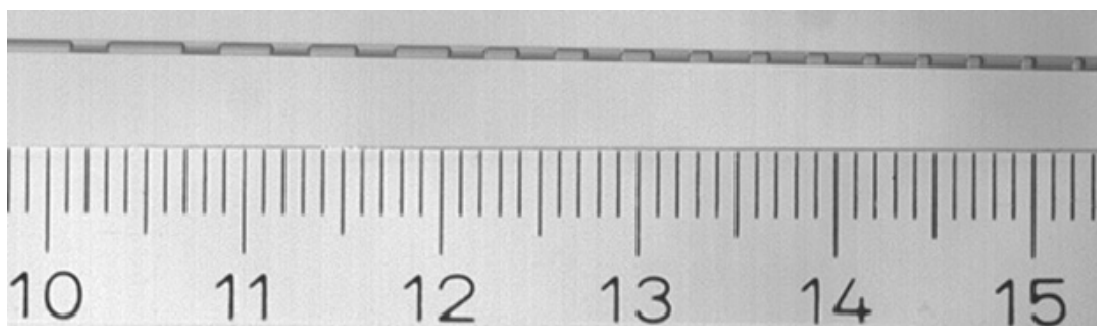
### *Decrease of dimensions of H<sub>2</sub> bubbles*

The decrease in H<sub>2</sub> bubble dimensions in a capillary during the hydrogenation of 3-methyl-1-pentyn-3-ol in ethanol is shown in Fig. A2a. A ruler bar was mounted below the capillary and series of ~ 30 H<sub>2</sub> bubbles were measured at the inlet and outlet. The H<sub>2</sub> bubble lengths were captured at the inlet and at the outlet of the capillary with a camera (Olympus i-speed 2, equipped with a Nikon 55 mm lens) at a frame rate of 150 fps. The H<sub>2</sub> bubble length as a function of the position in the capillary is depicted in Fig. A2b, and it shows the (exponential) decay of H<sub>2</sub> bubble length.

A tubular reactor can generally be operated in two different modes. For low conversion (differential mode) the rate can be considered constant over the reactor length and one can simply use  $r_i = (C_{i,0} - C_i)/\tau_m$  to calculate the rate. When operating a tubular reactor at high conversions, thus with a large concentration gradient over the length of the reactor (*i.e.*, integral operation), the form and/or reaction order of the rate expression is proposed, inserted in the design equation ( $r_i = dC/d(V/\Phi_v)$ ), which is integrated analytically or numerically. The parameters in the rate expression are varied in an iterative way to optimize the exit concentration to the measured one. A graph of concentration vs. residence time or reactor

length is then obtained. When the decay of H<sub>2</sub> bubble lengths is visually monitored, however, one can experimentally determine the amount left of H<sub>2</sub> in the gas phase at every position in the axial direction, allowing the experimental determination of the concentration at every axial position. Numerical differentiation directly yields reaction rates without use of a rate model.

(a)



(b)

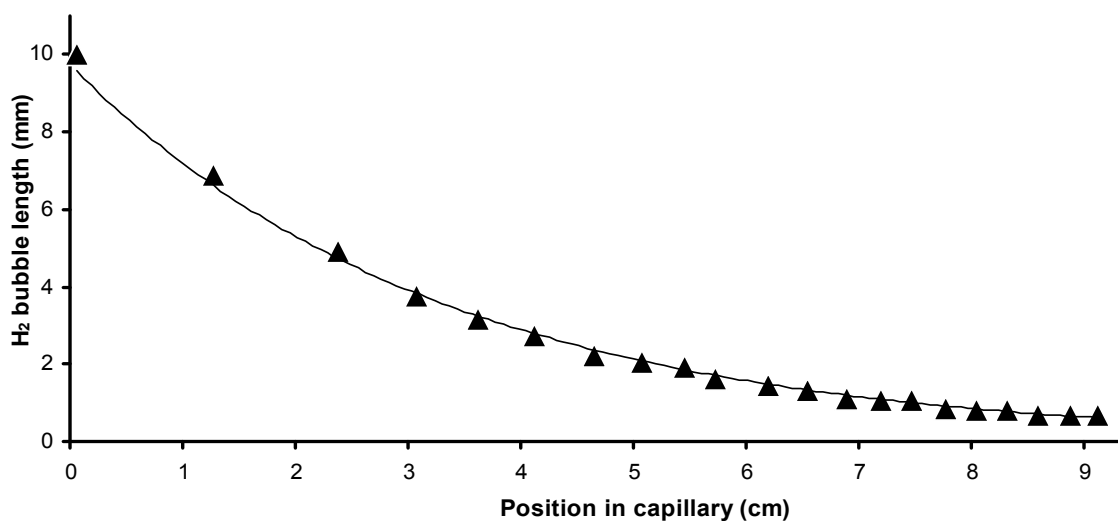


**Fig. A2.** (a) Visual observation of shrinking H<sub>2</sub> bubbles during the hydrogenation of 3-methyl-1-pentyn-3-ol (Y) in a Pd-capillary + ruler bar (cm). (b) H<sub>2</sub> bubble length as a function of the position in the capillary. Conditions: 1.1 wt% Pd,  $T = 25^\circ\text{C}$ ; 1.1 bar H<sub>2</sub>;  $C_{Y,0} = 294 \text{ mol m}^{-3}$ ;  $u_L = 100 \mu\text{l min}^{-1}$ ; and  $u_G = 470 \mu\text{l min}^{-1}$ .

Two typical hydrogenation examples are given where the conversion determined by GC analysis is compared with the conversion determined by visual inspection of shrinking H<sub>2</sub> bubbles. The conditions are given in Table A1. The H<sub>2</sub> bubble lengths that were obtained in these experiments are presented in Fig. A3. No H<sub>2</sub> bubble lengths were found outside the indicated range. A comparison of the conversion of H<sub>2</sub> determined by GC analysis

(concentration of alkene + alkane) and the conversion determined from visually observed shrinking H<sub>2</sub> bubbles (using a correction for the expansion of H<sub>2</sub> bubbles due to pressure drop [1]) is presented in Fig. A4.

**Table A1**  
3-methyl-1-pentyn-3-ol hydrogenation conditions

|  | Run 1 | Run 2 |
|--|-------|-------|
| Temperature /°C  | 26    | 26    |
| 3-methyl-1-pentyn-3-ol concentration<br>( $C_{Y,0}$ ) /mol m <sup>-3</sup> | 294   | 294   |
| Capillary length ( $l_{CAP}$ ) /m  | 0.25  | 0.25  |
| Amount of Pd /wt%  | 1.1   | 1.1   |
| H <sub>2</sub> flow rate ( $u_G$ ) /μl(STP) min <sup>-1</sup>              | 860   | 1000  |
| Liquid flow rate ( $u_L$ ) /μl min <sup>-1</sup>                           | 100   | 200   |

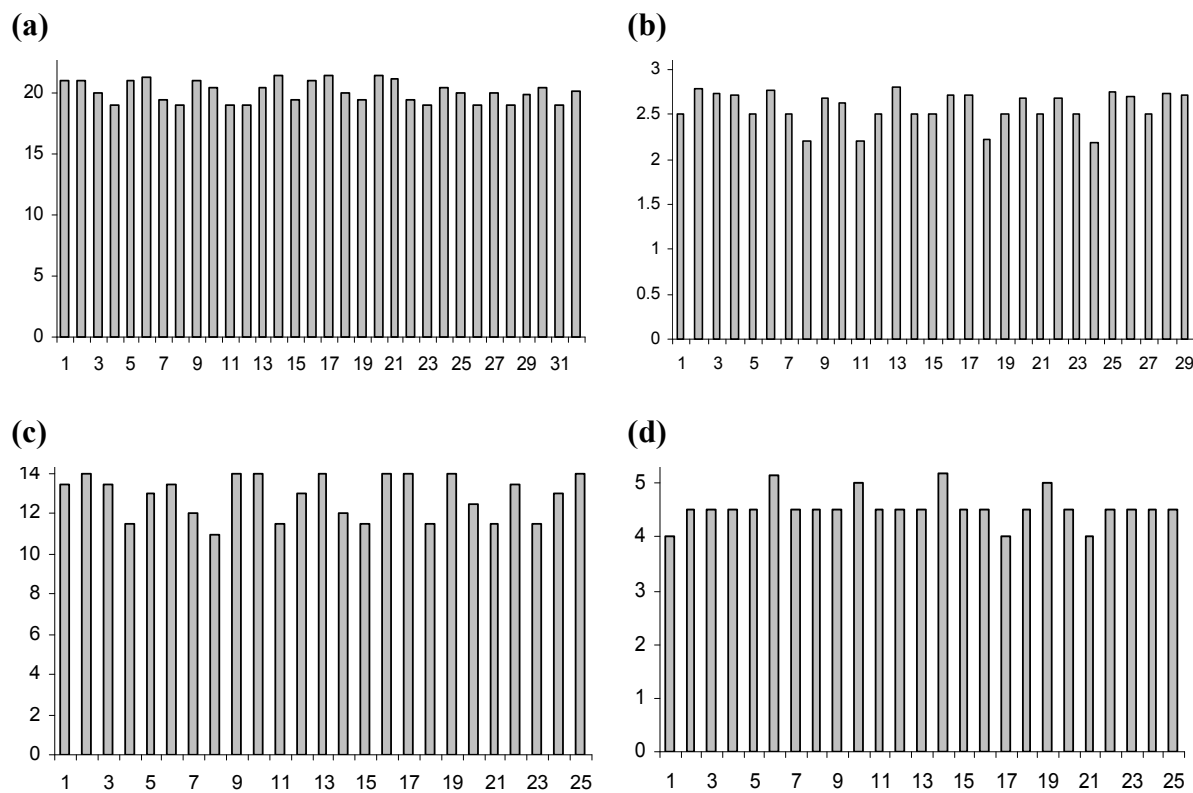


**Fig. A3.** H<sub>2</sub> bubble lengths (mm) vs. the number of bubbles for the hydrogenation of 3-methyl-1-pentyn-3-ol in a capillary. (a) Run 1 inlet; (b) Run 1 outlet; (c) Run 2 inlet; (d) Run 2 outlet.

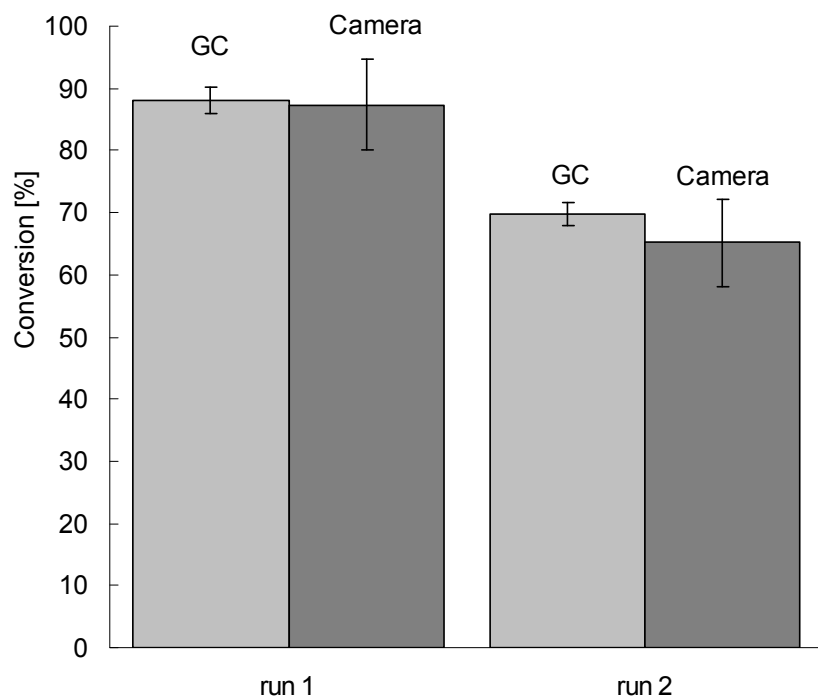


**Fig. A4.** The hydrogenation of 3-methyl-1-pentyn-3-ol in a Pd capillary flow device. Comparison of the conversion based on visual analysis of the evolution of H<sub>2</sub> bubble lengths (Camera) and determined by GC-analysis (GC). The applied conditions can be found in Table A1.

#### *Variation of residence-time*

There are two ways to vary the residence time in a continuous tubular reactor to obtain, for example, a concentration vs. time plot ('batch plot')

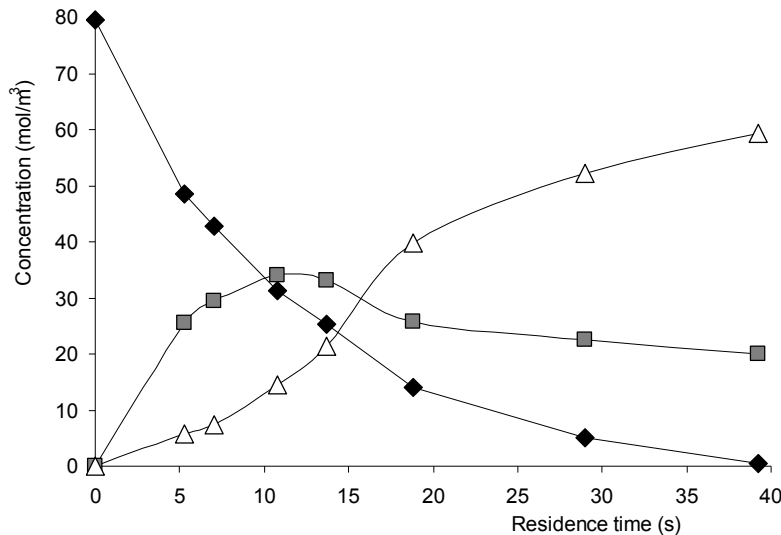
- Increase/decrease the capillary length.
- Increase/decrease the flow rate.

The hydrodynamics inside the reactor does not change when the reactor length is varied (unless the H<sub>2</sub> bubbles are completely consumed). If the second option is selected to vary residence times, the ratio of gas and liquid flow needs to be kept constant in order to keep the ratio of reactant to catalyst amount constant. However, the stagnant liquid film layer thickness at the wall increases with increasing bubble velocity [2]. This affects the mass transfer to the wall, of both the gas and liquid reactants.

Two examples of the hydrogenation of 3-methyl-1-pentyn-3-ol with two different Pd loadings at several residence times (by changing flow rate) at constant liquid holdups (0.1) are presented in Fig. A5. Note that the Pd crystallite size is also different for both examples. For the experiment at low flow rate the reaction process is slightly limited ( $Ca \sim 0.2$ ) in the alkyne transfer (Fig. A5a) and for the high flow rate experiment the rate is limited in both alkyne and H<sub>2</sub> transfer (Fig. A5b). Thus, increasing mass transfer limitations in alkyne reduces the

maximum yield of the desired intermediate product (alkene) as the latter will also suffer from the same resistance and has more chance to react further, all in agreement with theory [3].

**(a)** – ‘small’ Pd crystallite size, slight mass transfer limitations in alkyne



**(b)** – ‘big’ Pd crystallite size –mass transfer limited in alkyne and H<sub>2</sub>

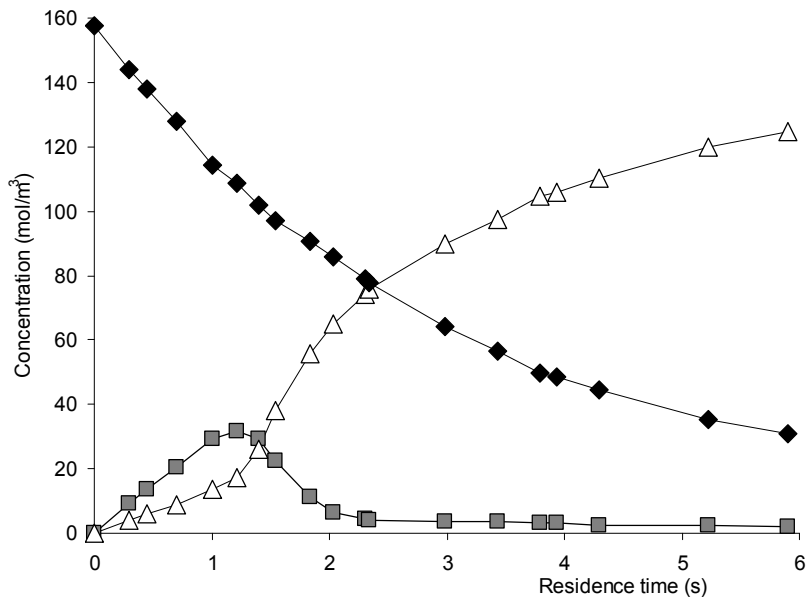


**Fig. A5.** Two ‘batch’ plots (concentration vs. residence time) obtained in a capillary varying flow rates at constant gas and liquid flow rates ( $u_G/u_L = 10$ ) for the hydrogenation of 3-methyl-1-pentyn-3-ol. (a) ‘small’ average Pd crystallite size (0.02 wt%, average Pd crystallite size  $< 2$  nm). Conditions: 1.1 bar H<sub>2</sub>, 26°C,  $C_{Y,0} = 80$  mol m<sup>-3</sup>. (b) ‘big’ average Pd crystallite size (5.7 wt%, average Pd crystallite size  $\sim 5$  nm). Conditions: 1.1 bar H<sub>2</sub>, 25°C,  $C_{Y,0} = 160$  mol m<sup>-3</sup>. ♦ = 3-methyl-1-pentyn-3-ol, □ = 3-methyl-1-penten-3-ol, △ = 3-methyl-3-pentanol. The lines are a guide for the eyes.

### *Structure sensitivity*

To draw proper conclusions about a possible size effect in catalysis, catalyst preparation (pretreatment, precursor ligands, calcination, activation etc.) and support should be taken into consideration because modifications of chemical and structural properties can affect performance. Hydrogenation is generally known as a structure insensitive reaction type. However, one of the exceptions to this ‘rule’ is the hydrogenation of terminal alkynes, which is *structure sensitive*. There is a general consensus that smaller Pd crystallites are less active [4, 5]. This is shown in Fig. A6, where under kinetically controlled conditions the *TOF* is higher for the larger Pd crystallite size. Altering the catalyst amount resulted in a change in Pd crystallite size which influences the activity and selectivity behavior. The observations agree with the fact that smaller crystallites are more electron deficient (less occupied *d*-band) and strongly coordinate with highly unsaturated electron-rich compounds (*i.e.*, alkynes) thereby reducing its intrinsic activity. In agreement with these observations are activity measurements for large crystallites ( $\sim 18$  nm) that showed *TOFs* up to  $15\text{ s}^{-1}$ ; under kinetic conditions these *TOFs* could even have been higher because they were affected by external mass transfer limitations. Semi-batch experiments with Pd on ACM monoliths also showed that the *TOF* decreases with a decreasing Pd crystallite size (not shown).

Size effects are basically structure effects since the relative amount of active sites governs the performance rather than the actual size of the crystallite. The *d*-band width of edge sites is narrower due to the lower coordination to fellow surface metal atoms (coordinatively unsaturated). The lower coordination results in a smaller *d*-band width. The smaller *d*-band width is compensated by an upshift of the *d*-band center towards the Fermi level of Pd since it is the only way to maintain the number of *d*-electrons. The electrons are thus higher in energy and concentrated closer to the Fermi level which renders them more available for bonding. Then, according to the *d*-band model of reactivity, adsorbates will bind more strongly [6].

### *Activation energy and selectivity*

The apparent activation energy ( $E_a$ ) for the 0.066 wt% Pd catalyst was  $42 \pm 3\text{ kJ mol}^{-1}$ , determined at low temperatures (*i.e.*, between 0 and  $30^\circ\text{C}$ ). The  $E_a$  was measured at low conversion levels (< 10%), under steady state conditions using increasing and decreasing temperatures and corrected for the  $\text{H}_2$  concentrations. The obtained  $E_a$  value is similar to other  $E_a$  values from literature, measured under kinetic control, of Pd-catalyzed alkyne hydrogenations which are typically  $30\text{-}50\text{ kJ mol}^{-1}$  [7, 8]. Selectivity towards the intermediate

alkene slightly increased with increasing temperature from 96 to 98% for the hydrogenation performed between 0 and 30°C. Above 30°C,  $E_a$  started to decrease due to diffusional limitations inside the  $\gamma$ -Al<sub>2</sub>O<sub>3</sub> support.

Smaller crystallites (with relatively more edge sites) were intrinsically less selective than larger crystallites (with relatively more plane sites) in the hydrogenation of 2-methyl-3-butene-2-ol. This was shown by Crespo-Quesado and co-workers: the active sites for selective alkyne hydrogenation are the plane sites (e.g., Pd(111), Pd(100)) [9] and the relative number of these sites increase with increasing crystallite size. The edge sites were identified as the active sites for over-hydrogenation to the alkane, presumably because of increased adsorption strength of the alkene. However, no effect of crystallite size on selectivity was observed for the two Pd catalysts shown in Fig. A6: the steady state selectivity of these two Pd catalysts was the same (~ 97%).

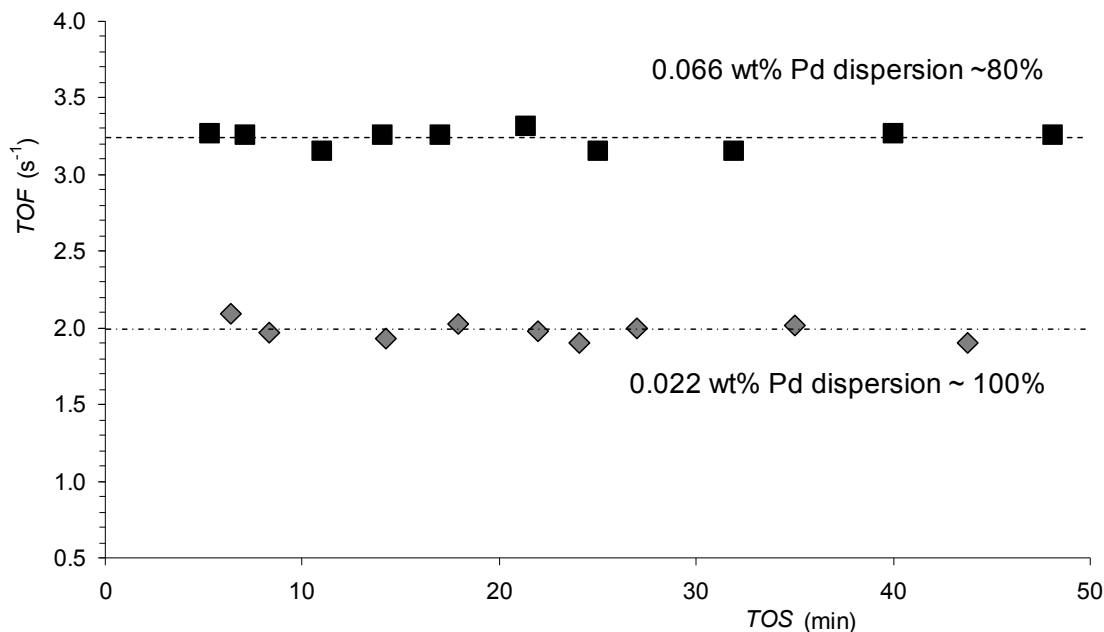


**Fig A6.** Steady state TOF vs. TOS at two different Pd loadings and crystallite sizes under kinetic control showing the structure sensitivity of the hydrogenation of 3-methyl-1-pentyn-3-ol. Conditions: 1.1 bar H<sub>2</sub>,  $C_{Y,0} = 360 \text{ mol m}^{-3}$ ,  $u_G/u_L = 10$ , 27°C,  $X_Y \sim 5\%$ .

#### Maximum yield of intermediate (alkene)

Under kinetic control at low initial concentration of alkynes (< 50 mol m<sup>-3</sup>) and similar Pd dispersion, the maximum yield observed in several different batch studies of the hydrogenation of 3-methyl-1-pentyn-3-ol in ethanol, including my own study in the monolithic stirrer reactor, with monometallic Pd catalysts supported on several SiO<sub>2</sub> and  $\gamma$ -Al<sub>2</sub>O<sub>3</sub> supports with different dispersions was 78–81% [10-11]. Hence,  $Y_{\max}$  was not

dependent on the type of support. Moreover, in the capillary set-up I could perfectly determine  $Y_{\max}$  (Fig. 4.4 Chapter 4) which was equal to  $Y_{\max}$  obtained in the semi-batch reactor; this result confirms that the capillary was operated in plug-flow as was explained in Chapter 4.

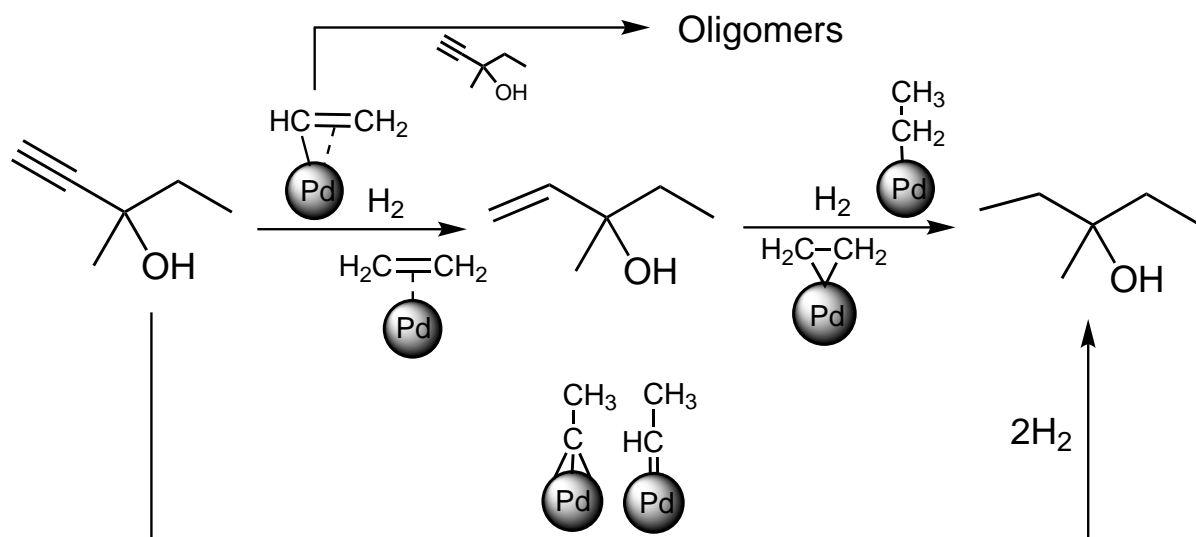
To achieve a high maximum yield of the intermediate alkene ( $Y_{\max}$ ) one should operate under conditions that assure the absence of alkyne mass transfer limitations (high concentration of alkyne) and/or operate under  $H_2$  limited conditions (low concentration of  $H_2$ ). A high concentration in alkyne reduces the possibility of the alkene to adsorb and further react to alkane, since the alkyne adsorbs much stronger than the alkene and acts like a poison for the over-hydrogenation to alkane. Alkyne adsorption is always more favorable than the adsorption of alkenes due to the  $C\equiv C$  bond. Increasing the  $H_2$  concentration (increasing  $H_2$  pressure) increases the rate of reaction since this reaction is generally first order in  $H_2$  (second addition of H atom is rate limiting), and, as a consequence, the possibility of alkyne limitations and thus over-hydrogenation which decreases  $Y_{\max}$ . Furthermore, the formation of the unselective  $Pd\beta$ -hydride phase is induced (as will be discussed in more detail later on). On the other hand, if also the hydrogen transport is limited this lowers its surface concentration and reduces the chance of overhydrogenation.

Alternately, bimetallic catalysts (*e.g.*,  $PdAg$  or  $PdCu$ ) can be applied to increase  $Y_{\max}$  by decreasing the adsorption of the alkene or by increasing the activation barrier for hydrogenation to alkane and decreasing the activation barrier for desorption of alkene [6]. Moreover, the ability to form  $Pd\beta$ -hydride is suppressed in bimetallic  $Pd$  catalysts.

#### *Mechanism of alkyne hydrogenation*

The reaction scheme for the hydrogenation of an alkyne is typically seen as a consecutive one where the hydrogen addition follows a Horiuti-Polanyi mechanism [13]. However, a very small amount of alkane is always observed at the start of an experiment and is explained by the direct hydrogenation of alkyne to alkane [14] (Scheme A1). The direct hydrogenation of alkyne to alkane is proposed to proceed via multiple bonded surface intermediates (*e.g.*, alkylidyne:  $Pd\equiv C-CH_3$ , alkylidene:  $Pd=CH-CH_3$ ) [14]. It should be noted that the adsorption of terminal alkynes is sterically less demanding than that of their corresponding alkenes due to the ability of the former to adsorb perpendicular (end-on). The formation of oligomers (C-C coupling) from 3-methyl-1-pentyn-3-ol was not observed at the applied conditions. The propensity for oligomerization *inversely* scales with the strength of alkyne adsorption (which

is high for Pd), decreases with increasing H<sub>2</sub> pressure and decreases with increasing carbon chain length [7, 15, 16].



**Scheme A1.** The hydrogenation of 3-methyl-1-pentyn-3-ol with the direct route to 3-methyl-3-pentanol and the formation of oligomers, with the most probable surface intermediates indicated. Note that the direct route towards the alkane can also be promoted by the availability of highly energetic bulk H from the Pd  $\beta$ -hydride phase.

The selectivity to alkene vs. TOS is presented in Fig. A7 for different treatments prior to the hydrogenation of 3-methyl-1-pentyn-3-ol. A less selective non-steady-state induction period is observed which is dependent on the pre-treatment of the Pd catalyst. During this induction period part of the high chemical potential (chemically less stable) alkyne molecules are fractionated into carbon. This was corroborated by fact that the mass balance was not fully closed during this induction period (not shown). The fractionated carbon can penetrate into the Pd lattice structure and form a subsurface Pd-C phase as will be discussed below. Reduction (12 h, 1 ml(STP) min<sup>-1</sup> at 1.1 bar H<sub>2</sub>) at RT induces the formation of the Pd  $\beta$ -hydride phase which is catalytically less selective. This phase is formed to a much lesser extent in the absence of pre-reduction and at reduction (12 h, 1 ml(STP) min<sup>-1</sup> at 1.1 bar H<sub>2</sub>) at 80°C (Pd  $\beta$ -hydride formation is exothermic). Without intermediate treatment between experiments (12 h) no decrease in selectivity is observed showing that this newly formed phase is stable at RT in air. Note that high steady state selectivities (~ 98.5%) are obtained under the conditions applied in Fig. A7 (high C<sub>Y,0</sub>) since the reaction is mass transfer limited in H<sub>2</sub>. The induction period of lower selectivity was also observed in semi-batch monolithic stirrer experiments (not shown).

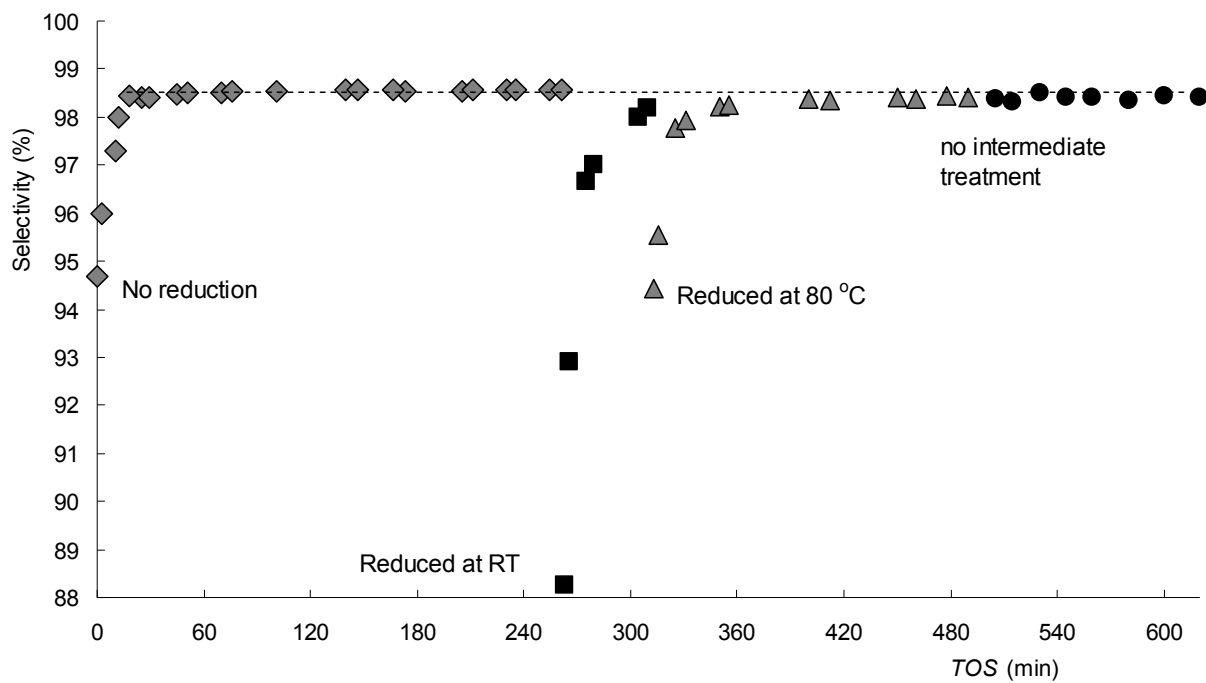


**Fig. A7.** Selectivity to alkene vs. time on stream (*TOS*) for the hydrogenation of 3-methyl-1-pentyn-3-ol showing the induction period for different treatments (indicated in the graph) prior to hydrogenation. Conditions: 1.1 bar H<sub>2</sub>, 25°C,  $C_{Y,0} = 530 \text{ mol m}^{-3}$ , 0.1 wt% Pd,  $X_Y = \text{constant at } 15\%$ .

#### *Formation of Pd hydride and Pd-C phases*

Recently, direct hydrogenation of alkyne to alkane is being investigated by several research groups and is attributed to the formation of an unselective Pd  $\beta$ -hydride phase which contains highly reactive bulk and subsurface hydrogen species [17]. In contrast, increased selective hydrogenation proceeds over a (subsurface) Pd-C phase. This Pd-C phase is formed during the first contact with alkyne species which undergo fragmentation followed by dissolution of carbon into the Pd lattice, and decouples energetic bulk hydrogen from the surface. C-C dissociation mainly takes place at defective sites and is a slow process on Pd since it only proceeds after C-H bond breaking [15]. These defective sites are likely poisoned by the formation of this carbide phase, also inducing an increase in selectivity (remember that the same sites were identified to be responsible for overhydrogenation of alkene to alkane [9]). Furthermore, the presence of Pd-C induces selectivity by destabilizing the adsorbed alkene (weakening the adsorption energy of alkene) and by suppressing the formation of alkylidene and alkylidyne intermediate species (which are intermediates for the formation of alkane, see Scheme A1). Note, that this Pd-C phase is not formed when a Pd catalyst is contacted with a corresponding alkene species as reactant. The strong affinity of the highly electronegative

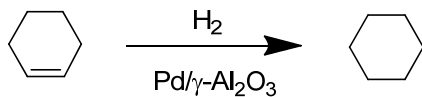
alkyne with the surface is a prerequisite for the fragmentation and formation of (subsurface) Pd-C [16]. Direct hydrogenation is thus dependent on the interplay between the reactant and the intrinsic properties of the Pd catalyst. Note that the modification of the Pd subsurface to a selective Pd-C layer or an unselective  $\beta$ -hydride phase is dependent on the ratio of H<sub>2</sub> to alkyne and Pd crystallite size. The Pd crystallite size governs the extent of  $\beta$ -hydride and Pd-C formation and this affects the intrinsic selectivity. The tendency to form the hydride phase decreases and the tendency to form Pd-C increases, respectively, with decreasing crystallite size [14]. In addition, hydrogen mass transfer limitations can thus induce the formation of a selective Pd-C phase. The metastable Pd-C can to a large extent be transformed to  $\beta$ -PdH under high enough H<sub>2</sub> pressure. The ability to form a  $\beta$ -hydride phase correlates with the over-hydrogenation to alkane. The formation of a Pd-C phase is hampered when the Pd  $\beta$ -hydride phase is already present by thermodynamic requirements and by reduction of step sites (larger Pd crystallites) [16]. In contrast, other researchers have shown that the unselective overhydrogenation can also proceed over Pd-C [18]. They appoint unselective hydrogenation, at high conversions, simply to a decreasing surface coverage of the ‘poisoning’ alkyne (mass transfer limitations in alkyne). Combining the findings of several research groups it is concluded that the formed Pd-C phase is selective as long as there are no alkyne limitations (keep a high surface coverage of the ‘poisoning’ alkyne) and the H<sub>2</sub> pressure should be kept low to avoid the destruction of the Pd-C phase and to keep the rate of hydrogenation low (again to avoid alkyne mass transfer limitations).

To summarize, the selective hydrogenation to alkene is mainly dependent on the surface coverage of the alkyne (a thermodynamic effect) suppressing the hydrogenation of alkene. Furthermore, the ratio of hydrogenation of alkyne to alkane or to alkene is dependent on the interplay of alkyne and H<sub>2</sub> transport and local concentrations, and intrinsic Pd properties (e.g., ability to form Pd  $\beta$ -hydride or Pd-C phases, crystallite size (type of surface sites), and coordination of adsorption). The parameters (indicated as ratios) determining a high selectivity to alkene can be summarized as

$$\frac{\text{Alkyne}}{\text{Pd}} \gg \quad \frac{\text{H}_2}{\text{Alkyne}} \ll \quad \frac{\text{Pd}_{\text{plane}}}{\text{Pd}_{\text{edge}}} \gg$$

### Cyclohexene hydrogenation: determination of kinetic parameters

The hydrogenation of cyclohexene over a Pd/ $\gamma$ -Al<sub>2</sub>O<sub>3</sub> catalyst was studied to determine the kinetic parameters (Scheme A2).



**Scheme A2:** The hydrogenation of cyclohexene to cyclohexane over a  $\gamma$ -Al<sub>2</sub>O<sub>3</sub>-supported Pd catalyst.

#### GC-analysis

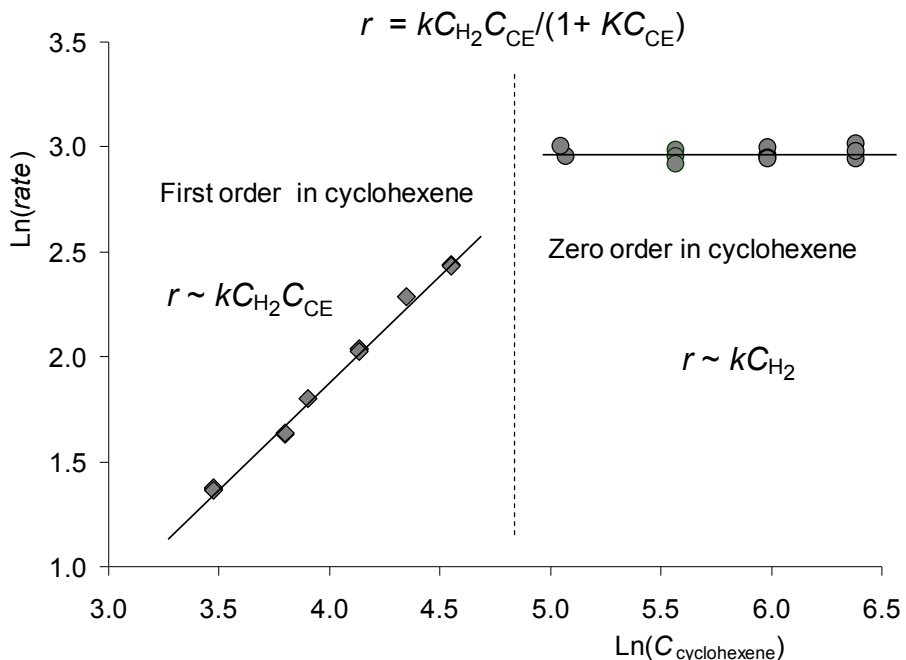
Cyclohexene hydrogenation experiments were analyzed using Varian CP-3380 GC with a Chrompack CP-SIL 8 CB (PBX5) column of 60 m (internal diameter 0.25 mm; injector temperature = 200°C; ramp = 10°C min<sup>-1</sup>; FID temperature = 330°C). Retention times were: 4.5 min (cyclohexene), 4.3 min (cyclohexane), 9.2 min (*n*-decane), and 4.0 min (ethanol).

#### Hydrogenation of cyclohexene

A typical hydrogenation of cyclohexene (Aldrich, used as received) was performed in a 0.2 m capillary with a Pd loading of 2.7 wt%. A hydrogenation experiment with purified cyclohexene, mixing cyclohexene with activated  $\gamma$ -Al<sub>2</sub>O<sub>3</sub> (Aldrich) for 12 h prior to hydrogenation to remove the stabilizer (BHT, 0.01 wt%), was also performed, however, equal results were obtained. The cyclohexene feed concentration was varied from 30 to 600 mol m<sup>-3</sup> in dry ethanol (Aldrich), *n*-decane (Merck) and a mixture of ethanol and water, which allowed us to determine the first-order part and the zero-order part of the Langmuir-Hinshelwood kinetic expression (Fig. A8a). The adsorption constant of cyclohexene was  $K \approx 0.01$  m<sup>3</sup> mol<sup>-1</sup>. The kinetic parameters were obtained at low cyclohexene conversions (< 20%), at intermediate conversion levels (20 to 70%) or at high conversion levels (> 70%). In all cases, the same values were obtained for the kinetic constants, indicating that axial dispersion or back-mixing had no negative impact on the measurement of kinetics. At low temperatures, cyclohexene hydrogenation follows normal Arrhenius behavior, however, at higher temperatures it starts to deviate (inverse Arrhenius behavior) due to thermodynamic limitations (dehydrogenation to benzene) and decreasing H<sub>2</sub> and cyclohexene surface coverage [19]. The apparent activation energy  $E_a$ , determined at low temperatures (< 40°C), was  $34 \pm 2$  kJ mol<sup>-1</sup> for the 2.7 wt% Pd catalyst (Fig. A8b) in a mixture of ethanol/water which was similar to the value determined by Boudart *et al.* [20]. It was found that the

apparent activation energy decreased at temperatures above  $\sim 45^\circ\text{C}$  to a new value of 14 kJ mol $^{-1}$ , indicating that at these hydrogenation temperatures internal diffusion was limiting the rate of reaction.

(a)



(b)

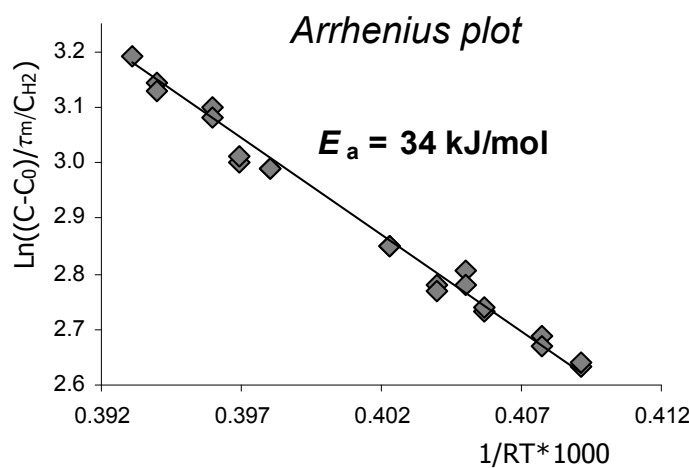


**Fig. A8.** The hydrogenation of cyclohexene in a mixture of ethanol/water in a capillary (2.7 wt% Pd) at 1.1 bar H<sub>2</sub> displaying the logarithmic rate of the hydrogenation of cyclohexene as a function of the logarithmic initial cyclohexene concentration to determine the kinetic parameters: reaction orders, rate constant  $k$ , adsorption constant  $K$  (a), and activation energy  $E_A$  (b). Every data point presented in these graphs is the average of 5 measurements with an interval of 30 min. The activation energy was first measured from high to low temperatures and subsequently from low to high temperatures at low conversion levels (< 10%). The presented data points are averaged from steady state conditions both in Taylor flow conditions and reaction rates (rates determined at the initial deactivation period were excluded). Note that the reaction rates were corrected for the concentration of H<sub>2</sub>: it increases with increasing temperature.

## The hydrogenation of 3-phenyl-propyl-azide: determination of catalyst activity, selectivity, and lifetime for differently prepared reaction mixtures

3-phenyl-propyl-azide **4** was synthesized in several ways (two synthesis routes in different solvents) and subsequently hydrogenated towards amines over a 5.7 wt% Pd catalyst as can be seen in Scheme 4.2, Chapter 4.

### *GC and HPLC analysis*

Concentrations of compounds in the reaction mixture were determined by HPLC (HP1050 with a Machery-Nagel ET 250/4 Nucleosil 120-5-C18 column). In addition, GC analysis (HP6890 with a CP-SIL 5CB-MS column) was used to determine the concentration of **4**. From samples taken prior to hydrogenation the following compounds could be identified by HPLC: the solvent (dry ethanol, toluene or NMP (Aldrich)), 3-phenyl-propyl-azide **4** (14.8 min), 3-phenyl-propanol **1** (3.8 min), 3-phenyl-propyl-mesylate **3** (5.8 min), 3-phenyl-propyl-chloride **2** (16.0 min) and NaN<sub>3</sub> (2.6 min). After hydrogenation, the HPLC chromatograms showed several new peaks. The main new peak (2.1 min) was identified as the primary amine 3-phenyl-propyl-amine **5**, as was verified by purchasing compound **5** (Aldrich) and running it through the HPLC.

### *Side-product determination*

During several hydrogenation runs at least two new peaks appeared in the HPLC diagrams with a retention time of 4.1 min and 4.9 min. The molar weight of a peak with a retention time of 4.9 min was 253 g mol<sup>-1</sup>, as determined by liquid chromatography equipped with a diode array detector and mass spectrometry detector (LC-DAD-MS), which corresponded to the secondary amine di-(3-phenyl-propyl)-amine **5b**, which was formed at high reactant concentrations, high temperature, and longer time-on-stream (TOS). In samples taken from hydrogenation runs in ethanol a third peak was detected, which has a molecular weight of 163 g mol<sup>-1</sup>. It was identified by using LC-DAD-MS as a secondary amine **5c** formed from condensation of **5** with the solvent ethanol. A fourth by-product (retention time = 4.1 min) was detected with a very small peak in the HPLC chromatograms. Most likely, this is a tertiary amine, as it was also found in batch experiments with long reaction times (20 h). Moreover, the conversion of **4** was followed by GC analysis. This analysis was performed by using a HP6890 with a CP-SIL 5CB-MS column.

*Aromatic azide in NMP, ethanol, and toluene: mesylate-derived*

**4** was synthesized by azidation of **3**, derived from **1**, or by azidation of 3-phenyl-propyl-chloride **2**. **3** was synthesized by reacting **1** with methane sulphonyl-chloride (Fluka) in  $\text{CH}_2\text{Cl}_2$  (Aldrich). Aqueous  $\text{NaN}_3$  (Janssen Chimica) reacted with **3** in NMP. NMP is a very polar solvent that dissolves  $\text{NaN}_3$  and that provides some homogeneity. The azidation was performed in a batch reactor at 55°C and in a continuous-flow stainless-steel tubular microreactor at 110°C, and both gave > 95% yield of **4** (Table A2, used as reactant in entry 1 and 2). Alternatively, **3** was dissolved in acetone and contacted with aqueous  $\text{NaN}_3$  at 52°C. The acetone was removed and extra water and diethyl ether were added. Subsequently, a solvent switch to ethanol resulted in a 1.04 wt% solution of **4** in ethanol with as impurities  $\text{NaN}_3$ , **3** (0.04 wt%), **1** (0.03 wt%), diethylether (0.8 wt%), water (0.09 wt%) and acetone (0.13 wt%) (Table A2, entry 3 to 5).

A solution of **4** in toluene was prepared by contacting **3** in toluene and a mixture of ammonium chloride in propanol/water with aqueous  $\text{NaN}_3$  at 82°C. Subsequently, adding toluene resulted in phase separation, the toluene was washed with water and azeotropic distillation resulted in a solution of **4** in toluene (Table A2, entry 6).

*Aromatic azide in ethanol/water: Chloride-derived*

**2** (Aldrich) was used without further purifications and dissolved in ethanol. Azidation was performed by reacting **2** with aqueous  $\text{NaN}_3$  in a continuous-flow steel microreactor at temperatures up to 200°C with up to 100% yield of **4** (Table 2 entry 7 to 9).

*Hydrogenation of aromatic azide*

Two different synthesis routes of 3-phenyl-propyl-azide **4** were applied: via mesylate and chloride intermediates. Several solvents or mixtures of solvents were used. There was a variation of impurities in the reaction mixtures prior to hydrogenation of **4** that could influence reaction rates, selectivity and stability. Moreover, the concentrations of these impurities varied for different batches. Most hydrogenation runs were performed at 24°C and at a  $\text{H}_2$  pressure of 1.1 bar, some runs were conducted at 61°C (see for example Table A2, entry 4). The liquid flow rate was varied from 100 to 300  $\mu\text{l min}^{-1}$ . The  $\text{H}_2$  flow rate was varied between 0 and 830  $\mu\text{l(STP) min}^{-1}$ .

**Table A2**

Summary of the hydrogenation of 3-phenyl-propyl-azide **4** in Pd-capillaries operated in Taylor flow over a 5.7 wt% Pd catalyst at 24°C and 1.1 bar H<sub>2</sub>.

| Entry            | Solvent<br>Reaction mixture<br>concentrations<br>/mmol l <sup>-1</sup>                      | Gas ( <i>u</i> <sub>G</sub> ) and<br>liquid ( <i>u</i> <sub>L</sub> )<br>flowrate<br>/ml min <sup>-1</sup> | Capillary<br>Length ( <i>l</i> <sub>CAP</sub> ) /cm<br>Residence time /s | Selectivity to <b>5</b> /%<br>at conversion of <b>4</b> /% | Pd<br>half-life /min<br><i>TON</i> <sup>[a]</sup> |
|------------------|---|--|--|--|---|
| 1                | NMP <sup>[d]</sup><br>57 <b>4</b> ; 1.0 <b>3</b> ;<br>3 NaN <sub>3</sub>                    | 0.3<br>0.2   | 45<br>11.4   | 100<br>60  | 15 <sup>[g]</sup><br>196                          |
| 2                | NMP <sup>[d]</sup><br>76 <b>4</b> ; 5.3 <b>3</b> ;<br>16 NaN <sub>3</sub>                   | 0.6<br>0.2   | 43<br>6.9  | 100<br>53  | 6 <sup>[g]</sup><br>92                            |
| 3                | EtOH <sup>[e]</sup><br>52 <b>4</b> ; 1.5 <b>3</b> ;<br>4 NaN <sub>3</sub>                   | 0.6<br>0.25  | 49<br>7.4  | 100<br>96  | 60<br>1815  |
| 4 <sup>[b]</sup> | EtOH <sup>[e]</sup><br>52 <b>4</b> ; 1.5 <b>3</b> ;<br>4 NaN <sub>3</sub>                   | 0.8<br>0.25  | 49<br>5.9  | 86<br>100  | 140<br>2911                                       |
| 5                | EtOH <sup>[e]</sup><br>94 <b>4</b> ; 3.0 <b>3</b> ;<br>7 NaN <sub>3</sub>                   | 0.6<br>0.25  | 49<br>7.4  | 97<br>74   | 33<br>1089  |
| 6                | Toluene <sup>[e]</sup><br>54 <b>4</b> ; 4.9 <b>3</b> ;<br>4 NaN <sub>3</sub>                | 0.6<br>0.25  | 49<br>7.4  | 96<br>87   | 15<br>298   |
| 7                | EtOH/H <sub>2</sub> O <sup>[f]</sup><br>56 <b>4</b> ; 11 <b>2</b> ;<br>139 NaN <sub>3</sub> | 0.6<br>0.1   | 29<br>5.6  | 82<br>70   | >205<br>>>2000 <sup>[c]</sup>                     |
| 8                | EtOH/H <sub>2</sub> O <sup>[f]</sup><br>154 <b>4</b> ; 5 <b>2</b> ;<br>55 NaN <sub>3</sub>  | 0.8<br>0.15  | 21<br>2.9  | 95<br>32   | 123<br>3816                                       |
| 9                | EtOH/H <sub>2</sub> O <sup>[f]</sup><br>154 <b>4</b> ; 5 <b>2</b> ;<br>55 NaN <sub>3</sub>  | 0.4<br>0.3   | 14<br>2.6  | 87<br>13   | 70<br>2697  |

<sup>[a]</sup> *TON* = turnover number (moles of **4** converted per mol Pd) when conversion of **4** has dropped to 50% of the initial value; <sup>[b]</sup> 61°C; <sup>[c]</sup> only 4% drop in selectivity after 205 min; <sup>[d]</sup>> 10% H<sub>2</sub>O; <sup>[e]</sup>< 5% H<sub>2</sub>O; <sup>[f]</sup> volume ratio EtOH:H<sub>2</sub>O = 6:4; <sup>[g]</sup> leaching of Pd occurred.

*Comparing hydrogenation of mesylate-derived and chloride-derived aromatic azide*

Fig. A9 displays two typical hydrogenation runs with a mesylate and chloride-derived **4** as reactant, Table A2 entries 3 and 8, respectively.

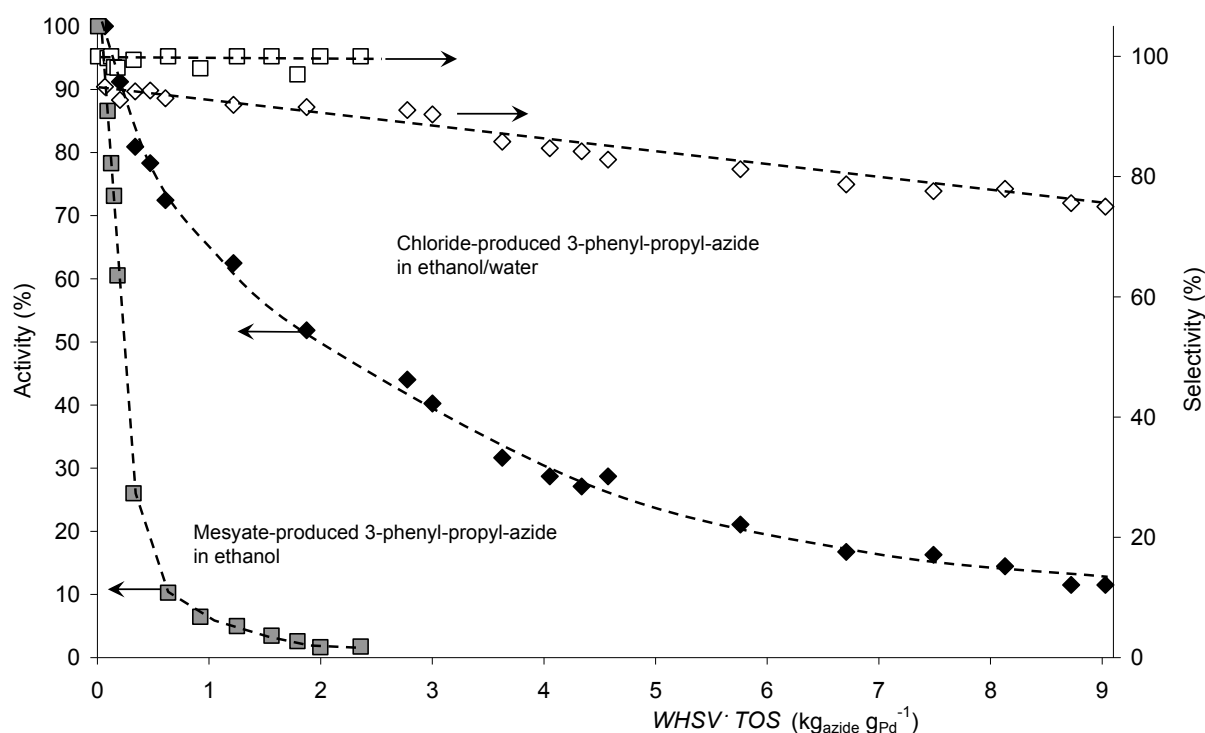


**Fig. A9.** Normalized activity (% initial conversion) and selectivity (towards 3-phenyl-propyl-amine **5**) vs. *WHSV*·*TOS* (weight hourly space velocity multiplied by time on stream,  $\text{kg}_{\text{azide}} \text{g}_{\text{Pd}}^{-1}$ ) profiles for 3-phenyl-propyl-azide **4** hydrogenation in a capillary flow device (5.7 wt% Pd). Key: black lozenges: 2.85 wt% chloride-produced 3-phenyl-propyl-azide **4** in ethanol/water:  $u_G/u_L = 5.5$ ,  $u_L = 150 \mu\text{l min}^{-1}$ ,  $l_{\text{CAP}} = 0.21 \text{ m}$ ,  $T = 24^\circ\text{C}$ ,  $X_{\text{azide}} = 32\%$ ; Open lozenges: selectivity to 3-phenyl-propyl-amine **5**; Grey squares: 1.04 wt% mesylate-produced 3-phenyl-propyl-azide in ethanol:  $u_G/u_L = 2.4$ ,  $u_L = 250 \mu\text{l min}^{-1}$ ,  $l_{\text{CAP}} = 0.49 \text{ m}$ ,  $T = 24^\circ\text{C}$ ,  $X_{\text{azide}} = 96\%$ . Open squares: selectivity to 3-phenyl-propyl-amine **5**. The squares correspond to entry 3 and the lozenges to entry 8 in Table A2. The dashed lines are guidance for the eyes.

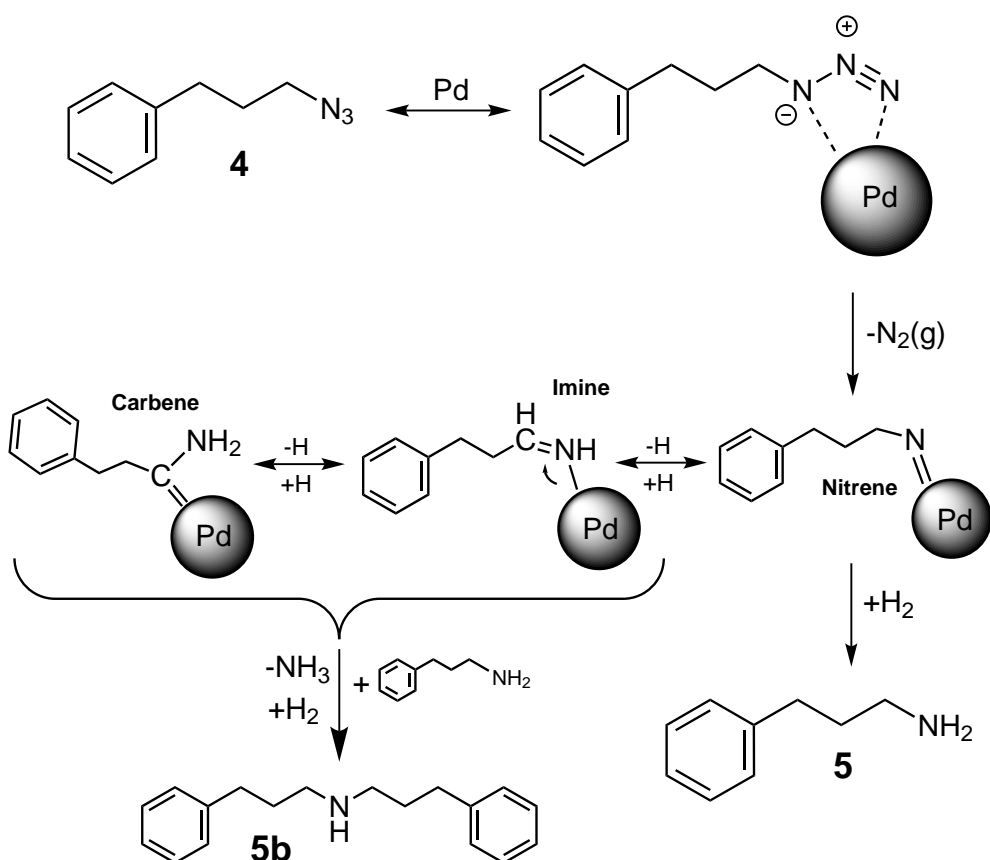
For the hydrogenation of the mesylate-derived 3-phenyl-propyl-azide **4**, > 99% (entry 3 Table A2) selectivity was observed for all *WHSV*·*TOS* (weight hourly space velocity multiplied by time on stream,  $\text{kg}_{\text{azide}} \text{g}_{\text{Pd}}^{-1}$ ). However, the catalyst activity decreased to < 2% at *WHSV*·*TOS* > 2  $\text{kg}_{\text{azide}} \text{g}_{\text{Pd}}^{-1}$ . The cyclohexene spiking experiments presented in Fig. 4.5 (Chapter 4) and an EDX-analysis (detection of sulfur on the catalyst surface with was not detected prior to hydrogenation) of the spent catalyst clearly pointed towards irreversible poisoning by mesylate species. The initially higher selectivity (~ 99%) compared with the chloride-derived

route (~ 95%), can be caused by the different solvents (ethanol and ethanol/water) used in these experiments. Note that these selectivities were compared at different conversion levels: at 100 and 32%. The condensation mechanism of secondary amines is generally explained by a nucleophilic attack of a primary amine on an electropositive carbon of a surface intermediate (*e.g.*, an imine) [21]. This reaction can be interpreted as a consecutive reaction that occurs only appreciably at a high extent of the first reaction. I rarely used residence times in excess of that needed for the first reaction to occur, and I did not observe increased formation of the secondary amine **5b** at high conversion levels. This suggests that the condensation reaction of an intermediate with **5** is slow compared to the hydrogenation reaction of the intermediate to **5**. Also, this finding indicates that selectivity can to a large extent be controlled by carefully choosing the reaction time. The condensation reaction was favoured by high amounts of *N*-containing compounds on the catalyst, and the experimental finding that more of **5b** was formed at high concentration of **4** supports this mechanism.

Typical for a consecutive reaction (*i.e.*, bimolecular reaction) is the initially *S*-shaped curve of **5b** formation. Normally, an increase in conversion would mean a decrease in selectivity to the primary amine **5** because of this consecutive condensation reaction to the secondary amine **5b**. Hence, one would expect that an experiment at higher conversion would result in a lower selectivity to **5** (the ‘intermediate’ product in a consecutive reaction **4**  $\rightarrow$  **5**  $\rightarrow$  **5b**). However, the opposite is observed, and can therefore be caused by the use of different solvents, as explained previously. Furthermore, the selectivity in the mesylate-derived **4** is initially ~ 100% and remained constant during deactivation down to conversion levels of ~ 5%. The same reasoning is applied in the following paragraph. The temperature influence for the mesylate-produced azide in ethanol was studied (entry 4 Table A2). The results indicated that the activation energy for the condensation reaction was higher than the activation energy for the hydrogenation to **5**. Such higher activation energies, relative to hydrogenation, have been reported for azide hydrogenation using Pd/C catalyst [22].

The hydrogenation of the chloride-derived **4** (entry 8 Table A2) resulted in a strongly increased catalyst lifetime compared to the hydrogenation of the mesylate-derived **4**. The catalyst activity was ~ 12% of its initial value after a *WHSV*·*TOS* of 9 kg<sub>azide</sub> g<sub>Pd</sub><sup>-1</sup>. However, the selectivity to 3-phenyl-propyl-amine **5** decreased from 95 to 75% with increasing *TOS* (Fig. A9). I speculate that the decrease in azide conversion activity and selectivity (towards the primary amine **5**) with increasing *TOS* are caused by a ligand effect (electronic effect) induced by strongly adsorbed chloride ions, an impurity from the preparation step prior to azide hydrogenation. This was corroborated by EDX analysis that showed no chloride on the

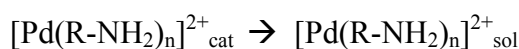
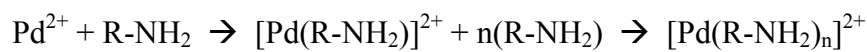
fresh catalyst, however, chloride was present on the spent catalyst. These changes of the surface and/or electron density of Pd could alter the adsorption strength, *e.g.*, stronger adsorption of primary amines (product inhibition) would decrease the azide conversion rate and increase the residence time of primary amines on the surface of the catalyst thereby inducing the condensation reaction to **5b**. Furthermore, the adsorption mode of the intermediate species could transform from nitrene into imine and finally carbene species for at least part of the surface intermediates; with the former surface species mainly forming primary amines since the  $\alpha$ -carbon is saturated and the latter, with an unsaturated  $\alpha$ -carbon, being more susceptible to nucleophilic attack by primary amines and thus forming **5b**. A mechanistic scheme of the hydrogenation of **4** with surface intermediates and probable products is presented in Scheme A3.



**Scheme A3.** Proposed mechanistic scheme of the hydrogenation of 3-phenyl-propyl-azide **4** to 3-phenyl-propyl-amine **5** and di-(3-phenyl-propyl)-amine **5b**. Initially, only nitrene species will be formed due to interaction with the Pd surface which is accompanied by the release of  $N_2$ . The transformation of nitrene into imine or carbene species proceeds via addition and abstraction of H via the Pd surface. The surface intermediates are shown with their most probable reaction products: nitrene species will mainly form **5** and the carbene and imine species are more susceptible to a nucleophilic attack of a primary amine forming **5b**. Note that the carbene and imine intermediates can also form **5** (not indicated for clarity).

### Surface rearrangement, agglomeration and leaching

The reaction mixture did not contain any leached Pd (ICP-OES) and no loss of Pd was detected when comparing the fresh and spent catalyst (AAS). CO-chemisorption measurements (with a Pd:CO ratio = 1:1) indicated that there was a small decrease in dispersion, however these measurements were close to the detection limit and within the experimental error (0.14 to 0.12  $\text{m}^2 \text{ g}_{\text{cap}}^{-1}$ ). Furthermore, several larger Pd crystallites ( $\sim 14 \text{ nm}$ ) were visible in TEM images of the spent Pd catalyst (mild sintering governed by complex formation), *i.e.*, extensive surface rearrangement had taken place (see Fig. A10 for TEM images of fresh and spent Pd catalysts). Fluid-mediated Pd rearrangement involves the formation of organometallic complexes. The strong adsorption on Pd and complex formation with Pd of *N*-containing compounds makes Pd susceptible to surface rearrangement. The strong Pd-adsorbate bonds of the *N*-containing compounds weaken the Pd-Pd and Pd- $\gamma$ -Al<sub>2</sub>O<sub>3</sub> interactions and facilitate Pd agglomeration [23]. Note, that the Pd crystallites were still well-dispersed on the  $\gamma$ -Al<sub>2</sub>O<sub>3</sub> support after hydrogenation. An accompanying effect of this surface restructuring/agglomeration could be that the hydrogenation to **5** is suppressed and facilitation of the condensation reaction to **5b** due to transformation of the type and amount of active sites (second possible mechanism of decreasing selectivity to **5** with increasing *TOS*). Surface restructuring and the increase of the Pd crystallites size with *TOS* could increase the amount of larger ensembles (geometric effect) which in its turn facilitate condensation reactions [24]. In contrast, if the capillary was operated without H<sub>2</sub>, the effluent was yellowish in color, indicating that strong Pd-organic complexes had formed which leached into the solution. Furthermore, a small amount of **4** was converted ( $\sim 3\%$ ) during experiments without H<sub>2</sub>. After operation without H<sub>2</sub> the catalyst was completely deactivated and no activity was observed when H<sub>2</sub> flow was switched on again. This showed that irreversible deactivation had occurred by means of leaching. In post-mortem analysis, no Pd could be detected with AAS analysis. Such formation of metal-organic complexes is fairly common and often easily visible by color changes. In the absence of H<sub>2</sub>, Pd leaching into the reaction mixture can be caused by oxidation of Pd and subsequent complex formation [25]



The availability of H<sub>2</sub> at the Pd surface thus protects the Pd from major soluble complex formation with compounds in the reaction mixture by keeping the Pd crystallites in a well-reduced metallic state.

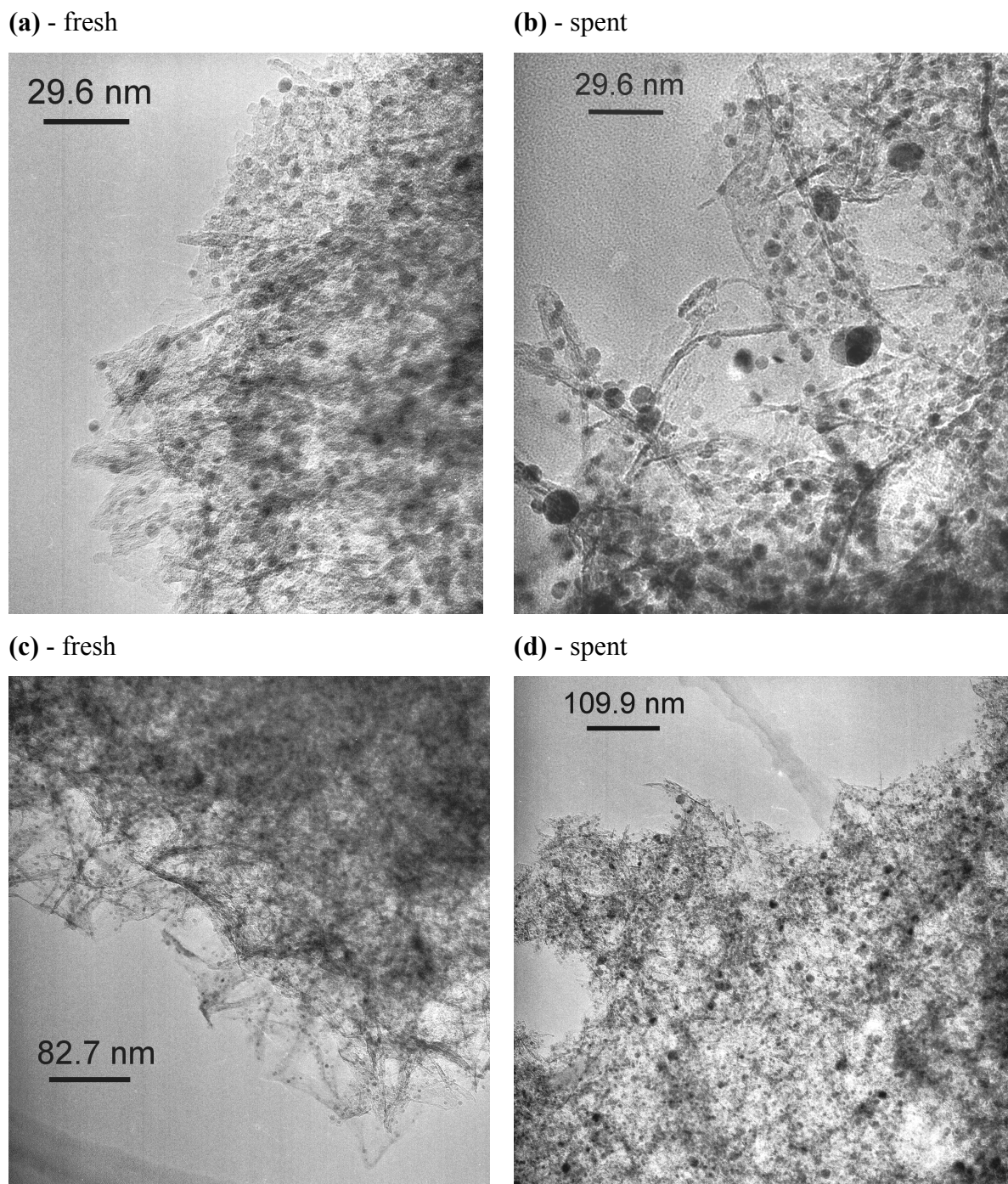


**Fig. A10.** TEM images of a fresh and spent  $\gamma$ -Al<sub>2</sub>O<sub>3</sub>-supported Pd catalyst. (a, c) Fresh catalyst. (b, d) Spent catalyst used in the hydrogenation of chloride-derived **5** (Table A2, entry 8). Note the different scales of images (c) and (d).

### Strong adsorption of amines

The desorption of strongly attached surface species during regeneration of the catalyst in flowing  $\text{N}_2$  (g) at 200°C for 2 h caused an increase in activity from 12 to 36% in a subsequent experiment (not shown). The desorbing species were probably strongly adsorbed amines (e.g., primary, secondary, tertiary amines). Amines are well-known for their poisoning activity [26].

The amount of **5** present in the capillary flow device had a clear influence on the deactivation rate: more amine led to faster deactivation. Amines are gradually poisoning the catalyst as can be seen in Fig. A11 where the activity vs.  $\text{WHSV} \cdot \text{TOS}$  for two different conversion levels are compared. This conclusion is corroborated by the observation that the reaction order was 1 (which indicates low occupancy of azides adsorbed on the catalyst) in the investigated concentration range.

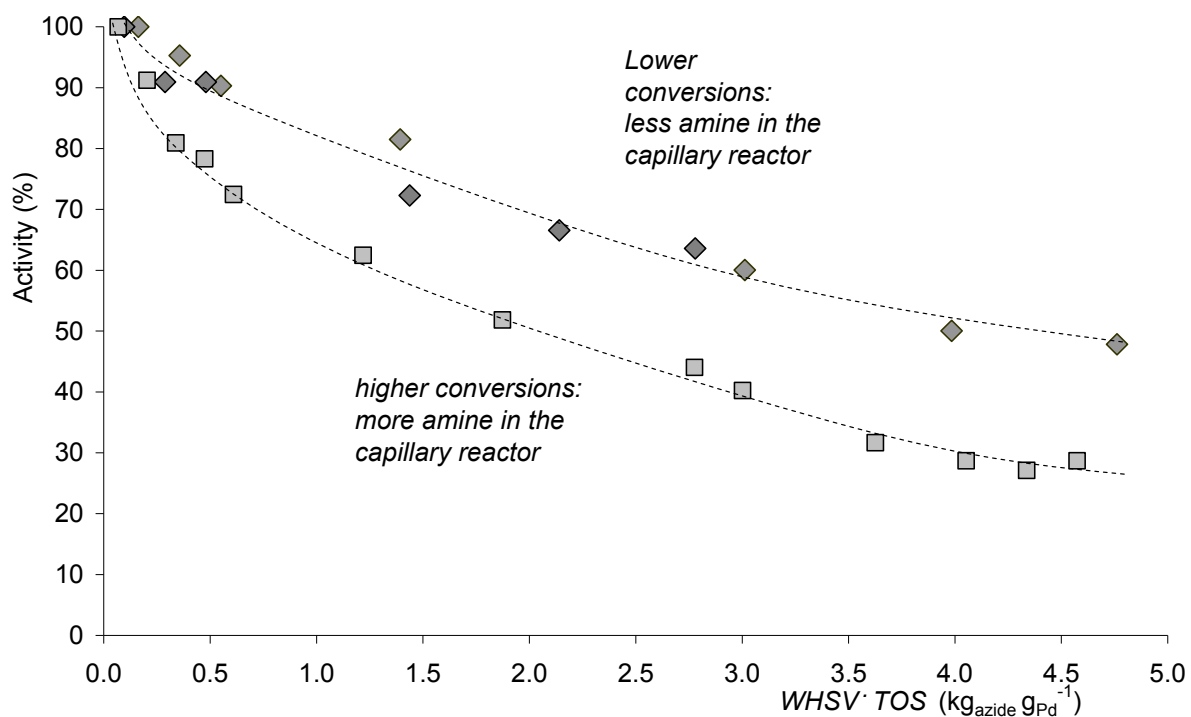


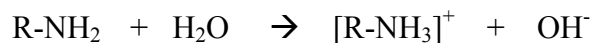
**Fig. A11.** Activity vs.  $\text{WHSV} \cdot \text{TOS}$  measured at two different conversion levels. Low conversion ( $X_{\text{azide},0} = 13\%$ :  $\blacklozenge$ ) and high conversion ( $X_{\text{azide},0} = 32\%$ :  $\square$ ) were obtained at different gas to liquid flow ratios:  $u_G/u_L = 1.3$  ( $u_L = 300 \mu\text{l min}^{-1}$ ,  $l_{\text{CAP}} = 0.14 \text{ m}$ ,  $T = 24^\circ\text{C}$ , 2.79 wt% **4**) and  $u_G/u_L = 5.5$  ( $u_L = 150 \mu\text{l min}^{-1}$ ,  $l_{\text{CAP}} = 0.21 \text{ m}$ ,  $T = 23^\circ\text{C}$  2.85 wt% **4**), respectively. The dashed lines are an indication of the trends.

So, the poisoning by amines (or strongly bound chloride species) contributed strongly to deactivation, then these deactivated Pd sites might no longer play a role in the hydrogenation

reaction to **5**, but they could participate in condensation to **5b**, explaining the increased condensation at longer *TOS*. This is a third speculated mechanism for the decrease in selectivity to **5** with increasing *TOS*. Deactivation of the metallic Pd sites then impedes the hydrogenation but leaves condensation to **5b** mostly untouched.

The toxicity of a substance is a combination of adsorbent strength and size. The effective toxicity of a catalyst poison usually increases with its size, because the larger a molecule is, the larger the amount of Pd sites it can cover. A possible explanation for the deactivation in the hydrogenation of the chloride-produced **4** is a high Pd surface coverage with strongly bound secondary and/or tertiary amines. Although it was not proven beyond any doubt that there is tertiary amine formation, there are indications that the second unknown peak in the HPLC diagram is the tertiary amine. Tertiary amines are a catalyst poison for Pt-type catalysts, which completely deactivated the catalyst in hydrogenations of nitriles [27, 28].

Note that water is present in the reaction mixture of chloride-derived **4**. Water is known to eliminate the catalyst toxicity of amines by shielding the free electron pair by converting it to a non-toxic shielded quaternary ammonium cation structure



The water should make the amines non-toxic, but as seen with the cyclohexene spiking experiments not all the activity is retained after removal of the amine (Fig. 4.5 Chapter 4). However, the high amounts of water in the reaction mixture of chloride-derived **4** (Table A2) causes a decrease of the initial rate of hydrogenation because of the lower H<sub>2</sub> solubility. The solubility of H<sub>2</sub> is ~ 4 times lower in water than in ethanol. Furthermore, the solubility of aromatic amines is lower in water than in ethanol resulting in higher amine coverage on the Pd surface in a mixture containing more water.

Spiking NaN<sub>3</sub> separately to the hydrogenation of cyclohexene showed that NaN<sub>3</sub> lowers the activity because of competitive adsorption, but it did not cause irreversible catalyst deactivation (See Fig. 4.5 Chapter 4). Spiking with the primary amine during cyclohexene hydrogenation did result in competitive adsorption reducing the rate of reaction: after switching off the spiking only 75% of the activity was recovered. This indicated that some irreversible deactivation had occurred even though water was present, probably because of Pd agglomeration or very strong amine adsorption. Care should be applied when extrapolating these results obtained with cyclohexene to the hydrogenation of **4**. Koubek *et al.* observed that a catalyst could be completely deactivated for one hydrogenation but remain active for

another one. Their systems were a nitrile hydrogenation and a cyclohexene hydrogenation over an activated carbon supported Pd catalyst [28], very similar to our systems. Their Pd catalyst was completely deactivated for the nitrile hydrogenation but still active for the cyclohexene hydrogenation.

Summarizing, catalyst characterization showed that a combination of the above speculated mechanisms governing the loss of performance are at play. In most cases the deactivation was irreversible and caused by several simultaneously operating mechanisms. The mechanisms of the irreversible deactivation was complex-formation and weakening of the Pd support bond, leading to Pd agglomeration and in extreme cases to Pd leaching (when the solvent is NMP or without H<sub>2</sub>). A reversible deactivation mechanism (when applying a proper regeneration step in between consecutive hydrogenations) was poisoning of the Pd catalyst by amines due to competitive adsorption.

## Bibliography

- [1] M.T. Kreutzer, F. Kapteijn, J.A. Moulijn, C.R. Kleijn, J.J. Heiszwolf, *AIChE J.* 9 (2005) 2428.
- [2] (a) M.T. Kreutzer, P. Du, J.J. Heiszwolf, F. Kapteijn, J.A. Moulijn, *Chem. Eng. Sci.* 56 (2001) 6015. (b) J.J. Heiszwolf, M.T. Kreutzer, M.G. van den Eijnden, F. Kapteijn, J.A. Moulijn, *Catal. Today* 69 (2001) 51.
- [3] F. Kapteijn, J.A. Moulijn, Laboratory testing of solid catalysts. In: *Handbook of heterogeneous catalysis*, edited by G. Ertl, H. Knözinger, F. Schüth, J. Weitkamp, Weinheim, Wiley-VCH, 2008, 2019.
- [4] J.P. Boitiaux, J. Cosyns, S. Vasudevan, *Appl. Catal.* 6 (1983) 41.
- [5] A. Sárkány, A.H. Weiss, L. Guczi, *J. Catal.* 98 (1986) 550.
- [6] (a) F. Studt, F. Abild-Pedersen, T. Bligaard, R.Z. Sørensen, C.H. Christensen, J.K. Nørskov, *Angew. Chem. Int. Ed.* 47 (2008) 9299. (b) J.K. Nørskov, T. Bligaard, J. Rossmeisl, C.H. Christensen, *Nature Chem.* 1 (2009) 37.
- [7] G.C. Bond, Fundamental and applied catalysis: Metal-catalyzed reactions of hydrocarbons, Springer US, 2005, 395.
- [8] (a) H. Molero, B.F. Bartlett, W.T. Tysoe, *J. Catal.* 181 (1999) 49. (b) M. Crespo-Quesada, M. Grasemann, N. Semagina, A. Renken, L. Kiwi-Minsker, *Catal. Today* 147 (2009) 247. (c) E. Joannet, C. Horny, L. Kiwi-Minsker, A. Renken, *Chem. Eng. Sci.* 57 (2002) 3453.
- [9] M. Crespo-Quesada, A. Yarulin, M. Jin, Y. Xia, L. Kiwi-Minsker, *JACS* 133 (2011) 12787.
- [10] M.P.R. Spee, J. Boersma, M.D. Meijer, M.Q. Slagt, G. van Koten, J.W. Geus, *J. Org. Chem.* 66 (2001) 1647.
- [11] T.A. Nijhuis, G. van Koten, F. Kapteijn, J.A. Moulijn, *Catal. Today* 79 (2003) 315.
- [12] M.A. Leon, T.A. Nijhuis, J. van der Schaaf, J.C. Schouten, *Chem. Eng. Sci.* 73 (2012) 412.
- [13] J. Horiuti, M. Polanyi, *Trans. Faraday Soc.* 30 (1934) 1164.
- [14] a) Á. Molnár, A. Sárkány, M. Varga, *J. Mol. Catal. A* 173 (2001) 185; b) A. Borodziński, G.C. Bond, *Cat. Rev. Sci Eng.* 50 (2008) 379.

- [15] B. Bridier, N. López, J. Pérez-Ramírez, Dalton Trans. 39 (2010) 8412.
- [16] M. García-Mota, B. Bridier, J. Pérez-Ramírez, N. López, J. Catal. 273 (2010) 92.
- [17] D. Teschner, E. Vass, M. Havecker, S. Zafeiratos, P. Schnorch, H. Sauer, A. Knop-Gericke, R. Schloegl, M. Chamam, A. Woottsch, A.S. Canning, J.J. Gamman, S.D. Jackson, J. McGregor, L.F. Gladden, J. Catal. 242 (2006) 26.
- [18] M.W. Tew, M. Janousch, T. Huthwelker, J.A. van Bokhoven, J. Catal. 283 (2011) 45.
- [19] R.M. Rioux, H. Song, P. Yang, G.A. Somorjai, Platinum nanoclusters' size and surface structure sensitivity of catalytic reactions, In: Metal nanoclusters in catalysis and materials science: The issue of size control, Edited by: B. Corain, G. Schmid, N. Toshima, Elsevier B.V., Amsterdam, 2008, 163.
- [20] E.E. Gonzo, M. Boudart, J. Catal. 52 (1978) 462.
- [21] P.Y. Bruice, Organic Chemistry, 4<sup>th</sup> ed., Pearson Prentice Hall, Upper Saddle River, 2004.
- [22] I. An, H. Seong, K.H. Ahn, Bull. Korean Chem. Soc. 25 (2004) 420.
- [23] W.M.H. Sachtler, Angewandte Chem. 80 (1968) 155.
- [24] D.J. Ostgard, E. Degussa, Spec. Chem. 28 (2008) 28.
- [25] R. Fisera, M. Kralik, J. Annus, V. Kratky, M. Zecca, M. Hronec, Collect. Czech. Chem. Commun. 62 (1997) 1763.
- [26] a) J.M. Devereux, K.R. Payne, E.R.A. Peeling, J. Chem. Soc. (1957) 2845; b) E.B. Maxted, M.S. Biggs, J. Chem. Soc. (1957) 3844; c) E.R.A. Peeling, D.K. Shipley, Chem. Ind. (1958) 362; d) H. Greenfield, J. Org. Chem. 29 (1964) 3082; e) P. Albers, J. Pietsch, S.F. Parker, J. Mol. Catal. A: Chemical 173 (2001) 275.
- [27] P.N. Rylander, J.G. Kaplan, US Patent 3,117,162, 1965.
- [28] J. Koubek, J. Pasek, J. Horyna, Chem. Prum. 56 (1981) 349.



# 5

## Catalyst performance changes induced by palladium phase transformation in the hydrogenation of benzonitrile

---

The influence of hydrogen pressure on the performance of a  $\gamma$ -alumina-supported palladium catalyst was studied for the multiphase selective hydrogenation of benzonitrile to benzylamine and byproducts. Semibatch experiments of benzonitrile hydrogenation in 2-propanol were performed with hydrogen pressures between 2.5 and 30 bar, at a constant temperature of 80°C. The intrinsic property of palladium to absorb hydrogen into its lattice structure has a strong influence on activity and selectivity. The transformation to stable palladium  $\beta$ -hydride above a threshold hydrogen pressure of 10 bar induces a persistent change in turnover frequency and byproduct selectivity. The turnover frequency increases from 0.32  $\text{s}^{-1}$  to a maximum of 0.75  $\text{s}^{-1}$  at this threshold pressure and decreases to 0.25  $\text{s}^{-1}$  with increasing hydrogen pressure. The palladium  $\beta$ -hydride phase suppresses the hydrogenolysis to toluene changing the selectivity from 6.5% to 2.0% and increasing the selectivity of the condensation to dibenzylamine from 1.6% to 2.7%, attributed to modified electronic interactions between catalyst and substrates. The selectivity to the desired product benzylamine is always high and increases with hydrogen pressure from 92.7% to 95.3%. The palladium catalyst state is mainly determined by the activation or operational hydrogen pressure, whichever was the highest, if the activation pressure was above 10 bar.

---

This Chapter and Appendix B are published in J. Catal. 274 (2010) 176.

## Introduction

The topic of this Chapter is structure sensitivity of palladium (Pd) catalysts, in particular the effect of structural changes due to Pd  $\beta$ -hydride ( $\beta$ -PdH) formation at higher hydrogen pressure ( $pH_2$ ). The reaction of interest is the hydrogenation of aromatic nitriles to the corresponding primary amines. Here, controlling the selectivity is a crucial demand and insight in the reaction mechanisms of desired and undesired reactions is very valuable.

Primary aromatic amines are important chemical compounds that have found widespread applications as chemical and pharmaceutical intermediates, solvents, paints, herbicides and synthetic textiles. A major route to produce primary aromatic amines is the heterogeneously catalyzed hydrogenation of aromatic nitriles [1-4]. However, during the hydrogenation of aromatic nitriles towards the aromatic amines several byproducts are usually formed, resulting in a loss of yield [1-4]. Activity and selectivity are mainly determined by the amount, type and mobility of surface intermediates and transition states which are controlled by the catalyst. Further it should be noted that the reactant concentration, type of solvent(s), reaction conditions and additives (*e.g.*, ammonia) also play an important role [2-4].

A scheme that depicts the reaction pathways during the hydrogenation of benzonitrile (BN) to benzylamine (BA) and the main byproducts can be found in Fig. 5.1. The reaction network is a combination of hydrogenation, condensation and hydrogenolysis reactions that can yield BA, *N*-benzylidenebenzylamine (DBI), dibenzylamine (DBA), and toluene (TOL), respectively. Ammonia ( $NH_3$ ) is formed during condensation reactions and hydrogenolysis to TOL. The reaction mechanism is generally explained by the premise of benzylideneimine (BI) or other semi-hydrogenated intermediates and a surface aminal (*i.e.*,  $\alpha$ -aminodialkylamine (BIBA)).

Several authors contributed to the elucidation of the reaction mechanism since the beginning of the 20th century by proposing that imines ( $-CH=NH$ ), Schiff bases ( $-C=N-C$ ), and enamines ( $-N-C=C-$ ) are the intermediates in the formation of primary, secondary, and tertiary amines [5-10]. However, this mechanism is based on a number of unproven assumptions that are corroborated only by indirect evidence: *e.g.*, Schiff bases have been identified in solution, imines were detected on the catalyst surface by IR spectroscopy and the absence of tertiary amine formation in the hydrogenation of BN has been observed. The inability to detect imine and enamine intermediates is attributed to their high reactivity.

From several BN hydrogenation studies and my own findings it can be concluded that the use of supported Pd catalysts results in high activity and, more important, a high selectivity towards BA compared to other platinum-group metal catalysts [11-15]. An overview of different catalysts used under many different conditions in the heterogeneous hydrogenation of BN is shown in Table 5.1. From my own investigations it appeared that a commercially available  $\gamma$ -Al<sub>2</sub>O<sub>3</sub>-supported Pd catalyst exhibited the highest selectivity and was therefore used in this study.

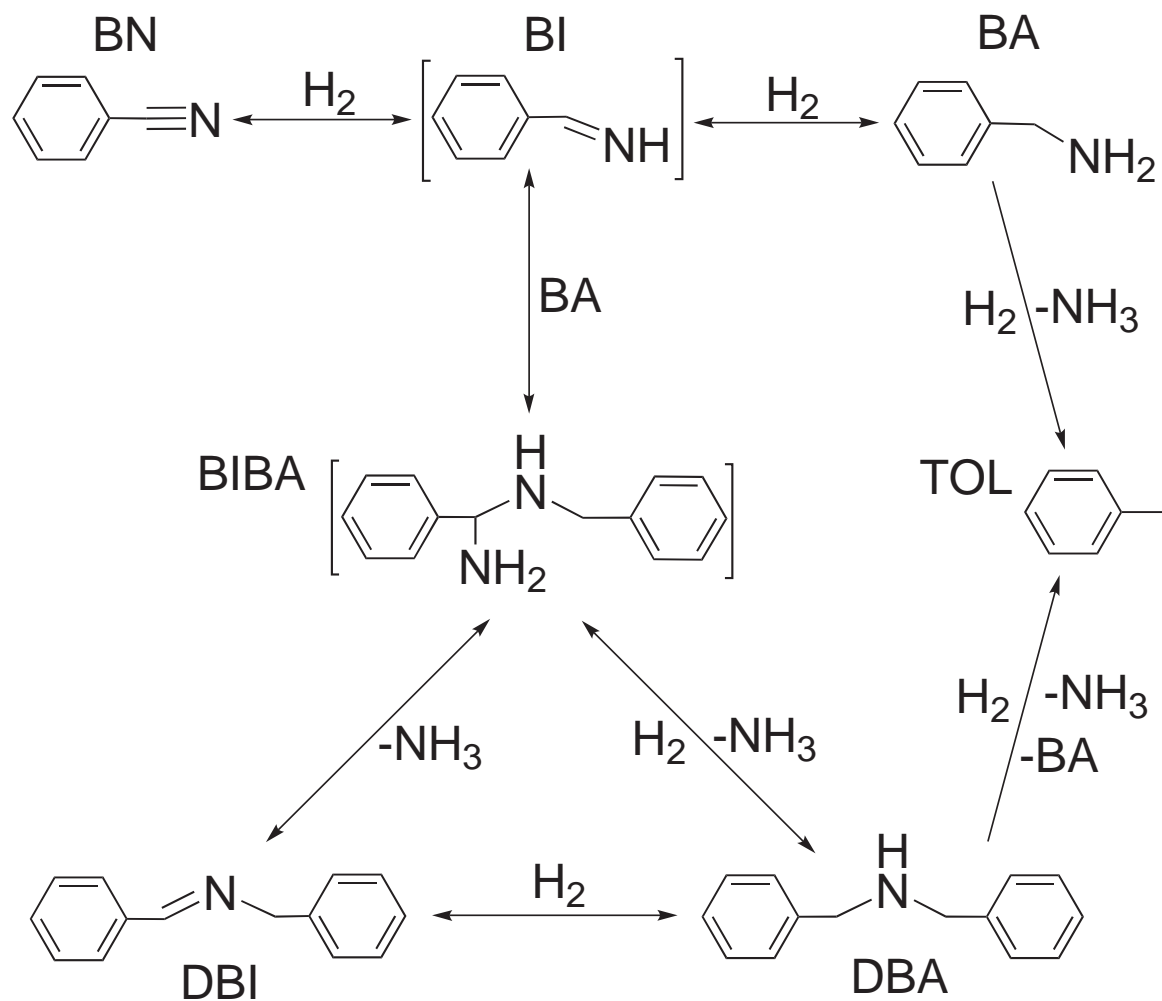


**Fig. 5.1.** Reaction pathways to different products in the hydrogenation of benzonitrile (BN): hydrogenation of BN to benzylamine (BA) via benzylideneimine (BI). Condensation of BA and BI via  $\alpha$ -aminodialkylamine (BIBA) and *N*-benzylidenebenzylamine (DBI) to dibenzylamine (DBA). Hydrogenolysis to toluene (TOL) of DBA and BA. Direct hydrogenolysis of BIBA to DBA is possible. Species in between straight brackets are surface intermediates never detected in solution.

While studying the effect of  $pH_2$  on activity and selectivity over this catalyst I encountered an unexpected anomaly: I found a maximum in catalyst activity with increasing  $pH_2$ , accompanied by a sudden selectivity shift in by-products leading to an increased yield of BA. Literature does not report such an effect during Pd-catalyzed nitrile hydrogenation. However, in the hydrogenation and hydrogenolysis of hydroxymatairesinol by using a Pd catalyst Bernas *et al.* also encountered a negative dependence on the  $pH_2$  above a certain pressure [16]. They explained this effect as a result of competitive adsorption of  $H_2$  and the reactant. Dubois *et al.* studied the hydrogenation combined with hydrogenolysis of 2-methyl-2-nitropropane over a supported Pd catalyst and also encountered an activity maximum; they gave two possible explanations for this effect: more favorable  $H_2$  adsorption for the same active sites or the formation of a new, less active, Pd phase [17]. Skakunova *et al.* hypothesized that the negative order effect in the hydrogenolysis of propane over a Pd-Ru catalyst was caused by competitive adsorption of  $H_2$  [18]. In general, hydrogenolysis reactions catalyzed by different supported metals are structure sensitive and often have a negative reaction order with respect to  $pH_2$  up to -2.5 [19-23].

I demonstrate that in BN hydrogenation, competitive adsorption between  $H_2$  and BN is not the explanation of the anomaly observed. Rather, my hypothesis is that structural changes of the Pd crystallites at higher  $pH_2$  explain the observed phenomena. A well-known property of Pd, discovered by Graham in 1866 [24] that differentiates it from all other metals, is the easy absorption of atomic hydrogen in large quantities in the Pd lattice, occupying the octahedral interstices of its face-centered-cubic Pd lattice structure already at ambient temperature and low  $pH_2$  [25-27]. Upon absorbing large amounts of hydrogen the lattice Pd expands (lattice constant increases) when the solid solution phase ( $\alpha$ -PdH) transforms into the  $\beta$ -PdH phase [28]. Moreover, the character of the electronic  $d$ -band of Pd changes [27, 29-32]. The amount of H absorbed within the Pd lattice depends on the  $H_2$  concentration in the liquid, temperature, Pd crystallite size, surface topography, support interactions, precursor, and pretreatment steps [28, 33, 34]. Structural changes upon transformation to  $\beta$ -PdH can have a profound effect on the adsorption strength, type, and amount of surface species and thus on the activity and selectivity [28, 35-42].

**Table 5.1**

Hydrogenation of BN: comparison of BN conversion ( $X_{\text{BN}}$ ), BA selectivity ( $S_{\text{BA}}$ ), and yield ( $Y_{\text{BA}}$ ) of different catalysts used in literature and this study

| Catalyst (wt%)  | $C_{\text{BN},0}$ (mol/m <sup>3</sup> ), Solvent | $T$ (°C), $p\text{H}_2$ (bar) | $X_{\text{BN}}$ (%) | $S_{\text{BA}}$ (%) | $Y_{\text{BA}}$ (%) | Remarks   |
|---|--|-------------------------------|---------------------|---------------------|---------------------|---|
| 5% Pt/C   | -  | 100, 35                       | 100                 | 0                   | 0                   | Pt: major product was [9, 43]                                 |
| 5% Pd/C   |  | 100, 35                       | 100                 | 19                  | 19                  | DBA   |
| 5% Rh/C   |  | 100, 83                       | 100                 | 22                  | 22                  | $\text{H}_2\text{O}$ added                                    |
| 5% Rh/C   | 2000, octane                                     | 25, 3.5                       | 100                 | 0                   | 0                   | Mostly DBA was [11-13]  |
| 5% Pt/C   |  |                               | 100                 | 0                   | 0                   | formed for Pt and Rh  |
| 5% Pd/C   | 2000, ethanol                                    |                               | 100                 | 63                  | 63                  | catalysts   |
| 5% Pd/C   | 2000, benzene                                    |                               | 100                 | 59                  | 59                  | Adding diethylamine   |
| 5% Pd/C   | 2000, hexane                                     |                               | 100                 | 34                  | 34                  | increased $Y_{\text{BA}}$ to 100% for Pd catalysts            |
| 5% Ru/C   |  | 25, 3.5                       | 0                   | 0                   | 0                   |   |
| 5% Pt/C   |  | 25, 3.5                       | 38                  | 7                   | 18                  |   |
| 5% Pd/C   |  | 25, 69                        | 100                 | 55                  | 55                  |   |
| 5% Rh/C   |  |                               | 100                 | 33                  | 33                  |   |
| Raney Ni  | 485, methanol                                    | 100, 40                       | n.a.                | 76                  | n.a.                | Several solvents used [44]                                    |
| 2.5% Ir/Al <sub>2</sub> O <sub>3</sub>                  | 220, ethanol                                     | 100, 21                       | 20                  | n.a.                | n.a.                | $Y_{\text{DBA}}$ was 36% [45]                                 |
| 65% Ni/SiO <sub>2</sub> /Al <sub>2</sub> O <sub>3</sub> | 1000, methanol                                   | 120, 10                       | n.a.                | n.a.                | 96                  | NH <sub>3</sub> /CH <sub>3</sub> OH added [46]                |
| 60% Ni/SiO <sub>2</sub>                                 |  |                               | n.a.                | n.a.                | 99                  | BN/NH <sub>3</sub> ratio = 2                                  |
| Pd/pyridyl  | -  | 100, 36                       | 100                 | 26                  | 26                  | 32% TOL, 37% DBI [47]   |
| Raney Ni  | 1530, methanol                                   | 75, 40                        | 88                  | 91                  | 80                  | [48, 49]  |
| Ni-Mo (CH <sub>2</sub> O)                               | 485, methanol                                    | 105, 41                       | 100                 | 99                  | 99                  | 32% NH <sub>3</sub> /H <sub>2</sub> O added                   |
| 10% Pd/C  | 323,   | 30, 6                         | 95                  | 95                  | 90                  | NaH <sub>2</sub> PO <sub>4</sub> ·H <sub>2</sub> O added [15] |
| 5% Pd/C   | H <sub>2</sub> O/di-chloro-                      |                               | 95                  | 94                  | 89                  |   |
| 5% Pd/TiO <sub>2</sub>                                  | methane  |                               | 71                  | 94                  | 67                  |   |
| 5% Pd/Al <sub>2</sub> O <sub>3</sub>                    |  |                               | 48                  | 90                  | 43                  |   |
| Ni catalyst   | n.a., ethanol                                    | 20, n.a.                      | 100                 | 61                  | 61                  | Thiophene added [50]  |
| 5% Pd/C   | 780,   | 85, 15                        | 100                 | 21                  | 21                  | Higher $S_{\text{BA}}$ achieved [14]                          |
| 5% Pd/BaSO <sub>4</sub>                                 | 2-propanol                                       |                               | 100                 | 24                  | 24                  | by adding NH <sub>3</sub>                                     |
| 5% Pd/CaCO <sub>3</sub>                                 |  |                               | 100                 | 15                  | 15                  |   |
| 5% Pt/C   |  |                               | 100                 | 10                  | 10                  |   |
| Raney Ni  |  |                               | 100                 | 36                  | 36                  |   |
| Pt-Sn/nylon   | 192, ethanol                                     | 60, n.a.                      | 100                 | 15                  | 15                  | Mostly DBA formed [51]  |
| Raney Ni  | -  | 100, 15                       | 100                 | 95                  | 95                  | Continuous [52]   |
| 1% Pt/Al <sub>2</sub> O <sub>3</sub>                    |  | 100, 7                        | 99                  | 0.1                 | 0.1                 | countercurrent reactor NH <sub>3</sub> accumulation           |
| Sn-Pt/SiO <sub>2</sub>                                  | 390, ethanol                                     | 60, 4                         | 100                 | 20                  | 20                  | DBA major product [53]  |
| 0.1% Pd/SiO <sub>2</sub>                                | -  | 145, 8.3                      | 46                  | n.a.                | n.a.                | Only $X_{\text{BN}}$ reported [54]                            |
| 5% Pt/Al <sub>2</sub> O <sub>3</sub>                    | 1000, methanol                                   | 100, 15                       | 40                  | 40                  | 16                  | Dibenzylhydrazine [55]  |
| 5% Pd/Al <sub>2</sub> O <sub>3</sub>                    | 520,   | 80, 10                        | 50                  | 94*                 | 86 <sup>#</sup>     | Main product for Pt/C was DBA [This study]                    |
| 5% Pt/C   | 2-propanol                                       |                               | 50                  | 1*                  | 3 <sup>#</sup>      |   |
| 5% Pd/C   |  |                               | 50                  | 81*                 | 61 <sup>#</sup>     | Main byproduct for Pd   |
| 5% Pd/BaCO <sub>3</sub>                                 |  |                               | 50                  | 34*                 | 29 <sup>#</sup>     | catalysts was TOL   |
| 5% Ru/Al <sub>2</sub> O <sub>3</sub>                    |  |                               | 0                   | 0*                  | 0 <sup>#</sup>      |   |

n.a. – not available.

\*  $S_{\text{BA}}$  at  $X_{\text{BN}} = 50\%$ , #  $Y_{\text{BA}}$  is maximum BA yield.

In this Chapter, I demonstrate that in  $\gamma$ -Al<sub>2</sub>O<sub>3</sub>-supported Pd-catalyzed BN hydrogenation, the  $\beta$ -PdH phase formed at increased  $pH_2$  is responsible for the activity and selectivity effects. The  $pH_2$  and the entailing transformation to  $\beta$ -PdH have a profound influence on the catalyst performance. Further, based on analysis of the reaction mixture and characterization of fresh, activated, and spent catalysts, a scheme of the reaction mechanism, modes of surface adsorption, and surface intermediates are presented. By combining *d*-band theory with simple frontier molecular orbital theory I explain the observed results.

## Experimental

### *Catalyst and materials*

Unless explicitly stated, the experiments were carried out using reduced 5 wt% Pd/ $\gamma$ -Al<sub>2</sub>O<sub>3</sub> supplied by Alfa Aesar. Blank experiments were performed using  $\gamma$ -Al<sub>2</sub>O<sub>3</sub> (99.97%) supplied by Alfa Aesar. The catalysts I studied and reported in Table 5.1 (5 wt% Pd/C, 5 wt% Pd/BaCO<sub>3</sub>, 5 wt% Ru/ $\gamma$ -Al<sub>2</sub>O<sub>3</sub>, and 5 wt% Pt/C) were supplied by Aldrich. The other chemicals used in this study were purchased from commercial suppliers and used as received (benzonitrile, 99%, Alfa Aesar; benzylamine, > 98%, Alfa Aesar; dibenzylamine, 98%, Alfa Aesar; toluene, 99.5%, J.T. Baker; n-isopropylbenzylamine, 98%, Alfa Aesar; 2-propanol, 99%, Aldrich;  $\gamma$ -Al<sub>2</sub>O<sub>3</sub>, 99.97%, Alfa Aesar).

### *Selective hydrogenation*

The selective hydrogenation experiments were carried out in a semi-batch mode in a high pressure stainless steel autoclave (Medimex Reactor CH-2543) equipped with baffles and a gas-induced stirrer. H<sub>2</sub> was continuously fed to the reactor to maintain a constant  $pH_2$  (units: bar gauge further denoted as bar) during a hydrogenation experiment. I used a simple alcoholic solvent, 2-propanol, and did not use any additives.

In a typical experiment, 0.5 g of 5 wt% Pd/ $\gamma$ -Al<sub>2</sub>O<sub>3</sub> was added to 150 ml of 2-propanol and subsequently fed to the reactor. Different cycles of pressurizing and depressurizing with N<sub>2</sub> were applied to remove the air from the reactor. Before a hydrogenation experiment the catalyst was activated in the reactor in 2-propanol under elevated  $pH_2$  at 80°C for 1 h. The typical  $pH_2$  used for the standard activation was 10 bar. In addition, the influence of activation  $pH_2$  (2.5, 10, and 30 bar) on the catalyst performance was also investigated.

After the *in-situ* activation of the catalyst the reactor was brought to reaction conditions, *i.e.*, a temperature ( $T$ ) of 80°C and a  $pH_2$  between 2 and 30 bar for the different experiments. Then 50 ml 2-propanol, adding up to 200 ml, with the appropriate amount of BN, was added to the autoclave via a pressurized filling tank ( $C_{BN,0} = 520 \text{ mol/m}^3$ ). Reference hydrogenation experiments ( $C_{BN,0} = 520 \text{ mol/m}^3$ ,  $T = 80^\circ\text{C}$ ,  $pH_2 = 10$  and 30 bar) were performed with a  $\gamma$ - $\text{Al}_2\text{O}_3$  support without Pd to determine its effect in the hydrogenation of BN. In addition, hydrogenation experiments with BA or mixtures of BN and BA were performed to get more insight into the mechanism. My results reported in Table 1 (bottom row) were achieved under standard hydrogenation conditions ( $C_{BN,0} = 520 \text{ mol/m}^3$ ,  $T = 80^\circ\text{C}$ ,  $pH_2 = 10 \text{ bar}$ ). The supported Pd catalysts were activated for 1 h *in-situ* in 2-propanol at 10 bar and 80°C. The supported Pt and Ru catalysts were activated under  $\text{H}_2$  flow for 1 h *ex-situ* at 350 and 250°C, respectively.

Samples were withdrawn from the reaction mixture during an experiment at selected intervals to determine the composition of the reaction mixture. Analysis of these samples was performed on a Chrompack CP9001 gas chromatograph equipped with FID detector and Chrompack LiquidSampler 9050 autosampler fitted with a CP-SIL 8 column (length 50 m, 0.25 mm ID). The GC temperature program ranged from 50 to 250°C at a heating rate of 10°C/min. The standard deviation of the integrated peaks of the FID signal of the GC was 2.5%. GC data were checked by comparing  $\text{H}_2$  flow into the autoclave with  $\text{H}_2$  consumption as calculated on the basis of reaction stoichiometry and GC data. A normalized carbon balance was performed to check if no other compounds were formed undetected by the GC analysis. The standard deviation of the balance was 2.4%.

No external and internal mass transfer limitations disguised the rate data. See Appendix B for the details about the measurements and calculations performed.

Density functional theory (DFT) calculations were executed using the Becke 3LYP 6-31G\* method to calculate the frontier orbital energy levels of the highest occupied molecular orbital (HOMO) and of the lowest unoccupied molecular orbital (LUMO) of the compounds involved in the hydrogenation of BN. These calculations were performed with the Spartan'06 package version 1.1.2 (a program for quantum mechanical computations) from Wavefunction, Inc. (<http://www.wavefun.com>).

The initial rate of consumption of BN is given as a turnover frequency (*TOF*) and is defined as

$$TOF = \frac{r}{\rho_{\text{sites}} \cdot a_{\text{Pd}}} \cdot N_A \quad (5.1)$$

where  $a_{\text{Pd}}$  is the specific surface area of Pd in  $\text{m}^2/\text{g}_{\text{Pd}}$  as determined by CO chemisorption,  $\rho_{\text{sites}}$  is the site density of Pd in sites/ $\text{m}^2$ ,  $N_A$  is the number of Avogadro in  $\text{mol}^{-1}$ , and  $r$  is the catalyst activity in  $\text{mol}/\text{g}_{\text{Pd}}/\text{s}$  and is defined as

$$r = \frac{dC_{\text{BN}}}{dt} \cdot \frac{1}{W_{\text{Pd}}} \quad (5.2)$$

where  $W_{\text{Pd}}$  is the concentration of Pd per liquid volume in  $\text{g}_{\text{Pd}}/\text{m}_{\text{liquid}}^3$ . The activity is determined at the start of a hydrogenation experiment up to 10% conversion of BN.

The conversion of BN ( $X_{\text{BN}}$ ) is defined as

$$X_{\text{BN}} = \left( \frac{C_{\text{BN},0} - C_{\text{BN}}}{C_{\text{BN},0}} \right) \cdot 100\% \quad (5.3)$$

where  $C_{\text{BN},0}$  is the concentration of BN at  $t = 0$  min and  $C_{\text{BN}}$  the actual concentration of BN both in  $\text{mol}/\text{m}^3$ .

All selectivities ( $S_x$ ) are determined at  $X_{\text{BN}} = 50\%$  and are defined as

$$S_x = \left( \frac{C_x}{C_{\text{BN},0} - C_{\text{BN}}} \right) \cdot 100\% \quad (5.4)$$

where x is BA, TOL, or DBA.

The desired product is BA and the maximum yield of BA ( $Y_{BA}$ ) is defined as

$$Y_{BA} = \left( \frac{C_{BA,max}}{C_{BN,0}} \right) \cdot 100\% \quad (5.5)$$

where  $C_{BA,max}$  is the maximum concentration of BA in mol/m<sup>3</sup>. The TOL yield ( $Y_{TOL}$ ) and DBA yield ( $Y_{DBA}$ ) are defined as  $C_{TOL}/C_{BN,0}$  and  $C_{DBA}/C_{BN,0}$ , respectively, at  $Y_{BA}$ .

#### *Catalyst characterization*

Prior to analysis, fresh, activated, and spent catalyst samples were dried in an oven (static air atmosphere) that was ramped up from room temperature at a heating rate of 0.5°C/min up to 120°C, followed by 2 h at 120°C.

The catalysts were characterized using X-ray powder diffraction (XRD), temperature programmed reduction (TPR), thermal gravimetric analysis (TGA), inductively coupled plasma optical emission spectroscopy (ICP-OES), diffuse reflectance infrared Fourier transform (DRIFT), CO chemisorption, N<sub>2</sub> physisorption, transmission electron microscopy (TEM), and laser diffraction. The details regarding these characterization methods can be found in Appendix B. Note that XRD and TPR were only performed on fresh and activated Pd/γ-Al<sub>2</sub>O<sub>3</sub> catalysts. To obtain references for TGA and DRIFT, fresh Pd/γ-Al<sub>2</sub>O<sub>3</sub> catalyst was soaked in pure BN, BA, and DBA for 4 h at 80°C. Fresh Pd/γ-Al<sub>2</sub>O<sub>3</sub> catalysts were also investigated with TGA and DRIFT. Characterization of spent Pd/γ-Al<sub>2</sub>O<sub>3</sub> catalysts using TGA and DRIFT was performed after hydrogenation experiments that were stopped at  $Y_{BA}$ . Characterization of spent Pd/γ-Al<sub>2</sub>O<sub>3</sub> catalysts using ICP-OES, CO chemisorption, N<sub>2</sub> physisorption, TEM, and laser diffraction was performed after hydrogenation experiments stopped at  $X_{BA} = 100\%$ .

## Results

### *Hydrogenation of benzonitrile*

Typical concentration-time profiles of the various components involved in the semi-batch hydrogenation of benzonitrile (BN) using a Pd/ $\gamma$ -Al<sub>2</sub>O<sub>3</sub> catalyst, activated at 10 bar, at 80°C with a  $pH_2$  of 5.3 and 15 bar are shown in Fig. 5.2a and b. Fig. 5.2a also shows where the catalyst performance parameters, *i.e.*, turnover frequencies, selectivities, and yields, were determined in the concentration-time profiles by using formulas (1) to (5) defined in the experimental part. Concentration-time profiles of the hydrogenation of BA ( $C_{BA,0} = 520$  mol/m<sup>3</sup>) and of a mixture of equimolar amounts of BN and BA ( $C_{BN,0} = C_{BA,0} = 300$  mol/m<sup>3</sup>) performed at  $pH_2 = 10$  bar and  $T = 80^\circ\text{C}$  (standard activation procedure applied) are shown in Fig. 5.2c.

The main product is benzylamine (BA) at the investigated  $pH_2$  range. The major byproducts are toluene (TOL) and dibenzylamine (DBA). Together with BN these three compounds make up more than 99% of the carbon mass balance. I did not find half-hydrogenated species, *e.g.*, benzylideneimine (BI) or N-benzylidenebenzylamine (DBI), in the reaction mixture. Also no DBI was found in solution, which is supposed to be a relatively stable imine [56] and has been detected by several researchers in the hydrogenation of BN [57]. A minor byproduct detected was N-isopropylbenzylamine (< 1%) which is a product of the reaction between BA and the solvent (2-propanol).

The initial concentration-time profile of DBA in Fig. 5.2a is an *s*-shaped curve whereas the formation of TOL starts from  $t = 0$  min onwards and a straight line can be fitted through the data points. This is an indication that TOL is also formed from BN directly, via surface intermediates, without desorption and readsorption of BA. After the maximum in  $C_{BA}$  (*i.e.*,  $Y_{BA}$ ), when BN was mostly depleted, hydrogenolysis of BA to TOL takes off (Fig. 5.2). The rate of TOL formation and BA depletion are equal after full conversion of BN.

TOFs, selectivities, and yield versus  $pH_2$  are given in Fig. 5.3. The standard condition is  $C_{BN,0} = 520$  mol/m<sup>3</sup>, but also experiments were conducted at  $C_{BN,0} = 300$  and 1000 mol/m<sup>3</sup> (Fig. 5.3a). Clearly, for these experiments the TOFs are the same as for the standard conditions.

Concentration-time profiles with variation of activation and hydrogenation pressure are shown in Fig. 5.4a and b. Fig. 5.4a shows two concentration-time profiles: one with activation at 10 bar followed by hydrogenation at 30 bar, and one with 30 bar activation followed by 10 bar hydrogenation. These two configurations give equal results.

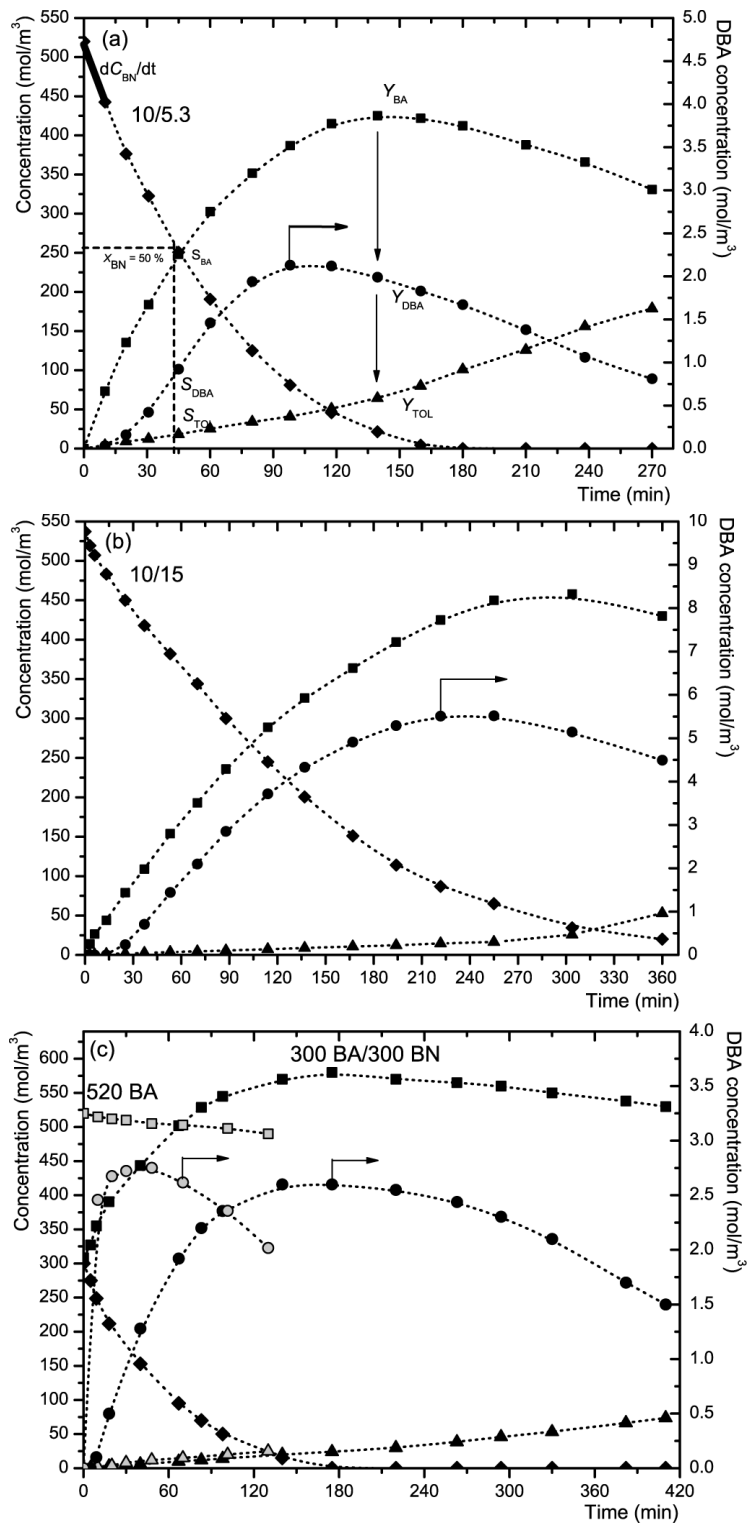


**Fig. 5.2.** Concentration ( $\text{mol}/\text{m}^3$ ) vs. time (min) profiles for BN hydrogenation at  $80^\circ\text{C}$  over a  $\text{Pd}/\gamma\text{-Al}_2\text{O}_3$  catalyst with  $C_{\text{BN},0} = 520 \text{ mol}/\text{m}^3$  performed at 5.3 (a) and 15 (b) bar  $\text{H}_2$ ; (c) Concentration ( $\text{mol}/\text{m}^3$ ) vs. time (min) profiles for BA hydrogenation with  $C_{\text{BA},0} = 520 \text{ mol}/\text{m}^3$  (grey symbols) and hydrogenation of a mixture of BN and BA with  $C_{\text{BN},0} = 300 \text{ mol}/\text{m}^3$  and  $C_{\text{BA},0} = 300 \text{ mol}/\text{m}^3$  (black symbols) at  $80^\circ\text{C}$  over a  $\text{Pd}/\gamma\text{-Al}_2\text{O}_3$  catalyst at 10 bar hydrogenation. All catalysts were activated at 10 bar. Left y-axis shows the concentration of BN, BA and TOL. The right y-axis shows the DBA concentration. Key:  $\blacklozenge = C_{\text{BN}}$ ;  $\blacksquare = C_{\text{BA}}$ ;  $\bullet = C_{\text{DBA}}$ ;  $\blacktriangle = C_{\text{TOL}}$ . The dashed lines are guidance for the eyes.

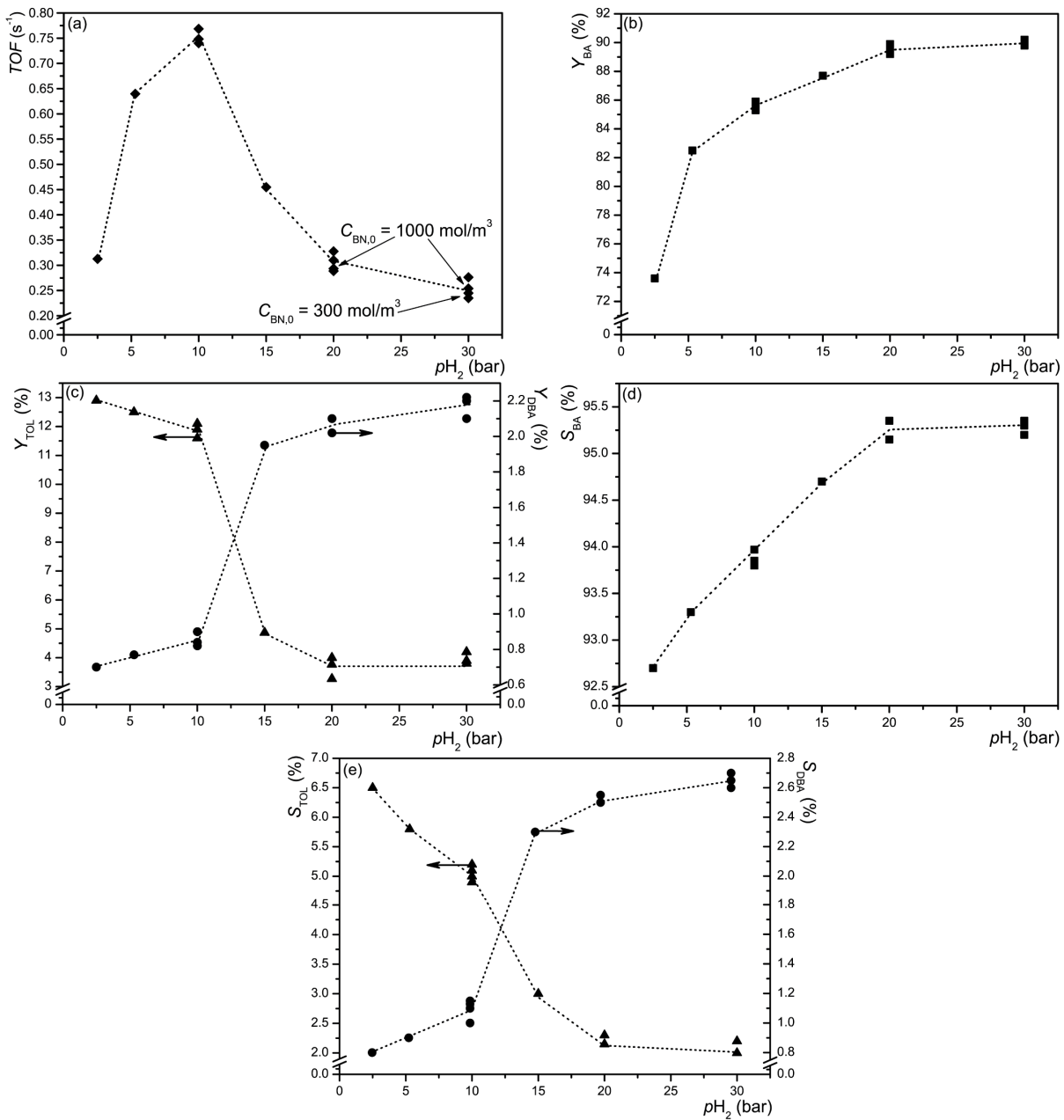


**Fig. 5.3.** Catalyst performance vs.  $pH_2$  (bar) for BN hydrogenation over a  $Pd/\gamma\text{-Al}_2\text{O}_3$  catalyst at  $80^\circ\text{C}$ ,  $C_{BN,0} = 520 \text{ mol/m}^3$ , and 10 bar activation: (a) Turnover frequencies ( $TOF$ ). The diamonds indicated by the arrows at 20 and 30 bar  $pH_2$  represent hydrogenations performed at  $C_{BN,0} = 1000 \text{ mol/m}^3$  and  $300 \text{ mol/m}^3$ ; (b) Maximum BA yield ( $Y_{BA}$ ); (c)  $Y_{TOL}$  (left y-axis) and  $Y_{DBA}$  (right y-axis) at  $Y_{BA}$ ; (d)  $S_{BA}$  at  $X_{BN} = 50\%$ ; (e)  $S_{TOL}$  (left y-axis) and  $S_{DBA}$  (right y-axis) at  $X_{BN} = 50\%$ . Key:  $\blacklozenge = TOF$ ;  $\blacksquare = S_{BA}$  or  $Y_{BA}$ ;  $\bullet = S_{DBA}$  or  $Y_{DBA}$ ;  $\blacktriangle = S_{TOL}$  or  $Y_{TOL}$ . The dashed lines are guidance for the eyes.

Fig. 5.4b shows three concentration-time profiles: 10 bar activation followed by 2.5 bar hydrogenation, 2.5 activation followed by 10 bar hydrogenation, and 10 bar activation followed by 10 bar hydrogenation. The activation at 2.5 bar followed by 10 bar hydrogenation

displays similar results as 10 bar activation followed by 10 bar hydrogenation, but 10 bar activation followed by 2.5 bar hydrogenation yields different results. The results for 30 bar activation followed by 10 bar hydrogenation (Fig. 5.4a) and 10 bar activation followed by 10 bar hydrogenation (Fig. 5.4b) are also dissimilar from each other.

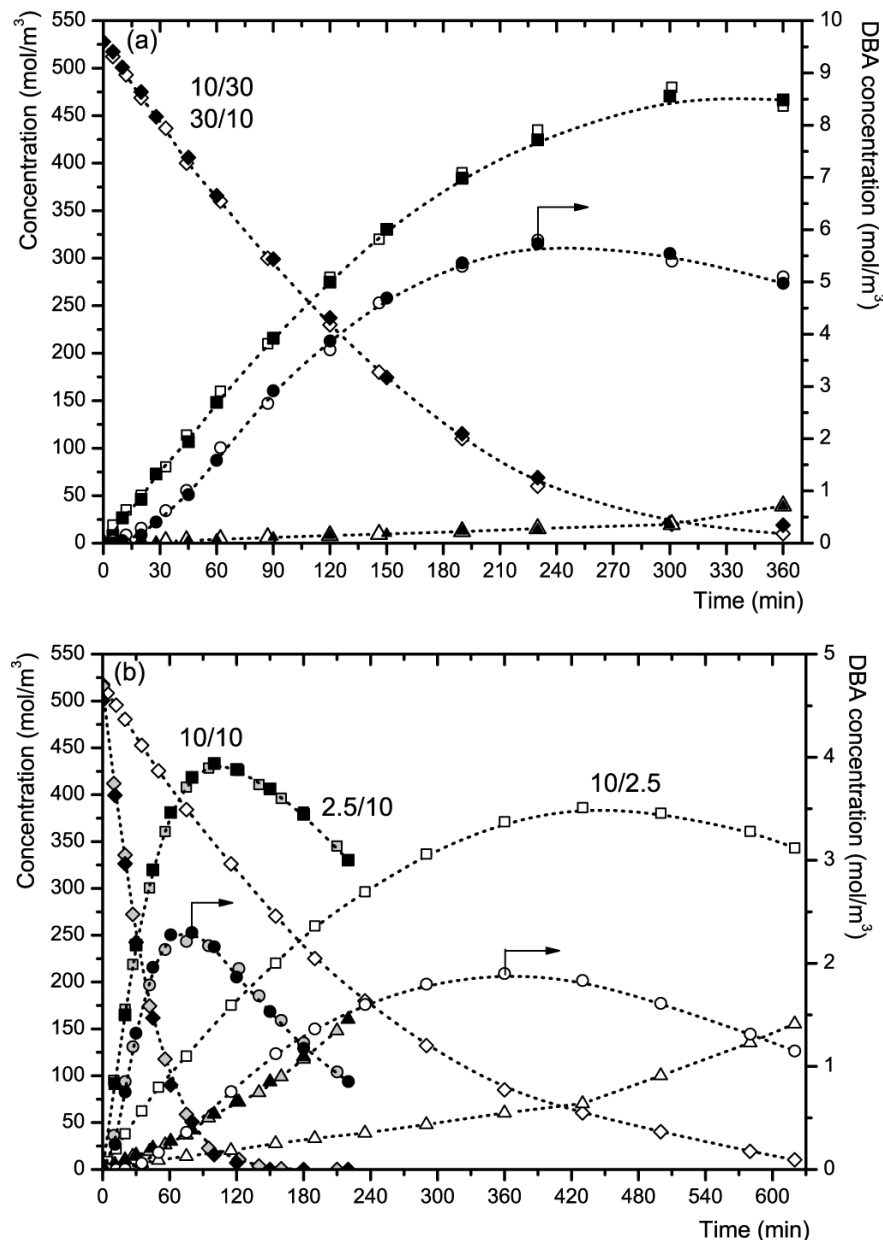


**Fig. 5.4.** Concentration ( $\text{mol}/\text{m}^3$ ) vs. time (min) profiles of BN hydrogenation over a  $\text{Pd}/\gamma\text{-Al}_2\text{O}_3$  catalyst at different activation and hydrogenation pressures at  $80^\circ\text{C}$  and  $C_{\text{BA},0} = 520 \text{ mol}/\text{m}^3$ : (a) 30 bar activation and 10 bar hydrogenation (open markers) and 10 bar activation and 30 bar hydrogenation (closed markers); (b) 10 bar activation and 10 bar hydrogenation (grey markers), 10 bar activation and 2.5 bar hydrogenation (open markers), and 2.5 bar activation and 10 bar hydrogenation (closed markers). Left y-axis shows the concentration of BN, BA, and TOL. The right y-axis shows the DBA concentration. Key:  $\blacklozenge = C_{\text{BN}}$ ;  $\blacksquare = C_{\text{BA}}$ ;  $\bullet = C_{\text{DBA}}$ ;  $\blacktriangle = C_{\text{TOL}}$ . The dashed lines are guidance for the eyes.

*Catalyst characterization*

An overview of the characterization of the fresh, activated, and spent Pd catalysts is shown in Table 5.2. The actual Pd content was 4.22 wt% in the fresh catalyst (ICP-OES). This value did not change during activation or hydrogenation at different  $p\text{H}_2$ , so, no leaching occurred during any of the activation steps or hydrogenation. The  $S_{\text{BET}}$  of the  $\gamma\text{-Al}_2\text{O}_3$  support was 154  $\text{m}^2/\text{g}$  with a pore volume of 0.47  $\text{cm}^3/\text{g}$ , and a mean pore diameter of 12 nm. The mean particle size of the  $\gamma\text{-Al}_2\text{O}_3$  support was 37  $\mu\text{m}$  and did not undergo any significant change during activation or hydrogenation.

**Table 5.2**

Summary of characterization results of fresh, activated, and spent 5 wt% Pd/ $\gamma\text{-Al}_2\text{O}_3$  catalyst

| Catalyst            | Average Pd crystallite size<br>(nm) | Pd loading<br>(wt%) | $S_{\text{BET}}$<br>( $\text{m}^2/\text{g}$ ) | $D < 50\%^*$<br>( $\mu\text{m}$ ) |                   |
|---------------------|-------------------------------------|---------------------|---|-----------------------------------|-------------------|
|                     | CO<br>chemisorption <sup>#</sup>    | TEM                 | ICP OES                                       | $\text{N}_2$ physisorption        | Laser diffraction |
| Fresh               | 5.6                                 | $4.2 \pm 0.6$       | 4.22  | 154                               | 37                |
| Activated at 10 bar | 5.6                                 | n.m.                | 4.22  | n.m.                              | n.m.              |
| Activated at 30 bar | 5.6                                 | n.m.                | 4.21  | 154                               | n.m.              |
| Spent 10 bar        | 6.2                                 | $4.2 \pm 0.9$       | 4.23  | n.m.                              | 37                |
| Spent 30 bar        | 6.2                                 | n.m.                | 4.22  | 150                               | n.m.              |

\*  $D < 50\% =$  diameter below which 50% of the crystallite volume is comprised.

# Assumptions: CO:Pd = 1 and spherically shaped crystallites.

n.m. – not measured.

The average size of the Pd crystallites of the fresh catalyst was 5.6 nm (dispersion = 20%) and 4.2 nm (dispersion = 26.7%) determined by CO chemisorption and TEM, respectively. The Pd crystallites were uniformly distributed over the  $\gamma\text{-Al}_2\text{O}_3$  support. The discrepancy between the Pd crystallite sizes can be explained by the error I introduce by assuming that the CO/Pd ratio is unity in the calculation of the Pd crystallite size from CO chemisorption measurements. CO is known to adsorb on Pd not only in a linear end-on configuration on smaller crystallites (Pd/CO = 1) but also in a bridged configuration on larger crystallites (Pd/CO = 2) [58-60]. After activation at 10 and 30 bar no changes to the average Pd crystallite size was observed, whereas the spent catalysts (hydrogenations performed at 10 and 30 bar) showed an increase of the average Pd crystallite size from 5.6 to 6.2 nm. However, TEM analysis did not show any growth of the Pd crystallite size: the average Pd crystallite size of

the fresh and spent catalyst was 4.2 nm. The increased average Pd crystallite size of the spent catalyst (*i.e.*, lower Pd surface area) as measured with CO chemisorption is probably caused by adsorbed species on the Pd surface that decrease the area that is available for chemisorption of CO.

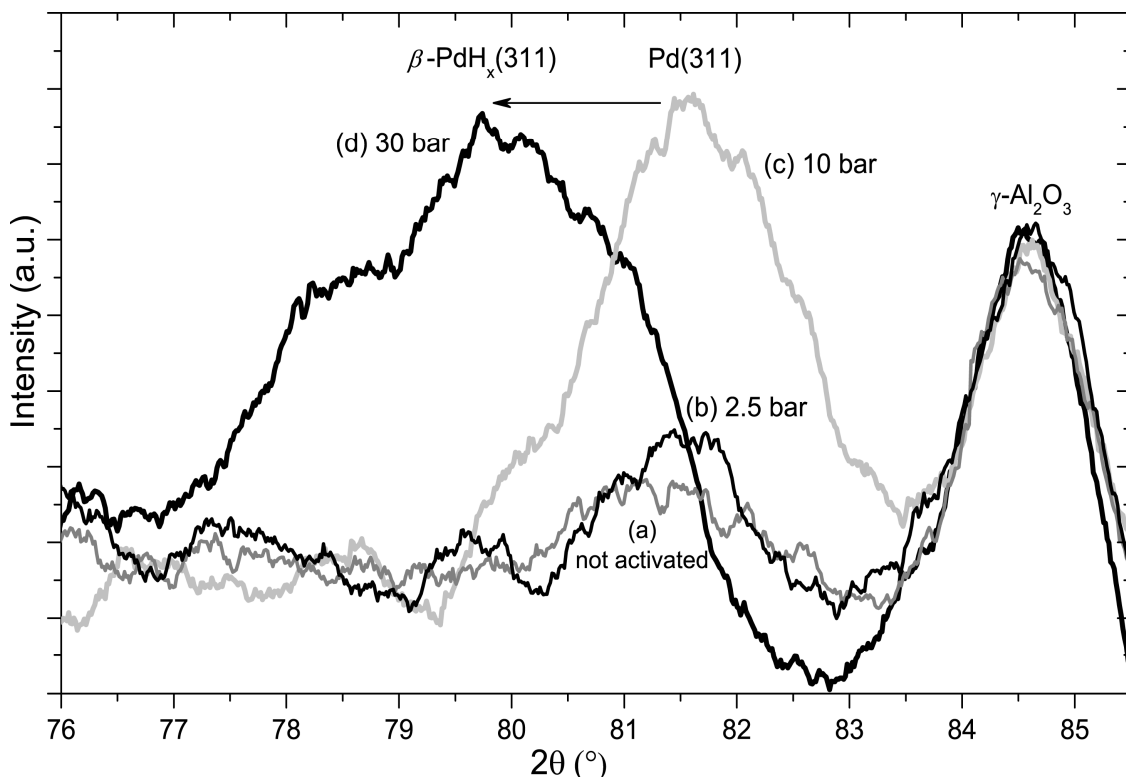


**Fig. 5.5.** Four *ex-situ* X-ray diffraction patterns of Pd/γ-Al<sub>2</sub>O<sub>3</sub> catalysts activated at different  $p\text{H}_2$  at 80°C in 2-propanol prior to XRD analysis. Key: (a) = not activated; (b) = activated at 2.5 bar; (c) = activated at 10 bar; (d) = activated at 30 bar.

*Ex-situ* X-ray diffraction patterns of four Pd/γ-Al<sub>2</sub>O<sub>3</sub> catalysts activated at different  $p\text{H}_2$  are shown in Fig. 5.5. The Pd(311) reflections region is presented because there is no interference of γ-Al<sub>2</sub>O<sub>3</sub> support peaks in this region. Note that the Pd(111) reflection showed the same trends but was heavily obscured by γ-Al<sub>2</sub>O<sub>3</sub> support reflections. The reflection at  $2\theta = 84.6^\circ$  is a reflection of the crystalline part of the γ-Al<sub>2</sub>O<sub>3</sub> support and is shown in Fig. 5.5 as a reference. The observed Bragg diffraction reflections correspond to Pd(311) and β-PdH<sub>x</sub>(311) reflections.

When H<sub>2</sub> is absorbed in the Pd lattice structure and β-PdH is formed the Bragg reflection shifts to smaller  $2\theta$  angles of around 79.7° (indicated with the arrow in Fig. 5.5) due to expansion of the Pd lattice. Reflections at 81.6° with a calculated lattice constant of 3.91 Å and 79.7° with a calculated lattice constant of 3.99 Å are from Pd(311) and β-PdH<sub>x</sub>(311),

respectively. So, the lattice constant of Pd increases with 2.0% when a  $p\text{H}_2$  of 30 bar is applied during the activation step (in 2-propanol at 80°C for 1h). The amount of hydrogen absorbed (represented by  $x$  in  $\beta\text{-PdH}_x$ ) in the Pd crystallites correlates with the location of the Bragg reflection and is determined by the Pd crystallite size: smaller Pd crystallites absorb less hydrogen in the  $\beta\text{-PdH}$  phase and more in the  $\alpha\text{-PdH}$  phase [33, 34, 61]. I determined  $x$  for the  $\beta\text{-PdH}$  phase using Vegard's law and lattice constants and  $x$ -values for similarly-sized nanoscale particles from literature as  $x = 0.43$  [62]. The lattice constant for Pd(311) is reported to be 3.89 Å [63]. Compared to my lattice constant of 3.91 Å it shows that the fresh catalyst and those activated at 2.5 and 10 bar experienced minor lattice expansion, obviously because of the pretreatment steps and  $x$  being 0.06. Note that the fresh catalyst had already been reduced by the supplier. The catalysts activated at 2.5 bar also showed a small reflection at 79.8° but the main reflection was from Pd(311) at 81.5°.

The catalyst activated at 10 and 30 bar showed a strong increase of intensity of the Pd(311) and  $\beta\text{-PdH}_{0.43}(311)$  reflections, respectively. Note that the 10 bar activation did not shift the 311 reflection to smaller 2 $\theta$  angles. However, a small shoulder is visible around 80° (Fig. 5.5c), indicating that a small part of Pd converted to  $\beta\text{-PdH}$ . The increase in intensity could be caused by a rise of the average length of an ordered row of atoms in the 311 crystallographic direction caused by structure rearrangement: exposure to  $\text{H}_2$  can result in ordering of Pd crystallites [64]. Although XRD is considered as a bulk characterization technique, surface topography changes can also enhance the intensity of a reflection since for nanoscale crystallites a substantial amount of the atoms is located at the surface. The observed broadening of the  $\beta\text{-PdH}_{0.43}(311)$  reflection (Fig. 5.5) is attributed to microstrain (e.g., from non-uniform lattice distortion) and solid solution inhomogeneity.

Three  $\text{H}_2$ -TPR curves, two of Pd/ $\gamma\text{-Al}_2\text{O}_3$  catalysts that were activated at 10 and 30 bar  $\text{H}_2$  (in 2-propanol at 80°C for 1 h) and a fresh Pd/ $\gamma\text{-Al}_2\text{O}_3$  catalyst, are shown in Fig. 5.6. The  $\text{H}_2$ -TPR curves all have a negative  $\text{H}_2$  peak around 83°C which is characteristic of Pd catalysts with Pd crystallite sizes larger than ~ 2 nm. This peak is attributed to the  $\text{H}_2$  desorption from the decomposition of the  $\beta\text{-PdH}_x$  formed by the uptake of  $\text{H}_2$  at room temperature (5 min) during the TPR experiment [65-68]. The area of the  $\beta\text{-PdH}_x$  decomposition peak was determined in the temperature range 60 – 100°C [60, 69-72]. The  $\beta\text{-PdH}_x$  decomposition peak area decreased by 20 and 28% (corrected by the weight of the samples) if the Pd/ $\gamma\text{-Al}_2\text{O}_3$  prior to  $\text{H}_2$ -TPR was activated at 10 and 30 bar, respectively.

The overall DRIFT spectra indicated that BA and BN were adsorbed in excess on the catalyst surface when comparing these spectra with reference spectra (not shown). An overall DRIFT spectrum of a spent Pd/ $\gamma$ -Al<sub>2</sub>O<sub>3</sub> catalyst used in hydrogenation at 20 bar is shown in Fig. 5.7a. The hydrogenations were stopped directly after  $Y_{BA}$  was reached. DRIFT spectra of the  $\nu(C\equiv N)$  stretching region of two spent Pd/ $\gamma$ -Al<sub>2</sub>O<sub>3</sub> catalysts from a 10 and 20 bar hydrogenation experiment are shown in Fig. 5.7b. The C≡N stretches are very valuable characteristics because they fall in a practically unpopulated spectral region [73]. A DRIFT spectrum of a fresh Pd/ $\gamma$ -Al<sub>2</sub>O<sub>3</sub> catalyst did not show any peaks in this region (not shown). Free BN shows a band at 2231.7 cm<sup>-1</sup> in 2-propanol [74]. Interactions of  $\gamma$ -Al<sub>2</sub>O<sub>3</sub> surface groups (e.g., acidic Al<sup>3+</sup><sub>T</sub> and Al<sup>3+</sup><sub>O</sub>, basic and acidic Al-OH groups) with BN are found above 2240 cm<sup>-1</sup> but most interactions of the acidic  $\gamma$ -Al<sub>2</sub>O<sub>3</sub> groups will be with NH<sub>3</sub> and amine species [75-77]. The interaction at 2245 cm<sup>-1</sup> is attributed to end-on adsorption via an acidic Al-OH of  $\gamma$ -Al<sub>2</sub>O<sub>3</sub>. Several configurations of BN adsorption are possible on Pd, *i.e.*, end-on and side-on. After hydrogenations at 10 and 20 bar both adsorption configurations were observed (Fig. 5.7b): side-on adsorption at  $\sim 2165$  cm<sup>-1</sup> and end-on at  $\sim 2229$  cm<sup>-1</sup>. Strikingly, there is a distinct difference between the BN adsorption configuration ratios (side-on/end-on) for both spent catalysts: this ratio is much larger for hydrogenation at 10 bar than at 20 bar.

Thermogravimetric analyses of two spent Pd/ $\gamma$ -Al<sub>2</sub>O<sub>3</sub> catalysts used in hydrogenations at 10 and 20 bar are compared in Fig. 5.8. It is also shown in Fig. 5.8 whether exothermic combustion or endothermic desorption occurred, as determined by single-point differential thermal analysis (STDA) present in the thermobalance. The total weight loss (discarding water and catalyst peaks) was  $3.1 \pm 0.1$  and  $4.3 \pm 0.2$  wt% for hydrogenations at 10 and 20 bar, respectively. The weight loss of  $2 \pm 0.1$  wt% at 75°C (endothermic) is due to desorption of physisorbed water. The weight loss at 190 and 215°C (both exothermic) for the 10 and 20 bar experiment, respectively, originates from decomposition of adsorbed species. From reference experiments (not shown) it is concluded that this weight loss (at 190 and 215°C) is from decomposition of BA. The catalyst used in hydrogenation at 20 bar showed more strongly adsorbed and larger amounts of BA on the catalyst surface:  $0.7 \pm 0.1$  and  $1.3 \pm 0.1$  wt% for hydrogenation at 10 and 20 bar, respectively. A weight loss of  $0.8 \pm 0.1$  wt% at 260°C (for hydrogenation at 10 and 20 bar) originates from desorption of the Pd precursor (endothermic), because this weight loss also occurred when TGA is performed using a fresh catalyst (not shown). The weight loss around 285°C (exothermic) observed in the thermographs of both spent catalysts, was not detected in the thermographs of a fresh catalyst

and catalysts used in the reference experiments. This weight loss was ascribed to decomposing semi-hydrogenated species that were chemisorbed on the Pd crystallites. The weight losses at 340 and 440°C (both exothermic) are from combustion of basic species (*e.g.*, BA, DBA, and NH<sub>3</sub>) deposited near Pd crystallites and on the  $\gamma$ -Al<sub>2</sub>O<sub>3</sub> support, respectively [78-81]. A catalyst used in hydrogenation at 10 bar contains less of these deposits on the surface: 2.0  $\pm$  0.1 and 3.0  $\pm$  0.1 wt% for hydrogenation at 10 and 20 bar, respectively.

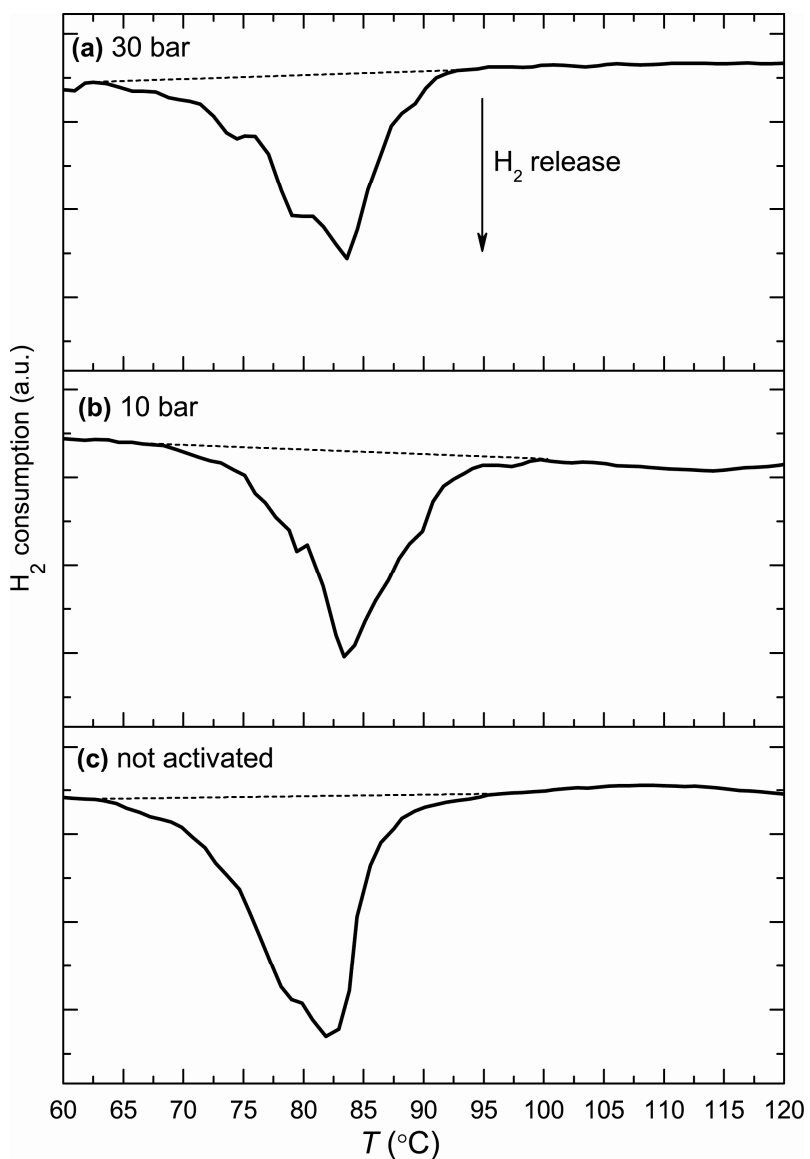


**Fig. 5.6.** H<sub>2</sub>-TPR profiles of three Pd/γ-Al<sub>2</sub>O<sub>3</sub> catalysts activated prior to H<sub>2</sub>-TPR at different pH<sub>2</sub> in 2-propanol for 1 h at 80°C. Key: (a) = 30 bar activation; (b) = 10 bar activation; (c) = not activated. The dashed lines show the baselines for the determination of the relative amounts of H<sub>2</sub> release.

The weight loss at 810°C (exothermic) is also seen in the TGA of a soaked catalyst in BN but was absent for the catalysts soaked in the other compounds. The weight losses were  $0.4 \pm 0.02$  and  $0.1 \pm 0.01$  wt% for the 10 and 20 bar experiment, respectively. The weight loss of  $0.5 \pm 0.02$  wt% at 860°C (exothermic) is from the phase transformation of  $\gamma\text{-Al}_2\text{O}_3$  to  $\delta\text{-Al}_2\text{O}_3$  [82] and was also visible in the TGA of a fresh catalyst sample.

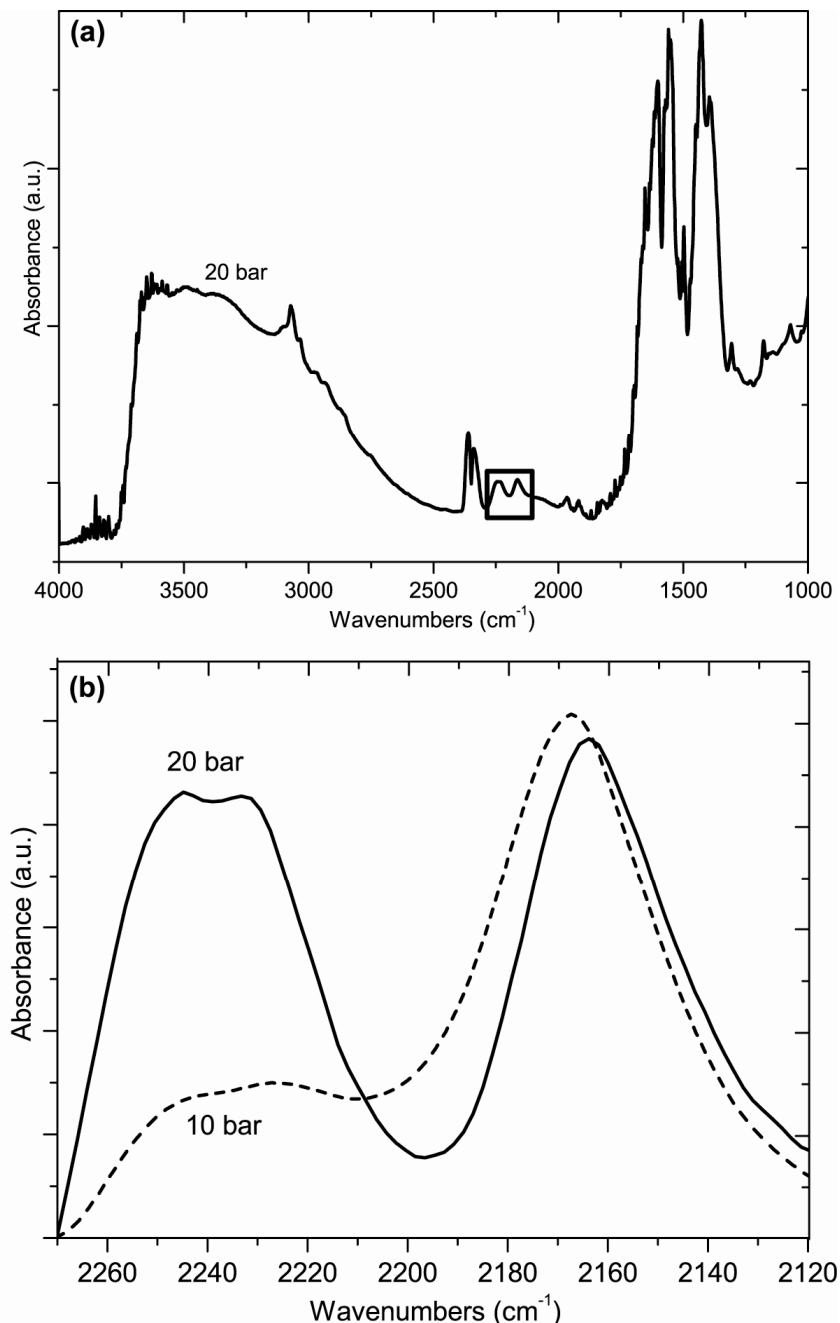


**Fig. 5.7.** DRIFT spectra of spent  $\text{Pd}/\gamma\text{-Al}_2\text{O}_3$  catalysts after BN hydrogenations performed at 10 and 20 bar at 80°C,  $C_{\text{BN},0} = 520 \text{ mol/m}^3$ , and 10 bar activation. The reactions were stopped at  $Y_{\text{BA}}$ : (a) Full spectrum for hydrogenation performed 20 bar showing the  $\text{C}\equiv\text{N}$  stretching region indicated by the square; (b) Enlarged  $\text{C}\equiv\text{N}$  stretching region for hydrogenation performed at 10 (dashed line) and 20 bar (full line).

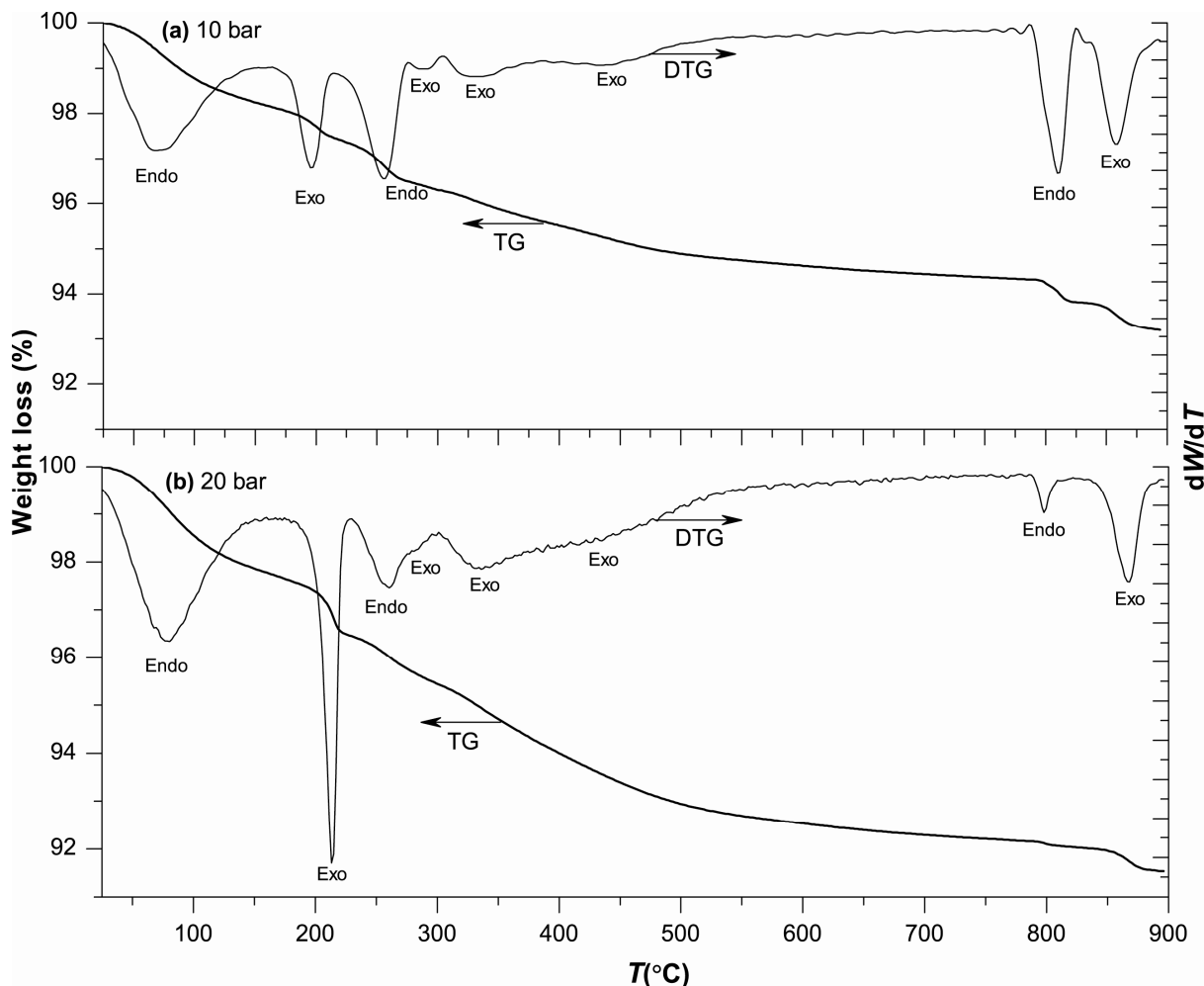


**Fig. 5.8.** Thermogravimetric (TG) and differential thermogravimetric (DTG) profiles in air of two spent Pd/γ-Al<sub>2</sub>O<sub>3</sub> catalysts after hydrogenation performed at 10 bar (a) and 20 bar (b) at 80°C, C<sub>BN,0</sub> = 520 mol/m<sup>3</sup>, and activated at 10 bar. The reactions were stopped at  $Y_{BA}$ . The left y-axis represents the weight loss and the right y-axis represents the differential weight loss. Key: endo = endothermal desorption process; exo = exothermal decomposition process; as determined by the single point differential thermal analysis (SDTA) present in the thermobalance.

#### Molecular orbital energy calculations

The calculated values of HOMO and LUMO energy levels are shown in Table 5.3. The LUMO level represents the ease to accept electrons: the lower the LUMO the easier it accepts electrons. The lowest calculated LUMO level is the  $\pi$  C≡N orbital of BN at -1.41 eV. The HOMO level represents the ease to donate electrons: the higher the HOMO level the better it donates electrons. BIBA, DBA, and BA show the highest HOMO levels at -6.11, -6.09, and -6.18, respectively. Note that the orbital energy levels were calculated without taking into

account any interaction with the Pd surface or solvent effects. The orbital levels for the intermediates are thereby speculative, firstly because the intermediates were not observed during reaction, and secondly because interaction with the surface might significantly alter the levels of these short-lived intermediates.

**Table 5.3**  
HOMO-LUMO levels

| Species          | HOMO <sup>*</sup><br>(eV) | LUMO <sup>#</sup><br>(eV) |
|------------------|---------------------------|---------------------------|
| BN               | -7.26                     | -1.41                     |
| BI ( <i>Z</i> )  | -6.61                     | -1.19                     |
| BI ( <i>E</i> )  | -6.84                     | -1.33                     |
| BA               | -6.18                     | 0.05                      |
| TOL              | -6.40                     | 0.14                      |
| NH <sub>3</sub>  | -6.87                     | 2.14                      |
| BIBA             | -6.11                     | 0.10                      |
| DBI ( <i>E</i> ) | -6.43                     | -1.18                     |
| DBI ( <i>Z</i> ) | -6.44                     | -1.07                     |
| DBA              | -6.09                     | 0.08                      |
| 2-propanol       | -7.10                     | 1.96                      |

\* HOMO = highest occupied molecular orbital.

# LUMO = lowest unoccupied molecular orbital.

Calculated using Becke 3LYP 6-31G\* method.

## Discussion

Some striking peculiarities related to the activity and selectivity of the hydrogenation of BN over Pd/ $\gamma$ -Al<sub>2</sub>O<sub>3</sub> have been observed. Upon increasing *pH*<sub>2</sub>, the activity of the catalyst goes through a maximum around 10 bar, while the product selectivities show a steep change around this *pH*<sub>2</sub>. Moreover, the *TOF* and selectivities depend on the activation *pH*<sub>2</sub> prior to hydrogenation.

### *Activity profile vs. pH<sub>2</sub>*

The *TOF* of BN hydrogenation increases with increasing  $pH_2$ , up to 10 bar, where it reached its maximum (Fig. 5.3a). Above the threshold  $pH_2$  of 10 bar, further increasing  $pH_2$  showed a strong inverse effect on the reaction rates and the order changed to  $\sim -1$ . This maximum in activity was not expected, and no Pd-catalyzed nitrile hydrogenation results are reported in literature showing this behavior. However, it is observed frequently in other hydrogenation and also in hydrogenolysis reactions using supported Pd catalysts where it is attributed to competitive adsorption [16-18, 83-86]. Hydrogenolysis of simple alkanes over different supported catalysts all exhibited a negative order in  $H_2$  and this was explained by the decreasing concentration of the dehydrogenated intermediate that undergoes C-C bond scission [20, 87], although it was also speculated that competitive adsorption between  $H_2$  and the hydrocarbons could play a role. To check if competitive adsorption could indeed be the reason for my observation, I performed hydrogenation experiments at 20 and 30 bar with other  $C_{BN,0}$  concentrations, *viz.*, 1000 mol/m<sup>3</sup> and 300 mol/m<sup>3</sup>. However, increasing or decreasing  $C_{BN,0}$  did not have any influence on the *TOF* (Fig. 5.3a) and, as a consequence, this explanation is rejected.

### *The $\beta$ -PdH phase*

The sudden drop in activity around a  $pH_2$  of 10 bar might be caused by the well-known formation of  $\beta$ -PdH. *Ex-situ* XRD analysis of activated and non-activated catalysts showed remarkable changes of the Pd crystallite lattice parameters after activation at increased  $pH_2$  (Fig. 5.5). The lattice constant of Pd increases by 2.0% after activation at 30 bar which is attributed to the formation of the  $\beta$ -PdH phase. This observation is remarkable because the XRD patterns were measured *ex-situ* and probably all the hydrogen was already desorbed from the catalyst samples.

The conditions for a transformation of nanoscale Pd crystallites into  $\beta$ -PdH have been studied extensively. Typically,  $\sim 1$  bar  $H_2$  is sufficient in the gas phase to transform supported nanoscale Pd crystallites into  $\beta$ -PdH at around 80°C [30, 88, 89]. In the liquid phase the critical value for  $pH_2$  is expected to be much higher because the  $H_2$  solubility in a liquid phase is an order of magnitude smaller than the  $H_2$  concentration in the gas phase [35, 41, 90]. This corresponds with a  $pH_2$  of  $\sim 10$  bar for liquid phase processes, nicely matching the  $pH_2$  of 10 bar for the maximum in Fig. 5.3a. Note that the transformation of Pd into  $\beta$ -PdH is accelerated when the solvent is an alcohol compared to non-alcoholic solvents and water [91].

Under TPR conditions the  $\beta$ -PdH phase is unstable above 80°C as can be seen in Fig. 5.6, but it is striking that the expansion/distortion of the Pd lattice was still retained, as shown by *ex-situ* XRD (Fig. 5.5), after activation at 30 bar and a drying step performed at 120°C in air. Several researchers observed the lattice distortion after the H<sub>2</sub> had been removed: only after annealing at 450°C the Pd atoms could be returned to their original position [25, 92]. This also implies that the persistent expansion of the Pd lattice after activation of 30 bar could still have an effect on the catalyst performance during a hydrogenation experiment even if the  $\beta$ -PdH phase is somehow eliminated in between activation and hydrogenation.

When the catalyst precursor contains carbonaceous material or when a carbon support is used, carbon might incorporate in the Pd lattice and yield a solid solution in Pd (Pd-C) which could give similar shifts in reflections as  $\beta$ -PdH [26, 93, 94]. In my case, a Pd-C phase might be formed with the solvent (*i.e.*, 2-propanol) as a carbon source. Formation of a Pd-C phase prohibits the formation of a  $\beta$ -PdH phase [65, 93]. TPR is a useful technique for elucidating this point. If no  $\beta$ -PdH decomposition peak would be observed in the TPR profiles of the 10 and 30 bar activated catalysts then, the catalysts could have been contaminated by carbon soluble in the Pd lattice. However,  $\beta$ -PdH decomposition peaks are observed in the TPR profiles (Fig. 5.6) after activation performed in 2-propanol so it is concluded that no extensive Pd-C phase has been formed during the activation step. It should be noted that Teschner *et al.* observed that also a metastable Pd-C phase in the top few layers can be formed in the early stage of the reaction. This phase was only stable under reaction conditions during the gas phase hydrogenation of acetylene at very low  $pH_2$  (< 0.13 bar) [95, 96]. If the  $pH_2$  is raised above a certain pressure, then this Pd-C surface phase disappears and a  $\beta$ -PdH phase is formed. Moreover, when trans-2-pentene is chosen as the reactant under similar reaction conditions, then no Pd-C phase is formed. Obviously, double bonds do not strongly fragment on the surface of Pd, hence the C≡C triple bond is essential in forming a Pd-C surface phase. This is supported by DFT calculations, which shows that only for certain reactants, in combination with a Pd surface, a Pd-C surface phase can be formed [97-99]. Note that the morphology of the Pd catalyst is also important: decomposition of organic species takes place more efficiently on stepped than on flat surfaces [100]. Since my experiments were performed under completely different conditions and with other reactants than the ones used by Teschner *et al.* [95], I would argue against the formation of a metastable Pd-C surface phase in my experiments especially in view of the used  $pH_2$ .

### *Influence of $\beta$ -PdH phase transformation on selectivity*

The hydrogenation of BN over Pd/ $\gamma$ -Al<sub>2</sub>O<sub>3</sub> in 2-propanol resulted in three products: BA, TOL, and DBA, at the investigated  $pH_2$  range from 2.5 to 30 bar (Fig. 5.2). The production of BA dominated over the formation of TOL and DBA up to nearly full conversion of BN ( $X_{BN} \sim 95\%$ ). The highest  $Y_{BA}$  and  $S_{BA}$  achieved were above 90% and 95%, respectively, when a  $pH_2$  was applied above 20 bar. This is an excellent result compared to other Pt-group catalysts and a good result compared to Ni catalysts (Table 5.1), considering that in this study no additives (e.g., NH<sub>3</sub>) were used. The maximum in catalyst activity at the threshold  $pH_2$  of 10 bar is accompanied by sharp change in selectivities of TOL and DBA (Fig. 5.3e). As competitive adsorption is ruled out as explanation for the activity maximum at this  $pH_2$ , this cannot be the cause of this sharp selectivity change. Since the trends in selectivity and yield are similar I will concentrate on the difference in selectivity in the following.

### *Influence of activation pressure*

The performance of a catalyst activated at 10 bar and applied in a BN hydrogenation experiment at 30 bar resulted in the same performance as one activated at 30 bar and hydrogenation applied at 10 bar (Fig. 5.4a). Clearly, at 30 bar the  $\beta$ -PdH phase was formed and this phase is stable during hydrogenation at lower  $pH_2$ . In agreement with this conclusion, activation at 2.5 bar and hydrogenation at 10 bar gave similar results as activation and hydrogenation at 10 bar. Apparently, if the  $pH_2$  is high enough, then the Pd crystallites transform into a stable  $\beta$ -PdH phase that still determines the catalyst performance, even if the hydrogenation is carried out at a lower  $pH_2$ . If no stable  $\beta$ -PdH is formed during the activation step, *i.e.*, at  $pH_2$  of 10 bar or lower, then the applied hydrogenation  $pH_2$  determines the catalyst performance (Fig. 5.4b). So, a higher BA productivity can be achieved by applying an activation step above 10 bar prior to hydrogenation of BN at 10 bar compared to a standard experiment of both activation and hydrogenation at 10 bar.

### *Electronic interactions*

The lattice expands and changes to the *d*-band of Pd occur upon transformation into the  $\beta$ -PdH phase [27, 29-32, 40, 101-105]

- Centre of the *d*-band ( $\varepsilon_d$ ) of  $\beta$ -PdH is shifted down compared to its Fermi level ( $E_f$ ). The energy level of  $E_f$  does not change significantly when  $x$  (in  $\beta$ -PdH<sub>x</sub>) is below 0.6 and is -5.22 eV for polycrystalline Pd.  $\varepsilon_d$  for Pd and  $\beta$ -PdH<sub>0.4</sub> are 1.83 eV and  $\sim$  2.2 below  $E_f$ , respectively. Catalytic activity is often related with the difference between  $\varepsilon_d$  and  $E_f$ : for a larger difference the transition metal becomes less reactive [106-109].
- Width of the *d*-band of  $\beta$ -PdH<sub>0.4</sub> is  $\sim$  15% narrower compared to Pd. A narrower *d*-band results in a decrease of Pauli repulsion. Weaker repulsive interactions increase the binding energy of adsorption with HOMO orbitals [110]. However, a spatially more extended *d*-band increases the propensity of rehybridization from  $\pi$  to di- $\sigma$  coordination to overcome the larger repulsive interaction [111].

Thus, the lower BN hydrogenation activity above the threshold pH<sub>2</sub> of 10 bar can be caused by the lower  $\varepsilon_d$  (compared to  $E_f$ ) and reduced width of the *d*-band of  $\beta$ -PdH compared to Pd.

Interaction of occupied (*e.g.*, HOMO) and unoccupied molecular orbitals (*e.g.*, LUMO) of an adsorbate with the broad *sp*-band of Pd is always attractive and causes these orbitals to broaden into resonances and shift to lower energy. Subsequently, hybridization between the *d*-band of Pd and the broadened molecular orbitals results in splitting of these orbitals, thereby forming bonding contributions at lower energies and antibonding ones at higher energies. The primary interactions during adsorption of BN are electron donation from occupied donative molecular orbitals of BN ( $\pi$  C≡N is the donating HOMO but also  $\sigma$ -donation from the lone pair on nitrogen is possible) to empty orbitals of Pd and backdonation from occupied *d*-orbitals of Pd to the unoccupied acceptor molecular orbitals of BN (LUMO is  $\pi^*$  C≡N), similar to the Blyholder model for CO adsorption on transition metals [112]. However, donative interactions are mainly repulsive (Pauli repulsion) due to orthogonalization between occupied orbitals of BN and occupied *d*-orbitals of Pd [113]. These can only become attractive when donative orbital-derived antibonding orbitals are shifted up through  $E_f$  and become empty ('relieved repulsion') [114]: a higher energy level of the donative orbital results in more attraction and a stronger bond to the Pd surface. Backdonation is attractive if the energy level of the acceptor orbital (LUMO) is low enough in energy to interact with the *d*-band of Pd. Backdonation is always attractive because the antibonding part of the LUMO is too high in energy to be filled.

BN is the best electron acceptor of all the compounds involved in the hydrogenation of BN since it has the lowest LUMO (Table 3). The interaction of BN with Pd upon adsorption is mainly governed by electron backdonation of Pd to the LUMO of BN. This interaction is higher when the energy level of  $\varepsilon_d$  is higher and the *d*-band is wider as is the case for Pd compared to  $\beta$ -PdH. However, not only the strength of adsorption increases when increased backdonation occurs but the LUMO of BN is of antibonding character with respect to the C≡N bond and thus weakens this intramolecular bond and increases the reactivity of BN [114]. Additionally, the orientation mode changes from a more end-on to a more side-on adsorption orientation. Interaction of the *d*-band with the HOMO of BN will be mostly repulsive because this orbital is low in energy thus the bonding and antibonding orbitals from coupling to the *d*-band will likely fall below  $E_f$ .

DBA and BA (and BIBA) are the best electron donors having the highest HOMOs (Table 5.3). In contrast to BN, the adsorption of BA and DBA on Pd is mainly governed by electron donation from their HOMO orbitals to unoccupied *d*-orbitals of Pd since the LUMOs of these amines have unfavorably high energy to sufficiently couple with the *d*-band of Pd. The HOMO of BA and DBA is localized on the lone pair of the nitrogen atom. The interaction is attractive since the HOMO of BA and DBA are sufficiently high-lying. This ensures that the antibonding orbitals originating from coupling of the *d*-band to the HOMO of BA (or DBA) are pushed above  $E_f$  and become empty. The interaction of the *d*-band of Pd with the HOMO of BA and DBA is increased upon a decrease of the width of the *d*-band (weaker repulsion) and a decrease of  $\varepsilon_d$ , as is the case for  $\beta$ -PdH. This is confirmed by TGA (Fig. 5.8). Operation above the threshold  $pH_2$  results in more amine surface species than operation at below the threshold  $pH_2$ . Interaction of the *d*-band of Pd with the LUMO of the amines will be much less effective than with the LUMO of BN since the LUMO of the amines is significantly higher in energy (Table 5.3).

In conclusion, a lowering of  $\varepsilon_d$  and decrease of the width of the *d*-band upon the transformation into  $\beta$ -PdH will not only change the strength and orientation of adsorption to the surface of Pd but it will have different effects on BN and BA thereby changing the adsorption ratio of BN/BA. The phase transformation of Pd results in a change of electronic and geometrical interactions with interacting species as schematically depicted in Fig. 5.9.

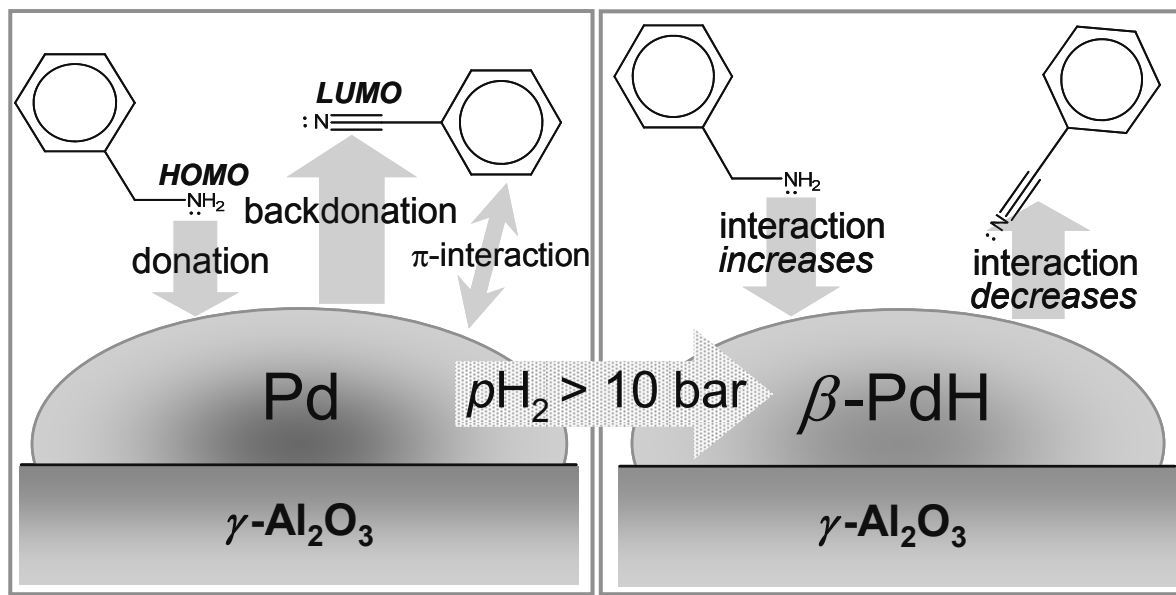


**Fig. 5.9.** Representation of major electron donation and electron withdrawing interactions between Pd, BN, and BA. Note the changing strength of interaction indicated by the arrow size, the changing orientation to the surface of BN, and the changing ratio of adsorption strengths BN/BA when Pd is transformed into  $\beta\text{-PdH}$  above the threshold  $p\text{H}_2$  of 10 bar.

#### Adsorption of BN

The possible coordination states of adsorption of BN on Pd are shown in Fig. 5.10a [115-118]

- End-on via  $\sigma$ -donation (I).
- Side-on via  $\sigma$ -donation and  $\pi$ -backdonation (II).
- Di- $\sigma$  rehybridization of the  $\text{C}\equiv\text{N}$  group to  $sp^2$  and  $sp^3$  configuration (III, IV).
- $\pi$ -interactions with the phenyl and/or  $\text{C}\equiv\text{N}$  group (V).

The extent of rehybridization is increased when backdonation increases and when the  $d$ -band is spatially more extended, as is the case for Pd compared to  $\beta\text{-PdH}$ . The DRIFT spectra shown in Fig. 5.7 give direct information on the modes of coordination of BN to Pd in catalysts used in hydrogenation at 10 and 20 bar. A blue shift in  $\nu(\text{C}\equiv\text{N})$  stretching compared to  $2231.7\text{ cm}^{-1}$  of free BN implies strengthening of the  $\text{C}\equiv\text{N}$  bond and is mostly explained as end-on adsorption via electron donation from the nitrogen lone pair to acid sites on the  $\gamma\text{-Al}_2\text{O}_3$  support [119]. Side-on adsorption, governed by electron backdonation, is not observed on  $\text{Al}_2\text{O}_3$  supports [120, 121]. So, the  $\text{C}\equiv\text{N}$  absorbance at wavenumbers below  $2231.7\text{ cm}^{-1}$  are attributed to adsorption of BN on the Pd crystallites. However, both electron donation and backdonation occur when BN adsorbs on Pd crystallites, which causes a red shift of the  $\text{C}\equiv\text{N}$  stretching: electron backdonation results in a more side-on adsorption mode and a weaker  $\text{C}\equiv\text{N}$  bond [122]. The absorbance at  $2230\text{ cm}^{-1}$  is attributed to an adsorption configuration,

dominated by the nitrogen lone pair donation bond which is more end-on with relatively less backdonation (I) and the peak at  $2165\text{ cm}^{-1}$  is attributed to a more side-on adsorption mode (II) with relatively more backdonation [117]. The differences of the 10 and 20 bar spectrum nicely supports the above reasoning: the absorbance intensity ratio of 2230 to  $2165\text{ cm}^{-1}$  is much smaller for 10 bar hydrogenation than for 20 bar hydrogenation because of the transformation of Pd to  $\beta$ -PdH going from 10 to 20 bar. The larger electron backdonation of Pd compared to  $\beta$ -PdH results in a more side-on adsorption and a weaker  $\text{C}\equiv\text{N}$  bond.

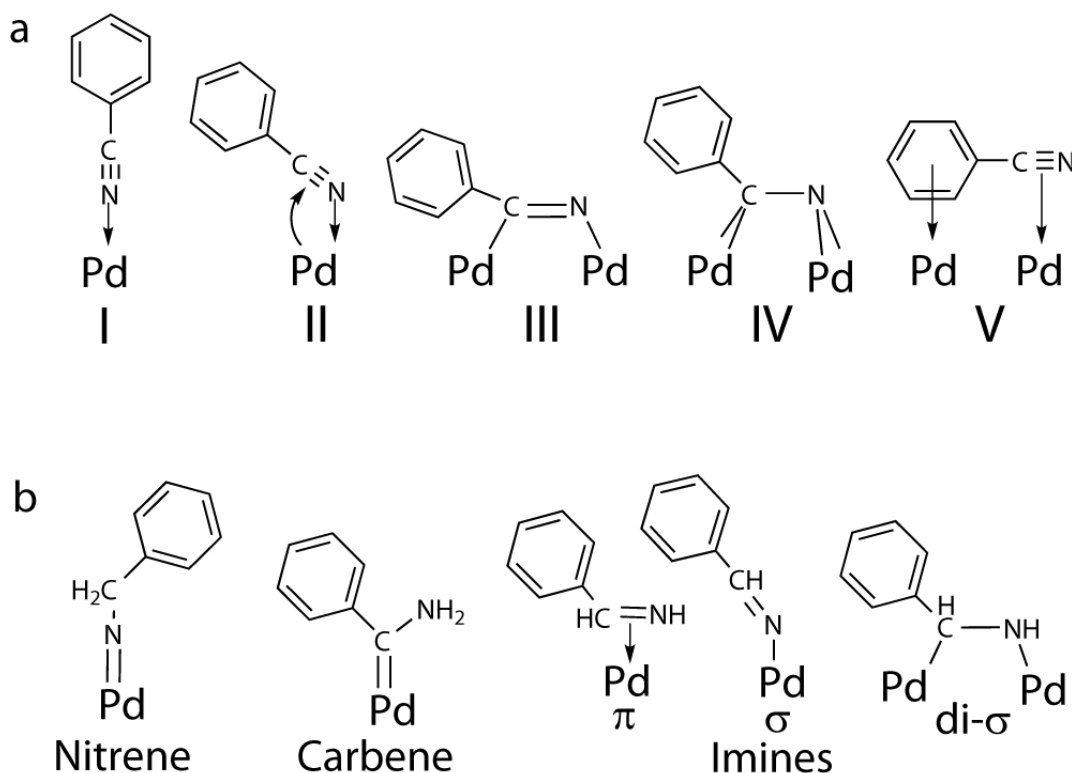


**Fig. 5.10.** (a) Possible adsorption modes of BN on Pd. (I)  $\sigma$  end-on adsorption; (II) side-on adsorption ( $\sigma + \pi$ ); (III) di- $\sigma$  rehybridized; (IV) further rehybridized; (V)  $\pi$ -interactions with phenyl and/or  $\text{C}\equiv\text{N}$  group. (b) Possible intermediate surface species after addition of two hydrogen atoms: nitrene, carbene and three differently coordinated imines:  $\sigma$ ,  $\pi$ , and di- $\sigma$ .

#### *The semi-hydrogenated intermediates*

The most abundant semi-hydrogenated intermediate is BI, although it is not detected in the reaction mixture, because it reacts at the surface to BA without desorbing first [49]. As direct experimental evidence of BI is not reported in literature, other possible surface intermediates might be present after partial hydrogenation of BN with two H atoms, such as nitrenes, carbenes, end-on,  $\pi$ -adsorbed, and rehybridized imines (Fig. 5.10b) [2, 123-128]. Recently,

Schärringer *et al.* found experimental evidence of nitrene intermediates in the hydrogenation of  $\text{CD}_3\text{C}\equiv\text{N}$  over Raney-Co [129]. In addition, interactions of the phenyl group of any of the intermediates with the Pd surface are possible [118]. For instance the most stable calculated adsorption mode for BI on Pd(111) is via a combination of the  $\text{C}=\text{N}$  and phenyl group [130]. A priori, it is not clear which of the intermediates forms BA, DBA, and TOL, and speculations are based on research with aliphatic nitrile hydrogenation without considering hydrogenolysis. For the nitrene intermediate the  $\alpha$ -carbon is already saturated with hydrogen and thus not likely to be involved in one of the above mentioned mechanisms, so nitrene intermediates will only form BA. In principle, the other intermediates can form BA, too, but can also undergo hydrogenolysis or condensation reactions. The most probable reaction pathways to BA, TOL, and DBA are shown in Fig. 5.11.

### *Hydrogenolysis to TOL*

The main byproduct in the hydrogenation of BN was TOL, but above the threshold  $p\text{H}_2$  a sharp decrease in  $S_{\text{TOL}}$  was observed as shown in Fig. 5.3e. From the discussion above, this can be related to the formation of  $\beta$ -PdH with its relatively low backdonation to the adsorbates, thereby reducing the activation of the  $\text{C}\equiv\text{N}$  bond.

I speculate that a multi-coordinated side-on adsorbed intermediate (*i.e.*,  $\sigma/\pi$ -adsorbed imine), with interaction between the delocalized  $\pi$ -electrons of the phenyl ring and the Pd surface, is responsible for the direct hydrogenolysis of BN to TOL (Fig. 5.11). The phenyl group in the vicinity of the  $\text{C}\equiv\text{N}$  group effectively lowers the activation energy towards TOL by stabilizing this adsorption mode internally by conjugation and by coordinating the phenyl group to the Pd surface [118]. This is seen more often in literature: the hydrogenation of  $\text{C}=\text{C}$  and  $\text{C}=\text{O}$  bonds of aromatic molecules over Pd catalysts are activated by the presence of a phenyl group. This phenyl activation implies that the phenyl group adsorbs on active sites [131, 132]. Carbene and nitrene species do not have a  $\pi$ -system so the adsorbate will be more perpendicular orientated to the surface and hydrogenolysis to TOL is less probable.

Hydrogenolysis of BN to TOL is much more facile than hydrogenolysis of BA to TOL over the same supported Pd catalysts and conditions [133]. The rate of hydrogenolysis of BA ( $C_{\text{BA},0} = 520 \text{ mol/m}^3$ ,  $p\text{H}_2 = 10 \text{ bar}$ ,  $T = 80^\circ\text{C}$ ) was 2.6 times lower than for BN and the overall hydrogenation activity was 42 times lower. So, even though BA is an intermediate in the hydrogenolysis of BN to TOL there are differences between the mechanism of BN and BA hydrogenolysis. BA will preferentially adsorb end-on with the lone pair of the nitrogen atom (highest HOMO). This explains the lower hydrogenolysis rate of BA compared to BN,

since for hydrogenolysis of BA interaction is needed with both the phenyl and NH<sub>2</sub> group or with the phenyl ring only [134-137]. I propose a  $\pi$ -benzyl complex as intermediate towards breakage of the C-N bond in BA (Fig. 5.11). An alternative mechanism is that BA first partially dehydrogenates to a hydrogen deficient intermediate, *i.e.*, di- $\sigma$  rehybridized semi-hydrogenated intermediate, followed by the breakage of the C-N bond, similar to that proposed for the hydrogenolysis of methylamines and alkanes [86, 138, 139].

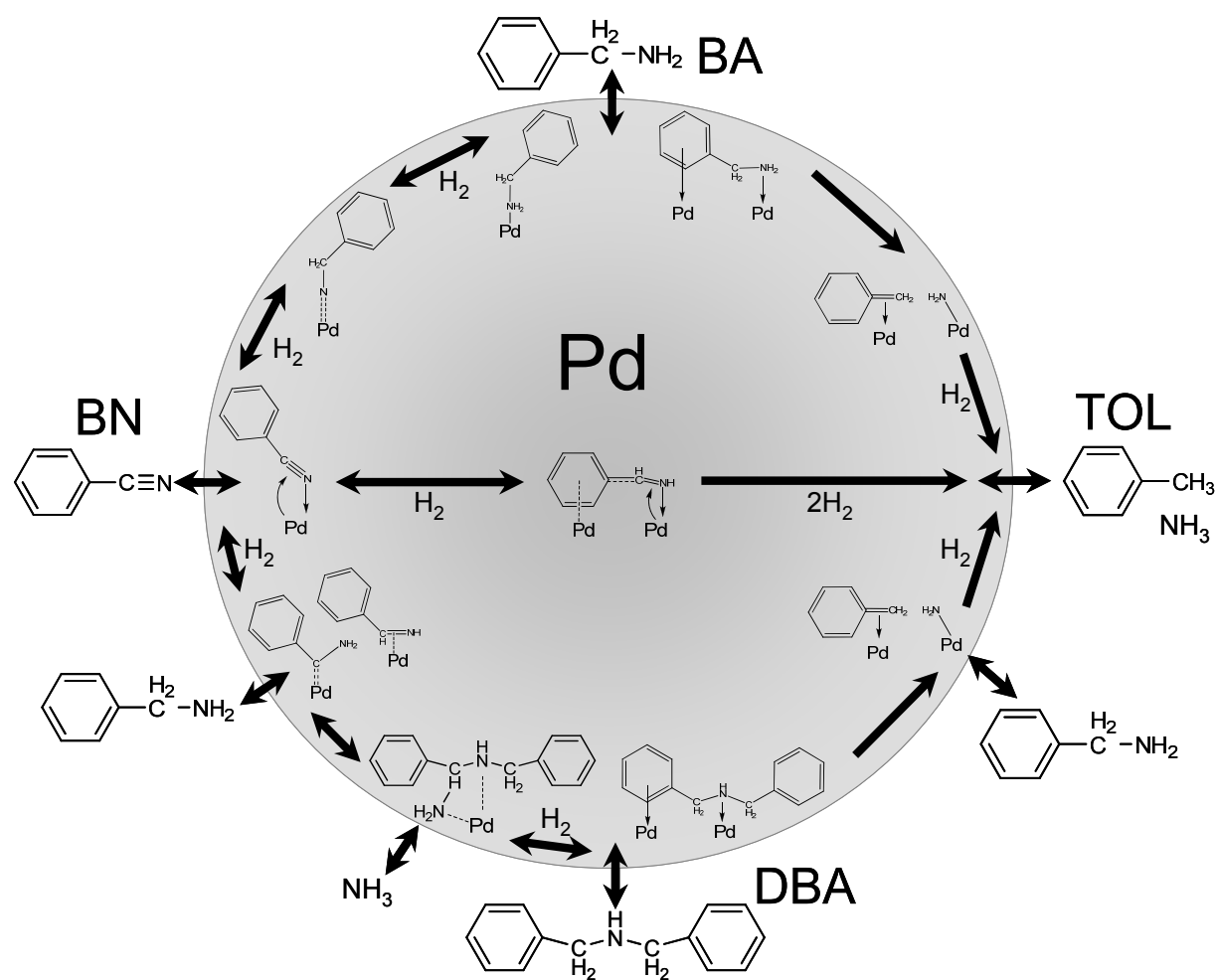


**Fig. 5.11.** Reaction scheme of the hydrogenation of BN showing the reaction pathways towards the products BA, DBA, and TOL. This scheme shows which semi-hydrogenated intermediates are most probable to form BA, DBA, and TOL and shows the multiple pathways to TOL: via BN (direct hydrogenolysis) and via readsorbed BA and DBA (BA and DBA hydrogenolysis). Note that all semi-hydrogenated intermediates (carbene, imine, and nitrene) can form BA (not indicated). The transformation of Pd to  $\beta$ -PdH above the threshold  $pH_2$  decreases the hydrogenolysis to TOL and increases the condensation to DBA.

Note that I propose that DBA forms TOL and BA via a similar mechanism. Furthermore, TOL is formed immediately after the reaction was started (*e.g.*, Fig. 5.2a) which is additional evidence for a direct hydrogenolysis route of BN to TOL via surface intermediates without intermediates (*i.e.*, BA and DBA) desorption [140, 141]. Hydrogenation of an equimolar mixture of BN and BA ( $pH_2 = 10$  bar and  $T = 80^\circ\text{C}$ ) gave 1.7 times lower overall hydrogenation activity and 3.4 times lower hydrogenolysis rate resulting in a higher  $S_{\text{BA}}$ . This shows that BN and BA adsorb competitively on the same active sites but BN adsorbs stronger than BA. Still, BA blocks active sites for BN hydrogenolysis by reducing the probability for multi-coordinated side-on adsorption. This together with the slower BA hydrogenolysis rate compared to BN hydrogenolysis, accounts for the lower  $S_{\text{TOL}}$ .

#### *Condensation to DBA*

Secondary amine formation is usually explained by the nucleophilic attack of a primary amine with the lone pair on the nitrogen atom on an electrophilic carbon atom of semi-hydrogenated intermediate (*i.e.*, imine, carbene, and rehybridized species). The initially *s*-shaped curve of DBA formation (Fig. 5.2a) is typical for a consecutive reaction, *i.e.*, the bimolecular reaction between a semi-hydrogenated intermediate and BA. Carbene and to a lesser extent imine intermediates have the highest probability to form DBA because of the unsaturated electrophilic carbon atom (Fig. 5.11). BIBA is assumed to be the intermediate, although it has never been observed [142].

The low  $S_{\text{DBA}}$ , over the whole investigated  $pH_2$ -range, can be explained by the low nucleophilicity of BA, caused by conjugation effects which delocalize the electron density of nitrogen. It is striking that DBA is the main product when BN is hydrogenated over supported Pt catalysts (Table 5.1). Clearly, the catalyst plays a crucial role in determining selectivity. The difference between Pt and Pd could be explained as follows. Compared to Pt (with a lower  $E_f$ , a lower  $\varepsilon_d$ , and a more extended *d*-band compared to Pd), the Pd surface is populated with semi-hydrogenated intermediates that are much less susceptible to condensation, *i.e.*, nitrenes, and the subsequent desorption of BA is easier. Furthermore, the fast rate of hydrogenation to BA of these intermediates compared to the slow formation from BN result in a low surface coverage.

TOL is the main byproduct:  $Y_{\text{TOL}}$  is always higher than  $Y_{\text{DBA}}$  (Fig. 5.3c). However, above the threshold  $pH_2$   $S_{\text{DBA}}$  becomes higher than  $S_{\text{TOL}}$  (Fig. 5.3e). This is attributed to an increased amount of BA on the surface of  $\beta$ -PdH compared to Pd because of the decreased Pauli

repulsion and the lower  $\varepsilon_d$ . The decreased  $S_{TOL}$  implies also a lower  $\text{NH}_3$  content ( $\text{NH}_3$  suppresses the condensation to DBA [4]). Moreover, the decreased electron backdonation of  $\beta\text{-PdH}$  to an intermediate results in a more electropositive carbon atom, which will be more susceptible to a nucleophilic attack by BA to DBA.

## Conclusions

The influence of hydrogen pressure on the semi-batch hydrogenation of benzonitrile to benzylamine over a  $\gamma$ -alumina-supported palladium catalyst in 2-propanol was investigated to explain the maximum in activity and the selectivity change around a certain hydrogen threshold pressure. An important message of this study for practical operation of selective hydrogenations over palladium catalysts is the careful selection of the operational and activation pressure. An optimum must be sought between activity and selectivity and the active phase structure of palladium. The changed electronic properties of palladium may result in drastic changes in adsorption strengths and modes, and consequently in activity and selectivity.

Other conclusions are

- The main product was benzylamine over the whole investigated pressure range. By-products were toluene and dibenzylamine. A yield of benzylamine up to 90% was reached without any additives.
- Palladium completely transforms into palladium  $\beta$ -hydride above the threshold hydrogen pressure of 10 bar, identified by *ex-situ* XRD. The expansion of the palladium lattice caused by hydrogen incorporation was irreversible at the applied conditions.
- The activation pressure influences the performance of the catalyst if the pressure is high enough to transform palladium into palladium  $\beta$ -hydride during activation. This palladium  $\beta$ -hydride, which is formed during activation, is then stable during hydrogenation at lower hydrogen pressure and results in equal activity and selectivities as hydrogenation at higher hydrogen pressures.

- The palladium  $\beta$ -hydride phase has a lower benzonitrile hydrogenation activity attributed to electronic modifications of the *d*-band of palladium upon the transformation to palladium which decreases the electron backdonation to benzonitrile, resulting in a less activated nitrile group.
- Toluene can be formed directly from benzonitrile and indirectly from readsorbed benzylamine and dibenzylamine. Both direct and indirect hydrogenolysis reactions proceed via different pathways: the rate of hydrogenolysis of benzylamine is slower than that of benzonitrile. Interaction via the  $\pi$ -electrons of the aromatic ring is a prerequisite for facile hydrogenolysis. For palladium  $\beta$ -hydride this interaction is less than for palladium.
- The changed electronic properties of palladium upon the formation of the palladium  $\beta$ -hydride modify the modes and strength of benzonitrile adsorption thereby influencing the type and amount of intermediates, resulting in a changed selectivity
  - Hydrogenolysis to toluene is decreased above the threshold pressure.
  - Condensation to dibenzylamine is increased above the threshold pressure.
- The formation of palladium  $\beta$ -hydride resulted in a higher amount of benzylamine on the surface due to the higher adsorption strength and a decreased benzylamine hydrogenolysis, explaining a higher degree of condensation to dibenzylamine.
- The condensation to dibenzylamine is further enhanced by the lower production of inhibiting ammonia and by the decreased electron backdonation, yielding surface intermediates that are more susceptible to an attack from nucleophiles.

## Bibliography

- [1] S. Nishimura, *Handbook of Heterogeneous Catalytic Hydrogenation for Organic Synthesis*. Wiley-VCH, New York, 2001, 254.
- [2] C. De Bellefon, P. Fouilloux, *Catal. Rev. - Sci. Eng.* 36 (1994) 459.
- [3] J. Volf, J. Pasek in: L. Cerveny, (Ed.), *Catalytic Hydrogenation*, Elsevier, Amsterdam. 1986, 105.
- [4] S. Gomez, J.A. Peters, T. Maschmeyer, *Adv. Synth. Catal.* 344 (2002) 1037.
- [5] P. Sabatier, J.R. Senderens, *C.R. Hebd. Seances Acad. Sci.* 140 (1905) 482.
- [6] G. Mignonac, *C.R. Hebd. Seances Acad. Sci.* 171 (1920) 114.
- [7] J. von Braun, G. Blessing, F. Zobel, *Chem. Ber.* 36 (1923) 1988.
- [8] K. Kindler, F. Hesse, *Arch. Pharm.* 27 (1933) 439.
- [9] H. Greenfield, *Ind. Eng. Chem. Prod. Res. Dev.* 15 (1976) 156.
- [10] Y. Huang, W.M.H. Sachtler, *J. Catal.* 184 (1999) 247.
- [11] P.N. Rylander, *Catalytic Hydrogenation in Organic Syntheses*, 1979, 138.
- [12] P.N. Rylander, L. Hasbrouck, I. Karpenko, *Ann. N. Y. Acad. Sci.* 214 (1973) 100.
- [13] P.N. Rylander, J.G. Kaplan, US Patent 3,117,162, 1964.
- [14] S.P. Bawane, S.B. Sawant, *Chem. Eng. J. (Lausanne)* 103 (2004) 13.
- [15] L. Hegedus, T. Máthé, *Appl. Catal. A* 296 (2005) 209.
- [16] H. Bernas, A. Taskinen, J. Wärnå, D.Y. Murzin, *J. Mol. Catal. A: Chem.* 306 (2009) 33.
- [17] V. Dubois, G. Jannes, J.L. Dallons, A. Van Gysel in: J.R. Kosak, T.A. Johnson, (Eds.), *Catalysis of Organic Reactions*, Marcel Dekker Inc. 1994.
- [18] E.V. Skakunova, M.M. Ermilova, V.M. Gryaznov, *Izv. Akad. Nauk Gruz. SSR, Ser. Khim.* (1988) 986.
- [19] J.H. Sinfelt, *Catal. Lett.* 9 (1991) 159.
- [20] J.H. Sinfelt, *Cat. Rev.* 3 (1969) 175.
- [21] J.H. Sinfelt, *Adv. Catal.* 23 (1973) 91.
- [22] J.H. Sinfelt, J.L. Carter, D.J.C. Yates, *J. Catal.* 24 (1972) 283.
- [23] J.H. Sinfelt, D.J.C. Yates, *J. Catal.* 8 (1967) 82.
- [24] T. Graham, *Philos. Trans. R. Soc.* 156 (1866) 399.
- [25] L.L. Jewell, B.H. Davis, *Appl. Catal. A* 310 (2006) 1.
- [26] N.K. Nag, *J. Phys. Chem. B* 105 (2001) 5945.

- [27] R.J. Davis, S.M. Landry, J.A. Horsley, M. Boudart, *Phys. Rev. B* 39 (1989) 10580.
- [28] K. Christmann in: Z. Paal, P.G. Menon, (Eds.), *Hydrogen Effects in Catalysis. Fundamentals and Practical Applications*, Marcel Dekker Inc., New York. 1988, 44.
- [29] I.P. Chernov, Y.M. Koroteev, V.M. Silkin, Y.I. Tyurin, *Dokl. Phys.* 53 (2008) 318.
- [30] M. Yamauchi, R. Ikeda, H. Kitagawa, M. Takata, *J. Phys. Chem. C* 112 (2008) 3294.
- [31] C.T. Chan, S.G. Louie, *Phys. Rev. B* 27 (1983) 3325.
- [32] J.S. Faulkner, *Phys. Rev. B* 13 (1976) 2391.
- [33] F. Pinna, M. Signoretto, G. Strukul, S. Polizzi, N. Pernicone, *React. Kinet. Catal. Lett.* 60 (1997) 9.
- [34] M. Boudart, H.S. Hwang, *J. Catal.* 39 (1975) 44.
- [35] A.J. Bird, D.T. Thompson in: W.H. Jones, (Ed.), *Catalysis in Organic Syntheses*, Academic Press, New York. 1980, 61.
- [36] A. Valcarcel, F. Morfin, L. Piccolo, *J. Catal.* 263 (2009) 315.
- [37] D. Teschner, J. Borsodi, A. Wootsch, Z. Revay, M. Hävecker, A. Knop-Gericke, S.D. Jackson, R. Schlögl, *Science* 320 (2008) 86.
- [38] D. Teschner, Z. Révay, J. Borsodi, M. Hävecker, A. Knop-Gericke, R. Schlögl, D. Milroy, S.D. Jackson, D. Torres, P. Sautet, *Angew. Chem.* 120 (2008) 9414.
- [39] F. Studt, F. Abild-Pedersen, T. Bligaard, R.Z. Sørensen, C.H. Christensen, J.K. Nørskov, *Angew. Chem. Int. Ed.* 47 (2008) 9299.
- [40] M.P. Jigato, B. Coussens, D.A. King, *J. Chem. Phys.* 118 (2003) 5623.
- [41] Á. Mastalir, Z. Király, F. Berger, *Appl. Catal. A* 269 (2004) 161.
- [42] G. Carturan, G. Facchin, G. Cocco, S. Enzo, G. Navazio, *J. Catal.* 76 (1982) 405.
- [43] H. Greenfield, R.S. Sekellick, US Patent 3,923,891, 1975.
- [44] O.G. Degischer, F. Roessler, P. Rys, *Chem. Ind.: Catal. Org. React.* 82 (2001) 241.
- [45] Y.M. Lopez-De Jesus, A. Vicente, G. Lafaye, P. Marecot, C.T. Williams, *J. Phys. Chem. C* 112 (2008) 13837.
- [46] T. Fuchigami, S. Takamizawa, N. Wakasa, US Patent 6,476,267 B1, 2002.
- [47] M.B. Dines, P.M. DiGiacomo, K.P. Callahan, US Patent 4,384,981, 1983.
- [48] D. Ostgard, M. Berweiler, S. Roder, US Patent 0173676 A1, 2002.
- [49] D.J. Ostgard, *Spec. Chem. Mag.* 28 (2008) 28.
- [50] K. Hata, K. Watanabe, *Bull. Chem. Soc. Jpn.* 32 (1959) 861.

- [51] S. Galvagno, A. Donato, G. Neri, R. Pietropaolo, *J. Mol. Catal.* 58 (1990) 215.
- [52] R.A. Plunkett, J.L. Neff, T.A. Bemish, US Patent 4,163,025, 1979.
- [53] S. Gobolos, N. Mahata, I. Borbath, M. Hegedus, J.L. Margitfalvi, *React. Kinet. Catal. Lett.* 74 (2001) 345.
- [54] O. Domínguez-Quintero, S. Martínez, Y. Henríquez, L. D'Ornelas, H. Krentzien, J. Osuna, *J. Mol. Catal. A: Chem.* 197 (2003) 185.
- [55] H. Paul, S. Basu, S. Bhaduri, G.K. Lahiri, *J. Organomet. Chem.* 689 (2004) 309.
- [56] A.W. Heinen, J.A. Peters, H. Van Bekkum, *Eur. J. Org. Chem.* (2000) 2501.
- [57] S. Enthaler, K. Junge, D. Addis, G. Erre, M. Beller, *ChemSusChem* 1 (2008) 1006.
- [58] C. Amorim, M.A. Keane, *J. Colloid Interface Sci.* 322 (2008) 196.
- [59] G. Fagherazzi, A. Benedetti, S. Polizzi, A. Mario, F. Pinna, M. Signoretto, N. Pernicone, *Catal. Lett.* 32 (1995) 293.
- [60] J. Sa, G.D. Arteaga, R.A. Daley, J. Bernardi, J.A. Anderson, *J. Phys. Chem. B* 110 (2006) 17090.
- [61] S. Huang, C. Huang, B. Chang, C. Yeh, *J. Phys. Chem. B* 110 (2006) 21783.
- [62] A.R. Denton, N.W. Ashcroft, *Phys. Rev. A* 43 (1991) 3161.
- [63] E.F. Skelton, P.L. Hagans, S.B. Qadri, D.D. Dominguez, A.C. Ehrlich, J.Z. Hu, *Phys. Rev. B* 58 (1998) 14775.
- [64] Z. Kaszkur, *J. Appl. Crystallogr.* 33 (2000) 1262.
- [65] C.M. Mendez, H. Olivero, D.E. Damiani, M.A. Volpe, *Appl. Catal. B* 84 (2008) 156.
- [66] N.S. Babu, N. Lingaiah, R. Gopinath, P.S. Sankar Reddy, P.S. Sai Prasad, *J. Phys. Chem. C* 111 (2007) 6447.
- [67] J. Panpranot, K. Pattamakomsan, P. Praserthdam, J.G. Goodwin, *Ind. Eng. Chem. Res.* 43 (2004) 6014.
- [68] J. Panpranot, O. Tangjittwattakorn, P. Praserthdam, J.G. Goodwin Jr, *Appl. Catal. A* 292 (2005) 322.
- [69] H. Lieske, J. Voelter, *J. Phys. Chem.* 89 (1985) 1841.
- [70] M. Gurrath, T. Kuretzky, H.P. Boehm, L.B. Okhlopkova, A.S. Lisitsyn, V.A. Likhlobov, *Carbon* 38 (2000) 1241.
- [71] B. Wen, Q. Sun, W.M.H. Sachtler, *J. Catal.* 204 (2001) 314.

[72] M. Bonarowska, J. Pielaśzek, W. Juszczysz, Z. Karpinski, *J. Catal.* 195 (2000) 304.

[73] H. Knoezinger, H. Krietenbrink, *J. Chem. Soc. Faraday Trans.* 71 (1975) 2421.

[74] R.A. Nyquist, *Appl. Spectrosc.* 44 (1990) 1405.

[75] H. Sato, Y. Kusumoto, S. Arase, M. Suenaga, S. Kammura, *J. Phys. Chem.* 82 (1978) 66.

[76] P. Hirva, T.A. Pakkanen, *Surf. Sci.* 277 (1992) 389.

[77] M. Skotak, Z. Karpinski, W. Juszczysz, J. Pielaśzek, L. Kepinski, D.V. Kazachkin, V.I. Kovalchuk, J.L. d'Itri, *J. Catal.* 227 (2004) 11.

[78] A. Quintanilla, J.J.W. Bakker, M.T. Kreutzer, J.A. Moulijn, F. Kapteijn, *J. Catal.* 257 (2008) 55.

[79] W.J. Kim, E.W. Shin, J.H. Kang, S.H. Moon, *Appl. Catal. A* 251 (2003) 305.

[80] P. Marécot, A. Akhachane, J. Barbier, *Catal. Lett.* 36 (1996) 37.

[81] J.-W. Park, Y.-M. Chung, Y.-W. Suh, H.-K. Rhee, *Catal. Today* 93-95 (2004) 445.

[82] M.R. Othman, I.S. Sahadan, *Microporous Mesoporous Mater.* 91 (2006) 145.

[83] F. Figueras, B. Coq, *J. Mol. Catal. A: Chem.* 173 (2001) 223.

[84] G. Meitzner, W.J. Mykytka, J.H. Sinfelt, *J. Catal.* 98 (1986) 513.

[85] G. Meitzner, W.J. Mykytka, J.H. Sinfelt, *Catal. Lett.* 37 (1996) 137.

[86] G. Meitzner, W.J. Mykytka, J.H. Sinfelt, *Catal. Lett.* 32 (1995) 335.

[87] L. Guczi, A. Sarkany, P. Tetenyi, *J. Chem. Soc. Faraday Trans.* 70 (1974) 1971.

[88] A. Pundt, R. Kirchheim, *Annu. Rev. Mater. Res.* 36 (2006) 555-608.

[89] A. Pundt, M. Suleiman, C. Bähtz, M.T. Reetz, R. Kirchheim, N.M. Jisrawi, *Mat. Sci. Eng. B* 108 (2004) 19.

[90] P.C. Aben, *J. Catal.* 10 (1968) 224.

[91] I.T. Caga, E. Shutt, J.M. Winterbottom, *J. Catal.* 44 (1976) 271.

[92] E.A. Owen, J.I. Jones, *Proc. Phys. Soc.* 49 (1937) 603.

[93] S.B. Ziemecki, G.A. Jones, *J. Catal.* 95 (1985) 621.

[94] E.J.A.X. van de Sandt, A. Wiersma, M. Makkee, H. van Bekkum, J.A. Moulijn, *Appl. Catal. A* 155 (1997) 59.

[95] D. Teschner, E. Vass, M. Havecker, S. Zafeiratos, P. Schnorch, H. Sauer, A. Knop-Gericke, R. Schloegl, M. Chamam, A. Wootsch, A.S. Canning, J.J. Gamman, S.D. Jackson, J. McGregor, L.F. Gladden, *J. Catal.* 242 (2006) 26.

- [96] D. Teschner, J. Borsodi, Z. Kis, L. Szentmiklosi, Z. Revay, A. Knop-Gericke, R. Schlogl, D. Torres, P. Sautet, *J. Phys. Chem. C* 114 (2010) 2293.
- [97] N. Seriani, F. Mittendorfer, G. Kresse, *J. Chem. Phys.* 132 (2010) 1.
- [98] P. Sautet, F. Cinquini, *ChemCatChem* 2 (2010) 636.
- [99] M. García-Mota, B. Bridier, J. Pérez-Ramírez, N. López, *J. Catal.* 273 (2010) 92.
- [100] J. Andersin, N. Lopez, K. Honkala, *J. Phys. Chem. C* 113 (2009) 8278.
- [101] D.A. Papaconstantopoulos, B.M. Klein, J.S. Faulkner, L.L. Boyer, *Phys. Rev. B* 18 (1978) 2784.
- [102] S. Mizusaki, N. Hiraoka, I. Yamamoto, M. Itou, Y. Sakurai, M. Yamaguchi, *J. Phys. Soc. Jpn.* 72 (2003) 1145.
- [103] D.E. Eastman, J.K. Cashion, A.C. Switendick, *Phys. Rev. Lett.* 27 (1971) 35.
- [104] W. Jaworski, *J. Phys. F: Met. Phys.* 17 (1987) 373.
- [105] M. Gupta, A.J. Freeman, *Phys. Rev. B* 17 (1978) 3029.
- [106] B. Hammer, J.K. Nørskov, *Surf. Sci.* 343 (1995) 211.
- [107] B. Hammer, J.K. Nørskov, *Nature* 376 (1995) 238.
- [108] A. Ruban, B. Hammer, P. Stoltze, H.L. Skriver, J.K. Nørskov, *J. Mol. Catal. A: Chem.* 115 (1997) 421.
- [109] P. Liu, J.K. Nørskov, *Phys. Chem. Chem. Phys.* 3 (2001) 3814.
- [110] P. Gallezot, D. Richard, *Catal. Rev. -Sci. Eng.* 40 (1998) 81.
- [111] B.A. Averill, I.M.C.M. Rietjens, P.W.N.M. Van Leeuwen, R.A. Van Santen, *Stud. Surf. Sci. Catal.* 123 (1999) 109.
- [112] G. Blyholder, *J. Phys. Chem.* 68 (1964) 2772.
- [113] T. Bligaard, J.K. Nørskov, *Chemical Bonding at Surfaces and Interfaces*. Elsevier, Amsterdam, 2008, 255.
- [114] I. Chorkendorff, J.W. Niemantsverdriet, *Concepts of Modern Catalysis and Kinetics*. WILEY-VCH Weinheim, 2003, 215.
- [115] K. Kishi, F. Kikui, S. Ikeda, *Surf. Sci.* 99 (1980) 405.
- [116] T. Nakayama, K. Inamura, Y. Inoue, S. Ikeda, K. Kishi, *Surf. Sci.* 179 (1987) 47.
- [117] O. Oranskaya, I. Semenskaya, V. Filimonov, *React. Kinet. Catal. Lett.* 5 (1976) 135.
- [118] S. Zou, C.T. Williams, E.K.Y. Chen, M.J. Weaver, *J. Phys. Chem. B* 102 (1998) 9039.

- [119] K.F. Purcell, R.S. Drago, *J. Am. Chem. Soc.* 88 (1966) 919.
- [120] E. Paukstis, E.N. Yurchenko, *Usp. Khim.* 52 (1983) 426.
- [121] O.M. Oranskaya, V.N. Filimonov, E.Y. Shmulyakovskii, *Vopr. Mol. Spektrosk.* (1974) 195.
- [122] J. Raskó, J. Kiss, *Appl. Catal. A* 298 (2006) 115.
- [123] A. Chojecki, H. Jobic, A. Jentys, T.E. Müller, J.A. Lercher, *Catal. Lett.* 97 (2004) 155.
- [124] A. Chojecki, M. Veprek-Heijman, T.E. Müller, P. Schärringer, S. Veprek, J.A. Lercher, *J. Catal.* 245 (2007) 237.
- [125] B. Coq, D. Tichit, S. Ribet, *J. Catal.* 189 (2000) 117.
- [126] B. Bigot, F. Delbecq, A. Milet, V.-H. Peuch, *J. Catal.* 159 (1996) 383.
- [127] P. Schärringer, T.E. Müller, J.A. Lercher, *J. Catal.* 253 (2008) 167.
- [128] J. Krupka, J. Patera, *Appl. Catal. A* 330 (2007) 96.
- [129] P. Schärringer, T.E. Müller, A. Jentys, J.A. Lercher, *J. Catal.* 263 (2009) 34.
- [130] L. Hegedus, T. Máthé, T. Kárpáti, *Appl. Catal. A* 349 (2008) 40.
- [131] J. Jenck, J.-E. Germain, *J. Catal.* 65 (1980) 141.
- [132] J.L. Dallons, G. Jannes, B. Delmon, *Catal. Today* 5 (1989) 257.
- [133] W.F. Maier, P. Grubmüller, I. Thies, P.M. Stein, M.A. McKervey, P.v.R. Schleyer, *Angew. Chem. Int. Ed.* 18 (1979) 939.
- [134] S. Mitsui, Y. Sugi, *Tetrahedron Lett.* 10 (1969) 1291.
- [135] Y. Sugi, S. Mitsui, *Tetrahedron* 29 (1973) 2041.
- [136] C.Ó. Murchú, *Tetrahedron Lett.* 10 (1969) 3231.
- [137] K. Ikeda, S. Suzuki, *Nippon Kagaku Kaishi* (1975) 234.
- [138] D.F. Johnson, Y. Wang, J.E. Parmeter, M.M. Hills, W.H. Weinberg, *J. Am. Chem. Soc.* 114 (1992) 4279.
- [139] J.R. Anderson, N.J. Clark, *J. Catal.* 5 (1966) 250.
- [140] M. Jian, F. Kapteijn, R. Prins, *J. Catal.* 168 (1997) 491.
- [141] T. Vergunst, F. Kapteijn, J.A. Moulijn, *Catal. Today* 66 (2001) 381.
- [142] Y. Huang, W.M.H. Sachtler, *Appl. Catal. A* 182 (1999) 365.



## **Appendix B - Supporting Information to Chapter 5**

### Check on internal and external mass transport limitations

To exclude that gas-liquid mass transfer limitations disguised my results, preliminary runs under different stirrer conditions were conducted. These experiments showed that above 1000 rpm the reaction rate was invariant to stirrer speed [1]. So, above 1000 rpm external mass transfer limitations were absent. The stirrer speed was maintained at 2000 rpm during all experiments. Criteria were applied to check for the presence of intra-particle diffusion limitations and external liquid-solid transport limitations. Next to the observed reaction rates liquid-solid mass transfer coefficients in semi-batch slurry reactors were used to determine the Carberry numbers ( $Ca$ ) for  $H_2$  and BN at the range of experimental conditions.  $Ca$  is defined as

$$Ca = \frac{r_{v,obs}}{k \cdot a \cdot C_B} = \frac{C_B - C_S}{C_B} < \frac{0.05}{|n|} \quad (B1)$$

where  $r_{v,obs}$  = observed rate,  $k$  = mass transfer coefficient,  $a$  = specific area ( $A/V$ ),  $C_B$  = bulk concentration,  $C_S$  = the surface concentration, and  $n$  = reaction order. The Weisz-Prater criterion  $\Phi$  was determined for  $H_2$  and BN by estimating the  $H_2$  concentration and diffusion coefficient in 2-propanol using averaged experimentally determined Henry's law constants and diffusion coefficients [2-6].  $\Phi$  is defined as

$$\Phi = \frac{r_{v,obs} \cdot L^2}{D_{eff} \cdot C_S} \left( \frac{n+1}{2} \right) < 0.15 \quad (B2)$$

where  $L$  = characteristic length ( $1/a$ ) and  $D_{eff}$  = effective diffusion coefficient. The diffusion coefficient of BN was estimated using a modified Wilke-Chang equation and compared with diffusion coefficients from similar molecules in 2-propanol using the molar volume of BN, estimated with the Tyn and Calus method [7-9]. Effective diffusion coefficients were estimated using catalyst porosity and tortuosity ( $D_{eff} = \varepsilon_p / \tau_p \cdot D$ ). The calculations showed the absence of external liquid-solid ( $Ca < 0.05/|n|$ ) and internal transport ( $\Phi < 0.15$ ) limitations of both  $H_2$  and BN [10].

From phase equilibrium calculations of mixtures of BN, BA, TOL, NH<sub>3</sub>, H<sub>2</sub>, and 2-propanol with different molar compositions, using Aspen Plus® from Aspen Technology, Inc. (<http://www.aspentechn.com>) by applying several thermodynamic models in a flash unit operation, it was calculated that at most experimental conditions the molar composition of the gas phase is > 95% H<sub>2</sub>. However, at a *p*H<sub>2</sub> of 2.5 bar, the gas phase is somewhat diluted (74% H<sub>2</sub>, 19% 2-propanol, and 7% NH<sub>3</sub>). BN, BA, and TOL are completely dissolved in the liquid phase under all applied experimental conditions and the concentration of H<sub>2</sub> in the liquid phase at 10 bar and 80°C is ~ 47 mol/m<sup>3</sup>.

### **Details of catalyst characterization techniques applied**

X-ray powder diffraction was performed on an X-Pert Philips MPD system employing Cu K $\alpha$  radiation. X-ray powder diffraction patterns of reduced samples have been recorded with a X-Pert Philips diffractometer (Cu  $K_{\alpha}$  radiation,  $\lambda = 1.5418 \text{ \AA}$ ) with 0.03° steps in a range from 15° to 100° 2 $\theta$  (Bragg's angle) with counting time equal to 4 s per step. The observed diffraction intensities have been compared to those calculated using the Pulverix program [11], and the values of the lattice parameters were refined using a least-squares routine. Crystalline phases were identified by references to the ASTM data files.

Temperature programmed reduction (TPR) was carried out in a TPR set-up equipped with a TCD (thermal conductivity detector). Catalyst samples (~ 165 mg) were exposed to 6% H<sub>2</sub>/Ar gas mixture with a total flow of 27 ml/min and were left at room temperature for 5 min and subsequently heated to 200°C at 5°C/min.

The catalysts were analyzed by inductively coupled plasma optical emission spectroscopy (ICP-OES) performed in the Perkin-Elmer Optima 5300 to determine the content of Pd. The catalyst samples are recovered in duplicate in a mixture of 1% hydrofluoric acid and 2.5% sulfuric acid. After a hydrogenation experiment, the amount of Pd in the spent catalyst samples was determined to check if leaching into the reaction mixture had occurred.

Diffuse reflectance infrared Fourier transform (DRIFT) spectra were recorded with a single beam Nicolet Magna 550 FTIR spectrometer in a Spectratech DRIFTS accessory, against a KBr background. The DRIFT chamber was flushed with N<sub>2</sub>. The spectra were obtained by collecting 64 scans at 8 cm<sup>-1</sup> resolution and displayed in absorption reflectance units.

Thermal gravimetric analysis (TGA) was performed on a Mettler-Toledo TGA/SDTA851<sup>e</sup> thermobalance. The sample powders were heated in air from room temperature to 900°C at a heating rate of 10°C/min.

CO adsorption measurements are performed at 35°C using CO as adsorptive and assuming a Pd/CO = 1:1 stoichiometry and spherical crystallite shape. Prior to chemisorption of CO, a sample is first dried in vacuum at 130°C (this sample weight is used in the calculations). Subsequently the sample is reduced (100% H<sub>2</sub>, 50 ml/min, 2 h) at 80°C, followed by evacuation (2 h) at 130°C. Both the *in-situ* pretreatment and the analysis are performed on the Quantachrome Autosorb-1C.

Prior to N<sub>2</sub> adsorption and desorption measurements, the samples were dried in vacuum at 130°C in order to remove moisture and other volatile components (this sample weight is used in the calculations). After pre-treatment, the N<sub>2</sub> adsorption and desorption isotherms were measured at -196°C on the Quantachrome Autosorb-6B. The isotherms provided information on the specific surface area (S<sub>BET</sub>), the pore volume (V<sub>p</sub>), the pore diameter (d<sub>p</sub>), and the micropore content.

Transmission electron microscopy (TEM) was performed using a Philips CM30UT electron microscope with a LaB6 filament as the source of electrons, both operated at 300 kV. Samples were mounted on Quantifoil microgrid carbon polymer supported on a copper grid by placing a few droplets of a suspension of ground sample in ethanol on the grid, followed by drying at ambient conditions.

The particle size of the  $\gamma$ -Al<sub>2</sub>O<sub>3</sub> was determined by laser diffraction in a Mastersizer S (Malvern Instruments Ltd.). The range of this apparatus is 0.04 – 3500  $\mu$ m. The Mastersizer S contains a 5 mW He Ne lasertube ( $\lambda$  = 632.8 nm), a standard detector, nine forward detectors, and a backscattering detector. Alignment is done automatically and 5000 sweeps are used for analysis. The relative standard deviation of this analysis is < 5%. The samples were measured before and after they had been put in an ultrasonic bath.

## Bibliography

- [1] M.M.P. Zieverink, M.T. Kreutzer, F. Kapteijn, J.A. Moulijn, *Ind. Eng. Chem. Res.* 45 (2006) 4574.
- [2] I.T. Caga, E. Shutt, J.M. Winterbottom, *J. Catal.* 44 (1976) 271.
- [3] T. Katayama, T. Nitta, *J. Chem. Eng. Data* 21 (1976) 194.
- [4] M.S. Wainwright, T. Ahn, D.L. Trimm, N.W. Cant, *J. Chem. Eng. Data* 32 (1987) 22.
- [5] E. Sada, S. Kito, T. Oda, Y. Ito, *Chem. Eng. J.* 10 (1975) 155.
- [6] K. Sporka, J. Hanika, V. Ruzicka, *Collect. Czech. Chem. Commun.* 34 (1969) 3145.
- [7] C.R. Wilke, P. Chang, *AIChE J.* 1 (1955) 264.
- [8] M.A. Lusis, G.A. Ratcliff, *AIChE J.* 17 (1971) 1492.
- [9] M.T. Tyn, W.F. Calus, *Processing* 21 (1975) 16.
- [10] F. Kapteijn, J.A. Moulijn in: G. Ertl, H. Knözinger, F. Schüth, J. Weitkamp (Eds.), *Handbook of heterogeneous catalysis*, Wiley VCH, Weinheim. 2008, 2019.
- [11] K. Yvon, W. Jeitschko, E. Parthé, *J. Appl. Crystallogr.* 10 (1977) 73.



# 6

## Evaluation

---

The multidisciplinary catalysis engineering research presented in this PhD thesis, focused on structure-performance relationships of supported palladium catalysis on all length scales, governed by both intrinsic and extrinsic effects, for heterogeneous hydrogenations carried out in monolithic, capillaries, and slurry multiphase reactors. The word *structure* used in the previous sentence can have several meanings as will be explained below. This Chapter evaluates the main results obtained during my PhD research.

---

## **Tuning wall properties of structured monolithic palladium catalysts – hydrodynamic properties and extrinsic effect governing performance**

I first investigated *structure* on a macroscopic and mesoscopic scale. In particular, I was interested in the relation between the macroporous structure, mass transfer, and performance. I investigated open, macroporous acicular mullite (ACM) monolithic supports and dense, mesoporous cordierite monolithic supports. The multiphase fluid mechanics were indeed different for these ACM and cordierite monoliths: in contrast to the classical cordierite system, the mass exchange between static liquid and dynamic liquid was much faster and the liquid phase could access the open volume of the permeable ACM monolith wall. The improved mass transfer was measured first by RTD experiments and later confirmed in reactive hydrogenation experiments. This favorable result opens an avenue to the synthesis of monolithic structures with higher catalyst loadings. However, this improvement occurred at the expense of reduced plug flow behavior. Moreover, optimization of several critical catalyst preparation steps was required to prevent the open wall structure of the ACM monolithic supports from filling up. Clearly, it is possible to use an open pore structure to enhance mass transfer which increases catalyst performance under internal transport limited conditions. It remains needed to create a pulsating flow. Particularly elegant about the approach was the use of pressure pulses of passing bubbles, which is much simpler than earlier research using external pulsing pumps [1].

### *Adoption by industry*

The use of *structured* monolithic reactors in general [2] in industry for fast multiphase (hydrogenation) reactions can have a great impact on process intensification and would allow large improvements to be made with respect to reactor performance. However, the cost of replacement of old reactor gear and knowhow in combination with the cost and required detailed knowledge of the art of preparation of ‘expensive’ monolithic reactors is still a bottleneck for industry. This is in contrast to the use of monolithic reactors for gas phase reactions since for these reactions the use of monoliths is standard in the automotive industry, compared to the chemical industry a huge market. Hence, it can be concluded that the cost do not need to be prohibitive. By further optimizing monolithic reactors for multiphase reactions to even higher performance and increasing the usually low catalyst density per reactor volume

by for example the proper use of the walls can greatly improve the long run economical benefits of using monolithic reactors instead of packed bed reactors. Thus, it is expected that the application of monolithic reactors in many industrial application will be feasible, provided that monoliths, improved as described here, will be commercially available. In this thesis, the hydrodynamic performance, catalyst preparation & characterization, and performance testing of a new type of monolith with structured “open walls” was evaluated for fast hydrogenation reactions. These monoliths were carefully coated with a thin catalytic layer of silica-supported palladium and compared with classical cordierite monoliths coated silica-supported palladium in a selective hydrogenation reaction of an alkynic alcohol to its alkenic product without overhydrogenation to the alkane. Structuring the walls of monolithic bodies greatly enhanced the extrinsic performance of a palladium catalyst when operated under internally diffusion limited conditions.

### **The use of commercially available capillaries as flow device for evaluation of intrinsic performance of a supported palladium catalyst located on the wall**

I investigated the use of commercially available gas chromatography fused-silica capillary columns coated with a thin  $\gamma$ -alumina layer, which I subsequently impregnated with palladium, as continuous-flow devices. The use of these capillaries resulted in rapid information about palladium catalyzed hydrogenation reactions in them and allowed a fast optimization of various aspects of heterogeneous catalysis and synthesis routes, such as solvent effects, competitive adsorption, and irreversible poisoning. The proof of principle of this new flow device was established by presenting several relevant examples of liquid-phase hydrogenation reactions. I performed these hydrogenation reactions in the *structured* Taylor flow regime to exemplify that visual observation allowed fast determination and optimization of various aspects of heterogeneous catalysis. Aside from the obvious advantages of using Taylor flow, the structured flow of separate gas and liquid slugs gives relevant information about (1) residence times resulting in rate determination from conversion data, (2) visible determination of conversion by measuring decreasing hydrogen gas bubble sizes, and (3) reactor behavior, *i.e.*, integral or differential behavior detection again by visible decreasing bubble sizes over the full length of the flow device, which gives hands-on control over the activity and deactivation of the catalyst and accelerates optimization of continuous-flow hydrogenations using heterogeneous catalysis. These visible features of Taylor flow under

reaction conditions can be used in labscale multiphase heterogeneous catalysis. Further, I demonstrated how to quickly identify deactivating species in multistep synthesis without intermediate workup. The relatively young science of flow chemistry is destined to have great impact on the benchscale operation of screening catalysts, performance testing and for small volume processing of fine chemistry applications, and the productions of chemicals via dangerous intermediates. The new flow device presented in this thesis, is a useful addition to the benchscale reactor inventory of chemists, scientists, and chemical engineers.

#### *Limitations and possibilities*

The major advantage of using palladium is the high reducibility (reduces at room temperature) and high oxidation resistance (slow transition of cubic Pd into hexagonal PdO). However, a limitation of this type of flow device is the limited maximum temperature of the outer capillary coating (*i.e.*, polyimide applied for flexibility) of around 350°C in air (up to 400°C in a N<sub>2</sub> atmosphere). This limits the maximum allowable calcination and regeneration temperatures during the catalyst preparation stage and in-between consecutive runs, respectively. Therefore, the use of catalyst precursors containing chloride ligands instead of organic ligand precursors (relatively easy to remove by calcination at moderate temperatures) is not recommended as chloride species will be very strongly bound to the support and this could result in negative influence on catalyst performance. The regeneration step in-between runs to remove strongly adsorbed species needs to be carefully investigated since high-temperature regeneration is not possible. The possibility to flush with other solvents to desorb poisonous species could be an interesting option to investigate. Furthermore, the use of other metals to catalyze hydrogenation reactions that require high activation temperatures in an atmosphere of hydrogen and tedious passivation (*e.g.*, platinum, ruthenium or nickel) will be limited although low temperature reduction using a strong chemical reductant is an option. Alternatively, one could produce colloidal nanoparticles of a desired metal catalyst, which are in the reduced state but protected by capping agents. By carefully selecting and applying the proper capping agent (*e.g.*, nitrogen-based, weakly adsorbing) one can obtain high activity and selectivity [4].

Another drawback is the limited possibility to characterize the fresh and spent catalyst compared to slurry catalysts, since the low loading of noble metal (catalyst support + fused silica + polyimide) is often close to the detection limit of the applied characterization techniques. There is also the added possibility of maldistribution (catalytic material distribution, support layer thickness) across the length of the capillary similar to other

macroscopic bodies both for the support and active catalytic species, although that can usually be directly observed (for higher loadings) by color gradation down the capillary length or by cutting a capillary in several pieces of equal length and then compare their activity under kinetically controlled conditions. I noticed that such gradients mostly occur at the ends, which I cut off after preparation and excluded from further analysis or use. Since, the GC suppliers are specialized in pretreatment and subsequently coating fused silica capillaries with for example  $\gamma$ -alumina, it would be of interest to reduce the workload to cooperate with them on the possibilities of applying other coatings (*e.g.*, high-surface area  $\text{SiO}_2$ ,  $\text{TiO}_2$ ,  $\text{MgO}$ ,  $\text{CeO}_2$ ) since these type of supports normally used in catalysis are not commercially available. Note that all these disadvantages mentioned above also apply to catalysis in microchips as flow devices.

The methodology of visual observation of bubble shrinkage to follow chemistry can easily be extended to other processes, *e.g.*, solubility and diffusion of  $\text{CO}_2$  as has been shown by Lefortier [5], but could also be applied in, *e.g.*, fermentation reactions where the conversion of yeast can be followed by the growth of  $\text{CO}_2$  bubbles. Another microfluidic example is shown by Li and co-workers [6] where  $\text{CO}_2$  bubble shrinkage is used to determine rate constants and conversion of a fast gas-liquid reaction with secondary amines. A limitation of the ‘visual observation of chemistry by bubble shrinkage’ methodology becomes clear when there is also gas formation, as I demonstrated in one of the hydrogenation examples (azide hydrogenation) where also a gaseous reactant is formed ( $\text{N}_2$  formation). Then this method cannot be applied.

#### *Multi-step synthesis with hazardous intermediates*

One of the major problems of flow chemistry, if one-pot synthesis is not possible, is the workup in-between reaction steps of a multi-step process. A typical chemical synthesis in flow devices involves multiple reaction steps with an off-line separation step (workup) in-between them. These workup steps are expensive, tedious, time consuming and can produce wastes of hazardous intermediates, as shown by the research on azides of Jensen and co-workers [7]. Here, I demonstrated, as part of a multi-step process to synthesize amines from hazardous intermediates (azides), that it is possible to produce the desired amine without intermediate workup by carefully choosing the proper leaving group in combination with a proper solvent. Micro-separation is, in comparison with micro-reaction, still in its infancy, and a lot of further research is needed. As a recent industrial patent shows, it now makes commercial sense to avoid intermediate work-up [8]. This methodology could be applied to

numerous other multi-step chemical syntheses where one wants to render the workup obsolete and diminish the ‘lifetime’ of dangerous and hazardous intermediates.

*Comparing catalytic studies with each other*

Comparing results of catalytic performance studies, focusing here on palladium-catalyzed hydrogenations of alkynes, should be done with great caution, since obtained activities and selectivities depend on numerous factors, notably on

- The palladium dispersion; smaller crystallites are more electron deficient and adsorb alkynic species stronger than bigger crystallites, thereby decreasing the rate. Furthermore, crystallite size influences ensemble effects, possible hydride formation, coordination number, distribution of active sites (plane/edge site ratio) and spillover effects.
- The applied support; amount and type of surface groups, impurities, and metal-support interactions can influence selectivity and activity.
- The atomic alkyne/Pd ratios; unoccupied active sites reduce selectivity: alkene can adsorb.
- The atomic hydrogen/alkyne ratios; hydrogen limitation increases selectivity towards the intermediate product and influence possible hydride/carbide formation.
- The history and pretreatment of the catalyst; fresh/spent, ligand residue can influence performance and subsurface composition determines performance, in particular for alkynic species as proven by Teschner and co-workers [3].
- The absolute hydrogen concentration and temperature; can influence the palladium phase.
- The solvent used and temperature of reaction.

## Catalyst performance changes induced by palladium phase transformation -Intrinsic microscopic effect governing performance

I studied the influence of hydrogen pressure on the performance of a  $\gamma$ -alumina-supported palladium catalyst for the multiphase selective hydrogenation of benzonitrile to benzylamine and byproducts. I demonstrated that the intrinsic microscopic property of palladium to absorb hydrogen into its lattice structure has a strong influence on activity and selectivity in the selective hydrogenation of an aromatic nitrile to its primary amine. The transformation of the intrinsic palladium *structure* to stable palladium  $\beta$ -hydride above a threshold hydrogen pressure induces a persistent change in performance attributed to modified electronic interactions between catalyst and reactants. The change in palladium to its hydride (or carbide structure) under reaction conditions is often observed for many different hydrogenation reactions. However, in my case this crystal phase is still visible after reaction (shown by ex-situ XRD) and I demonstrated that this phase change that occurred during the activation step was stable under reaction conditions at lower hydrogen pressures. The structure of palladium is thus mainly determined by the activation or operational hydrogen pressure, whichever was the highest. The rule of thumb that a hydrogenation reaction is first order in hydrogen must thus be applied with care when utilizing a palladium catalyst. By selecting the proper conditions, *e.g.*, by altering hydrogen pressure one can reduce, by a large extent, the selectivity to the unwanted product. This observation is a lead in R&D aiming at improvements for other palladium catalyzed hydrogenations. Activation conditions in an elevated hydrogen pressure environment prior to hydrogenation can thus have great impact on the palladium state under reactions conditions. Therefore, in palladium catalysis carefully choosing the activation conditions is a must.

The change in performance was explained by combining the metal *d*-band model of reactivity and simple frontier electron orbital theory. The combination of these theoretical models, and the observations presented in literature that the *d*-band centre decreases in energy and decreases in width, enabled the interpretation of the observed reactivity and selectivity changes. Thus, I could fully explain the change in catalytic behavior upon phase transformation. In contrast, in the *d*-band model, it is common that a decrease in *d*-band width is accompanied by a shift *upwards* in energy of the *d*-band centre (more reactive) which is caused for example by an increase in lattice spacing. However, for this specific case the *d*-band of palladium is also modified by the interaction with absorbed hydrogen.

I proposed a mechanism including surface intermediates for the hydrogenation of benzonitrile catalyzed by the  $\gamma$ -alumina-supported palladium that elucidated the reaction pathways towards the observed products. Note that this mechanism is applicable to benzonitrile on palladium only and cannot be extrapolated to other aromatic or aliphatic nitriles because the mutual interaction of the benzene ring and the nitrile group multicoordinated side-on adsorbed on the palladium surface determines the selectivity to certain products. Hence, when palladium is applied in aliphatic nitrile hydrogenation mostly secondary amines are formed with very low selectivity to the desired primary amine. Furthermore, the facile hydrogenolysis to toluene of benzonitrile is also explained by this mutual interaction. Moreover, hydrogenation of benzylamine as reactant under equal conditions does not produce toluene that facile. Previously, this hydrogenolysis step was not well-understood in nitrile hydrogenation literature. In addition, a recent article of Pasek and Krupka [9] reviewing the mechanisms of nitrile hydrogenation in general and benzonitrile in particular showed that the authors fully agree with my deductions, based on their own benzonitrile hydrogenation studies, about the mechanistic concepts of benzonitrile hydrogenation and toluene formation.

## Bibliography

- [1] B.A. Wilhite, R. Wu, X. Huang, M.J. McCready, A. Varma, *AIChE J.* 47 (2001) 2548.
- [2] J.A. Moulijn, M.T. Kreutzer, T.A. Nijhuis, F. Kapteijn, *Adv. Catal.* 54 (2011) 249.
- [3] D. Teschner, Z. Revay, J. Borsodi, M. Havecker, A. Knop-Gericke, R. Schlogl, D. Milroy, S. David Jones, D. Torres, P. Sautet, *Angew. Chem.* 120 (2008) 9414.
- [4] A. Quintanilla, V.C.L. Butselaar-Orthlieb, C. Kwakernaak, W.G. Sloof, M.T. Kreutzer, F. Kapteijn, *J. of Catal.* 271 (2010) 104.
- [5] S.G.R. Lafortier, P.J. Hamersma, A. Bardow, M.T. Kreutzer, *Labchip* (2012) submitted.
- [6] W. Li, K. Liu, R. Simms, J. Greener, D. Jagadeesan, S. Pinto, A. Gunther, E. Kumacheva, *JACS* 134 (2012) 3127.
- [7] H.R. Sahoo, J.G. Kralj, K.F. Jensen, *Angew. Chem. Int. Ed.* 46 (2007) 5704.
- [8] R.W.E.G. Reintjens, Q.B. Broxterman, M. Kotthaus, P. Poechlauer, US Patent 8,106,242 2012.
- [9] J. Krupka, J. Pasek, *Current Org. Chem.* 16 (2012) 998.



# 7

## **Multiscale Structure-Performance Relationships in Supported Palladium Catalysis for Multiphase Hydrogenations**

**- Summary**

---

This Chapter summarizes the main conclusions of this thesis.

---

### Tuning wall properties of structured monolithic palladium catalysts – hydrodynamic properties and extrinsic effect governing performance

A new class of structured, highly porous ceramic acicular mullite (ACM) monolith with an interconnected pore system (Fig 7.1a), was evaluated under *cold flow* conditions (room temperature) operated in the gas-liquid Taylor flow (segmented flow) regime in a continuous downflow set-up as well as under *hydrogenation* conditions in a semi-batch operated monolithic stirrer reactor.

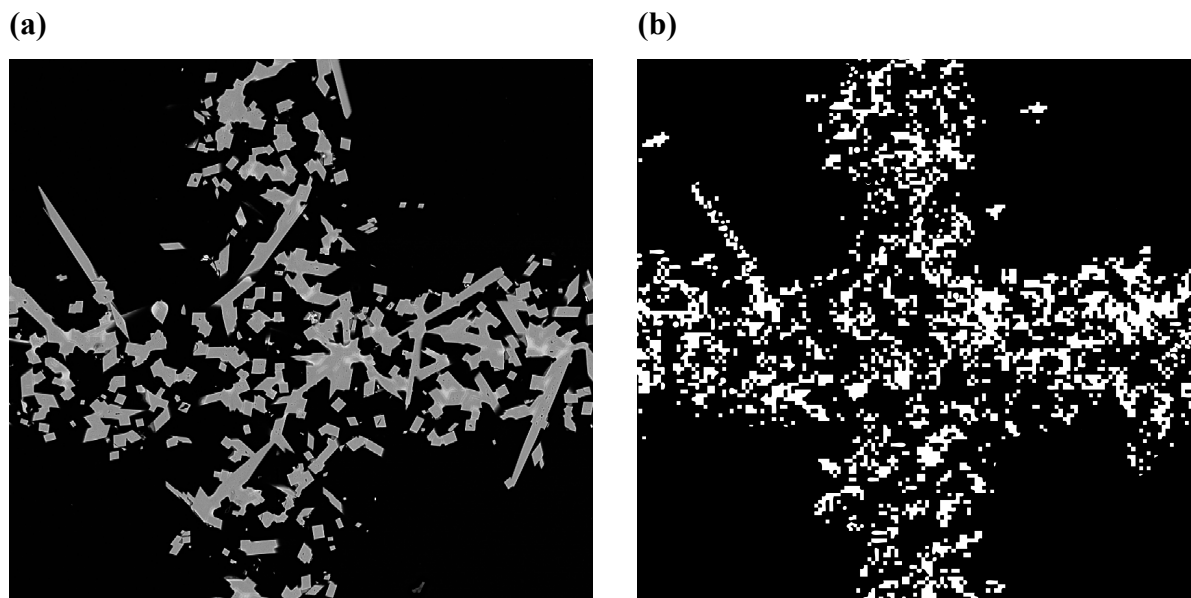


**Fig. 7.1.** Backscatter electron image of the intersection of a structured, highly porous ceramic ACM monolith wall (a) and the distribution of palladium inside the ACM walls as measured with EPMA (b).

#### *Hydrodynamic properties of an 'open wall' structured monolith reactor*

The hydrodynamic behavior of these ACM monoliths operated in Taylor flow was investigated by cold-flow tracer residence time distribution experiments and compared with the hydrodynamic behavior of classical cordierite monoliths in terms of static liquid fraction, maldistribution and mass exchange between the dynamic liquid zone and the static liquid zone. The piston-dispersion-exchange model was successfully applied to describe the experimental data. The multiphase fluid mechanics were different for ACM and cordierite monoliths: in contrast to the classical cordierite system, the mass exchange between static liquid and dynamic liquid was much higher and the liquid phase could access the open space

of the permeable ACM monolith wall (Fig. 7.2). However, the larger velocity maldistribution, larger static liquid fraction and the liquid interaction between adjacent ACM microchannels resulted in less plug flow behavior.

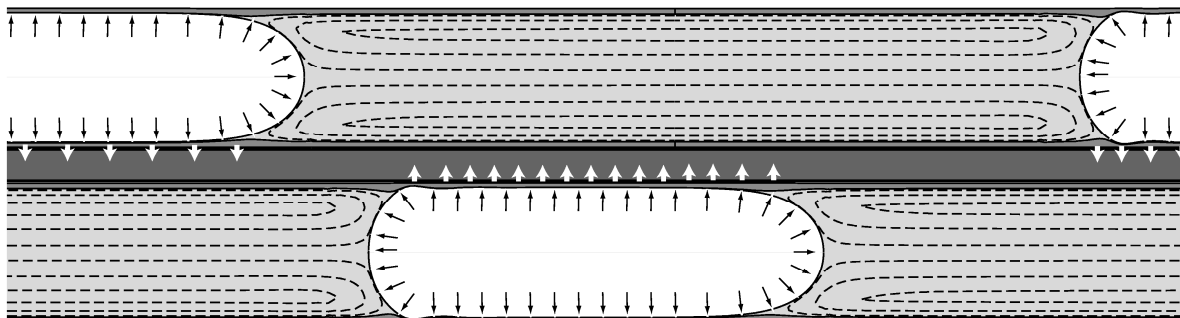


**Fig. 7.2.** Schematic representation of gas-liquid Taylor flow in ACM monoliths. A passing liquid bubble pushes the liquid into the highly porous permeable ACM wall. The black arrows represent the surface tension forces and the white arrows represent the radial convective transport of liquid into the ACM walls.

*Enhancement of catalyst performance using pressure pulses on macroporous structured supported palladium monoliths*

The preparation of catalysts based on the macroporous ACM monoliths was optimized for several critical preparation steps (pretreatment with  $\text{HNO}_3$ , modified pore filling method, microwave drying and palladium deposition using a newly designed forced flow device) and resulted in a uniformly distributed high surface area silica coating with evenly dispersed palladium crystallites on all length scales of the ACM monoliths. The open character and high permeability of the walls was preserved and resulted in a short effective diffusion length (Fig 7.1b).

The relationship between the wall structure of the ACM monolith and catalytic hydrogenation performance was investigated for the selective hydrogenation of 3-methyl-1-pentyn-3-ol in a monolithic stirrer reactor, under internal diffusion limited conditions, using ACM and cordierite silica-supported palladium monoliths. At 2.3 bar  $\text{H}_2$ , 20 mol/m<sup>3</sup> 3-methyl-1-pentyn-3-ol and 24°C, using equal catalyst loadings, the activity per unit monolith volume was 100% higher and the maximum yield of the desired product, 3-methyl-1-penten-3-ol, was 9% higher for the ACM monolith than for the eggshell coated monolith with impermeable walls. This confirms that internal diffusional limitations were reduced. Pressure pulses generated by passing hydrogen bubbles inside the monolith channels induced a convective enhancement

(Fig. 7.3), thereby decreasing the effective internal diffusion lengths and making mass transport limitations inside the highly permeable walls absent.

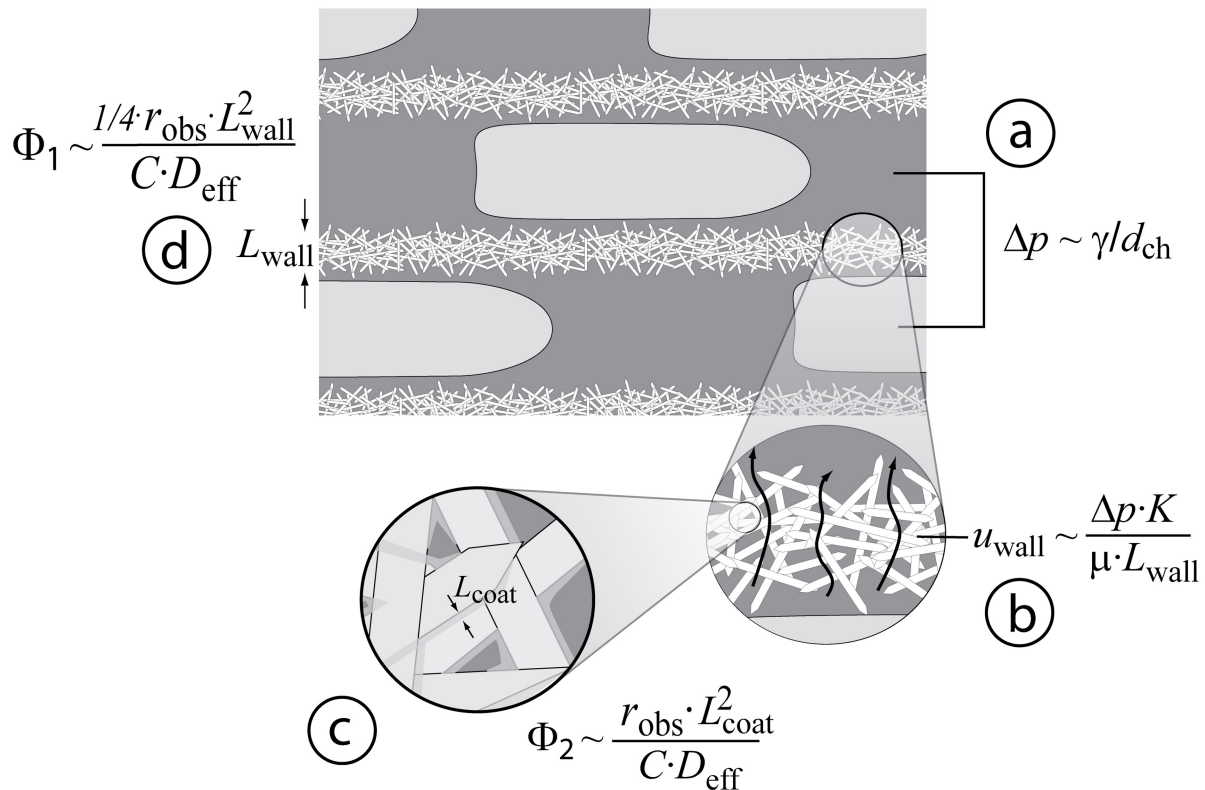


**Fig. 7.3.** Artists' impression of the mechanism of convective enhancement in ACM monolith channels displaying pressure difference created by passing bubbles (a), generation of flow through ACM monolith walls (b), ratio of coating diffusion and reaction time (c), ratio of wall diffusion time (enhanced by convective flow) and reaction time (d).

### Capillary flow device operated in Taylor flow regime for evaluation performance of supported palladium catalyst located on the wall

The use of a commercially available gas chromatography capillary as flow device operated in the Taylor flow regime, coated with a supported palladium catalyst on the inside capillary wall, gave rapid information about catalytic hydrogenation reactions. These fused-silica capillaries coated with a 6  $\mu$ m thick layer of high surface area  $\gamma$ -alumina were pretreated and subsequently impregnated with a palladium acetate solution. This resulted in nanosized palladium crystallites evenly dispersed on the  $\gamma$ -alumina coating layer over the full length of the capillary. The average palladium crystallite size inversely scaled with the palladium

concentration of the impregnation solution. It was shown how these visible features of Taylor flow under reaction conditions can be used in labscale multiphase heterogeneous catalysis.

Several hydrogenation reactions were performed to exemplify that visual observation of decreasing hydrogen bubbles allowed fast determination of conversion, deactivation and reaction rates under integral reaction conditions and so optimization of various aspects of heterogeneous catalysis.

Two specific examples show the benefits of the elimination of internal diffusion and axial dispersion. In the first example, “the proof of principle experiments”, the wall-coated palladium capillary flow device was used to determine the intrinsic catalytic activity in the model hydrogenation of cyclohexene to cyclohexane. It was shown that internal diffusional effects were absent for this fast hydrogenation reaction. The second example illustrated that the capillary flow device was operated under plug flow conditions in the selective hydrogenation of 3-methyl-1-pentyn-3-ol to 3-methyl-1-penten-3-ol without overhydrogenation to 3-methyl-3-pentanol. It was shown that with the capillary flow device the same selectivity for the intermediate product in this consecutive reaction scheme was obtained as in batch operation ensuring the absence of axial dispersion. The residence time and conversion were monitored visually, greatly simplifying bench-scale optimization (Fig 7.4).

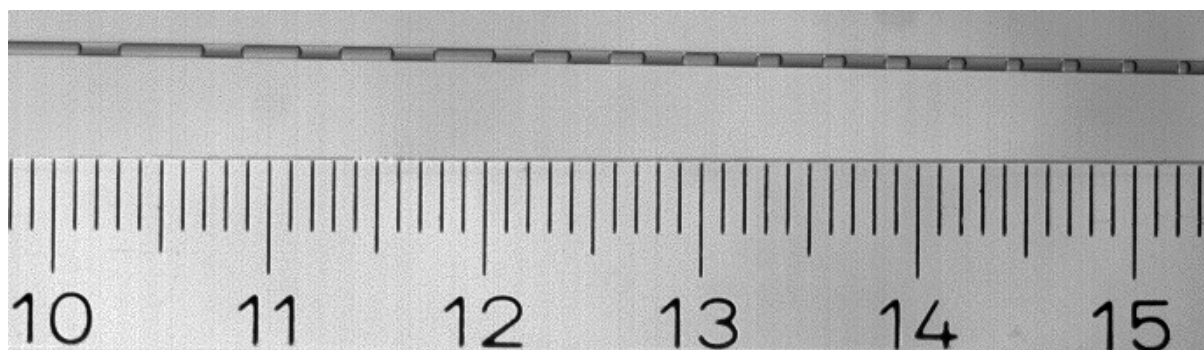


**Fig. 7.4.** Visual observation of decreasing hydrogen gas bubbles during the hydrogenation of 3-methyl-1-pentyn-3-ol in a Pd-capillary flow device (the ruler bar is graded in cm).

Further, it was demonstrated how to quickly identify deactivating species in multistep synthesis without intermediate workup. A self-synthesized mixture of mainly 3-phenyl-propyl-azide was hydrogenated towards the desired primary amine and the time on stream activity and selectivity behavior of the wall-coated palladium capillary were determined. The formation of nitrogen during this reaction discarded the use of the visible conversion determination by decreasing gas bubble sizes. A decrease in activity and selectivity was observed with time-on-stream during these hydrogenation experiments. Spiking experiments

with potential inhibitors were executed in a clean model hydrogenation reaction to quickly elucidate the source of these changes in catalyst performance with respect to deactivation.

**Catalyst performance changes induced by palladium phase transformation in the hydrogenation of benzonitrile -Intrinsic microscopic effect governing performance**

The influence of hydrogen pressure on the performance of a  $\gamma$ -alumina-supported palladium catalyst was studied for the multiphase selective hydrogenation of benzonitrile to benzylamine and byproducts. Semi-batch experiments of benzonitrile hydrogenation in 2-propanol were performed with hydrogen pressures between 2.5 and 30 bar, at a constant temperature of 80°C. The intrinsic property of palladium to absorb hydrogen into its lattice structure has a strong influence on activity and selectivity. The transformation to stable palladium  $\beta$ -hydride above a threshold hydrogen pressure of 10 bar induces a persistent change in turnover frequency and byproduct selectivity. The turnover frequency increases from  $0.32\text{ s}^{-1}$  to a maximum of  $0.75\text{ s}^{-1}$  at this threshold pressure and decreases to  $0.25\text{ s}^{-1}$  with further increasing hydrogen pressure. The formation of a palladium  $\beta$ -hydride phase suppresses the hydrogenolysis to toluene, changing the selectivity from 7% to 2% and increasing the selectivity of the condensation to dibenzylamine from 2% to 3% (Fig. 7.5).

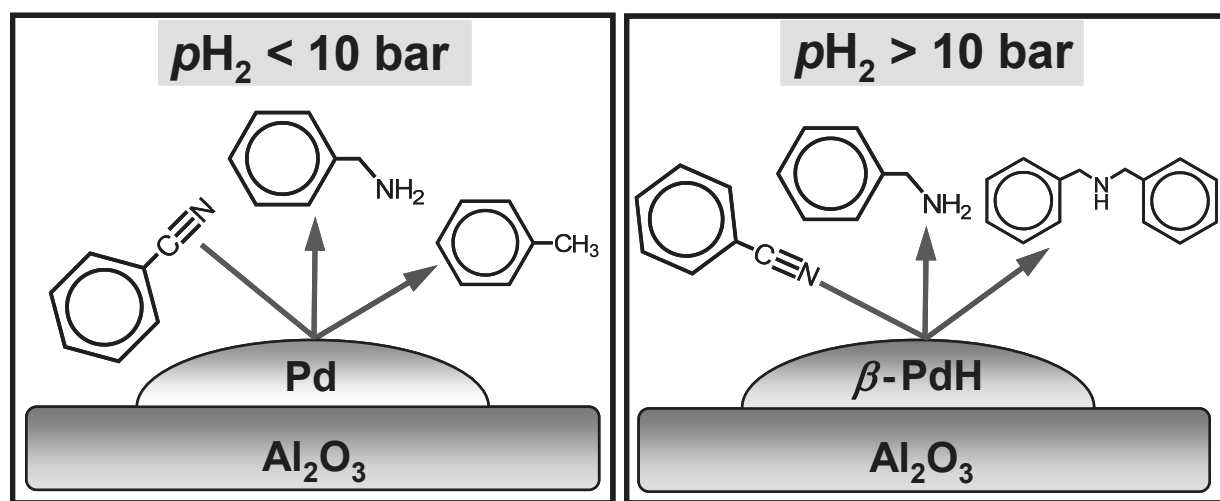


**Fig. 7.5.** The influence of hydrogen pressure ( $p\text{H}_2$ ) on the performance of a  $\gamma$ -alumina-supported palladium (Pd) catalyst was studied for the multiphase selective hydrogenation of benzonitrile to benzylamine and byproducts. The transformation to palladium  $\beta$ -hydride ( $\beta\text{-PdH}$ ) above a threshold  $p\text{H}_2$  of 10 bar induces a change in turnover frequency and byproduct selectivity.

These changes were attributed to modified electronic interactions between catalyst and substrates. The selectivity change was explained by combining the metal *d*-band model of reactivity and simple frontier electron orbital theory. The selectivity to the desired product benzylamine is always high and increases with hydrogen pressure from 93% to 95%. A detailed mechanism including surface intermediates for the hydrogenation of benzonitrile catalyzed by the  $\gamma$ -alumina-supported palladium was proposed that elucidated the reaction pathways towards the observed products. The physical state of the palladium catalyst is mainly determined by the activation or operational hydrogen pressure, whichever was the highest, if the activation pressure was above 10 bar.



# **Multiscale Structuur-Performance Relaties in Gedragen Palladium Katalyse voor Meerfase Hydrogeneringen**

## **Samenvatting**

Dit proefschrift beschrijft een gedeelte van het onderzoek dat is uitgevoerd naar de relatie tussen de prestaties en structuur, op alle lengteschaal niveaus, van palladium katalysatoren in meerfase hydrogeneringen. De prestaties van katalysatoren kan op alle structuur niveaus worden beïnvloed, zoals op reactorniveau door middel van het gas-vloeistof stromingspatroon, op katalysatordragerniveau door middel van het tekort aan reactant aan het katalysator oppervlak, en op moleculair niveau door middel van veranderingen in de kristalstructuur van de palladium katalysator.

### **Aanpassen van de wandeigenschappen van gestructureerde monolithische palladiumkatalysatoren – beïnvloeden van hydrodynamische eigenschappen en katalysatorprestaties**

Een nieuwe klasse van zeer poreuze keramische monolietstructuren van naaldvormig mulliet met een open poriesysteem werd onder cold-flow condities (kamer temperatuur) geëvalueerd in het Taylorstroming regime, in een continue downflow opstelling, evenals onder hydrogeneringsomstandigheden in een semibatch bedreven reactor.

### *Hydrodynamische eigenschappen van een gestructureerde monoliet reactor met 'open wanden'*

Het hydrodynamische gedrag van deze nieuwe mulliet monolieten werd onderzocht onder Taylorstroming condities door middel van cold-flow tracer verblijftijdspreidingsexperimenten en vergeleken met het hydrodynamische gedrag van klassieke cordieriet monolieten. Het ‘zuiger-dispersie-uitwisselings’ model werd succesvol toegepast om de experimentele gegevens te beschrijven. De meerfase stromingspatronen verschilden voor mulliet en cordieriet monolieten: in tegenstelling tot klassieke cordieriet monolieten was de massa-uitwisseling tussen de statische en dynamische vloeibare vloeistof veel hoger en kan de vloeistoffase de open ruimte van de permeabele mulliet wandjes binnendringen. De grotere malverdeling van kanaalsnelheden, de grotere statische vloeistoffractie en de vloeistof interactie tussen aangrenzende mulliet kanalen leiden tot verminderd propstroomgedrag.

### *Verbetering van palladium katalysatorprestatie door middel van drukpulsen in gestructureerde macroporeuze mulliet monolieten*

De bereiding van katalysatoren op basis van de macroporeuze mulliet monolieten werd, via enkele essentiële bereidingsstappen, geoptimaliseerd en resulteerde in een gelijkmatig verdeelde silica coating met een hoog specifiek oppervlak en met daarin een gelijkmatige verdeling van palladium deeltjes op alle lengteschalen van de mulliet monolieten. De hoge permeabiliteit van de wanden werd daarbij behouden en resulteerde in een korte effectieve diffusielengte.

De relatie tussen de wandconstructie van de mulliet monoliet en de hydrogenering prestatie gekatalyseerd door palladium werd onderzocht voor de selectieve hydrogenering van 3-methyl-1-pentyn-3-ol onder interne diffusie gelimiteerde omstandigheden in mulliet- en cordieriet monolieten. Het werd visueel waargenomen dat waterstof gasbelletjes de monoliet kanalen werden ingevoerd. De activiteit per monoliet volume voor de ‘open wand’ mulliet monoliet was 100% hoger en de maximale opbrengst van het gewenste product, 3-methyl-1-penteen-3-ol, was 9% hoger dan de cordieriet monoliet met ondoorlaatbare wand en gelijke katalysator belading onder 2.3 bar waterstof druk en 20 mol/m<sup>3</sup> 3-methyl-1-pentyn-3-ol bij 24°C. Dit bevestigt dat interne diffusielimiteringen werden verminderd. De drukpulsen gegenereerd door het passeren van waterstof belletjes in de monoliet kanalen veroorzaakt een convectieve vloeistofverversing in de wand, waardoor de effectieve interne diffusie lengtes verminderen en massa transport limiteringen afwezig zijn in de mullietwanden.

## Capillair-reactor voor evaluatie van de prestaties van palladium katalysatoren

Het gebruik van een commercieel verkrijgbare gaschromatografie capillair als reactor, in het Taylorstroming regime, bekleed met een gedragen palladium katalysator op de binnenzijde van de capillaire wand gaf snel informatie over katalytische hydrogeneringsreacties. Deze fused-silica capillairen voorzien van een 6  $\mu\text{m}$  dikke laag van aluminiumoxide waren voorbehandeld en vervolgens geïmpregneerd met een palladiumzoutoplossing. Dit resulteerde in palladium kristallieten gelijkmataig verdeeld in de aluminiumoxide laag over de gehele lengte van het capillair. Er werd aangetoond hoe deze zichtbare kenmerken van Taylorstroming onder reactieomstandigheden toegepast kunnen worden in labschaal meerfase heterogene katalyse. Verschillende hydrogeneringsreacties werden uitgevoerd waarbij de visuele waarneming van afnemende lengte van waterstof bellen een snelle bepaling van de conversie toelaat. Twee specifieke voorbeelden wijzen op de eliminatie van interne diffusielimitering en axiale dispersie. In het eerste voorbeeld, de "proof of principle", is het capillair gebruikt om de intrinsieke katalytische activiteit van een model-hydrogenering (cyclohexeen naar cyclohexaan) te bepalen. Er werd aangetoond dat interne diffusielimiteringen afwezig waren tijdens deze snelle hydrogeneringsreactie. Het tweede voorbeeld illustreerde dat het capillair werd bedreven onder propstroomomstandigheden tijdens de selectieve hydrogenering van 3-methyl-1-pentyn-3-ol tot 3-methyl-1-penteen-3-ol. Er werd aangetoond dat met het capillair dezelfde selectiviteit voor het tussenproduct werd verkregen, en axiale dispersie voorkomen werd. De verblijftijd en conversie werden visueel geverifieerd, waardoor optimalisatie eenvoudiger wordt.

Verder werd aangetoond hoe het deactiveren door verschillende componenten snel opgehelderd kan worden in meerstapssynthese zonder tussenliggende opwerking van gevormde intermediairen. Een zelfgesynthetiseerd mengsel van voornamelijk 3-fenyl-propylazide werd gehydrogeneerd tot de gewenste primaire amine en daarbij werd de time-on-stream activiteit en selectiviteit van het palladium capillair bepaald. Tijdens deze hydrogeneringsexperimenten werd een afname in activiteit en selectiviteit waargenomen. 'Spiking'-experimenten met mogelijke reactieremmers werd uitgevoerd in een model hydrogenering waarmee de bron van deactivering snel opgehelderd kon worden.

## **Veranderende katalysator prestaties geïnduceerd door een palladium fasetransformatie tijdens de hydrogenering van benzonitril**

De invloed van waterstofdruk op de prestaties van een aluminiumoxide gedragen palladium katalysator werd bestudeerd voor de selectieve hydrogenering van meerfase benzonitril naar benzylamine en derivaten. Semibatch benzonitril hydrogenering proeven in 2-propanol werden uitgevoerd onder waterstofdrukken tussen 2.5 en 30 bar, bij een constante temperatuur van 80°C. De intrinsieke eigenschap van palladium om waterstof te absorberen in zijn rooster structuur heeft een sterke invloed op de activiteit en selectiviteit. De transformatie naar de stabiele palladium  $\beta$ -hydride fase boven een drempelwaarde, een waterstofdruk van 10 bar, induceert een blijvende verandering in intrinsieke omzettingssnelheid ( $TOF$ , turn-over frequentie) en bijproduct selectiviteit. De  $TOF$  neemt toe van  $0.32\text{ s}^{-1}$  tot  $0.75\text{ s}^{-1}$  bij deze waterstofdruk en daalt vervolgens tot  $0.25\text{ s}^{-1}$  met een verdere verhoging van waterstofdruk. De vorming van de palladium  $\beta$ -hydride fase onderdrukt de hydrogenolyse tot tolueen, dit verlaagde de selectiviteit van 7% naar 2%, en verhoogde de selectiviteit van condensatie tot dibenzylamine van 2% naar 3%. Deze veranderingen werden toegeschreven aan de gewijzigde elektronische interacties tussen katalysator en substraten. De selectiviteitsverandering werd verklaard door het combineren van het  $d$ -band model voor reactiviteit en de moleculaire ‘frontier electron orbital’ theorie. De selectiviteit naar het gewenste produkt (benzylamine) was altijd hoog en neemt toe met waterstofdruk van 93% tot 95%. Een gedetailleerd mechanisme is gepresenteerd voor de hydrogenering van benzonitril gekatalyseerd door aluminiumoxide gedragen palladium. De palladium katalysatortoestand wordt voornamelijk bepaald door de hoogste waterstofdruk tijdens activering of reactie, indien een van deze drukken hoger was dan 10 bar.

# Publications and presentations

## Publications

- [1] K.M. de Lathouder, **J.J.W. Bakker**, M.T. Kreutzer, F. Kapteijn, J.A. Moulijn, S.A. Wallin, *Chem. Eng. Sci.* 59 (2004) 5027.
- [2] M.T. Kreutzer, **J.J.W. Bakker**, P.J.T. Verheijen, F. Kapteijn, J.A. Moulijn, *Ind. Eng. Chem. Res.* 44 (2005) 4898.
- [3] K.M. de Lathouder, **J.J.W. Bakker**, M.T. Kreutzer, S.A. Wallin, F. Kapteijn, J.A. Moulijn, Sustainable (Bio)Chemical Process Technology - Incorporating the 6<sup>th</sup> International Conference on Process Intensification. Delft, The Netherlands, 2005, 21.
- [4] **J.J.W. Bakker**, M.T. Kreutzer, K.M. de Lathouder, F. Kapteijn, J.A. Moulijn, S.A. Wallin, *Catal. Today* 105 (2005) 385.
- [5] M.T. Kreutzer, **J.J.W. Bakker**, S.A. Wallin, F. Kapteijn, J.A. Moulijn, K.M. de Lathouder, Patent WO2005/084805 A1 2005.
- [6] K.M. de Lathouder, **J.J.W. Bakker**, M.T. Kreutzer, F. Kapteijn, J.A. Moulijn, S.A. Wallin, *Chem. Eng. Res. Dev.* 84 (2006) 390.  
*IChE Moulton Metal Award 2006.*
- [7] **J.J.W. Bakker**, W.J. Groendijk, K.M. de Lathouder, F. Kapteijn, J.A. Moulijn, M.T. Kreutzer, S.A. Wallin, *Ind. Eng. Chem. Res.* 46 (2007) 8574.
- [8] A. Quintanilla, **J.J.W. Bakker**, M.T. Kreutzer, J.A. Moulijn, F. Kapteijn, *J. Catal.* 257 (2008) 55.

[9] **J.J.W. Bakker**, A.G. van der Neut, M.T. Kreutzer, J.A. Moulijn, F. Kapteijn, *J. Catal.* 274 (2010) 176.

[10] **J.J.W. Bakker**, M.M.P. Zieverink, R.W.E.G. Reintjens, F. Kapteijn, J.A. Moulijn, M.T. Kreutzer, *ChemCatChem* 3 (2011) 1155.

[11] V.P. Santos, **J.J.W. Bakker**, M.T. Kreutzer, F. Kapteijn, J. Gascon, *ACS Catal.* 2 (2012) 1421.  
*Featured as front cover.*

[12] V.P. Santos, O.S.G.P. Soares, **J.J.W. Bakker**, F. Kapteijn, M.F.R. Pereira, J.J.M. Órfão, J. Gascon, F. Kapteijn, J.L. Figueiredo, *J. Catal.* 293 (2012) 165.

[13] K. Kowlgi, **J.J.W. Bakker**, H. Jansma, M. Makkee, P.J. Kooyman, S. Picken, G. Koper, *Carbon* (2012).  
*Submitted.*

### Oral presentations

[1] K.M. de Lathouder, A.F. Perez Cadenas, **J.J.W. Bakker**, F. Kapteijn, J.A. Moulijn, Workshop on carbon nanofibers. TU Twente, Enschede, The Netherlands, 2004.

[2] S.A. Wallin, K.M. de Lathouder, **J.J.W. Bakker**, M.T. Kreutzer, F. Kapteijn, J.A. Moulijn, 18<sup>th</sup> International Symposium on Chemical Reaction Engineering. Chicago, USA, 2004.

[3] K.M. de Lathouder, **J.J.W. Bakker**, M.T. Kreutzer, S.A. Wallin, F. Kapteijn, J.A. Moulijn, Sustainable (Bio)Chemical Process Technology - Incorporating the 6<sup>th</sup> International Conference on Process Intensification, The Netherlands, September 27-29, 2005.

[4] **J.J.W. Bakker**, M.T. Kreutzer, K.M. de Lathouder, F. Kapteijn, J.A. Moulijn, S.A. Wallin, ICOSCAR-2, Delft, The Netherlands, 2005.

[5] **J.J.W. Bakker**, M.M.P. Zieverink, M.T. Kreutzer, F. Kapteijn, J.A. Moulijn, NCCC VIII, Noordwijkerhout, The Netherlands, 2007.

[6] **J.J.W. Bakker**, M.T. Kreutzer, K.M. de Lathouder, F. Kapteijn, J.A. Moulijn, CAMURE 6 & ISMR 5, Pune, India, 2007.

[7] **J.J.W. Bakker**, A.G. van der Neut, J.A. Moulijn, M.T. Kreutzer, F. Kapteijn, EUROPACAT VIII, Turku, Finland, 2007.

### **Poster presentations**

[1] **J.J.W. Bakker**, W. Wei, M.T. Kreutzer, F. Kapteijn, J.A. Moulijn, Meeting Mastering Molecules in Manufacturing, Delft, The Netherlands, 2002.

[2] **J.J.W. Bakker**, M.M.P. Zieverink, M.T. Kreutzer, F. Kapteijn, J.A. Moulijn, NPS6, Velthoven, The Netherlands, 2006.

[3] M.T. Kreutzer, **J.J.W. Bakker**, F. Kapteijn, J.A. Moulijn, ISMR3, Bath, UK, 2003.

[4] V.P. Santos, **J.J.W. Bakker**, J. Gascon, M.T. Kreutzer, F. Kapteijn, NPS11, Velthoven, The Netherlands, 2011.



# Dankwoord / Acknowledgements

Hierbij wil ik de mensen bedanken die hebben bijgedragen aan dit proefschrift. Om te beginnen wil ik mijn promotoren, Jacob Moulijn, Michiel Kreutzer, en Freek Kapteijn, bedanken dat jullie mij de mogelijkheid hebben geboden om deel uit te maken van jullie vakgroep. Tevens wil ik jullie bedanken voor de hulp bij het tot stand komen van mijn onderzoek en de hulp bij het schrijven van de wetenschappelijke artikelen. Michiel Kreutzer, mijn dagelijkse begeleider, ik wil je speciaal bedanken voor je hulp bij vrijwel alle facetten van de wetenschap en het schrijven van wetenschappelijke teksten in het bijzonder.

Ik wil DSM N.V., en Raf Reintjens in het bijzonder, bedanken voor de zeer prettige samenwerking, de mogelijkheid om de vele ‘gevaarlijke’ experimenten bij jullie in het lab in Geleen uit te voeren, kennis te maken met zeer prettige labmedewerkers en natuurlijk de financiële steun voor Hoofdstuk 4. Also, I would like to thank the DOW Chemical Company, and specifically, Sten Wallin, for the fruitful cooperation and financial support related to Chapter 2 and 3.

Karin de Lathouder, Edwin Crezee en Martijn Zieverink wil ik bedanken voor de intensieve en zeer prettige samenwerking op het gebied van hoge druk autoclaven, monolieten, enzymen, koolstoffibers en minuscule buisreactoren. Grote dank ben ik verschuldigd aan mijn afstudeerders, Willem Groendijk en Anne Geert van der Neut, die een aanzienlijk deel van de experimenten in Hoofdstuk 3 en 5 hebben uitgevoerd. I also want thank my Erasmus student Petr Martinek, for his experimental work related to several parts of Chapter 4. Mijn dank is groot voor de hulp van Harrie Jansma en Bart van der Linden bij het oplossen van de vele technische problemen. Johan Groen en Sander Brouwer wil ik bedanken voor de hulp bij de karakterisering van de palladiumkatalysatoren. I thank Canan Güçüyener and Vera Santos for reviewing this PhD thesis. Verder wil ik de super secretaresses Els Arkesteijn en Elly Hilkhuijsen heel erg bedanken voor alle hulp.

Special thanks to all my (former) roommates; Nari, Agus, Edwin, Nakul, Asun, Jianrong, Bandar, Leticia, Joana, and Vera: it was an honour to have shared a room with all of you! Thanks for the very nice times and the many discussions about all facets of life, even including some scientific ones. I also want to thank all other (former) colleagues, too many to mention them all, of the CE-group for the nice working environment. Tot slot wil ik Angelique bedanken voor haar onvoorwaardelijke steun en liefde!



# Curriculum Vitae

Jasper Jacobus Wilhelmus Bakker werd geboren op 21 februari 1974 te Dordrecht. Na het behalen van zijn VWO diploma aan de scholengemeenschap professor Zeeman te Zierikzee, begon hij in september 1993 met zijn studie Chemische Technologie aan de HTS te Dordrecht. In juni 1998 studeerde hij af bij Unimills B.V. te Zwijndrecht. In september 1998 begon hij zijn studie Scheikundige Technologie aan de Technische Universiteit te Delft en studeerde hij af onder begeleiding van prof. dr. ir. M.T. Kreutzer in december 2002. In januari 2003 begon hij als promovendus met zijn promotieonderzoek aan de Technische Universiteit Delft in de vakgroep Reactor & Catalysis Engineering van prof. dr. J.A. Moulijn. De resultaten van dat onderzoek zijn beschreven in dit proefschrift. Op dit moment is hij werkzaam als postdoc researcher bij de Technische Universiteit Delft in de vakgroep Catalysis Engineering van prof. dr. F. Kapteijn.



